C. ELEGANS BEHAVIOUR AND BRAIN DYNAMICS; A PHYSICAL EXPLORATION

Willem Mathijs Rozemuller

This thesis was reviewed by:

dr. G. J. Stephens,	Vrije Universiteit Amsterdam
prof. dr. ir. E. J. G. Peterman,	Vrije Universiteit Amsterdam
dr. E. C. M. Carroll,	Technische Universiteit Delft
dr. G. Jansen,	Erasmus Medisch Centrum
prof. dr. W. Ryu,	University of Toronto

The work described in this thesis was performed at AMOLF, Science Park 104, 1098XG, Amsterdam, The Netherlands.

This thesis was printed by Ipskamp.

ISBN 978-94-6473-089-0

An electronic version of this thesis can be obtained from `www.amolf.nl` and `www.ub.vu.nl`. Printed copies can be obtained by request via library@amolf.nl

VRIJE UNIVERSITEIT

C. ELEGANS BEHAVIOUR AND BRAIN DYNAMICS; A PHYSICAL EXPLORATION

ACADEMISCH PROEFSCHRIFT

ter verkrijging van de graad Doctor of Philosophy aan
de Vrije Universiteit Amsterdam,
op gezag van de rector magnificus
prof.dr. J.J.G. Geurts,
in het openbaar te verdedigen
ten overstaan van de promotiecommissie
van de Faculteit der Bètawetenschappen
op woensdag 26 april 2023 om 13.45 uur
in een bijeenkomst van de universiteit,
De Boelelaan 1105

door

Willem Mathijs Rozemuller

geboren te Amsterdam

promotor:	prof. dr. T. S. Shimizu
promotiecommissie:	dr. G. J. Stephens
	prof. dr. ir. E. J. G. Peterman
	dr. E. C. M. Carroll
	dr. G. Jansen
	prof. dr. W. Ryu

CONTENTS

1

INTRODUCTION

Available evidence suggests that humans have been fascinated by animals and their behaviour from long before recorded history. From prehistoric cave paintings to the beasts of Greek mythology, animal behaviour has featured prominently in our imaginations since ancient times. Today, we are no less enthusiastic about our zoological kin, flocking to the zoo on a hot day, spending our holidays on remote safaris, and keeping pets for amusement and companionship. The fascination has not been lost on scientists, who have amassed a large body of work on animal behaviour over the past centuries, from two contrasting perspectives. The first, which might be called the *functional perspective* on behaviour, pioneered by Darwin [1], emphasises how behaviour impacts an organism's fitness in an evolutionary context, and has led to the modern field of ethology [2, 3]. The second, which might be called the *mechanistic perspective* on behavior, arose nearly a century earlier from physiological studies perhaps best exemplified by the iconic bioelectricity experiments of Galvani [4] and Volta [5]. It emphasises how behaviour is implemented by the underlying anatomy and physiology of an organism, and has since developed into the modern field of neuroscience [6, 7]. These two academic traditions offer starkly different kinds of explanations to the same question, *"What shapes animal behavior?"* Simply stated, the functional perspective aims to answer *why* behaviour is as we see it, whereas the mechanistic perspective strives to uncover *how* those behaviours are generated.

Traditionally, these two classes of explanations have involved contrasting approaches to studying behaviour, each with associated challenges. A functional explanation usually entails careful observation and classification of behaviour, followed by interpretation of it as part of an evolutionary *strategy*. The latter often requires a deep understanding of the complex ecological context, and hence much work in this direction is carried out in the field, outside of controlled laboratory settings. A mechanistic explanation usually entails studying the control and actuation of behaviour as the output of relevant anatomical and physiological *systems*. The complexity of the latter is epitomised by the human brain, but even in simpler organisms, understanding the collective dynamics of more than a handful of neurons remains an unsolved problem and much of contemporary neuroscience is dedicated to studying the dynamics of neural subcircuits of the brain — identified by anatomical or functional connectivity — in genetic model organisms amenable to laboratory experiments.

A common challenge faced by both approaches is the difficulty in avoiding *subjectivity*. In the ethological approach, progress has relied on expert insight not only in how to observe behavior, but, more fundamentally, also in defining the behaviours to be observed. In the neuroscience approach, progress has relied on expert-guided choices about which specific neurons, or brain regions, to focus on. Recent technological advances make it possible to collect expansive data sets on both behaviour [8–11] and the brain [12–16], giving rise to powerful data-driven approaches that can drastically reduce the degree of subjectivity in both functional [17] and mechanistic [18] studies of behavior. While these advances in behavioral and neural data throughput are exciting in their own right, the advent of data-driven approaches in both ethology and neuroscience have arguably brought these historically separated approaches and their practitioners closer together. With the parallel development of data-driven approaches in both arenas, the gulf between the fields is narrowing. This thesis aspires to contribute to this trend by developing data-driven approaches to both behaviour and the brain in one of the simplest organisms amenable to such studies — the nematode worm *C. elegans*. This is one of a handful of organisms in which whole-brain imaging and high-throughput behavioural recordings are currently possible, and it is by far the simplest of them.

We focus on motile behavior, which is readily quantified by imaging. A key feature of our approach is to leverage behavioural variability. When studying motile behaviour, no two repetitions of the same experiment yield the exact same outcome. Even for genetically identical organisms under identically controlled conditions, variability is a generic property of any living system, and can be observed in various quantitative traits [19], including those associated with behaviour [20]. The potential causes of variability are diverse. At the molecular level, all biological systems depend on interactions that are fundamentally stochastic, due to processes carried out by finite numbers of molecules, inevitably resulting in 'noise' [21–23]. Variability may also manifest at larger scales such at the level of the synapse [24], chaotic dynamics in the neuronal network [25], or even the entire organism. An illustrative example of variability at the organism scale is the unique preferential locomotor handedness observed across individuals within an isogenic (genetically identical) population of *Drosophila* [26, 27]. Another striking example of (non-genetic) individuality is the armadillo *Dasypus novemcinctus* where developmental stochasticity can explain a substantial portion of variation [28]. At the level of behaviour, stochasticity can place limits on the organism's capacity to exert control — for example, the ability to reproducibly form a stimulus dependent behavioural response. These limitations in turn constrain the repertoire of behavioural strategies an organism can implement/deploy, and it can be expected that behaviours could evolve to optimally mitigate detrimental effects of variability.

From the experimenter's point of view, behavioural variability necessitates the observation of many individuals in studies of behavior. Typically, most information about the variability is disregarded, reporting average responses under various controlled conditions. In this thesis, we take a contrasting approach, in which we seldom perturb or change the animal's environment, but rather focus on leveraging the variability in behaviour observed across individuals under identically controlled conditions. This approach has a number of advantages. First, because each individual behaves uniquely, the ensemble of behavioural recordings across individuals allows us to map a space of *naturally relevant* behavioural phenotypes without resorting to perturbations (which, unless very carefully chosen and calibrated, may provoke unnatural or extreme responses). Second, studying the statistics of behavioural phenotypes within the mapped behavioural space has the potential to uncover interesting strategies deployed by the organism that may otherwise be masked by averaging. One such example is the bet-hedging strategy [29, 30], wherein stochastic behavioural variability is beneficially added, preparing the population for unpredictable situations. Finally, clues about the mechanistic origins of variability can be provided by studying the partitioning of variability across time, individuals, or even genotypes (e.g. strains or species). For example, if multiple phenotypic traits change in a correlated way across species, it could suggest a common genetic or regulatory pathway. As for temporal dynamics, sub-second fluctuations could be of neuronal origin, fluctuations at the hour timescale could be of gene expression origin, and static differences (i.e. individuality) in isogenic populations could be of developmental origin.

A major challenge for developing a mechanistic understanding of behaviour is the interdependence and sheer complexity of the relevant anatomy and physiology, which comprise innumerable interactions that play out over many orders of magnitude in time and length scales. Actuation of a movement involves molecular interactions of proteins at the manometer scale, generation of action potentials of a neuron at the micrometre scale, coordination of brain dynamics at the millimetre to centimeter scale, to movement through muscle activation at the organism scale. While many of these interactions occur on subsecond timescales, longer-time processes could be relevant, such as the history of experience, potentially up to the life time of the organism (e.g. via neuronal plasticity [31]), or even further, spanning multiple generations through epigenetics [32]. To be able to respond fast and adequately to many different inputs, the system's architecture, especially at the level of the brain, is highly interconnected with non-linear interactions. Thus, the response of a neuron is dependent on many other neurons, and its function may only be interpreted in the context of the other neurons. Therefore, it is useful to study brain dynamics using whole-brain imaging. More so, combining two approaches, recording brain dynamics simultaneously with motile behaviour, could be a crucial step towards acquiring a better understanding of the brain [12], because it provides behavioural context for brain dynamics. One of the two approaches to understanding behaviour in this thesis takes a step in this direction by developing a system where, by choosing the right model organism, and with controlled input signals, both whole-brain dynamics and a simple form of motile behavioural output can be observed simultaneously.

Our goal is to go beyond simply amassing volumes of data, or to report on the myriad of correlations and other statistical features of these rich datasets. In this thesis, we strive for fundamental understanding by developing a physics-inspired approach to dissecting behaviour and brain dynamics in a principled way. Although studying behavioural variability and whole-brain dynamics has many potential benefits, it is also opening a can of worms. With modern cameras, terabytes of observational data can be produced with ease, yielding an overwhelming amount of information with almost as much variability. To navigate this wealth of data, we take a top-down approach to both brain and behavior, focusing on large-scale phenomena of the brain dynamics and generalizable aspects of behaviour. This requires compression of the data, using some form of dimensionality reduction, while retaining biologically relevant information. We rely on the construction and exploration of models to create a framework from which to interpret the data and analyze its implications. Such models should be minimalistic for interpretability while describing the relevant dynamics, including variability.

C. elegans, a unique model system for behavior and brain

The nematode *Caenorhabditis elegans* possesses a number of properties that make it an excellent model organism for our purposes. Firstly, when well maintained in the lab, the most commonly used N2 strain of *C. elegans* is predominantly a hermaphrodite (although there can be a small fraction of males with largely the same genome, lacking an X chromosome). Therefore, populations are isogenic, eliminating genotypically induced variability. In addition, their generation time of ≈ 3.5 days at room temperature allows for rapid propagation of laboratory populations and a short experimental cycle. Secondly, an adult hermaphrodite is only ≈ 1 mm long and possesses only 959 somatic cells, which include the epidermis, muscles, digestive system, and nervous system. Their body layout is highly stereotyped (i.e. different individuals have the same number of cells with the same functions in similar positions), which allows for the study of internal processes across individuals at the single-cell level. In addition, the worm is transparent and therefore well suited for non-invasive optical methods to probe internal processes *in vivo*. Collectively, these properties have made *C. elegans* an extensively studied model organism — indeed, it was the first multicellular organism to have its genome fully sequenced [33], and was for decades the only animal in which the full wiring diagram of its nervous system, the *connectome*, has been mapped to completion [34] (the only other organisms with a mapped connectome are the larve *Ciona intestinalis*[35], *Platynereis dumerilii*[36], and *Drosophila*[37]).

The motile behaviour of *C. elegans*.

In nature *C. elegans* can be encountered in rotting plant material [38], feasting on the bacteria that grow there. Within the laboratory, its motile behaviour can readily be studied on the agar plates, as they tend to incessantly crawl on their surface. One of the main advantages of studying the worm is the simplicity with which its behaviour at the most basic level can be quantified. *C. elegans* has a bendable rod-like body shape and moves, laying on its side, by means of undulatory propulsion (*i.e.* like a snake) driven by a coupled set of motor neurons [39] that generate oscillatory bending waves that travel along the dorso-ventral body direction. Numerous tracking systems have been developed to monitor worm motility [40, 41], tracking the worm's centroid position and may also resolve the underlying postural dynamics in fine detail and/or allow tracking of multiple worms simultaneously. Worm posture provides a compact yet rich basis for describing worm movements. It can be described by a smooth and unbranched curve tracing the body contour from head to tail, thereby compressing in every image frame the state of the anatomy to a vector of angles. Studying changes in this posture (using a PCA on the postural angle temporal dynamics along the body axis) has revealed that the worm has stereotypic motile behavior, which can be described in a low dimensional configuration space with 95% of variation described as a superposition of four basic shapes called 'Eigenworms' [8, 42], further compressing the posture to just 4 mode weights. Changes in posture on time scales similar to a body wave (∼ 1 s) describe the most elemental behaviours of the worm: forward crawling, reverse crawling (a brief inversion of the body wave phase velocity), pause [43], and turning, often in the form of a sharp Ω [44] or δ [45] turn. The δ-turn [45] is a recently discovered sharp turn type that could be discovered using a large data set and machine learning tools. How this turn type is strategically used by the worm in different environments has not yet been studied, and is one of the topics of this thesis.

Despite only possessing a few motile behavioural elements, the worm is able to perform a diverse set of navigational tasks, as the frequency and duration of these basic behavioural elements are modulated by the environment. In the lab setting, while on an agar plate shortly after being taken off food, a worm will typically spend the majority of time crawling forward, with brief interruptions for reversals or sharp turns. A strong aversive stimulus such as touch [46] (to escape from traps [47]), or a strong repellent e.g. sodium dodecyl sulfate (SDS) applied at the head [48], may trigger an escape response; a reversal following a sharp turn, using the neuromodulator Tyramine [49, 50]. Although this is a highly stereotypical behaviour, there is evidence that the reversal duration is modulated by the strength and amplitude of the stimulus in response to heat [51–53]. To navigate up or down a gradient (e.g. NaCl [54]), a stochastic strategy is deployed, where the 'pirouette' (bouts of reversals and sharp turns) probability is down- or up regulated depending on whether the worm moves towards or away from the preferred gradient, respectively [55] causing a biased random walk, a strategy similar to the run-and-tumble mechanism of *E. coli* [56]. The worm can navigate up and down a wide range of concentrations by computing the relative concentration change [57]. In addition, a 'weathervaning' strategy is deployed, which more gradually veers the worm towards the preferred gradient during forward locomotion [58]. To oxygen, the worm could also modulate its speed [59]. In a situation where the worm is crawling on a food patch, worms switch behavioural states where the extremes [60] are described as dwelling (exploitation) behavioural state with many reversals and turns, a roaming (exploration) state with long uninterrupted forward runs [61, 62], and quiescence [63] (no crawling).

The worm has the capacity to adapt its strategy by incorporating time scales far exceeding the orientation decorrelation time. Upon removal from food, the frequency of sharp turns, reversals, and pirouettes (bursts of reversals and turns) is gradually decreased, resulting in a larger explored space [64–66], which may even be superdiffusive [67]. An environmental condition can be associated with the presence of food, changing the preferable concentration during NaCl chemotaxis [68] (encoded in the ASER sensory neuron [69, 70]) or thermotaxis [71]. Long time-scale changes in worm behaviour, such as the quiescent sleep state during lethargus [72, 73], may be part of a stereotyped developmental program [74]. Some worms exhibited increased (non-heritable) dwelling or roaming throughout development, indicating a personality [74].

The nervous system

Among the 959 somatic cells of the hermaphrodite are 302 neurons, one of the tiniest brains known in the animal kingdom. It is therefore, with current technology, one of the few organisms where it is feasible to study and understand neuronal processing down to the level of a single neuron. *C. elegans* was the first organism with a fully mapped hermaphrodite connectome already in 1986 [34, 75], recently also updated for males [76], and across development [77]. The nervous system can be divided into 118 neuron classes [34], often a left/right symmetric pair. These classes form three groups (some neurons occupy multiple groups): sensory neurons collecting information about the internal state and environment, interneurons processing the information, and motorneurons controlling the muscles.

Information between neurons is transmitted through synapses or neuromodulators. The connectome of the hermaphrodite consists of chemical synapses releasing neurotransmitters with an excitatory or inhibitory effect on the activity of the target neuron, gap junctions (or electrical synapses) creating a bidirectional direct connection between the cytoplasm of two neurons, and neuromuscular junctions controlling the contraction of muscle fibres for motor activity. The total number of chemical synapses in *C. elegans*, around ~ 8000 [77], is similar to that of a single human neuron, but encodes the entire behavioural repertoire, which requires complex functionality such as neuronal plasticity [78]. Although the synaptic connections between neurons are mostly conserved (~ 72%), it should be noted that there is a substantial number of variable synapses (~ 1100), accounting for half the connected neuron pairs [77]. It is therefore plausible that individual behavioural variability is imposed by variability in the wiring diagram. Besides synapses, which require neurons to be in extreme proximity and are therefore easily identified, neurons can also communicate via neuromodulators: molecules released by neurons that travel further and thereby influence (multiple) neurons at a distance. These effects may last minutes and alter the way information is processed to adapt to the environment [79]. For instance, PDF and serotonin encode for exploration (roaming) and exploitation (dwelling) behaviors, respectively [61]. Of particular interest are biogenic amines that can be taken up by the worm and may be applied exogenously during experiments. The worm uses four biogenic amines: octopamine, tyramine, dopamine, and serononin, which may function as neuromodulators or neurotransmitters to respond to the environment by influencing pharyngeal pumping, egg laying, learning, and locomotion [80]. The effect of neuromodulators on motile behaviour has been extensively studied [79], however its impact on the global brain dynamics underpinning this behaviour is open. Such an understanding could bridge knowledge of local impact on target neurons and the output behaviour.

Although a fully mapped connectome is a valuable tool for neuronal research, it does not predict behaviour because of unknown types of chemical connections, and the number of connections does not predict the functional weight (which may vary under certain conditions) of the connection [81]. Studying functional relationships therefore requires intervention to change the connectome or direct recordings of the neuronal activity. Traditionally, neuronal functions and the underlying circuitry is probed by studying behaviour, such as chemotaxis [54, 58], foraging [82], navigation [64], under ablation (killing of neurons using a laser) of specific neurons [83] or by mutations. Removal of functionality of neurons provides insight, but is highly disruptive and doesn't allow for the study of brain signalling dynamics. Initially, neuronal activity was recorded using electrophysiological recordings [84], but this is invasive, labor-intensive, and performed on single cells. Advances in genetics enabled to study brain dynamics non invasively using sensitive genetically encoded Ca^{2+} indicators (GECIs) (often an optimized version of GCaMP [85, 86]), fluorescent proteins where the fluorescent properties depend on the presence of calcium, a proxy for the neuronal activity [87]. Leveraging the transparency of the worm, knowledge of worm genetics, and advances in imaging techniques, these can be expressed and recorded in targeted neurons. In rapid succession, these have been used in more complex settings: from single neurons in semi constrained worms with [88] or without [89] using optogenetics, to single neurons in freely moving worms with [90, 91] and without [92] the use of optogenetics, to single neurons in multiple worms simultaneously [93]. There has also been a trend toward increasing the number of recorded neurons [94]. Leveraging the worms small brain, recent measurements started to record activity of most (or as many as possible) neurons simultaneously in the worm head, containing the majority of sensory and interneurons [14, 73, 95–104]. This requires rapid volumetric acquisition of fluorescent light, for which various microscopy techniques have been used, such as spinning disc confocal microscopy [14, 73, 95–97, 102, 103], light field microscopy [101], wide-field temporal focusing [99], wide field microscopy with deconvolution [105], and light sheet microscopy [100, 104]. Whole-brain imaging has even been performed on moving animals [95, 96, 100], enabling the possibility to relate brain signalling dynamics with behaviour [98].

Multiple neuron recordings have yielded new insights into internal processing. Gordus. et. al. showed that feedback from the brain state is an important factor in the response to a stimulus [106], contributing to a new paradigm where processing occurs dynamically with feedback from motor neurons, sensory neurons, and interneurons rather than a feed-forward system [107]. On immobilised worms, brain dynamics are low-dimensional and globally distributed, with three PCA components accounting for 65% of the variance [14]. Different regions of the PCA phase space were marked by high activity of neurons associated with behaviours such as forward, reversal and turning of freely moving worms [14]. It should be noted that brain dynamics in freely moving worms show considerately more complexity [96, 102]. The sleep state is also encoded globally and associated with a reduction of the majority of otherwise active neurons [73, 97]. Although highly valuable, these studies only scratch the surface and much more can be learned from whole-brain recordings, in particular the processing of stimuli and the relation between brain dynamics and motility. What is missing in particular is a system that can combine controlled delivery of stimuli, a motility readout, and full brain recordings. Such a system would benefit from longer brain recordings than 20 min, which is the maximum duration of most studies, to gather sufficient statistics to uncover these relationships.

Thesis outlook

In this thesis, two approaches, divided over three chapters, are used to understand animal behaviour: studying behaviour through behavioural variability and through studying brain dynamics. As aforementioned, studies of behaviour require quantification and interpretation, which are aided by building models of behaviour. Therefore, in **chapter 2** [108], a predictive model is constructed that describes the worm's centroid position, quantifying fluctuations in speed, reversals, and body orientation. This model is used to study variability of worm behaviour between individuals, also across nematode species as well as different strains of *C. elegans* in an off-food environment in the absence of (intentionally applied) external stimuli. Because the model describes many different aspects of motile behaviour, covarying relations can be extracted across individuals. We found that behaviour across worms varies along a common mode reminiscent with roaming and dwelling behaviour. Individuals' behaviour projected onto this mode revealed significant variation both across and within species.

Based on these results and the model, experiments have been conducted to relate individual behavioural differences in crawling speed with gene expression using RNA sequencing. Unfortunately, no direct relationship could be extracted, therefore it is not presented as a separate chapter. However, from the data generated by these experiments clusters of covarying genes could be extracted using a method developed predominantly by dr. Steffen Werner (which I co-author), using the percolation properties of the noise background [109]. Some of these clusters contained genes associated with long term feeding experience memory [110], possibly across generations [111].

Turning is a particularly interesting aspect of motile behaviour, because the worm has to 'manage' its internal biases that pose limitations for the control mechanisms, such as a ventral sharp turning preference over dorsal and an Ω turn over δ, arising from the breaking of body symmetries. **Chapter 3** focuses specifically on turning behaviour within an isogenic population of N2 for longer time-periods (2 hours). The long time-scale measurements result in sufficient statistics about the individual that can be leveraged to study worm-to-worm variability in the context of performance. This required resolving worm postures during the thousands of self-occluding sharp turns [45] and is therefore a unique data set in the field. Variation in turning statistics persistent over the length of the measurement could be identified across individuals, most notably a rotational crawling bias that impairs exploration and could possibly be a limit of control. By constructing a minimal model of the persistence length, we showed that the sharp turn rate and diffusion are, on average, optimally tuned to maximise exploration. In addition, we are the first to describe how the worm leverages its diverse sharp turn repertoire to overcome its sharp turn biases in the event of an escape from SDS to minimise toxic exposure.

Finally, to gain insight into the control circuitry underpinning motile behaviour, whole-brain dynamics should be studied simultaneously with motile behaviour. Interpretation of complex brain dynamics is aided by knowledge of the input signals, preferably a repeated stimulus such that variable responses can be studied. Therefore, in **chapter 4** we developed a pipeline to study whole-brain response dynamics to repeated chemical stimuli in semi-constrained worms for time scales exceeding an hour. With this system, we investigate three existing hypotheses: (1) the collective motor-command hypothesis, stating that collective modes of neural activity serve as motor commands; (2) the apparent stochasticity hypothesis, by studying the brain response to repeated salt and SDS stimuli; and (3) the neuromodulated brain-states hypothesis, by studying sleep-like reversible quiescence induced by exogenous serotonin. Our results yield positive evidence in support of each of these hypotheses.

BIBLIOGRAPHY

[1] Darwin C. The expression of the emotions in man and animals. In: The expression of the emotions in man and animals. University of Chicago press; 1872/1965. .

[2] Tinbergen N. On aims and methods of ethology. Zeitschrift für tierpsychologie. 1963;20(4):410–433.

[3] Tinbergen N. The study of instinct. Pygmalion Press, an imprint of Plunkett Lake Press; 2020.

[4] Galvani L. Opere edite ed inedite del professore Luigi Galvani. Dall'Olmo; 1841.

[5] Volta A. XVII. On the electricity excited by the mere contact of conducting substances of different kinds. In a letter from Mr. Alexander Volta, FRS Professor of Natural Philosophy in the University of Pavia, to the Rt. Hon. Sir Joseph Banks, Bart. KBPR S. Philosophical transactions of the Royal Society of London. 1800;(90):403–431.

[6] Sotelo C. Viewing the brain through the master hand of Ramón y Cajal. Nature Reviews Neuroscience. 2003;4(1):71–77.

[7] Hodgkin AL, Huxley AF. Action potentials recorded from inside a nerve fibre. Nature. 1939;144(3651):710–711.

[8] Stephens GJ, Johnson-Kerner B, Bialek W, Ryu WS. Dimensionality and dynamics in the behavior of C. elegans. PLoS Comput Biol. 2008;4(4):e1000028.

[9] Berman GJ, Choi DM, Bialek W, Shaevitz JW. Mapping the stereotyped behaviour of freely moving fruit flies. Journal of The Royal Society Interface. 2014;11(99):20140672.

[10] Pereira TD, Aldarondo DE, Willmore L, Kislin M, Wang SSH, Murthy M, et al. Fast animal pose estimation using deep neural networks. Nature methods. 2019;16(1):117–125.

[11] Mathis MW, Mathis A. Deep learning tools for the measurement of animal behavior in neuroscience. Current opinion in neurobiology. 2020;60:1–11.

[12] Urai AE, Doiron B, Leifer AM, Churchland AK. Large-scale neural recordings call for new insights to link brain and behavior. Nature neuroscience. 2022:1–9.

[13] Ahrens MB, Li JM, Orger MB, Robson DN, Schier AF, Engert F, et al. Brain-wide neuronal dynamics during motor adaptation in zebrafish. Nature. 2012;485(7399):471–477.

[14] Kato S, Kaplan HS, Schrödel T, Skora S, Lindsay TH, Yemini E, et al. Global brain dynamics embed the motor command sequence of Caenorhabditis elegans. Cell. 2015;163(3):656–669.

[15] Steinmetz NA, Aydin C, Lebedeva A, Okun M, Pachitariu M, Bauza M, et al. Neuropixels 2.0: A miniaturized high-density probe for stable, long-term brain recordings. Science. 2021;372(6539):eabf4588.

[16] Siegle JH, Jia X, Durand S, Gale S, Bennett C, Graddis N, et al. Survey of spiking in the mouse visual system reveals functional hierarchy. Nature. 2021;592(7852):86–92.

[17] Brown AE, De Bivort B. Ethology as a physical science. Nature Physics. 2018;14(7):653–657.

[18] Anderson DJ, Perona P. Toward a science of computational ethology. Neuron. 2014;84(1):18–31.

[19] Gärtner K. A third component causing random variability beside environment and genotype. A reason for the limited success of a 30 year long effort to standardize laboratory animals? Laboratory animals. 1990;24(1):71–77.

[20] Honegger K, de Bivort B. Stochasticity, individuality and behavior. Current Biology. 2018;28(1):R8–R12.

[21] Elowitz MB, Levine AJ, Siggia ED, Swain PS. Stochastic gene expression in a single cell. Science. 2002;297(5584):1183–1186.

[22] Raj A, Van Oudenaarden A. Nature, nurture, or chance: stochastic gene expression and its consequences. Cell. 2008;135(2):216–226.

[23] Keegstra JM, Kamino K, Anquez F, Lazova MD, Emonet T, Shimizu TS. Phenotypic diversity and temporal variability in a bacterial signaling network revealed by single-cell FRET. Elife. 2017;6:e27455.

[24] Faisal AA, Selen LP, Wolpert DM. Noise in the nervous system. Nature reviews neuroscience. 2008;9(4):292–303.

[25] McDonnell MD, Goldwyn JH, Lindner B. Neuronal stochastic variability: influences on spiking dynamics and network activity. Frontiers in computational neuroscience. 2016;10:38.

[26] Buchanan SM, Kain JS, De Bivort BL. Neuronal control of locomotor handedness in Drosophila. Proceedings of the National Academy of Sciences. 2015;112(21):6700–6705.

[27] Ayroles JF, Buchanan SM, O'Leary C, Skutt-Kakaria K, Grenier JK, Clark AG, et al. Behavioral idiosyncrasy reveals genetic control of phenotypic variability. Proceedings of the National Academy of Sciences. 2015;112(21):6706–6711.

[28] Ballouz S, Pena MT, Knight FM, Adams LB, Gillis JA. The transcriptional legacy of developmental stochasticity. bioRxiv. 2019.

[29] Slatkin M. Hedging one's evolutionary bets. Nature. 1974;250(5469):704–705.

[30] Philippi T, Seger J. Hedging one's evolutionary bets, revisited. Trends in ecology & evolution. 1989;4(2):41–44.

[31] Cooke S, Bliss T. Plasticity in the human central nervous system. Brain. 2006;129(7):1659–1673.

[32] Weaver IC, Cervoni N, Champagne FA, D'Alessio AC, Sharma S, Seckl JR, et al. Epigenetic programming by maternal behavior. Nature neuroscience. 2004;7(8):847–854.

[33] The C, Wilson RK. How the worm was won: the C. elegans genome sequencing project. Trends in Genetics. 1999;15(2):51–58.

[34] White JG, Southgate E, Thomson JN, Brenner S. The structure of the nervous system of the nematode Caenorhabditis elegans. Philos Trans R Soc Lond B Biol Sci. 1986;314(1165):1–340.

[35] Ryan K, Lu Z, Meinertzhagen IA. The CNS connectome of a tadpole larva of Ciona intestinalis (L.) highlights sidedness in the brain of a chordate sibling. Elife. 2016;5:e16962.

[36] Verasztó C, Jasek S, Gühmann M, Shahidi R, Ueda N, Beard JD, et al. Whole-animal connectome and cell-type complement of the three-segmented Platynereis dumerilii larva. BioRxiv. 2020:2020–08.

[37] Winding M, Pedigo BD, Barnes CL, Patsolic HG, Park Y, Kazimiers T, et al. The connectome of an insect brain. Science. 2023;379(6636):eadd9330.

[38] Félix MA, Braendle C. The natural history of Caenorhabditis elegans. Current Biology. 2010;20(22):R965–R969.

[39] Wen Q, Po MD, Hulme E, Chen S, Liu X, Kwok SW, et al. Proprioceptive coupling within motor neurons drives C. elegans forward locomotion. Neuron. 2012;76(4):750–761.

[40] Husson SJ, Costa WS, Schmitt C, Gottschalk A. Keeping track of worm trackers. In: WormBook: The Online Review of C. elegans Biology [http://www.wormbook.org]. WormBook; 2012. .

[41] Itskovits E, Levine A, Cohen E, Zaslaver A. A multi-animal tracker for studying complex behaviors. BMC biology. 2017;15(1):1–16.

[42] Stephens GJ, Johnson-Kerner B, Bialek W, Ryu WS. From modes to movement in the behavior of Caenorhabditis elegans. PloS one. 2010;5(11):e13914.

[43] Roberts WM, Augustine SB, Lawton KJ, Lindsay TH, Thiele TR, Izquierdo EJ, et al. A stochastic neuronal model predicts random search behaviors at multiple spatial scales in C. elegans. Elife. 2016;5:e12572.

[44] Croll NA. Behavioural analysis of nematode movement. In: Advances in parasitology. vol. 13. Elsevier; 1975. p. 71–122.

[45] Broekmans OD, Rodgers JB, Ryu WS, Stephens GJ. Resolving coiled shapes reveals new reorientation behaviors in C. elegans. Elife. 2016;5:e17227.

[46] Chalfie M, Sulston JE, White JG, Southgate E, Thomson JN, Brenner S. The neural circuit for touch sensitivity in Caenorhabditis elegans. Journal of Neuroscience. 1985;5(4):956–964.

[47] Maguire SM, Clark CM, Nunnari J, Pirri JK, Alkema MJ. The C. elegans touch response facilitates escape from predacious fungi. Current Biology. 2011;21(15):1326–1330.

[48] Hilliard MA, Bargmann CI, Bazzicalupo P. C. elegans responds to chemical repellents by integrating sensory inputs from the head and the tail. Current Biology. 2002;12(9):730–734.

[49] Pirri JK, McPherson AD, Donnelly JL, Francis MM, Alkema MJ. A tyramine-gated chloride channel coordinates distinct motor programs of a Caenorhabditis elegans escape response. Neuron. 2009;62(4):526–538.

[50] Donnelly JL, Clark CM, Leifer AM, Pirri JK, Haburcak M, Francis MM, et al. Monoaminergic orchestration of motor programs in a complex C. elegans behavior. PLoS Biol. 2013;11(4):e1001529.

[51] Mohammadi A, Rodgers JB, Kotera I, Ryu WS. Behavioral response of Caenorhabditis elegansto localized thermal stimuli. BMC neuroscience. 2013;14(1):66.

[52] Ghosh R, Mohammadi A, Kruglyak L, Ryu WS. Multiparameter behavioral profiling reveals distinct thermal response regimes in Caenorhabditis elegans. BMC biology. 2012;10(1):85.

[53] Leung K, Mohammadi A, Ryu WS, Nemenman I. Stereotypical escape behavior in Caenorhabditis elegans allows quantification of effective heat stimulus level. PLoS computational biology. 2016;12(12):e1005262.

[54] Bargmann CI, Horvitz HR. Chemosensory neurons with overlapping functions direct chemotaxis to multiple chemicals in C. elegans. Neuron. 1991;7(5):729–742.

[55] Pierce-Shimomura JT, Morse TM, Lockery SR. The fundamental role of pirouettes in Caenorhabditis elegans chemotaxis. Journal of Neuroscience. 1999;19(21):9557–9569.

[56] Berg HC, Brown DA. Chemotaxis in Escherichia coli analysed by three-dimensional tracking. Nature. 1972;239(5374):500–504.

[57] Larsch J, Flavell SW, Liu Q, Gordus A, Albrecht DR, Bargmann CI. A circuit for gradient climbing in C. elegans chemotaxis. Cell reports. 2015;12(11):1748–1760.

[58] Iino Y, Yoshida K. Parallel use of two behavioral mechanisms for chemotaxis in Caenorhabditis elegans. Journal of Neuroscience. 2009;29(17):5370–5380.

[59] Hums I, Riedl J, Mende F, Kato S, Kaplan HS, Latham R, et al. Regulation of two motor patterns enables the gradual adjustment of locomotion strategy in Caenorhabditis elegans. Elife. 2016;5:e14116.

[60] Gallagher T, Bjorness T, Greene R, You YJ, Avery L. The geometry of locomotive behavioral states in C. elegans. PloS one. 2013;8(3):e59865.

[61] Flavell SW, Pokala N, Macosko EZ, Albrecht DR, Larsch J, Bargmann CI. Serotonin and the neuropeptide PDF initiate and extend opposing behavioral states in C. elegans. Cell. 2013;154(5):1023–1035.

[62] Arous JB, Laffont S, Chatenay D. Molecular and sensory basis of a food related two-state behavior in C. elegans. PloS one. 2009;4(10):e7584.

[63] You Yj, Kim J, Raizen DM, Avery L. Insulin, cGMP, and TGF-β signals regulate food intake and quiescence in C. elegans: a model for satiety. Cell metabolism. 2008;7(3):249–257.

[64] Gray JM, Hill JJ, Bargmann CI. A circuit for navigation in Caenorhabditis elegans. Proceedings of the National Academy of Sciences. 2005;102(9):3184–3191.

[65] Salvador LC, Bartumeus F, Levin SA, Ryu WS. Mechanistic analysis of the search behaviour of Caenorhabditis elegans. Journal of The Royal Society Interface. 2014;11(92):20131092.

[66] Bartumeus F, Campos D, Ryu WS, Lloret-Cabot R, Méndez V, Catalan J. Foraging success under uncertainty: search tradeoffs and optimal space use. Ecology letters. 2016;19(11):1299–1313.

[67] Peliti M, Chuang JS, Shaham S. Directional locomotion of C. elegans in the absence of external stimuli. PLoS One. 2013;8(11):e78535.

[68] Saeki S, Yamamoto M, Iino Y. Plasticity of chemotaxis revealed by paired presentation of a chemoattractant and starvation in the nematode Caenorhabditis elegans. Journal of Experimental Biology. 2001;204(10):1757–1764.

[69] Kunitomo H, Sato H, Iwata R, Satoh Y, Ohno H, Yamada K, et al. Concentration memory-dependent synaptic plasticity of a taste circuit regulates salt concentration chemotaxis in Caenorhabditis elegans. Nature communications. 2013;4(1):1–11.

[70] Luo L, Wen Q, Ren J, Hendricks M, Gershow M, Qin Y, et al. Dynamic encoding of perception, memory, and movement in a C. elegans chemotaxis circuit. Neuron. 2014;82(5):1115–1128.

[71] Hedgecock EM, Russell RL. Normal and mutant thermotaxis in the nematode Caenorhabditis elegans. Proceedings of the National Academy of Sciences. 1975;72(10):4061–4065.

[72] Raizen DM, Zimmerman JE, Maycock MH, Ta UD, You Yj, Sundaram MV, et al. Lethargus is a Caenorhabditis elegans sleep-like state. Nature. 2008;451(7178):569–572.

[73] Nichols AL, Eichler T, Latham R, Zimmer M. A global brain state underlies C. elegans sleep behavior. Science. 2017;356(6344).

[74] Stern S, Kirst C, Bargmann CI. Neuromodulatory control of long-term behavioral patterns and individuality across development. Cell. 2017;171(7):1649–1662.

[75] Varshney LR, Chen BL, Paniagua E, Hall DH, Chklovskii DB. Structural properties of the Caenorhabditis elegans neuronal network. PLoS Comput Biol. 2011;7(2):e1001066.

[76] Cook SJ, Jarrell TA, Brittin CA, Wang Y, Bloniarz AE, Yakovlev MA, et al. Whole-animal connectomes of both Caenorhabditis elegans sexes. Nature. 2019;571(7763):63–71.

[77] Witvliet D, Mulcahy B, Mitchell JK, Meirovitch Y, Berger DK, Wu Y, et al. Connectomes across development reveal principles of brain maturation in C. elegans. bioRxiv. 2020.

[78] Sasakura H, Mori I. Behavioral plasticity, learning, and memory in C. elegans. Current opinion in neurobiology. 2013;23(1):92–99.

[79] Alcedo J, Prahlad V. Neuromodulators: an essential part of survival. Journal of neurogenetics. 2020;34(3-4):475–481.

[80] Chase DL, Koelle MR. Biogenic amine neurotransmitters in C. elegans. In: WormBook: The Online Review of C. elegans Biology [http://www.wormbook.org]. WormBook; 2007. .

[81] Bargmann CI, Marder E. From the connectome to brain function. Nature methods. 2013;10(6):483.

[82] Zheng Y, Brockie PJ, Mellem JE, Madsen DM, Maricq AV. Neuronal control of locomotion in C. elegans is modified by a dominant mutation in the GLR-1 ionotropic glutamate receptor. Neuron. 1999;24(2):347–361.

[83] Bargmann CI, Avery L. Laser killing of cells in Caenorhabditis elegans. Methods in cell biology. 1995;48:225.

[84] Lockery SR, Goodman M. [13] Tight-seal whole-cell patch clamping of caenorhabditis elegans neurons. In: Methods in enzymology. vol. 293. Elsevier; 1998. p. 201–217.

[85] Akerboom J, Chen TW, Wardill TJ, Tian L, Marvin JS, Mutlu S, et al. Optimization of a GCaMP calcium indicator for neural activity imaging. Journal of neuroscience. 2012;32(40):13819–13840.

[86] Chen TW, Wardill TJ, Sun Y, Pulver SR, Renninger SL, Baohan A, et al. Ultrasensitive fluorescent proteins for imaging neuronal activity. Nature. 2013;499(7458):295–300.

[87] Broussard GJ, Liang R, Tian L. Monitoring activity in neural circuits with genetically encoded indicators. Frontiers in molecular neuroscience. 2014;7:97.

[88] Guo ZV, Hart AC, Ramanathan S. Optical interrogation of neural circuits in Caenorhabditis elegans. Nature methods. 2009;6(12):891–896.

[89] Chronis N, Zimmer M, Bargmann CI. Microfluidics for in vivo imaging of neuronal and behavioral activity in Caenorhabditis elegans. Nature methods. 2007;4(9):727–731.

[90] Faumont S, Rondeau G, Thiele TR, Lawton KJ, McCormick KE, Sottile M, et al. An image-free opto-mechanical system for creating virtual environments and imaging neuronal activity in freely moving Caenorhabditis elegans. PloS one. 2011;6(9):e24666.

[91] Shipley FB, Clark CM, Alkema MJ, Leifer AM. Simultaneous optogenetic manipulation and calcium imaging in freely moving C. elegans. Frontiers in neural circuits. 2014;8:28.

[92] Arous JB, Tanizawa Y, Rabinowitch I, Chatenay D, Schafer WR. Automated imaging of neuronal activity in freely behaving Caenorhabditis elegans. Journal of neuroscience methods. 2010;187(2):229–234.

[93] Larsch J, Ventimiglia D, Bargmann CI, Albrecht DR. High-throughput imaging of neuronal activity in Caenorhabditis elegans. Proceedings of the National Academy of Sciences. 2013;110(45):E4266–E4273.

[94] Zheng M, Cao P, Yang J, Xu XS, Feng Z. Calcium imaging of multiple neurons in freely behaving C. elegans. Journal of neuroscience methods. 2012;206(1):78–82.

[95] Venkatachalam V, Ji N, Wang X, Clark C, Mitchell JK, Klein M, et al. Pan-neuronal imaging in roaming Caenorhabditis elegans. Proceedings of the National Academy of Sciences. 2016;113(8):E1082–E1088.

[96] Nguyen JP, Shipley FB, Linder AN, Plummer GS, Liu M, Setru SU, et al. Whole-brain calcium imaging with cellular resolution in freely behaving Caenorhabditis elegans. Proceedings of the National Academy of Sciences. 2016;113(8):E1074–E1081.

[97] Skora S, Mende F, Zimmer M. Energy scarcity promotes a brain-wide sleep state modulated by insulin signaling in C. elegans. Cell reports. 2018;22(4):953–966.

[98] Chen X, Randi F, Leifer AM, Bialek W. Searching for collective behavior in a small brain. Physical Review E. 2019;99(5):052418.

[99] Schrödel T, Prevedel R, Aumayr K, Zimmer M, Vaziri A. Brain-wide 3D imaging of neuronal activity in Caenorhabditis elegans with sculpted light. Nature methods. 2013;10(10):1013–1020.

[100] Voleti V, Patel KB, Li W, Campos CP, Bharadwaj S, Yu H, et al. Real-time volumetric microscopy of in vivo dynamics and large-scale samples with SCAPE 2.0. Nature methods. 2019;16(10):1054–1062.

[101] Prevedel R, Yoon YG, Hoffmann M, Pak N, Wetzstein G, Kato S, et al. Simultaneous whole-animal 3D imaging of neuronal activity using light-field microscopy. Nature methods. 2014;11(7):727–730.

[102] Scholz M, Linder AN, Randi F, Sharma AK, Yu X, Shaevitz JW, et al. Predicting natural behavior from whole-brain neural dynamics. bioRxiv. 2018:445643.

[103] Ji N, Madan GK, Fabre GI, Dayan A, Baker CM, Kramer TS, et al. A neural circuit for flexible control of persistent behavioral states. Elife. 2021;10:e62889.

[104] Awal MR, Wirak GS, Gabel CV, Connor CW. Collapse of global neuronal states in Caenorhabditis elegans under isoflurane anesthesia. Anesthesiology. 2020;133(1):133–144.

[105] Kotera I, Tran NA, Fu D, Kim JH, Rodgers JB, Ryu WS. Pan-neuronal screening in Caenorhabditis elegans reveals asymmetric dynamics of AWC neurons is critical for thermal avoidance behavior. Elife. 2016;5:e19021.

[106] Gordus A, Pokala N, Levy S, Flavell SW, Bargmann CI. Feedback from network states generates variability in a probabilistic olfactory circuit. Cell. 2015;161(2):215–227.

[107] Kaplan HS, Nichols AL, Zimmer M. Sensorimotor integration in Caenorhabditis elegans: a reappraisal towards dynamic and distributed computations. Philosophical Transactions of the Royal Society B: Biological Sciences. 2018;373(1758):20170371.

[108] Helms SJ, Rozemuller WM, Costa AC, Avery L, Stephens GJ, Shimizu TS. Modelling the ballistic-to-diffusive transition in nematode motility reveals

variation in exploratory behaviour across species. Journal of the Royal Society Interface. 2019;16(157):20190174.

[109] Werner S, Rozemuller M, Ebbing A, Alemany A, Traets J, van Zon JS, et al. Functional modules from variable genes: Leveraging percolation to analyze noisy, high-dimensional data. bioRxiv. 2020.

[110] Freytag V, Probst S, Hadziselimovic N, Boglari C, Hauser Y, Peter F, et al. Genome-wide temporal expression profiling in Caenorhabditis elegans identifies a core gene set related to long-term memory. Journal of Neuroscience. 2017;37(28):6661–6672.

[111] Webster AK, Jordan JM, Hibshman JD, Chitrakar R, Baugh LR. Transgenerational effects of extended dauer diapause on starvation survival and gene expression plasticity in Caenorhabditis elegans. Genetics. 2018;210(1):263–274.

2

MODELING THE BALLISTIC-TO-DIFFUSIVE TRANSITION IN NEMATODE MOTILITY REVEALS VARIATION IN EXPLORATORY BEHAVIOR ACROSS SPECIES

2.1. INTRODUCTION

A ubiquitous feature of biological motility is the combination of stereotyped movements in seemingly random sequences. Capturing the essential characteristics of motion thus requires a statistical description, in close analogy to the random-walk formulation of Brownian motion in physics. A canonical example is the "run-and-tumble" behavior of *E. coli* bacteria, in which relatively straight paths (runs) are interspersed by rapid and random reorientation events (tumbles) [1]. The random walk of *E. coli* can thus be characterized by two random variables (run length and tumble angle) and two constant parameters (swimming speed and rotational diffusion coefficient), and detailed studies over decades have yielded mechanistic models that link these key behavioral parameters to the underlying anatomy and physiology [2–5]. Random-walk theory has been fruitfully applied also to studies of eukaryotic cell migration in both two [6–8] and three [9] dimensions.

Can a similar top-down approach be fruitfully applied to more complex organisms–for example, an animal controlled by a neural network? Animal behavior is both astonishing in its diversity and daunting in its complexity, given the inherently high-dimensional space of possible anatomical, physiological, and environmental configurations. It is therefore essential to identify appropriate models and parameterizations to succinctly represent the complex space of behaviors — a non-trivial task that has traditionally relied on the insights of expert biologists. In this study, we ask if one can achieve a similar synthesis by an alternative, physically-motivated approach [10]. We seek a quantitative model with predictive power over behavioral statistics, and yet a parameterization that is simple enough to permit meaningful interpretations of phenotypes in a reduced space of variables. As an example, we focus on the motile behavior of nematodes, which explore space using a combination of random and directed motility driven by undulatory propulsion.

The nematode *C. elegans* has long been a model organism for the genetics of neural systems [11, 12], and recent advances in imaging have made it feasible to record a large fraction of the worm's nervous system activity at single-cell resolution [13–15]. These developments raise the compelling possibility of elucidating the neural basis of behavioral control at the organism scale, but such endeavors will require unambiguous definitions of neural circuit outputs and functional performance. The worm's behavioral repertoire [16, 17] is commonly characterized in terms of forward motion occasionally interrupted by brief reversals [18–20], during which the undulatory body wave that drives its movement [21] switches direction. In addition, worms reorient with a combination of gradual curves in the trajectory ("weathervaning") [22, 23] and sharp changes in body orientation (omega-turns [19] and delta-turns [24]). These elementary behaviors are combined in exploring an environment [22, 25]. Environmental cues such as chemical, mechanical, or thermal stimuli [26] lead to a biasing of these behaviors, guiding the worm in favorable directions [22, 25, 27]. Finally, in practical terms, the worm's small size (~1 mm in length), moderate propulsive speed ($\sim 100\,\mu\mathrm{m\,s}^{-1}$) and short generation time (~3 days) allow a considerable fraction of its behavioral repertoire to be efficiently sampled in the laboratory [18, 28]. An influential example of such an analysis is the "pirouette" model proposed by Pierce-Shimomura and Lockery [25] which describes the worm's exploratory behavior as long runs interrupted occasionally by bursts of reversals and omega turns that reorient the worm, in close analogy to the run-and-tumble model of bacterial random walks [1]. Later work by Iino et al. identified that worms also navigate by smoother modulations of their direction during long runs ("weathervaning") [22], and Calhoun et al. have suggested that *C. elegans* may track the information content of environmental statistics in searching for food [29], a motile strategy that has been termed 'infotaxis' [30]. A recent study by Roberts et al. [20] analyzed high (submicron) resolution kinematics of *C. elegans* locomotion and developed a stochastic model of forward-reverse switching dynamics that include the short-lived (~0.1 s) pause states that were identified between forward and reverse runs.

Importantly, while these previous studies have illuminated different modes of behavioral control, they were not designed to obtain a predictive model of the trajectory statistics and thus a succinct parameterization of *C. elegans* motility remains an important open problem. A quantitative parameterization capturing the repertoire of *C. elegans*' behavioral phenotypes would facilitate data-driven investigations of behavioral strategies: for example, whether worms demonstrate distinct modes of motility (characterized by correlated changes in parameters) over time, or in response to changes in environmental conditions [28, 31–33]. Variation in the obtained parameters among individuals can inform on the distribution of behavioral phenotypes within a population, and reveal evolutionary constraints and trade-offs between strategies represented by distinct parameter sets [34].

C. elegans is a member of the *Nematoda* phylum, one of the largest and most diverse phylogenetic groups of species [35, 36]. Despite the diversity of ecological niches these animals inhabit [35], comparisons of nematode body plans have revealed a remarkable degree of conservation, even down to the level of individual neurons [37]. This combination of highly conserved anatomy and ecological diversity makes nematode motility a compelling case for studies of behavioral phenotypes. Anatomical conservation suggests it might be possible to describe the behavior of diverse nematodes by a common model, and identifying the manner in which existing natural variation is distributed across the parameter space of the model could reveal distinct motility strategies resulting from optimization under different environmental conditions.

In this study, we develop a simple random walk model describing the translational movements of a diverse collection of nematode species, freely-moving on a two-dimensional agar surface. In addition to providing a quantitative and predictive measure of trajectory dynamics, the parameters of our model define a space of possible behaviors. Variation within such a space can occur due to changes in individual behavior over time (reflecting temporal variation in the underlying sensorimotor physiology, or "mood"), differences in behavior among individuals (reflecting stable differences in physiology, or "personality") and differences between strains and species (reflecting cumulative effects of natural selection). By quantitative analyses of such patterns of variation, we seek to identify simple, organizing principles underlying behavior.

2.2. RESULTS

2.2.1. NEMATODES PERFORM RANDOM WALKS OFF-FOOD WITH A BROAD RANGE OF DIFFUSIVITIES ACROSS STRAINS

In order to identify conserved and divergent aspects of motility strategies, we sampled motile behavior over a broad evolutionary range. We selected a phylogenetically diverse collection of nematodes with an increased sampling density closer to the laboratory strain *C. elegans* (Figure 2.1A and Supplementary Information, SI). To sample individual variation, we recorded the motility of up to 20 well-fed individuals per strain and each individual for 30 minutes on a food-free agar plate at 11.5 Hz with a resolution of 12.5 µm/px (see SI).

We measured the centroid position ($\vec{x}(t)$) and calculated the centroid velocity ($\vec{v}(t)$), using image analysis techniques (Figure S2.11 and SI). We chose the centroid as the measure of the worm's position because it effectively filters out most of the dynamics of the propulsive body wave. There was considerable variation in the spatial extent and degree of turning visible in the trajectories both within and across strains (Figure 2.1A, S2.2).

As previously seen in *C. elegans* [38], the measured mean-squared displacement,

$$\langle[\Delta x(\tau)]^2\rangle \equiv \langle|\vec{x}(t+\tau)-\vec{x}(t)|^2\rangle, \tag{2.1}$$

revealed a transition from ballistic to diffusive motion within a 100 s timescale (Figure 2.1B, S2.3). Over short times, the worm's path was relatively straight, with the mean-squared displacement scaling quadratically with the time lag τ and speed s as $\langle s^2\rangle\tau^2$ (*i.e.* a log-log slope of 2). Over longer times, the slope decreased with τ reflecting the randomization of orientation characteristic of diffusion, and an effective diffusivity D_{eff} was extracted by fits to $\langle[\Delta x(\tau)]^2\rangle = 4D_{\mathrm{eff}}\tau$ (see SI). On the time scales at which the worms start encountering the walls of the observation arena, the slope of the mean-squared displacement decreased yet further, which has been shown to be a property of confined random walks [39]. Nonetheless, we have confirmed that the decay of the velocity autocorrelation function is not significantly affected by the confinement, and is consistent with a ballistic to diffusive transition (Figure S2.1). This analysis revealed that the visible differences in the spatial extent of these 30-minute trajectories stem from variation by nearly an order of magnitude in speed and two orders of magnitude in diffusivity (Figure 2.1C, Tables S2.1 & S2.2).

2.2.2. THE RANDOM WALK OF NEMATODES CAN BE DECOMPOSED INTO SPEED, TURNING AND REVERSAL DYNAMICS

The broad range of observed speeds and diffusivities suggest that these diverse nematodes have evolved a variety of strategies for spatial exploration. To gain

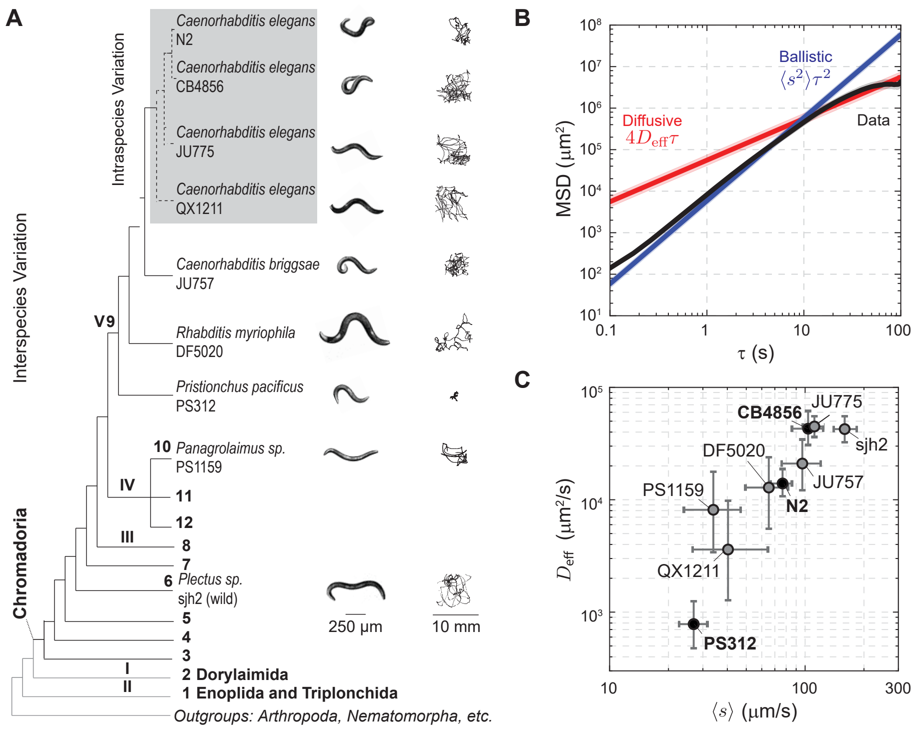

Figure 2.1: Nematodes perform random walks off-food with a mean speed and effective diffusivity that varies across strains. (A) Phylogenetic tree with the strains used in this study. The bold numbers are the major clades of *Nematoda*. The gray box indicates genetically distinct wild isolates of *C. elegans*. A representative worm image and 30 minute trajectory are shown to the right. (B) The average mean-squared displacement, MSD, across N2 individuals is shown in black. For comparison, we show the MSD expected from ballistic (blue) and diffusive (red) dynamics. The motility transitions from a ballistic to diffusive regime within a time scale of tens of seconds. Shaded regions indicate a 95% confidence interval. (C) Mean speed $\langle s \rangle$ and effective diffusivity D_{eff} (mean and 95% confidence intervals) for each strain, calculated from fits of the mean-squared displacement as in B. Across strains, both $\langle s \rangle$ and D_{eff} vary by orders of magnitude.

further insights into the manner in which such contrasting behaviors are implemented by each strain, we sought to extract a minimal model of the nematodes' random walk by further decomposing the trajectory statistics of all nine measured strains. In this and the following three sections, we illustrate our analysis and model development with data from three contrasting strains: CB4856 and PS312, which demonstrated two of the most extreme phenotypes, and the canonical laboratory strain N2 (see SI for equivalent data for all strains).

The translational motion of the worm can be described by the time-varying centroid velocity $\vec{v}(t)$ which can in turn be decomposed into speed $s(t)$ and direction of motion (hereafter referred to as its "bearing") $\phi(t)$:

$$\vec{v}(t) = \frac{d\vec{x}(t)}{dt} = s(t)\left[\cos\phi(t), \sin\phi(t)\right] \tag{2.2}$$

To account for head-tail asymmetry in the worm's anatomy, we additionally define the body orientation ($\psi(t)$; hereafter referred to simply as "orientation") by the angle of the vector connecting the worm's centroid to the head (Figure 2.2A). The centroid bearing is related to this orientation of the worm by

$$\phi(t) = \psi(t) + \Delta\psi(t) \tag{2.3}$$

where the difference $\Delta\psi(t)$ is a measure of the alignment of the direction of movement with the worm's body orientation (hereafter referred to simply as "alignment"). We found for all strains that the distribution of $\Delta\psi(t)$ was bimodal with peaks at 0°and 180°(Figure 2.2C, S2.7A). These match the forward and reverse states of motion described in *C. elegans* [18, 19].

Each of the three components of the worm's motility (speed, orientation, and alignment) varied considerably over time and in qualitatively different ways between strains (Figure 2.2B). For example, the three strains shown in Figure 2.2B differed not only in their average speed, but also in the amplitude and timescale of fluctuations about the average speed. Similarly, the statistics of orientation fluctuations about the drifting mean also differed visibly between strains. Finally, transitions between forward and reverse runs were far more frequent in PS312 as compared to N2 and CB4856. Given the apparently random manner in which these motility components varied over time, we proceeded to analyze the dynamics of each of these three components as a stochastic process.

2.2.3. SPEED DYNAMICS

Speed control has not been extensively studied in *C. elegans*, but it is known that worms move with a characteristic speed that is influenced by stimuli [26]. When intervals corresponding to transitions between forward and reverse runs were excluded from the time series, we found that the autocorrelation in speed fluctuations decayed exponentially over a few seconds (Figure 2.3A, S2.5A), a timescale similar to the period of the propulsive body wave. These dynamics are naturally captured by an Ornstein-Uhlenbeck process [40], which describes random fluctuations arising from white noise (increments of a diffusive Wiener process, dW_t [40]) with magnitude $\sqrt{2D_s}$ that relax with timescale τ_s back to an average value, $\mu_s = \langle s \rangle$:

$$ds(t) = \tau_s^{-1}\left[\mu_s - s(t)\right]dt + \sqrt{2D_s}dW_t \tag{2.4}$$

Numerical integration of this equation closely reproduced the observed speed distributions during runs (Figure S2.5B).

2.2.4. DIFFUSIVE TURNING WITH DRIFT

The orientation $\psi(t)$ captures turning dynamics that are independent of abrupt changes in bearing $\phi(t)$ due to reversals. To change orientation, *C. elegans* executes a combination of large, ventrally-biased [41] sharp turns [18, 24] and gradual "weathervaning" [22], both of which contribute to randomization of orientation over time. This random walk in orientation was not purely diffusive: the orientation correlation $C_\psi(\tau) = \langle \cos\left[\psi(t+\tau) - \psi(t)\right]\rangle$ does not decay exponentially (Figures 2.3B Inset, S2.6B), and the mean-squared angular displacement, $\mathrm{MSAD}(\tau) = \langle[\psi(t+\tau) - \psi(t)]^2\rangle$, increases nonlinearly with time (Figures 2.3B, S2.6A).

We found that this nonlinear MSAD of $\psi(t)$ could be well fit by a quadratic function of the time delay τ: $\mathrm{MSAD}(\tau) = k_{\psi\mathrm{rms}}^2\tau^2 + 2D_\psi\tau$, corresponding to a diffusion-and-drift model with root-mean-square (rms) drift magnitude $k_{\psi\mathrm{rms}}$ and angular diffusion coefficient D_ψ (see Supporting Information for derivation). A non-zero drift magnitude $k_{\psi\mathrm{rms}} \neq 0$ indicates that in addition to purely random (diffusive) changes in orientation, there is an underlying bias (i.e. directional persistence) in the worms' turning over 100 s windows, consistent with previous studies in larger arenas [23].

These observations lead to a simple model for the orientation dynamics that combines drift (approximated as a deterministic linear process over a 100 s window) with stochastic diffusion:

$$d\psi(t) = k_\psi dt + \sqrt{2D_\psi}dW_t, \tag{2.5}$$

where we set the drift magnitude $k_\psi = k_{\psi\mathrm{rms}}$ and dW_t represents increments of a Wiener process [40].

We note that while this model described well the orientation dynamics within 100 s windows, over longer timescales additional dynamics may be relevant. The magnitude of k_ψ in our data ($\sim 1\,^\circ\mathrm{s}^{-1}$) was similar to that of weathervaning excursions reported for *C. elegans* navigating in salt gradients [22].

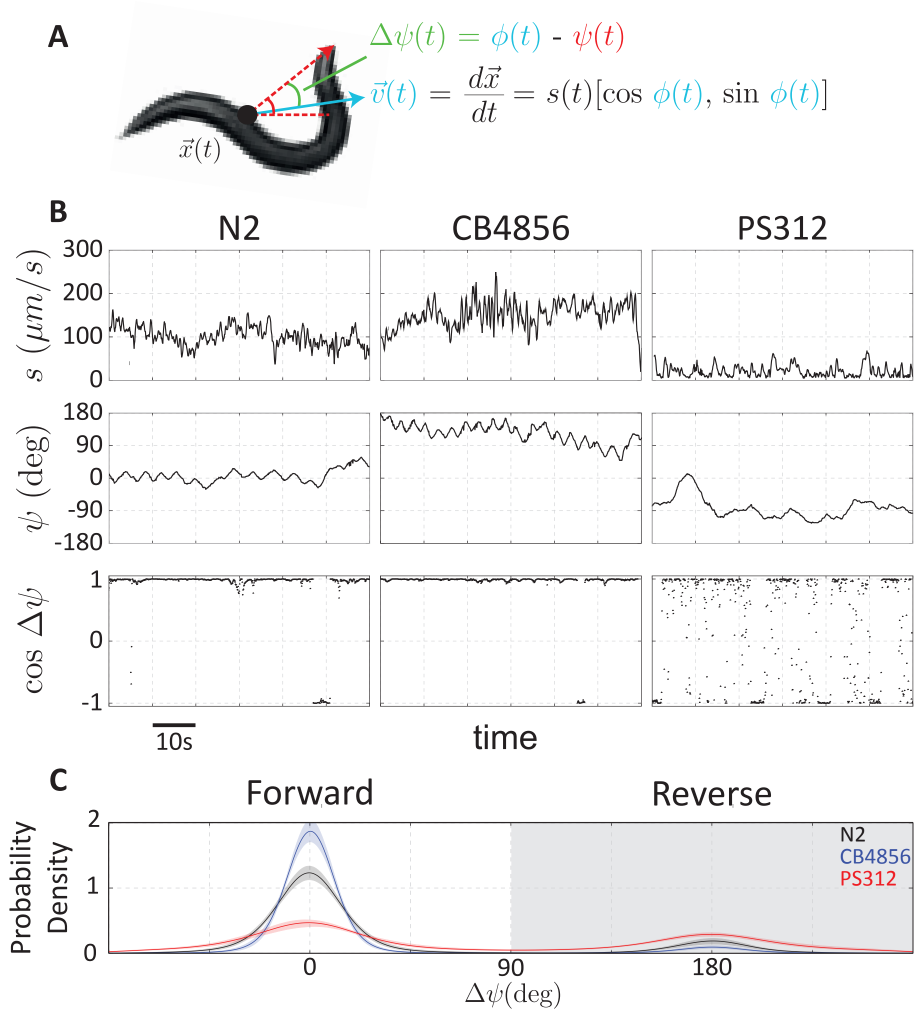

Figure 2.2: The random walk of nematodes is composed of speed, turning, and reversal dynamics. (A) We describe the motility of the worm by the time-varying quantities $s(t)$ (speed; black), $\psi(t)$ (orientation; red), and $\Delta\psi(t)$ (alignment; green) which measures the difference between the alignment of the velocity $\phi(t)$ (blue) and $\psi(t)$. (B) One minute examples of speed, orientation, and velocity alignment time series for individuals from three exemplar strains. (C) The probability distribution of $\Delta\psi(t)$ reveals bimodality corresponding to forward and reverse motion. Shaded regions indicate a 95% confidence interval.

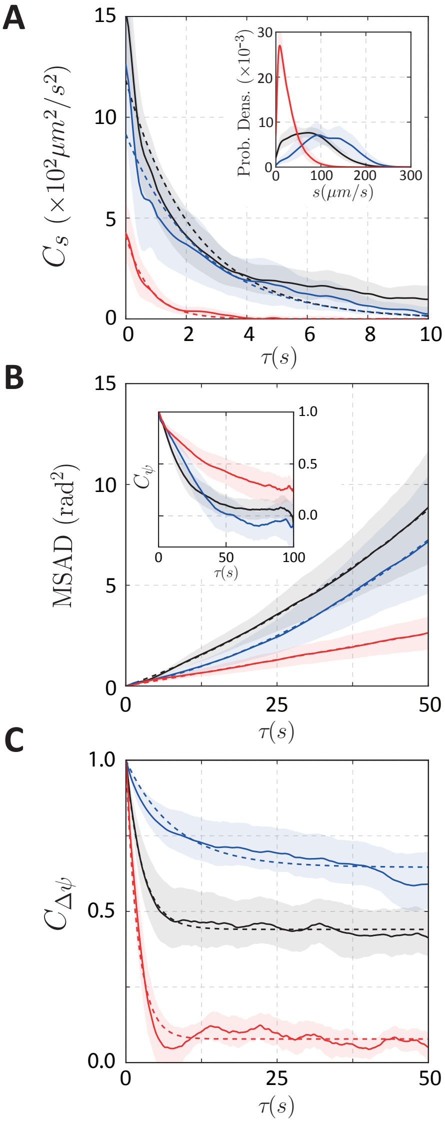

Figure 2.3: Statistical characterization of the motility dynamics. (A) The autocorrelation of the speed indicated that fluctuations decayed exponentially over a few seconds. (A, inset) Speed distributions for three exemplar strains. (B) The mean-squared angular displacement (MSAD) increased quadratically. (B, inset) The orientation autocorrelation function did not decay exponentially, with some worms demonstrating significant undershoots below zero. (C) The velocity alignment autocorrelation decayed exponentially over tens of seconds to a positive constant. In each plot, the ensemble average for all individuals from the strains are shown with solid lines and trends are shown with dashed liens. Shaded regions indicate a 95% confidence interval.

2.2.5. FORWARD AND REVERSE RUNS

The observation that motion during runs switched abruptly between forward and reverse states (with $\Delta\psi \approx \{0°, 180°\}$, respectively; Figures 2.2B,C,S2.7A) suggested that reversals could be described as a discrete stochastic process. The manner in which reversals contribute to randomization of bearing over a time lag τ is captured by the autocorrelation function of $\Delta\psi(t)$, $C_{\Delta\psi}(\tau) \equiv \langle\cos(\Delta\psi(t+\tau) - \Delta\psi(t))\rangle$. We found that $C_{\Delta\psi}(\tau)$ decayed nearly exponentially to a non-zero baseline (Figure 2.3C, Figure S2.7C). This is the predicted behavior for the autocorrelation function of the simplest of two-state processes (a "random telegraph process"):

$$P(T_{\text{fwd}} > t) = \exp(-t/\tau_{\text{fwd}}) \tag{2.6}$$

$$P(T_{\text{rev}} > t) = \exp(-t/\tau_{\text{rev}}), \tag{2.7}$$

in which the distribution of forward and reverse run intervals (T_{fwd} and T_{rev}) are completely determined by a single time constant (τ_{fwd} and τ_{rev}, respectively). The random telegraph process yields an autocorrelation function that decays exponentially as $C_{\Delta\psi}(\tau) = C_{\Delta\psi}(\infty) + \left(1 - C_{\Delta\psi}(\infty)\right) e^{-\tau/\tau_{RT}}$ to a minimum value $C_{\Delta\psi}(\infty) \equiv ((\tau_{\text{fwd}} - \tau_{\text{rev}})/(\tau_{\text{rev}} + \tau_{\text{fwd}}))^2$ with a timescale $\tau_{RT} \equiv \left(\tau_{\text{fwd}}^{-1} + \tau_{\text{rev}}^{-1}\right)^{-1}$ [42]. Results obtained from fitting the autocorrelation function are consistent with those obtained from the distribution of time intervals between detected switching events (Figure S2.7, SI). In principle, the forward and reverse states could be characterized by differences in motility parameters of our model other than these transition times, as forward and reverse motion are driven by distinct command interneurons in *C. elegans* [43, 44]. However, we found that run speeds were nearly identical between forward and reverse runs (Figure S2.8). While we expect that this symmetry will be broken under some specific conditions, such as the escape response [45], the strong speed correlation between the two states motivates the assumption, adopted in our model, that reversals change only the bearing (by 180°) and the propensity to reverse direction, represented in our model by the time constants τ_{fwd} and τ_{rev}.

2.2.6. A MODEL WITH INDEPENDENT SPEED, TURNING AND REVERSALS CAPTURES THE BALLISTIC-TO-DIFFUSIVE TRANSITION IN NEMATODE MOTILITY

Given that the dynamics of the worm's speed, turning and reversals could be described as simple stochastic processes, we asked whether combining them as independent components in a model of the worms' random walk could sufficiently describe the observed motility statistics (Figure 2.4A). We simulated trajectories of worms by numerically integrating equations (2.4)-(2.7) for the speed, orientation, and reversal dynamics, respectively, which yields the worm's velocity dynamics through equations (2.2) and (2.3), with $\Delta\psi(t)$ equal to 0° during forward runs and 180° during reverse runs. Simulations of this model using parameters fit to individual worms produced trajectories that qualitatively resembled real trajectories and varied considerably in their spatial extent (Figure 2.4B).

Next, we quantitatively assessed the performance of the model in reproducing the statistics of the observed trajectories over the time scale of 100 s, within which all strains completed the transition from ballistic to diffusive motion (Figure 2.4C). We found that the model based on independent speed, turning and reversal dynamics closely reproduced not only the diffusivity of each strain but also the time evolution of the mean-squared displacement ($\langle[\Delta x(\tau)]^2\rangle$) across the ballistic-to-diffusive transition (Figure 2.4C, top). A closer inspection of the dynamics across this transition is possible by examining the velocity autocorrelation function ($C_{\vec{v}}(\tau)$), the time integral of which determines the slope of the mean-squared displacement through $(d/dt)\langle[\Delta x(\tau)]^2\rangle = 2\int_0^\tau d\tau' C_{\vec{v}}(\tau')$, a variant of the Green-Kubo relation [46, 47]. The transition from ballistic to diffusive motion is characterized by the manner in which the normalized velocity autocorrelation $C_{\vec{v}}(\tau)/C_{\vec{v}}(0)$ decays over the time lag τ from unity (at $\tau = 0$) to zero (as $\tau \to \infty$). We found that $C_{\vec{v}}(\tau)$ varied considerably across strains, not only in the overall ballistic-to-diffusive transition time, but also in the more detailed dynamics of the autocorrelation decay over time (Figure 2.4C, middle). Salient features, such as the transition time, of the measured velocity autocorrelation functions $C_{\vec{v},\text{obs}}$ were reproduced closely by the simulated velocity autocorrelation functions $C_{\vec{v},\text{model}}$, but there were also subtle deviations in the detailed dynamics for a number of strains.

Given our model's simplifying assumption that dynamics for $s(t)$, $\psi(t)$, and $\Delta\psi(t)$ are independent stochastic processes, we asked whether the remaining discrepancies between the simulated and measured velocity autocorrelation dynamics could be explained by violations of this assumption of independence. As a model-free assessment of the degree of non-independence, we first calculated the predicted velocity autocorrelation for the case that the dynamics of all three components are independent, $C_{\vec{v},\text{indep}}(\tau) = C_s(\tau)C_\psi(\tau)C_{\Delta\psi}(\tau)$, where $C_s(\tau)$, $C_\psi(\tau)$, and $C_{\Delta\psi}(\tau)$ are the autocorrelation functions of the measured data for each of the components (see Supporting Information for derivation). We then compared the differences $C_{\vec{v},\text{obs}} - C_{\vec{v},\text{indep}}$ (blue curve in Figure 2.4C, bottom) and $C_{\vec{v},\text{obs}} - C_{\vec{v},\text{model}}$ (red curve in Figure 2.4C, bottom). Indeed, there were subtle differences both on shorter (∼1 s) and longer timescales (∼10 s). However, these errors for the simulated model were very similar to, or less than, those for the model-free prediction from the data under the assumption of independence (*i.e.*, $C_{\vec{v},\text{obs}} - C_{\vec{v},\text{model}} \lesssim C_{\vec{v},\text{obs}} - C_{\vec{v},\text{indep}}$). These results demonstrate that modeling $s(t)$, $\psi(t)$, and $\Delta\psi(t)$ as independent stochastic processes provides a very good

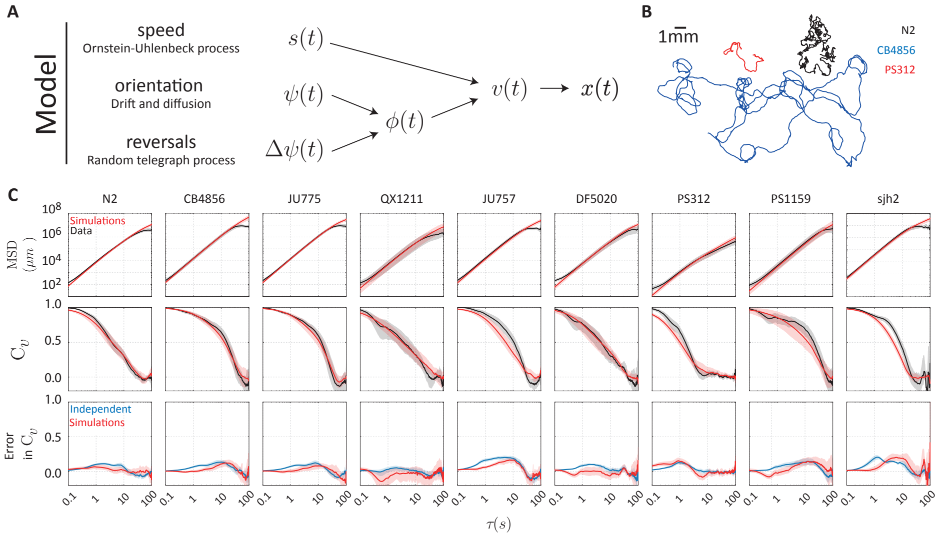

Figure 2.4: A model consisting of independent speed (Ornstein-Uhlenbeck process), turning (drift and diffusion), and reversal dynamics (random telegraph process) quantitatively captures nematode motility. (A) Summary of the model. (B) Simulated trajectories for the three exemplar strains. (C) Statistical comparison of the data (black) and simulations (red), ensemble averaged across individuals for each strain. (C, top) The mean-squared displacement (MSD) was closely reproduced in all cases. (C, middle) The normalized velocity autocorrelation, $C_{\vec{v}}(\tau)/C_{\vec{v}}(0)$, (VACF) was less well captured. (C, bottom) The relatively small errors in the simulated VACF (red) can be traced to the assumption of independence in the dynamics of the speed, orientation, and velocity alignment (blue). Shaded regions indicate a 95% confidence interval.

approximation to trajectory statistics across the ballistic-to-diffusive transition. The relatively subtle differences between the data and model arise primarily in instances where this assumption of independence between the three motility components breaks down. Consistent with these conclusions, inspection of cross-correlation functions computed from the data revealed that correlations between $s(t)$, $\psi(t)$, and $\Delta\psi(t)$ are largely absent, with only weak correlations between speed (s) and reversals ($\Delta\psi$) in a subset of strains (Figure S2.9).

2.2.7. Variation of exploratory behavior across Species

The results presented in the previous sections demonstrate that a random-walk model with seven parameters describing independent speed, turning and reversal dynamics, provides a good approximation of the worms' motile behavior over the $\sim$100 s timescale spanning the ballistic-to-diffusive transition. The model parameters thus define a seven-dimensional space of motility phenotypes in which behavioral variation across strains and species can be examined. If components of behavior were physiologically regulated or evolutionarily selected for in a coordinated manner, we would expect to find correlated patterns in the variation of these traits.

We fit our model to the trajectory statistics of each individual worm and built a phenotype matrix of 106 worms x 7 behavioral parameters (summarized in Tables S2.2, 2.3, 2.4). The correlation matrix for these 7 parameters, Figure 2.5A, demonstrates that the forward and reverse state lifetimes (τ_{fwd}, τ_{rev}) were the strongest correlated, followed by those describing speed and forward state life times (μ_s, τ_{fwd}). More broadly, there were extensive correlations among the model parameters, not only within the parameters of each motility component (speed, orientation, reversals) but also between those of different components.

We looked for dominant patterns in the correlations using principal component analysis [48] (Figure 2.5B), uncovering a single dominant mode of correlated variation (Figure 2.5B, left). Dominant modes are obtained by diagonalizing the correlation matrix. The eigenvalues of the correlation matrix capture the amount of variance of the variables that can be accounted by linear correlation, and therefore the magnitude of these eigenvalues organise the eigenvectors in terms of explained variance. For more details on the principal component analysis, see Supporting Information. This principal mode (mode 1), capturing nearly 40% of the total variation, described significant correlations among all the parameters except for D_s and D_ψ (Figure 2.5B, right, Table S2.5). We did not attempt to interpret higher modes since, individually, they either did not significantly exceeded the captured variance under a randomization test (mode 3 and higher; see SI, and Figure 2.5B, left) or were found upon closer inspection to be dominated by parameter correlations arising from fitting uncertainties (mode 2).

We used numerical simulations to determine the effects on motile behavior of varying parameters along the principal mode. The measured trajectory phenotypes projected onto this mode fall in the range $\{-4, 2\}$: the mode projections are not evenly distributed around the average phenotype at the origin. We performed simulations for parameter sets evenly sampled along this range, which largely reproduced the observed variation in the measured diffusivities D_{eff} as a function of the projection along the first mode. The agreement was particularly good at higher values (> -1) of the mode projection, but at lower values we noted a tendency for the D_{eff} from simulations to exceed that of the data. The latter discrepancy can be explained by elements of behavior not captured by our model (see Discussion). Nevertheless, as illustrated by simulated trajectories (Figure 2.5C, bottom), trajectories became more expansive as the mode projection increased, as did D_{eff} by nearly two orders of magnitude over the tested range. This suggested that the

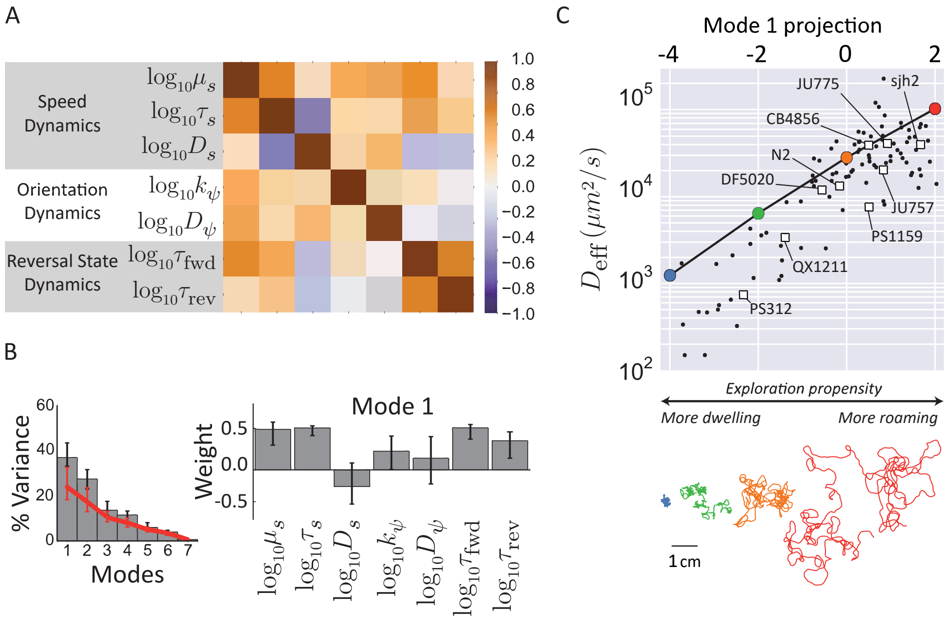

Figure 2.5: Motility parameters co-vary along an axis controlling exploratory behavior. (A) Correlation matrix of the behavioral parameters across the whole dataset. (B, left) Fraction of variance captured by each mode and the amount expected for an uncorrelated dataset (red line) (B, right) The components of the top eigenvector. (C) The effective diffusivity (top) and a 30 minute trajectory (bottom, colors match points on graph) from simulations in which the projection onto the top eigenvector was varied; the principal mode can be used as an effective phenotype from a more *dwelling* to a more *roaming* behavior. The projections and effective diffusivity of the measured trajectories are shown as black points, and the average of each strain is shown as a square. Mode projections are obtained by the dot product of the 7-dimensional vector of parameters obtained for each trajectory, and the principal eigenmode.

principal mode indicates exploratory propensity (Figure 2.5C), and we confirmed that it is indeed more strongly associated with changes in D_{eff} than expected for randomly generated parameter sets (Figure S2.10). Interestingly, this mode of variation we found across individual phenotypes is reminiscent of “roaming” and “dwelling” behavioral variability that has been shown within individuals across time, in *C. elegans* [28, 32] as well as other organisms [49, 50].

2.2.8. SPECIALIZED AND DIVERSIFIED BEHAVIORAL STRATEGIES ACROSS STRAINS

The principal behavioral mode discussed in the preceding section was identified by analyzing variation across all individual worms measured in this study, coming from diverse strains and species that differ in their average behavior (see Tables S2.2, 2.3, 2.4). How does the variability among individuals of a given strain compare to differences between the average phenotypes of strains/species? On the one hand, each strain might be highly "specialized", with relatively small variation within strains as compared to that across strains. On the other hand, strains might implement "diversified" strategies in which genetically identical worms vary strongly in their behavior. To address these two possibilities, we analyzed the distribution of individual phenotypes within each strain, as well as that of the set of averaged species phenotypes.

For each measured individual, we computed the projection of its motility parameter set along the principal behavioral mode and estimated strain-specific distributions of this reduced phenotype (Figure 2.6, Table S2.6). In principle, any detail in the shape of these distributions could be relevant for evolutionary fitness, but here we focused our analysis on the mean and standard deviation, given the moderate sampling density (≤ 20 individuals per strain). Further, we computed the principal-mode projection of the average phenotype of each species to define an interspecies phenotype distribution (Figure 2.6).

Strains varied considerably in both the position and breadth of their phenotypic distributions along the principal behavioral mode. Remarkably, variation across individuals within each strain was comparable in magnitude to that for the set of average phenotypes across species (Figure 2.6). Some strains were specialized towards roaming or dwelling behavior, such as CB4856 and PS312, respectively, with a strong bias in their behavior and comparatively low individual variability. Others, such as QX1211 and PS1159, appeared more diversified with an intermediate average phenotype and higher individual variability. These considerable differences in phenotype distributions across strains reveal the evolutionary flexibility of population-level heterogeneity in nematodes, and suggest a possible bet-hedging mechanism for achieving optimal fitness in variable environments [51, 52].

In assessing such variability of phenotypes, it is essential to ask how uncertainty in the determined parameters (obtained from model fits) contribute to the observed variability in phenotypes. We therefore computed the contribution of uncertainties in the individual phenotype determination by bootstrap resampling of the 100 s windows of each individual's recorded trajectory (see SI). The uncertainties thus computed reflect contributions from both parameter uncertainties in curve fitting of data, as well as temporal variability in an individual's parameters over timescales longer than the window size (100 s). With the exception of two strains (sjh2 and CB4856), this measure of uncertainty accounted for less than half of the individual variation within each strain (Figure 2.6B). These findings support the view that the phenotypic variation estimated in the current analysis largely represented stable differences in individual behavior.

2.3. DISCUSSION

We have presented a comparative quantitative analysis of motile behavior across a broad range of strains and species of the nematode phylum, ranging from the lab strain *C. elegans* N2 to *Plectus* sjh2 at the base of the chromadorean nematode lineage. Despite the vast evolutionary distances spanned by strains in this collection [53], we found that a behavioral model described by only seven parameters could account for much of the diversity of the worms' translational movement across the ~100 s timescale spanning the ballistic-to-diffusive transition. This simple model provides a basis for future studies aiming to capture more detailed aspects of nematode behavior, or to connect sensory modulation of behavior to the underlying physiology. More generally, our results demonstrate how quantitative comparisons of behavioral dynamics across species can provide insights regarding the design of behavioral strategies.

2.3.1. THE MINIMAL MODEL: WHAT DOES IT CAPTURE, AND WHAT DOES IT MISS?

We focused on a high-level output of behavior — translational and orientational trajectory dynamics — and sought to build the simplest possible quantitative model that could capture the observed behavioral statistics. We found that a model with only three independent components — (1) speed fluctuations that relax to a set point on a timescale of a few seconds, (2) orientation fluctuations with drift, and (3) stochastic switching between forward and reverse states of motion — describes well, overall, the trajectory statistics of all tested nematode species across the ballistic-to-diffusive transition (Figure 2.4).

Notably, we have not included explicit representations of some reorientation mechanisms that have been studied in the past, such as the deep turns (omega- and delta-turns) [18, 24], or the combination of such turns with reversals (pirouettes) [25]. In our data, we find that the timing of the initiation and termination of reversals, which would both count as runs in the pirouette description, follow exponential distributions with similar time constants as previously reported for the pirouette run distribution. While omega and delta turns must indeed be mechanistically distinct from gradual turns, we have chosen here not to explicitly model their occurrence since orientation changes in our trajectory data were adequately described by a continuous diffusion-drift process (Figures 2.3B, S2.6A). It is possible, however, that explicit representations of pirouettes and/or omega turns would be important in other experimental scenarios, e.g. those that include navigation in the presence of gradient stimuli.

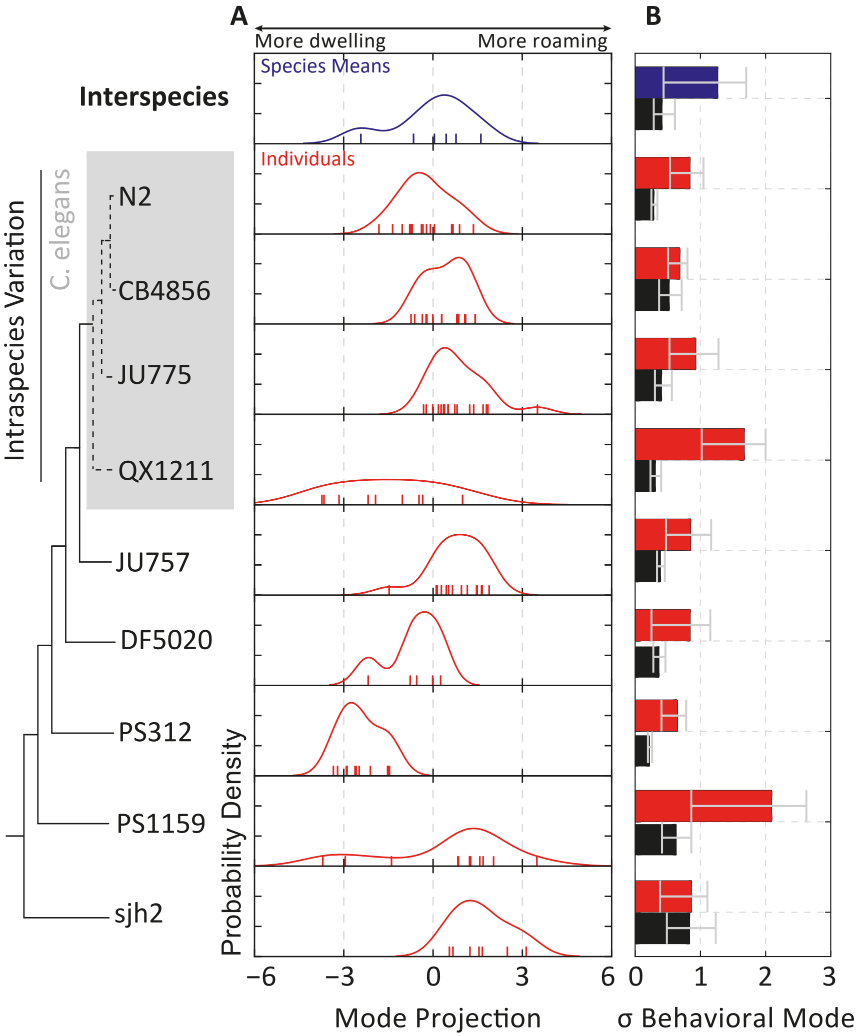

Figure 2.6: Variation of model parameters reveal specialized and diversified behavioral strategies across strains. (A) Distribution of the average phenotype for each species (*interspecies* variation, blue) or individuals within a strain (red). Note that the variation of individual phenotypes in some strains (e.g. QX1211, PS1159) is comparable in magnitude to that of interspecies variation. Observations are indicated with colored ticks. (B) Comparison of the width of the phenotype distributions (colored bars), quantified as the bootstrapped standard deviation of the data points in (A), with the uncertainty in the determination of the phenotype (black bars), quantified as the standard deviation of individual phenotype determinations over bootstrapped 100 s time windows. Error bars correspond to 95% confidence intervals across bootstrap samples.

In our model, "roaming" and "dwelling" were not assigned discrete behavioral states (as was done *e.g.* in [28, 31, 32]), but instead emerged as a continuous pattern of variation among motility parameters describing the worm's random walk. However, robust extraction of motility parameters required pre-filtering of trajectory data that likely biased them towards more "roaming" phenotypes (see SI), which we believe account for the noted tendency of model simulations to overestimate D_{eff} that was more pronounced for trajectories at the "dwelling" end of the spectrum (Figure 2.5C).

In its current form, our simple model does not account for possible correlations between the dynamics of the three motility components (speed, orientation, and reversals). Indeed, at least weak correlations do exist between the components (Figure S2.9). Comparisons of simulated versus measured trajectories demonstrated that the effects of such correlations on the motility statistics are small but detectable (Figure 2.4C). The differences were most significant for the velocity-autocorrelation dynamics on a ~10 s timescale, and were similar to those for model-free predictions obtained by combining component-wise correlation functions under the assumption of independence. Discrepancies on this intermediate timescale occurred most often in fast-moving strains that frequently approached the repellent boundary. Therefore, we suspect that the discrepancy arises from a stereotyped sequence, such as the escape response [45], that introduces temporal correlations between speed changes, turning, and reversals.

While here we have focused on the transition to diffusive motion, some recent experiments suggest that *C. elegans* might engage in superdiffusive behavior on timescales longer than 100 s [23, 33]. Superdiffusive behavior could arise from nonstationarities in motile behavior, such as the roaming/dwelling transitions on timescales of several minutes [32]. Another mechanism for superdiffusion is *directed* motility [23] in response to external stimuli such as chemical or thermal gradients. In such environments, nematodes are known to use at least two distinct mechanisms for navigation [22, 25] and the model here could be extended by studying the dependence of motility parameters on environmental statistics.

Information about the body shape can be incorporated to build a more complete behavioural model that also includes dynamics hidden by centroid behaviour [38, 54]. Indeed, work by Brown et al. showed that a rich repertoire of dynamics can be identified as temporal “motifs” in the postural time series of *C. elegans* and used to classify mutants with high discriminatory power [55]. We have found that all of the species tested here can also be described with a common set of postural modes (not shown), suggesting future directions on the evolutionary space of postural dynamics.

2.3.2. THE EXPLORATORY BEHAVIORAL MODE: VARIABILITY AND ITS PHYSIOLOGICAL BASIS

While we found that a single behavioral model could be used to characterize nematode motility across the chromadorean lineage, the parameters of the model varied extensively from strain to strain. Quantitatively, about 37% of the variation corresponded to a correlated change in the parameters underlying the timing of forward and reverse runs and the dynamics controlling speed and turning (Figure 2.5B). We find that this principal mode of variation is associated with strong changes in exploratory propensity, as characterized by D_{eff} (Figure 2.5C). This pattern of parameter variation drove a change from low speed short runs to high speed long runs, resembling the canonical descriptions of roaming and dwelling in *C. elegans* [32].

Roaming and dwelling are thought to represent fundamental foraging strategies reflecting the trade-off between global exploration and local exploitation of environmental resources [56]. Recent work has suggested that such archetypal strategies can be recovered by quantitatively analyzing the geometry of phenotypic distributions in parameter space [31, 34]. The motility phenotypes we found in the present study were biased along one principal dimension, with the extremes corresponding to roaming and dwelling behaviors. This observation compels us to suggest that an exploration-exploitation trade-off is the primary driver of phenotypic diversification in the motility of chromadorean nematodes in the absence of stimuli. Interestingly, a recent study on the motility of a very different class of organisms (ciliates) yielded a similar conclusion [50]: across two species and different environments, the diversity of motility phenotypes was found to be distributed principally along an axis corresponding to roaming and dwelling phenotypes. The emergence of roaming/dwelling as the principal mode of variation in such disparate species underscores the idea that the exploration-exploitation trade-off is a fundamental constraint on biological motility strategies.

A surprising finding in our study was that, for a majority of strains, the extent of behavioral variability across individuals within a strain was comparable to that for variation of phenotypes across species (Figure 2.6). In slowly changing environments, the most evolutionarily successful species are those that consistently perform well in that environment. This can be achieved by evolving a specialized, high fitness phenotype that varies little among individuals (such as with PS312 and sjh2). However, increased phenotypic variability among individuals can improve fitness in more variable environments if some individuals perform much better in each condition—a so-called "bet-hedging" strategy [51, 52]. The large variability we observed among individual phenotypes within each strain might reflect such a bet-hedging strategy in nematode exploratory behavior.

The observation that the variation among genetically identical individuals can be comparable to that between disparate species raises the intriguing possibility that there exist conserved molecular and/or physiological pathways driving diversification of spatial exploration strategies. Analogous variation in exploratory behavior was also detected in an analysis of nonstationarity in the behavior of wild-type and mutant *C. elegans* under various nutritional conditions [31]. Physiologically, protein kinase G (PKG) signaling and DAF-7 (TGF-β) signaling from the ASI neuron are thought to be major mechanisms controlling roaming and dwelling in *C. elegans* [28, 31]. PKG signaling is also involved in controlling foraging in *Drosophila* and other insects as well as many aspects of mammalian behavior [57, 58]. Flavell et al. also elucidated a neuromodulatory pathway involving serotonin and the neuropeptide pigment dispersing factor (PDF) controlling the initiation and duration of roaming and dwelling states [32].

Perturbations to the molecular parameters of such pathways underlying global behavioral changes might provide a mechanism for the observed correlated variations at the individual, intra-, and inter-species levels. The identification of such conserved pathways affecting many phenotypic parameters is of fundamental interest also from an evolutionary perspective, as they have been proposed to bias the outcome of random mutations towards favorable evolutionary outcomes [59, 60]. Our simple model provides a basis for future investigations to uncover conserved mechanisms that generate behavioral variability, by defining a succinct parameterization of behavior that can be combined with genetic and physiological methods.

ACKNOWLEDGMENTS

We thank Massimo Vergassola, Vasily Zaburdaev, Alon Zaslaver, and Jeroen van Zon for helpful suggestions and critical reading of the manuscript, Will Ryu, Aravi Samuel and Andre Brown for inspiration and encouragement, and members of the Shimizu lab for discussions. Casper Quist and Hans Helder of Wageningen University provided wild nematodes isolated from soil and useful information regarding the ecology of nematodes.

BIBLIOGRAPHY

[1] Berg HC, Brown DA. Chemotaxis in Escherichia coli analysed by Three-dimensional Tracking. Nature. 1972 Oct;239(5374):500–504.

[2] Lovely PS, Dahlquist FW. Statistical measures of bacterial motility and chemotaxis. J Theor Biol. 1975;50:477–496.

[3] Schnitzer M, Block S, Berg H, Purcell E. Strategies for chemotaxis. Symp Soc Gen Microbio. 1990;46:15–34.

[4] De Gennes PG. Chemotaxis: The role of internal delays. Eur Biophys J. 2004;33:691–693.

[5] Celani A, Shimizu TS, Vergassola M. Molecular and Functional Aspects of Bacterial Chemotaxis. J Stat Phys. 2011;144:219–240.

[6] Gail MH, Boone CW. The locomotion of mouse fibroblasts in tissue culture. Biophys J. 1970 Oct;10(10):980–993.

[7] Tranquillo RT, Lauffenburger DA, Zigmond SH. A stochastic model for leukocyte random motility and chemotaxis based on receptor binding fluctuations. J Cell Biol. 1988 Feb;106(2):303–309.

[8] Selmeczi D, Mosler S, Hagedorn PH, Larsen NB, Flyvbjerg H. Cell motility as persistent random motion: theories from experiments. Biophys J. 2005 Aug;89(2):912–931.

[9] Wu PH, Giri A, Sun SX, Wirtz D. Three-dimensional cell migration does not follow a random walk. PNAS. 2014 Mar;111(11):3949–3954.

[10] Brown AE, De Bivort B. Ethology as a physical science. Nature Physics. 2018:1.

[11] Brenner S. The Genetics of Caenorhabditis elegans. Genetics. 1974;77(1):71–94.

[12] Bargmann CI, Marder E. From the connectome to brain function. Nature methods. 2013;10(6):483–490.

[13] Kato S, Kaplan HS, Schrödel T, Skora S, Lindsay TH, Yemini E, et al. Global brain dynamics embed the motor command sequence of Caenorhabditis elegans. Cell. 2015;163(3):656–669.

[14] Venkatachalam V, Ji N, Wang X, Clark C, Mitchell JK, Klein M, et al. Pan-neuronal imaging in roaming Caenorhabditis elegans. PNAS. 2016;113(8):E1082–E1088.

[15] Nguyen JP, Shipley FB, Linder AN, Plummer GS, Liu M, Setru SU, et al. Whole-brain calcium imaging with cellular resolution in freely behaving Caenorhabditis elegans. PNAS. 2016;113(8):E1074–E1081.

[16] Gjorgjieva J, Biron D, Haspel G. Neurobiology of Caenorhabditis elegans Locomotion: Where Do We Stand? Bioscience. 2014 May;64(6):476–486.

[17] Cohen N, Sanders T. Nematode locomotion: dissecting the neuronal–environmental loop. Curr Opin Neurobiol. 2014 Apr;25:99–106.

[18] Croll NA. Components and patterns in the behaviour of the nematode Caenorhabditis elegans. J Zool. 1975;176:159–176.

[19] Croll NA. Behavioural analysis of nematode movement. Adv Parasitol. 1975 Jan;13:71–122.

[20] Roberts WM, Augustine SB, Lawton KJ, Lindsay TH, Thiele TR, Izquierdo EJ, et al. A stochastic neuronal model predicts random search behaviors at multiple spatial scales in C. elegans. Elife. 2016;5:e12572.

[21] Gray J, Lissmann HW. The locomotion of nematodes. J Exp Biol. 1964 Mar;41:135–54.

[22] Iino Y, Yoshida K. Parallel use of two behavioral mechanisms for chemotaxis in Caenorhabditis elegans. J Neurosci. 2009 Apr;29(17):5370–80.

[23] Peliti M, Chuang JS, Shaham S. Directional locomotion of C. elegans in the absence of external stimuli. PLoS One. 2013 Jan;8(11):e78535.

[24] Broekmans OD, Rodgers JB, Ryu WS, Stephens GJ. Resolving coiled shapes reveals new reorientation behaviors in C-elegans. eLife. 2016;5.

[25] Pierce-Shimomura JT, Morse TM, Lockery SR. The fundamental role of pirouettes in Caenorhabditis elegans chemotaxis. J Neurosci. 1999 Nov;19(21):9557–69.

[26] Faumont S, Lindsay T, Lockery S. Neuronal microcircuits for decision making in C. elegans. Curr Opin Neurobiol. 2012 Jun;22(4):580–591.

[27] Ryu WS, Samuel ADT. Thermotaxis in Caenorhabditis elegans analyzed by measuring responses to defined thermal stimuli. J Neurosci. 2002 Jul;22(13):5727–33.

[28] Fujiwara M, Sengupta P, McIntire SL. Regulation of body size and behavioral state of C. elegans by sensory perception and the EGL-4 cGMP-dependent protein kinase. Neuron. 2002 Dec;36(6):1091–102.

[29] Calhoun AJ, Chalasani SH, Sharpee TO. Maximally informative foraging by Caenorhabditis elegans. Elife. 2014 Jan;3.

[30] Vergassola M, Villermaux E, Shraiman BI. 'Infotaxis' as a strategy for searching without gradients. Nature. 2007;445(7126):406–409.

[31] Gallagher T, Bjorness T, Greene R, You YJ, Avery L. The geometry of locomotive behavioral states in C. elegans. PLoS One. 2013 Jan;8(3):e59865.

[32] Flavell SW, Pokala N, Macosko EZ, Albrecht DR, Larsch J, Bargmann CI. Serotonin and the neuropeptide PDF initiate and extend opposing behavioral states in C. elegans. Cell. 2013 Aug;154(5):1023–1035.

[33] Salvador LCM, Bartumeus F, Levin SA, Ryu WS. Mechanistic analysis of the search behaviour of Caenorhabditis elegans. J R Soc Interface. 2014;11:20131092–20131092.

[34] Shoval O, Sheftel H, Shinar G, Hart Y, Ramote O, Mayo A, et al. Evolutionary trade-offs, Pareto optimality, and the geometry of phenotype space. Science. 2012 Jun;336(6085):1157–60.

[35] De Ley P. A quick tour of nematode diversity and the backbone of nematode phylogeny. WormBook. 2006.

[36] Corsi AK, Wightman B, Chalfie M. A Transparent Window into Biology: A Primer on Caenorhabditis elegans. Genetics. 2015 Jun;200(2):387–407.

[37] Rabinowitch I, Schafer W. Neuronal remodeling on the evolutionary timescale. J Biol. 2008 Jan;7(10):37.

[38] Stephens GJ, Johnson-Kerner B, Bialek W, Ryu WS. From modes to movement in the behavior of Caenorhabditis elegans. PLoS One. 2010 Jan;5(11):e13914.

[39] Vahabi M, Schulz JHP, Shokri B, Metzler R. Area coverage of radial Lévy flights with periodic boundary conditions. Physical Review E - Statistical, Nonlinear, and Soft Matter Physics. 2013;87(4):1–10.

[40] Kampen NGV. Stochastic Processes in Physics and Chemistry. North Holland; 2007.

[41] Gray JM, Hill JJ, Bargmann CI. A circuit for navigation in Caenorhabditis elegans. PNAS. 2005 Mar;102(9):3184–91.

[42] Papoulis A. Probability, Random Variables, and Stochastic Processes. 2nd ed. New York: McGraw-Hill; 1984.

[43] Chalfie M, Sulston J, White J, Southgate E, Thomson J, Brenner S. The neural circuit for touch sensitivity in Caenorhabditis elegans. J Neurosci. 1985 Apr;5(4):956–964.

[44] Piggott BJ, Liu J, Feng Z, Wescott SA, Xu XZS. The neural circuits and synaptic mechanisms underlying motor initiation in C. elegans. Cell. 2011 Nov;147(4):922–933.

[45] Culotti JG, Russell RL. Osmotic avoidance defective mutants of the nematode Caenorhabditis elegans. Genetics. 1978 Oct;90(2):243–56.

[46] Green MS. Markoff Random Processes and the Statistical Mechanics of Time-Dependent Phenomena. II. Irreversible Processes in Fluids. J Chem Phys. 1954 Dec;22(3):398.

[47] Kubo R. Statistical-Mechanical Theory of Irreversible Processes. I. General Theory and Simple Applications to Magnetic and Conduction Problems. J Phys Soc Japan. 1957 Jun;12(6):570–586.

[48] P Murphy K. Machine Learning: A Probabilistic Perspective. Cambridge, MA: The MIT Press; 2012.

[49] Osborne Ka, Robichon A, Burgess E, Butland S, Shaw RA, Coulthard A, et al. Natural behavior polymorphism due to a cGMP-dependent protein kinase of Drosophila. Science. 1997 Aug;277(5327):834–6.

[50] Jordan D, Kuehn S, Katifori E, Leibler S. Behavioral diversity in microbes and low-dimensional phenotypic spaces. PNAS. 2013 Aug;110(34):14018–23.

[51] Slatkin M. Hedging one's evolutionary bets. Nature. 1974 Aug;250(5469):704–705.

[52] Philippi T, Seger J. Hedging one's evolutionary bets, revisited. Trends Ecol Evol. 1989 Feb;4(2):41–44.

[53] Kiontke K, Fitch DHA. Nematodes. Curr Biol. 2013 Oct;23(19):R862–R864.

[54] Stephens GJ, Johnson-Kerner B, Bialek W, Ryu WS. Dimensionality and dynamics in the behavior of C. elegans. PLoS Comput Biol. 2008 Apr;4(4):e1000028.

[55] Brown AEX, Yemini EI, Grundy LJ, Jucikas T, Schafer WR. A dictionary of behavioral motifs reveals clusters of genes affecting Caenorhabditis elegans locomotion. PNAS. 2013 Jan;110(2):791–6.

[56] Davies NB, Krebs JR, West SA. An Introduction to Behavioural Ecology. 4th ed. Wiley-Blackwell; 2012.

[57] Reaume CJ, Sokolowski MB. cGMP-dependent protein kinase as a modifier of behaviour. Handb Exp Pharmacol. 2009 Jan;191:423–43.

[58] Kaun KR, Sokolowski MB. cGMP-dependent protein kinase: linking foraging to energy homeostasis. Genome. 2009 Jan;52(1):1–7.

[59] Kirschner M, Gerhart J. Evolvability. Proc Natl Acad Sci USA. 1998 Jul;95(15):8420–7.

[60] Gerhart J, Kirschner M. The theory of facilitated variation. Proc Natl Acad Sci U S A. 2007 May;(suppl_1):8582–9.

2.4. SI MATERIALS

2.4.1. SI METHODS

SELECTION OF STRAINS

A phylogenetic tree with the strains used in this study is shown in Figure 1A. The nematode phylum is classically divided into three major branches—chromadorea, enoplea, and dorylaimia—that are broken into a total of five major ‘B-clades’ [S2] and twelve minor ‘H-clades’ [S3]. The chromadorean lineage is the largest, spanning B-clades III-V and H-clades 3-12 [S2,S3]. *C. elegans* is located in clade V9 (the rhabditids), one of the most diverse clades [S4]. In addition to the lab strain N2, we selected three of the most genetically distinct wild isolates of *C. elegans* (CB4856, JU775, and QX1211) to sample intraspecies variation [S5]. From H-clade 9 in order of increasing evolutionary distance, we selected *Caenorhabditis briggsae* JU757, *Rhabditis myriophila* DF5020, and *Pristionchus pacificus* PS312. The next closest major group, B-clade IV, contains H-clades 10-12. H-clade 12 contains the plant parasitic tylenchs and was thus not included in this study. H-clades 10 and 11 contain many bacterial feeders, of which we selected *Panagrolaimus sp.* PS1159. Finally, from the basal chromadorea, we obtained *Plectus sp.* sjh2, a member of H-clade 6.

C. elegans N2, CB4856 and JU775 were provided by the Caenorhabditis Genetics Center, which is funded by NIH Office of Research Infrastructure Programs (P40 OD010440). *C. elegans* QX1211 was kindly provided by Erik Andersen (Northwestern Univ.). *Plectus sp.* sjh2 was isolated from a soil sample using morphological criteria by Casper Quist and Hans Helder (Wageningen Univ.). SJH then isolated a single species by starting cultures with a single worm. The remaining strains were used in previous studies by Avery [S6].

CULTIVATION OF WORMS

Worms were grown on NGM-SR plates (3 g NaCl, 24 g agar, 2.5 g peptone, 1 mL 5 $\mathrm{mg\,mL^{-1}}$ cholesterol in EtOH in 975 mL water, with 1 mL 1 M $CaCl_2$, 1 mL 1 M $MgSO_4$, 25 mL 1 M K_2PO_4 pH 6, 1 mL 200 $\mathrm{mg\,mL^{-1}}$ streptomycin in water, and 0.23 g 5 mL 40 $\mathrm{mg\,mL^{-1}}$ nystatin in DMSO, added after autoclaving) seeded with *E. coli* HB101, as previously described [S7]. *E. coli* HB101 was first cultured in M9 minimal media (3 g KH_2PO_4, 6 g Na_2HPO_4, 5 g NaCl, 1 mL 1 M $MgSO_4$ in 1 L water) supplemented with 10% Luria broth and 10 $\mathrm{mg\,mL^{-1}}$ streptomycin [S8]. Plates were incubated with a light circle of HB101 culture for a day at 37 °C and then stored at 4 °C. For *Plectus sp.* sjh2, low salt plates (2% agar supplemented with 5 $\mathrm{mg\,L^{-1}}$ of cholesterol from a 5 $\mathrm{mg\,mL^{-1}}$ EtOH solution) were used as previously described [S9]. On NGM-SR plates, these worms became shriveled and died. As the plates did not have nutrients for the bacteria to grow, HB101 was grown to high density in Luria broth overnight at 37 °C, washed 3X in water, resuspended at 10X concentration, and applied to the plates.

Nematodes were cultured by either transferring a few worms by worm pick or a chunk of agar to a new plate after the worms reached adulthood. The plates were then incubated at 20 °C. The growth rate varied considerably among strains, with *Plectus sp.* sjh2 taking nearly two weeks to reach adulthood. We avoided starving the worms at any point during their cultivation, especially in the period before behavioral experiments were performed, as this can induce transgenerational phenotypic changes [S10,S11], and we have observed transient effects on motility lasting at least a couple of generations (data not shown).

IMAGING

The imaging experiments were done on 3.5 cm plates containing the same media used for cultivation. A 2×2 10 mm repellant grid was made by etching the plate with a tool dipped in 1% sodium dodecyl sufate, a detergent that *C. elegans* and most other nematodes avoided. (Whereas many *C. elegans* studies have used copper rings as a repellant boundary [S12], we found that it did not sufficiently repel other nematodes; data not shown). Four young adult, well-fed nematodes were transferred individually by worm pick to a 10 µL drop of M9 (water for *Plectus sp.* sjh2) to remove bacteria stuck to the worms. The worms were then transferred by pipette in a minimal amount of buffer to the imaging plate, and excess buffer was removed as much as possible. The plate was imaged 10-20 minutes after picking the worms, minimizing most transient behaviors. The plate was placed on a custom imaging rig in an inverted, uncovered configuration with illumination by a Schott MEBL-CR50 red LED plate. The behavior was recorded for 30 minutes using a Point Grey Grasshopper Express GX-FW-60S6M-C camera equipped with an Edmund Optics NT54-691 lens (set to a magnification of 0.5X) at a resolution of 2736x2192 (12.5 µm/px) at 11.5 frames/s using a custom National Instruments LabView acquisition program. The video was subsequently compressed using the open-source XVid MPEG-4 compression algorithm using maximal quality settings.

TRACKING AND IMAGE ANALYSIS

The behavioral videos were analyzed using a custom automated analysis program in MathWorks Matlab. The average background was calculated from 50 frames evenly sampled across the entire video. The background was then subtracted from each frame and a global threshold was applied. The thresholded image was cleaned by applying a series of morphological operations: Incomplete thresholding of the worm was smoothed by applying morphological closing with a disk with a similar radius as the worm. Any remaining holes were filled in using a hole-filling algorithm. Small holes or ones with a low perimeter to area ratio were excluded as they sometimes fill in worms undergoing an omega turn, as described in [S13]. Finally, regions in which the worm was just barely touching itself were split by sequentially applying open, diagonal fill, and majority morphological operations. The worm was then identified as the largest connected component with an area within 2-fold of the expected value. The centroid was tracked across frames to obtain $\vec{x}(t)$. In addition, the image skeleton was calculated. Sample images from each of the processing steps are shown in Figure 2.11.

The head of the worm was automatically identified using two statistical properties of the worm's behavior, namely (i) on average, the head of the worm moves more than the tail, and (ii) on average, worms spend more time moving forward (in the direction of their head) than they do moving in reverse. The procedure is based on skeletonization and centroid detection of the worm image, which can fail in situations where image contrast is low (e.g. due to non-uniform background), so trajectories were first divided into segments that contain no more than 3 frames missing the skeleton and centroid information, and the head orientation was assigned within each segment based on local behavioral statistics. Finding statistical criteria that allow unambiguous assignment of head orientation across all strains studied here was challenging because of the diversity in their behavior, but the following procedure was found to work well empirically. The identity of the two ends of the skeleton across image frames were accounted for by a simple tracking algorithm based on minimizing the total distance between skeleton points. For segments longer than 150 frames (with no more than ten consecutive missing skeletons), we found that we could apply property (i) by computing the variance in body angles within 10% of the body length from the ends, and assigning the head to the end with the greater summed variance. However, manual inspection revealed that this sporadicly resulted in misassignment of the head, identifiable as long reversals interrupted by short forward runs. Therefore, in addition, for segments longer than 200 frames (with no more than five consecutive missing centroids), we used property (ii), defining the head as the end of the skeleton that spent the majority of the trajectory at the leading edge of movement. Segments shorter than 150 frames were discarded from further analysis.

The velocity $\vec{v}(t)$ was calculated from the centroid position $\vec{x}(t)$ using the derivative of a cubic polynomial fit to a sliding 1 s window. The direct estimation of the velocity using a symmetrized derivative had a large δ-correlated component that interfered with later analysis. The use of the cubic polynomial did not noticeably distort the correlation functions (Figure 2.12). When the worm's speed $s(t) = |\vec{v}(t)|$ is very low, its projections on the lab-frame x- and y-axes $v_x = \vec{v}(t) \cdot \hat{x}$ and $v_y = \vec{v}(t) \cdot \hat{y}$ become dominated by discretization (pixelation) noise, and the bearing $\phi(t) = \tan^{-1}(v_y/v_x)$ is poorly defined. This in turn leads to large fluctuations in $\Delta\psi(t) = \phi(t) - \psi(t)$, which can introduce a large number of false reversal events, noticeable as a steep decrease in the autocorrelation $C_{\Delta\psi}(\tau) = \langle\cos(\Delta\psi(t+\tau) - \Delta\psi(t))\rangle$ at small values of the delay τ. We therefore exclude segments of the trajectories corresponding to run intervals shorter than six frames (less than half a second). When these artifacts are filtered out in this manner, the $\Delta\psi$ autocorrelation functions were well described by single exponentials (Figure 2.7C). We note that the exclusion of short runs effectively excludes segments of data in which the worm remains stopped (or at a very low speed) — a feature that is more pronounced in some strains than others — and this leads to a systematic bias for simulated model trajectories to have a higher effective diffusivity D_{eff} than the data for the corresponding strain (as can be seen in Figure 5C).

CALCULATION OF BEHAVIORAL STATISTICS

The worm's behavior fluctuated or sometimes drifted over long times (Figure 2.4), but the average statistics over 100 s windows were approximately stationary. In order to focus on dynamics within the 100 s timescale, the mean-squared displacement and all auto- and cross-correlation functions were calculated for 100 s windows and then averaged. This reduced the influence of longer timescale fluctuations in the speed and reversal rate. For all calculations, observations near the boundaries and pairs of points between which the worm approached the boundary were excluded. The uncertainty of each individual's phenotype projection on the principal behavioral mode was computed by projecting the motility parameters after bootstrapping over the 100s windows of each individual's trajectory. The standard deviation of the bootstrapped projections is used as uncertainty.

CALCULATION OF EFFECTIVE DIFFUSIVITY, D_{EFF}

To estimate the effective diffusivity D_{eff}, we fit the mean-squared displacement $\langle[\Delta x(\tau)]^2\rangle$ over the diffusive regime. For this purpose, we defined the diffusive regime as the time-lag interval after which the normalized velocity autocorrelation $C_{\vec{v}}(\tau)/C_{\vec{v}}(0)$ decayed to below 0.1. We note that in some cases (especially for fast-moving strains such as CB4856, JU775 and sjh2) the fit to $\langle[\Delta x(\tau)]^2\rangle = 4D_{\text{eff}}\tau$ in this regime was poor due to boundary effects arising from the finite size of the behavioral arena. For these strains, D_{eff} should be regarded as a lower bound for the true diffusivity.

REVERSAL ANALYSIS

The reversal state was assigned as described in the main text by analysis of $\Delta\psi(t)$. Assuming a random telegraph process that generates states $\Delta\psi = 0$ (forward) and

$\Delta\psi = \pi$ (reverse) with probabilities $1 - f_{rev}$ and f_{rev}, respectively, the autocorrelation at long time lags is $C_{\Delta\psi}(\tau \to \infty) = (1 - 2f_{rev})^2$. For the proposed telegraph process, each state has an exponentially distributed lifetime $(\tau_{\text{fwd}}, \tau_{\text{rev}})$ and therefore $f_{rev} = \dfrac{\tau_{\text{rev}}}{\tau_{\text{rev}} + \tau_{\text{fwd}}}$. The expected correlation timescale for the mixture of the two states is $\tau_{RT}(\tau_{\text{rev}}, \tau_{\text{fwd}}) = \left(\tau_{\text{fwd}}^{-1} + \tau_{\text{rev}}^{-1}\right)^{-1}$. The $\Delta\psi$ autocorrelation function was therefore fit to

$$C_{\Delta\psi}(\tau) = [1 - C_{\Delta\Psi\infty}(\tau_{\text{rev}}, \tau_{\text{fwd}})]\exp\left[-\frac{\tau}{\tau_{RT}(\tau_{\text{rev}}, \tau_{\text{fwd}})}\right] + C_{\Delta\Psi\infty}(\tau_{\text{rev}}, \tau_{\text{fwd}}) \quad (2.8)$$

where $C_{\Delta\Psi\infty}(\tau_{\text{rev}}, \tau_{\text{fwd}}) = (\dfrac{\tau_{\text{fwd}} - \tau_{\text{rev}}}{\tau_{\text{fwd}} + \tau_{\text{rev}}})^2$. The fraction of time spent reversing is: $f_{\text{rev}} = 0.5 - \sqrt{C_{\Delta\Psi\infty}(\tau_{\text{rev}}, \tau_{\text{fwd}})/4}$, where $f_{\text{rev}} \in [0, 0.5]$. The transition time constants are then $\tau_{\text{rev}} = \dfrac{\tau_{RT}(\tau_{\text{rev}}, \tau_{\text{fwd}})}{1 - f_{\text{rev}}}$ and $\tau_{\text{fwd}} = \dfrac{\tau_{RT}(\tau_{\text{rev}}, \tau_{\text{fwd}})}{f_{\text{rev}}}$.

To validate our approach, we compared the parameters obtained with our fitting procedure with those obtained from the distribution of time intervals between detected switching events (Figure S7). For both forward and reverse states, the distribution of time intervals between detected switching events (Figure S7B) were well-fit by a biexponential distribution $P(T_{\text{run}} > t) = C_{\Delta\Psi\infty} \exp(-t/\tau_{\text{short}}) + (1 - C_{\Delta\Psi\infty})\exp(-t/\tau_{\text{long}})$ with the time constants τ_{short} and τ_{long} typically separated by > 10-fold, and the fraction of short intervals $C_{\Delta\Psi\infty}$ varying broadly over its full range, $0 \le C_{\Delta\Psi\infty} \le 1.0$ (Figure S7D,E). Values for τ_{short} were typically below 1 s (Figure S7D). While some fraction of these short intervals might represent true runs, they could also arise from spurious detection of switches in velocity bearing due to noise in estimating the centroid (see legend of Figure S7D) and in any event, contribute little to the overall dynamics of bearing decorrelation.

Values for τ_{fwd} and τ_{rev} obtained by fitting equation S1 to the measured autocorrelation functions correlated well with τ_{long} (Figure S7E), thus confirming that τ_{long} contributes to bearing randomization. We conclude that the forward/reverse switching dynamics are well described by equations (6) and (7), with parameters τ_{fwd}, and τ_{rev}.

SPEED ANALYSIS

Transitions between forward and reverse runs tended to be excluded from the analysis because the speed crosses zero, rendering ϕ a noisy variable generating many short runs below our exclusion threshold of 6 frames (see above). The speed set point μ_s was fit by taking the mean. The remaining parameters of the speed dynamics (3) were fit by its analytical autocorrelation function: $C_s(\tau) = D_s\tau_s \exp(-\tau/\tau_s)$.

ORIENTATION ANALYSIS

Changes in orientation during runs (*i.e.* intervals between reversal events) were analyzed with respect to their mean-squared angular displacements (MSAD) over time, corresponding to a model for angular diffusion with drift

For an object lying on a two-dimensional plane, rotational diffusion about an axis normal to the plane leads to fluctuations in the orientation (an angle measured in the lab frame) $\psi(t)$ over time according to:

$$d\psi(t) = \sqrt{2D_\psi} dW_t, \tag{2.9}$$

where D_ψ is the rotational diffusion coefficient, and dW_t represents increments of a Wiener process. Bias in these fluctuations over time can be captured, to first order, by adding a linear drift term so that

$$d\psi(t) = k_\psi dt + \sqrt{2D_\psi} dW_t, \tag{2.10}$$

with k_ψ the drift coefficient.

If k_ψ and D_ψ are constant in time, the mean-squared angular displacement $\mathrm{MSAD}(\tau) = \langle[\psi(t+\tau)-\psi(t)]^2\rangle$, is a quadratic function of the time delay τ:

$$\langle[\psi(t+\tau)-\psi(t)]^2\rangle = \langle[k_\psi\tau + \sqrt{2D_\psi}(W_{t+\tau}-W_t)]^2\rangle = k_\psi^2\tau^2 + 2D_\psi\tau, \tag{2.11}$$

where $\langle\cdot\rangle$ denotes averaging over all time pairs separated by τ and the last equality follows from the Wiener process properties $\langle W_{t+\tau}-W_t\rangle = 0$ and $\langle[W_{t+\tau}-W_t]^2\rangle = \tau$.

More generally, if $k_\psi(t)$ and $D_\psi(t)$ are time-varying quantities, we can still approximate within a finite time window (centered about time t_w) the “local” values $k_{\psi,w} \approx k_\psi(t_w)$ and $D_{\psi,w} \approx D_\psi(t_w)$. In this study, we extract estimates of these (possibly time varying) parameters from fits to the averaged MSAD computed over time windows:

$$W^{-1}\sum_{w=1}^{w=W}\langle[\psi(t+\tau)-\psi(t)]^2\rangle = \langle k_\psi^2\rangle_w\tau^2 + 2\langle D_\psi\rangle_w\tau, \tag{2.12}$$

where W is the number of windows and $\langle x\rangle_w = W^{-1}\sum_{w=1}^{w=W} x_w$ represents averages over windows. By fitting this averaged MSAD by a quadratic function $a\tau + b\tau^2$, we thus obtain the estimates $a/2 = \langle D_\psi\rangle_w$ and $\sqrt{b} = \langle k_\psi^2\rangle_w^{1/2}$. Note that $a/2$ obtained by this procedure yields an estimate of the mean value for D_ψ, but $\sqrt{b}$ corresponds to an estimate not of the mean value, but the root-mean-square (rms) value for k_ψ. Throughout the text, we therefore explicitly refer to the latter estimate as $k_\psi$rms (and refer to the former simply as D_ψ).

SIMULATIONS

Reversals, orientation, and speed dynamics were all simulated independently using the model described. Forward and reverse run durations were chosen according to equations (5) and (6) by drawing exponential random numbers with mean value τ_{fwd} or τ_{rev}. During reverse runs, $\Delta\psi$ was set to π. The orientation (4) and speed (3) dynamics were simulated using the Euler-Maruyama method [S14] with a time step that matched the frame rate. To prevent negative speeds, a reflective boundary condition was imposed by taking the absolute value of the speed at each simulation step. The velocity was then calculated from the decomposition in (1) and trapezoidally integrated to give the centroid position $\vec{x}(t)$.

BEHAVIORAL MODE ANALYSIS

The model parameters were fit to each trajectory to give a phenotypic matrix $\mathbf{T}$. The phenotypic matrix was centered by subtracting the mean phenotype, $\hat{\mathbf{T}} = \mathbf{T} - \langle\mathbf{T}\rangle_{\mathrm{indiv.}}$. The correlation matrix was then calculated, $\mathbf{C_T} = \mathrm{corr}\,\hat{\mathbf{T}}$, and decomposed into eigenvalues λ and eigenvectors (behavioral modes) $\mathbf{b}$, $\mathbf{C_T b} = \lambda \mathbf{b}$. To reduce any bias coming from a single trajectory, this calculation was bootstrapped 1000 times. The significance of the k-th top mode is assessed by a comparison with the expected variance explained of the k-th top mode of randomly chosen directions in the behavioral space. We use the explained variance of the k-th mode of a newly created set of modes where the first $k-1$ modes are equal to the top behavioral modes and the remaining modes are pointing in randomly chosen orthogonal directions. This process is repeated 1000 times.

The projections of each trajectory on these behavioral modes were calculated by $\mathbf{P} = \hat{\mathbf{T}}\mathbf{b}$. The uncertainty in the locus of each individual phenotype along the behavioral mode was computed by projecting the motility parameters after bootstrapping over the 100 second windows and taking the standard deviation.

STATISTICS

Unless otherwise indicated, errorbars and confidence intervals represent the 2.5% and 97.5% percentiles (spanning the 95% confidence interval) estimated from 1000 bootstrap samples. All probability distributions were empirically estimated using kernel density methods in Python's Seaborn package with a bandwidth automatically selected using Scott's rule of thumb [S15]. Tabulated mean values of the effective diffusivity model and the motility model (Table 2.1-2.4) represent geometric rather than arithmetic means was used as the parameters varied log-normally.

DERIVATION OF THE VELOCITY AUTOCORRELATION FUNCTION UNDER THE ASSUMPTION OF INDEPENDENCE

The velocity autocorrelation function can be written in terms of the motility components,

$$\begin{aligned} C_{\vec{v}}(\tau) &= \langle \vec{v}(0) \cdot \vec{v}(\tau) \rangle \\ &= \langle s(0) \left[\cos\left[\psi(0) + \Delta\psi(0)\right], \sin\left[\psi(0) + \Delta\psi(0)\right]\right] \times \\ &\quad \times s(\tau) \left[\cos\left[\psi(\tau) + \Delta\psi(\tau)\right], \sin\left[\psi(\tau) + \Delta\psi(\tau)\right]\right] \rangle \end{aligned} \tag{2.13}$$

The expected value of the product of independent random variables is the product of the expected value of each variable, i.e. $\langle xy \rangle = \langle x \rangle \langle y \rangle$. Therefore we can factor out $C_s = \langle s(0) s(\tau) \rangle$, leaving the vector product with ψ and $\Delta\psi$. The expanded vector product is:

$$\begin{aligned} C_{\vec{v}}(\tau) = C_s(\tau) \times \langle &\cos\left[\psi(0) + \Delta\psi(0)\right] \cos\left[\psi(\tau) + \Delta\psi(\tau)\right] \\ &+ \sin\left[\psi(0) + \Delta\psi(0)\right] \sin\left[\psi(\tau) + \Delta\psi(\tau)\right] \rangle \end{aligned} \tag{2.14}$$

The trigonometric functions on $\psi(t) + \Delta\psi(t)$ can be rewritten as products of trigonometric functions of the terms:

$$\begin{aligned} \cos\left[\psi(t) + \Delta\psi(t)\right] &= \cos\psi(t) \cos\Delta\psi(t) - \sin\psi(t) \sin\Delta\psi(t) \\ \sin\left[\psi(t) + \Delta\psi(t)\right] &= \sin\psi(t) \cos\Delta\psi(t) + \cos\psi(t) \sin\Delta\psi(t) \end{aligned}$$

However, since $\Delta\psi(t) = \{0, \pi\}$, $\sin\Delta\psi(t) = 0$:

$$\begin{aligned} \cos\left[\psi(t) + \Delta\psi(t)\right] &= \cos\psi(t) \cos\Delta\psi(t) \\ \sin\left[\psi(t) + \Delta\psi(t)\right] &= \sin\psi(t) \cos\Delta\psi(t) \end{aligned}$$

Substituting into (2.14),

$$\begin{aligned} C_{\vec{v}}(\tau) = C_s(\tau) \times \langle &\cos\psi(0) \cos\psi(\tau) \cos\Delta\psi(0) \cos\Delta\psi(\tau) + \\ &\sin\psi(0) \sin\psi(\tau) \cos\Delta\psi(0) \cos\Delta\psi(\tau) \rangle \end{aligned} \tag{2.15}$$

We can now factor out $C_\psi(\tau) = \langle \cos\left[\psi(\tau) - \psi(0)\right] \rangle = \langle \cos\psi(0) \cos\psi(\tau) + \sin\psi(0) \sin\psi(\tau) \rangle$ to get:

$$C_{\vec{v}}(\tau) = C_s(\tau) C_\psi(\tau) \langle \cos\Delta\psi(0) \cos\Delta\psi(\tau) \rangle$$

Finally, we substitute (again dropping $\sin\Delta\psi(t)$ terms):

$$C_{\Delta\psi}(\tau) = \langle \cos\left[\Delta\psi(0) - \Delta\psi(\tau)\right] \rangle = \langle \cos\Delta\psi(0) \cos\Delta\psi(\tau) \rangle$$

to get:

$$C_{\vec{v},\mathrm{indep}}(\tau) = C_s(\tau) C_\psi(\tau) C_{\Delta\psi}(\tau)$$

2.4.2. SI FIGURES

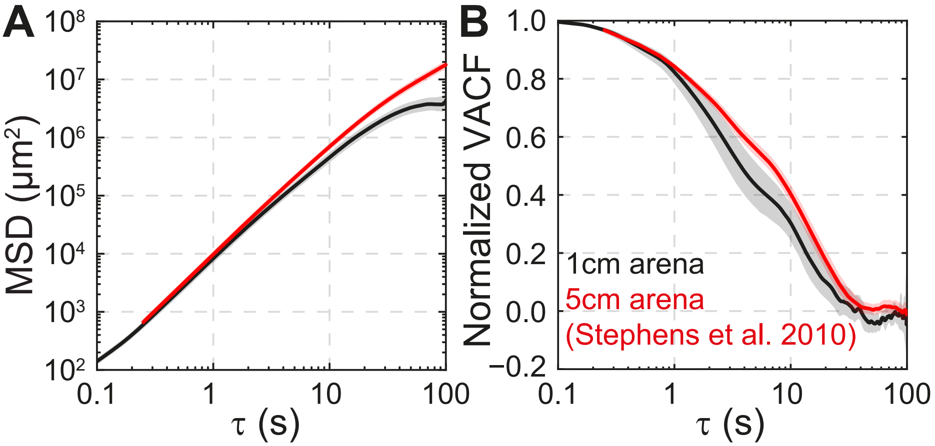

Figure S 2.1: Confinement by the boundary affects the mean-squared displacement (MSD) at long times, but does not impair resolution of the ballistic to diffusive transition. We compare the statistical behavior of *C. elegans* N2 in the experiments presented here within small (1-cm) arenas (black) and a previously reported dataset that used larger (5-cm) arenas [S1] (red). The MSD (A), defined as $\langle[\Delta x(\tau)]^2\rangle \equiv \langle|\vec{x}(t+\tau)-\vec{x}(t)|^2\rangle$, of our small-arena dataset is similar to that of the large-arena dataset at short times, but does show mild effects of confinement at long times ($\gtrsim 100\,\mathrm{s}$). The ballistic to diffusive transition can be more closely studied by examining decay of the velocity autocorrelation function (VACF), defined as $C_v(\tau) \equiv \langle\vec{v}(t)\cdot\vec{v}(t+\tau)\rangle$ (B), which is related to MSD (*i.e.* $[\Delta x(\tau)]^2$) by $(d/d\tau)\langle[\Delta x(\tau)]^2\rangle = 2\int_0^\tau d\tau' C_{\vec{v}}(\tau')$ [S16]. The decay of the VACF to zero, which indicates orientation randomization and hence the transition from the ballistic to diffusive regime, is not significantly affected by the presence of the confining boundary.

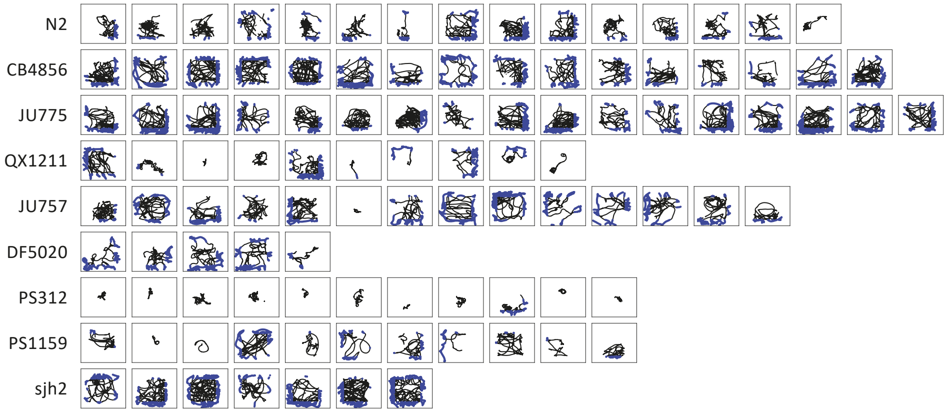

Figure S 2.2: An overview of the dataset. Trajectories of all worm included in the study. Each box represents a 10 mm by 10 mm chamber. In blue, we highlight points excluded from the analysis because they were influenced by the boundary.

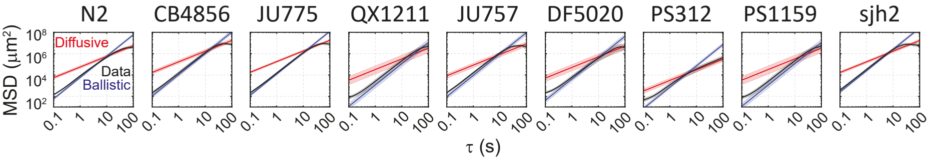

Figure S 2.3: The ballistic to diffusive transition for all strains. We show the average mean-squared displacment (MSD), calculated across individual trajectories, for each strain (black). The expected ballistic (blue) and diffusive MSD curves (red), as in Figure 1B.

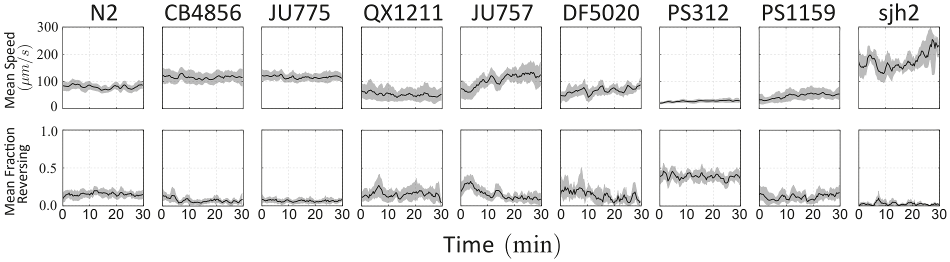

Figure S 2.4: The worms' behavior was approximately stationary. For each strain, we show the average speed (top) and fraction of time spent reversing (bottom) calculated over 100 s sliding windows and averaged across individuals.

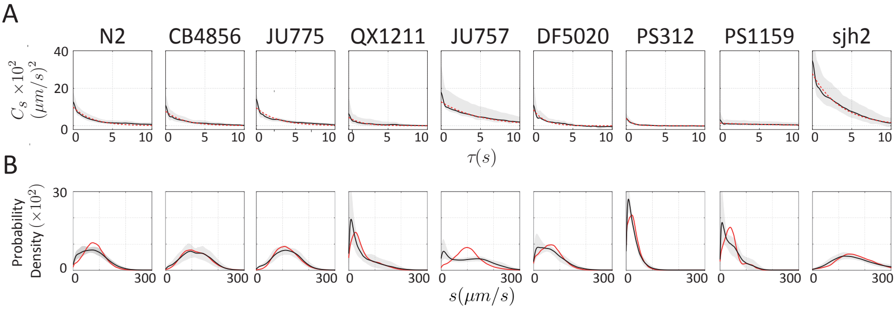

Figure S 2.5: Characterization of speed statistics across strains. (A) The speed autocorrelation (black) of each strain decays exponentially (red). (B) The speed distribution (black) of each strain is closely reproduced by model simulations (red).

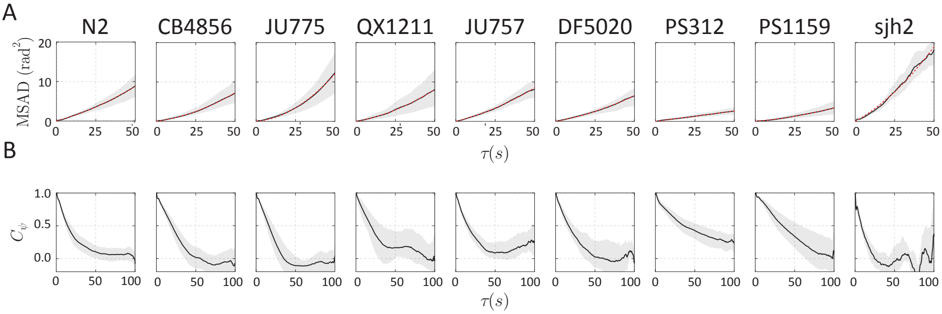

Figure S 2.6: Characterization of orientation statistics across strains. (A) The mean squared angular displacement of body orientation (black) was fit to a quadratic function (red) in all strains. (B) The orientation correlation (black) decays non-exponentially for many strains.

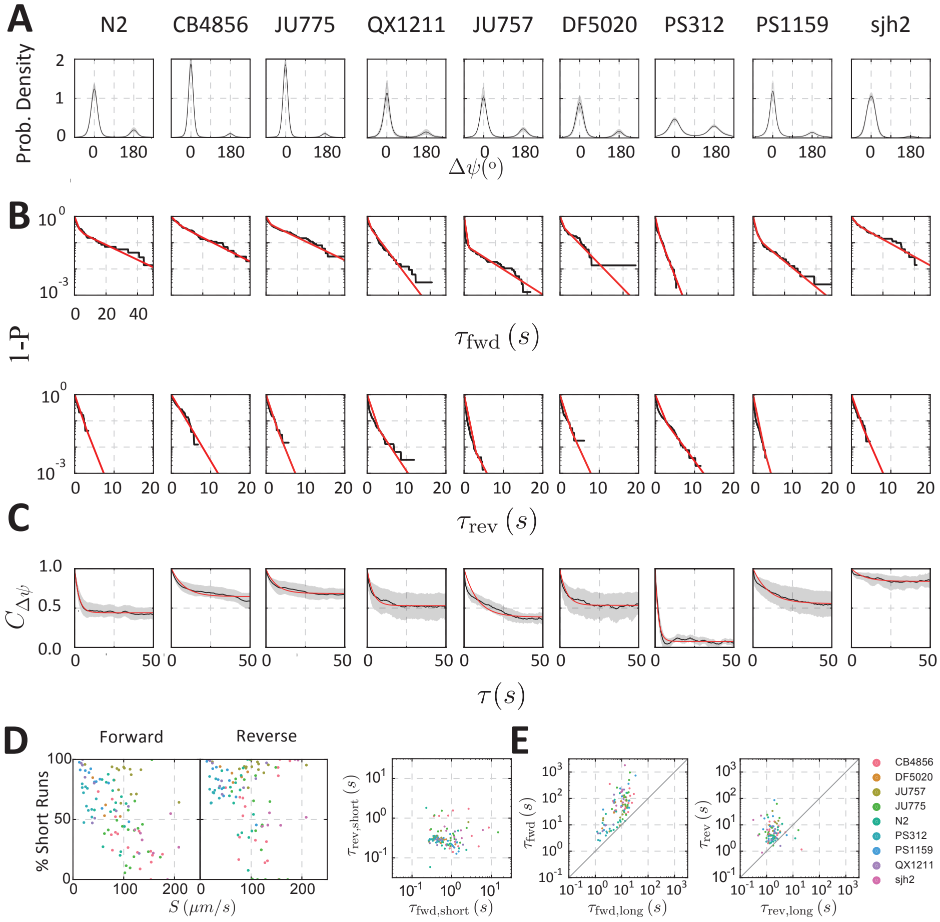

Figure S 2.7: Characterization of reversal statistics across strains. (A) Distribution of $\Delta\psi$ for each strain shows two prominent peaks at 0° and 180°. (B) Cumulative distributions of the forward and reverse run durations ($T_{\text{fwd}}, T_{\text{rev}}$) for an individual worm from each strain (black), fit to a biexponential function (red). (C) The autocorrelation function of $\Delta\psi$ for each strain (black) along with exponential fit (red). (D, left) The fraction of short runs measured by the biexponential fits of the transition time distributions (as in B) was inversely correlated with the average speed of the worm. At low speed, the bearing (and therefore also $\Delta\psi$, which is used to identify runs) is expected to be dominated by noise (e.g. pixelation artifacts). (D, right) The fitted time constants for short forward and reverse intervals were uncorrelated (unlike those for long runs, see E and also Figure 5A), and typically below the timescale of smoothing filter for velocity data (1 s), further motivating the exclusion of short intervals in modeling reversal dynamics. (E) τ_{long}, extracted from fits to the transition time distributions, were correlated with τ_{fwd} and τ_{rev}, estimated from $C_{\Delta\psi}$ (panel C).

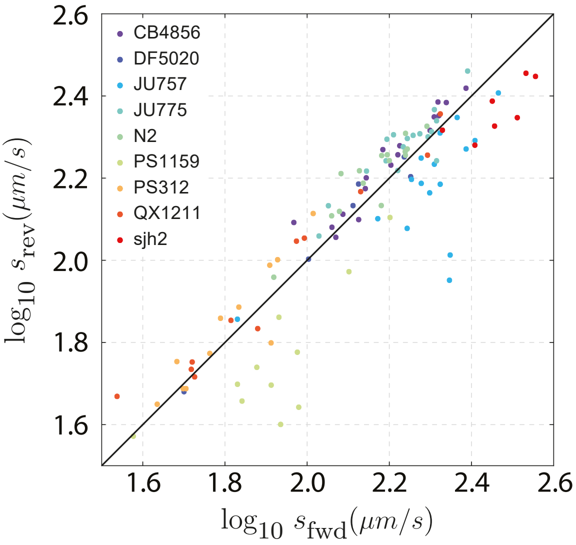

Figure S 2.8: Worm run speeds are similar during forward and reverse runs for individual trajectories (dots, colored by strain). We define run speed as the top speed during runs (rather than the mean speed, to avoid biases due to run-length differences). The top speed is computed as the 95th percentile of the speed distribution (rather than the maximum, to avoid outlier effects).

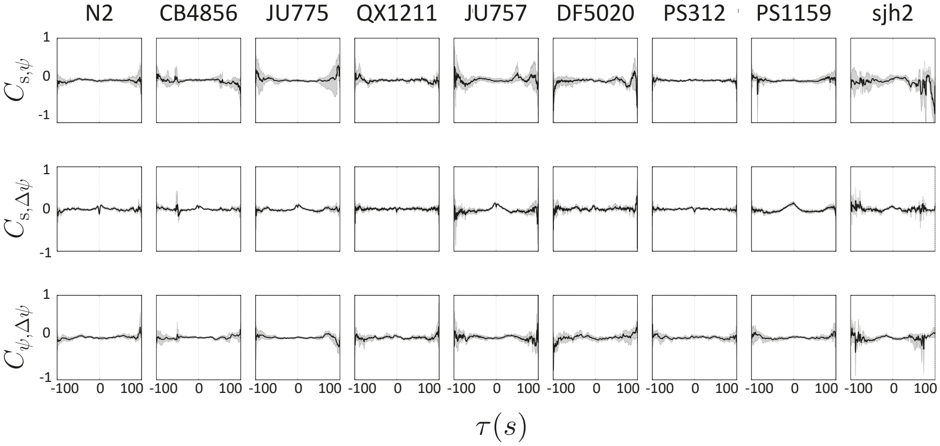

Figure S 2.9: Cross-correlation analysis of motility dynamics. The cross-correlation between (top) speed and bearing changes, (middle) speed and velocity alignment, and (bottom) bearing changes and velocity alignment are shown for each strain. There is very little cross-correlation among the motility variables in any of the strains. All cross-correlations were normalized to unit variance by dividing by the product of the standard deviation (σ) of the two components.

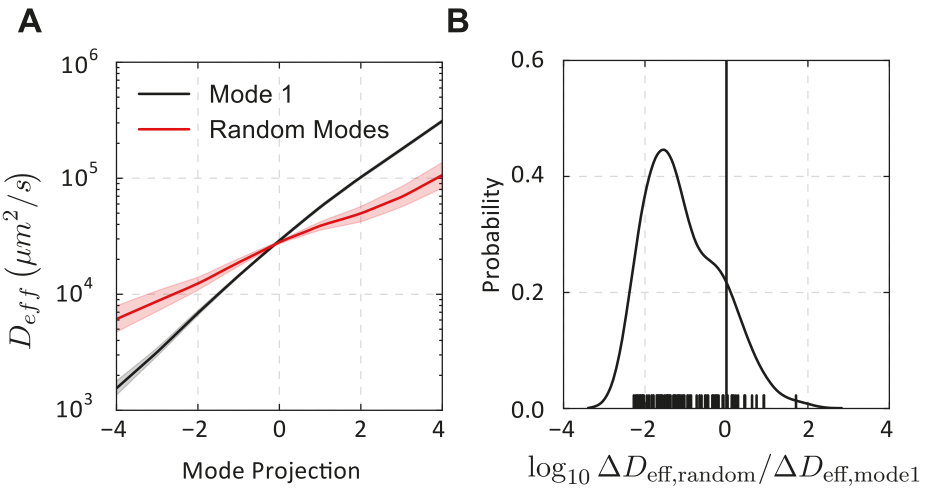

Figure S 2.10: The top behavioral mode effectively captures changes in diffusivity compared to random projections. (A) The effect of variation on the top behavioral mode (black, as in Figure 5C) compared with a sampling of 100 random modes (red) on the diffusivity of simulated trajectories. For random modes, the sign of the mode was chosen such that the diffusivity increased with the projection along the mode. (B) For each random mode we compute the relative change in diffusivity between mode values $\Delta D_{\mathrm{eff}} = D_{\mathrm{eff}}(2)/D_{\mathrm{eff}}(-2)$ and compare to the same relative diffusivity computed from the top behavioral mode. The kernel density distribution of the observed change is shown for the 100 samples (ticks). The black line indicates a ratio of 1 (no difference) and most random projections exhibit less range in ΔD_{eff}.

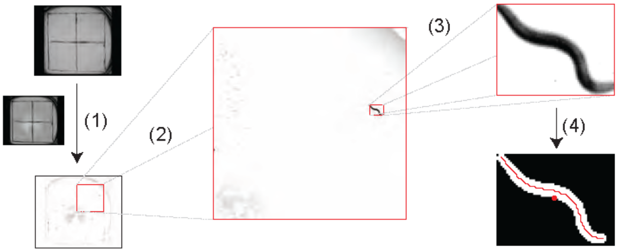

Figure S 2.11: An Overview of the image processing steps. The video frames were processed by (1) subtracting the average of 50 frames evenly sampled from the entire movie and (2) cropping to each of the SDS-enclosed regions. (3) The largest worm-sized object was identified following several image morphology operations, and (4) the centroid and image skeleton were measured.

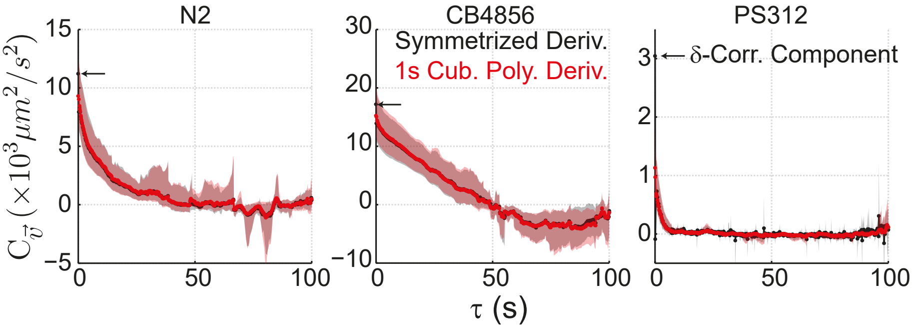

Figure S 2.12: Comparison of velocity calculation methods. Velocity autocorrelation functions for the three example strains with and without filtering of the data and without averaging over 100 s windows. The unfiltered velocity (black), estimated using a symmetrized derivative, contained a δ-correlated short-timescale component in all strains that was particularly prominent in slow-moving strains such as PS312. The velocity calculated using a 1 s cubic polynomial filter (red) does not contain this δ-correlated component.

Table S 2.1: The geometric mean of the effective diffusivity for each strain. For each trajectory, an effective diffusivity (D_{eff}) was extracted by analysis of mean-squared displacements and the velocity autocorrelation function.

	$D_{\text{eff}} \times 10^2$ $(\mu m^2/s)$		
Strain	Mean	2.5%	97.5%
N2	140	105	185
CB4856	429	307	620
JU775	448	360	558
QX1211	36	12	98
JU757	210	123	327
DF5020	128	55	255
PS312	8	5	13
PS1159	81	32	183
sjh2	425	314	553

Table S 2.2: The model parameters related to the speed dynamics are listed for each strain. For each worm in a strain, time-averaged parameters were calculated.

	μ_s $(\mu m/s)$			τ_s (s)			$D_s \times 10^2$ $((\mu m/s)^2/s)$		
Strains	Mean	2.5%	97.5%	Mean	2.5%	97.5%	Mean	2.5%	97.5%
N2	77	68	85	1.9	1.5	2.4	5.8	4.3	7.9
CB4856	108	91	128	1.8	1.5	2.3	4.0	3.1	5.2
JU775	112	98	127	2.1	1.6	2.7	4.3	3.3	5.5
QX1211	40	26	66	0.7	0.4	1.1	7.5	4.6	11.6
JU757	97	72	120	4.2	3.3	5.2	3.8	2.8	5.0
DF5020	65	50	83	1.1	0.8	1.3	11.7	9.1	14.4
PS312	27	23	32	0.7	0.6	0.8	5.3	3.7	7.4
PS1159	38	26	53	3.1	1.4	6.2	0.6	0.3	1.1
sjh2	159	138	184	3.3	2.5	4.7	8.8	5.8	13.2

Table S 2.3: The model parameters related to the orientation dynamics are listed for each strain. For each worm in a strain, time-averaged parameters were calculated.

	k_{ψ}rms (rad/s)			$D\psi$ $\left(rad^2/s\right)$		
Strains	Mean	2.5%	97.5%	Mean	2.5%	97.5%
N2	0.036	0.026	0.048	0.034	0.017	0.054
CB4856	0.029	0.018	0.041	0.024	0.018	0.033
JU775	0.038	0.026	0.053	0.021	0.016	0.030
QX1211	0.040	0.028	0.056	0.017	0.009	0.036
JU757	0.039	0.030	0.052	0.036	0.021	0.054
DF5020	0.037	0.032	0.042	0.033	0.026	0.041
PS312	0.017	0.011	0.029	0.021	0.014	0.028
PS1159	0.023	0.015	0.031	0.009	0.005	0.017
sjh2	0.066	0.057	0.077	0.090	0.065	0.127

Table S 2.4: The model parameters related to the reversal state dynamics are listed for each strain. For each worm in a strain, time-averaged parameters were calculated.

	τ_{fwd} (s)			τ_{rev} (s)		
Strains	Mean	2.5%	97.5%	Mean	2.5%	97.5%
N2	23.8	13.9	41.1	4.1	3.0	5.7
CB4856	78.6	56.5	109.5	4.3	2.8	6.3
JU775	85.3	51.5	144.0	8.0	4.2	16.3
QX1211	26.5	12.5	63.0	3.7	2.7	5.2
JU757	32.3	20.5	50.5	6.4	4.1	10.3
DF5020	32.7	15.2	63.2	4.8	3.2	7.2
PS312	5.6	4.2	7.4	3.3	2.9	3.9
PS1159	80.8	38.0	174.6	8.8	5.2	16.2
sjh2	155.5	75.2	419.9	4.9	2.3	10.8

Table S 2.5: The loadings of each parameter on the top behavioral mode are listed.

	Loading		
Parameter	Mean	2.5%	97.5%
$\log_{10} \mu_s$	0.50	0.25	0.58
$\log_{10} \tau_s$	0.51	0.40	0.54
$\log_{10} D_s$	-0.19	-0.43	0.08
$\log_{10} k_\psi$	0.24	-0.04	0.43
$\log_{10} D_\psi$	0.15	-0.22	0.40
$\log_{10} \tau_{fwd}$	0.50	0.36	0.55
$\log_{10} \tau_{rev}$	0.35	0.15	0.48

Table S 2.6: The phenotypic projection along the first behavioral mode is listed for each strain. For each worm in a strain, a time-averaged projection was calculated.

	Projection		
Strain	Mean	2.5%	97.5%
N2	-0.24	-0.47	0.51
CB4856	0.41	-0.37	0.83
JU775	0.83	-0.03	1.07
QX1211	-1.45	-1.70	0.40
JU757	0.79	-0.09	1.22
DF5020	-0.64	-0.73	1.10
PS312	-2.39	-2.71	-0.23
PS1159	0.37	-2.68	0.82
sjh2	1.66	0.85	2.35

BIBLIOGRAPHY

[1] Stephens, G. J, Johnson-Kerner, B, Bialek, W, & Ryu, W. S. (2010) From modes to movement in the behavior of Caenorhabditis elegans. *PLoS One* **5**, e13914.

[2] Blaxter, M. L, De Ley, P, Garey, J. R, Liu, L. X, Scheldeman, P, Vierstraete, a, Vanfleteren, J. R, Mackey, L. Y, Dorris, M, Frisse, L. M, Vida, J. T, & Thomas, W. K. (1998) A molecular evolutionary framework for the phylum Nematoda. *Nature* **392**, 71–5.

[3] Holovachov, O, van Megen, H, Bongers, T, Bakker, J, Helder, J, van den Elsen, S, Holterman, M, Karssen, G, & Mooyman, P. (2009) A phylogenetic tree of nematodes based on about 1200 full-length small subunit ribosomal DNA sequences. *Nematology* **11**, 927–950.

[4] Kiontke, K & Fitch, D. (2005) The phylogenetic relationships of Caenorhabditis and other rhabditids. *WormBook*.

[5] Andersen, E. C, Gerke, J. P, Shapiro, J. A, Crissman, J. R, Ghosh, R, Bloom, J. S, Félix, M.-A, & Kruglyak, L. (2012) Chromosome-scale selective sweeps shape Caenorhabditis elegans genomic diversity. *Nat. Genet.* **44**, 285–90.

[6] Chiang, J.-T. A, Steciuk, M, Shtonda, B, & Avery, L. (2006) Evolution of pharyngeal behaviors and neuronal functions in free-living soil nematodes. *J. Exp. Biol.* **209**, 1859–73.

[7] Davis, M. W, Somerville, D, Lee, R. Y, Lockery, S, Avery, L, & Fambrough, D. M. (1995) Mutations in the Caenorhabditis elegans Na,K-ATPase alpha-subunit gene, eat-6, disrupt excitable cell function. *J. Neurosci.* **15**, 8408–18.

[8] Stiernagle, T. (2006) Maintenance of C. elegans. *WormBook*.

[9] Lahl, V, Halama, C, & Schierenberg, E. (2003) Comparative and experimental embryogenesis of Plectidae (Nematoda). *Dev. Genes Evol.* **213**, 18–27.

[10] Hall, S. E, Beverly, M, Russ, C, Nusbaum, C, & Sengupta, P. (2010) A cellular memory of developmental history generates phenotypic diversity in C. elegans. *Curr. Biol.* **20**, 149–55.

[11] Rechavi, O, Houri-Ze'evi, L, Anava, S, Goh, W. S. S, Kerk, S. Y, Hannon, G. J, & Hobert, O. (2014) Starvation-Induced Transgenerational Inheritance of Small RNAs in C. elegans. *Cell* **158**, 277–87.

[12] Hart, A. (2006) Behavior. *WormBook*.

[13] Huang, K.-M, Cosman, P, & Schafer, W. R. (2006) Machine vision based detection of omega bends and reversals in C. elegans. *J. Neurosci. Methods* **158**, 323–36.

[14] Kloeden, P. E & Platen, E. (1992) *Numerical Solution of Stochastic Differential Equations.* (Springer Berlin Heidelberg, Berlin, Heidelberg).

[15] Scott, D. W. (1992) *Multivariate density estimation: theory, practice, and visualization.* (John Wiley & Sons).

[16] Chaikin, P. M., Lubensky, T. C. & Witten, T. A. (1995) Principles of condensed matter physics.. Cambridge University Press)..

3

VARIABILITY REVEALS OPTIMALITY AND CONTROL IN *C. elegans* TURNING BEHAVIOUR

ABSTRACT

The statistics of reorientation behaviours determine exploration and navigation performance in the locomotion of many animals. Yet optimization of turning statistics is often subject to constraints arising in the actuating anatomy, control physiology, or both. Here, we use the nematode *C. elegans* as a minimal model system to ask whether and to what extent turning behaviours are optimised under such constraints by evolutionary selection and physiological control. We focus on turning behaviours under two contrasting environmental contexts: (i) random exploration in the absence of strong stimuli and (ii) acute avoidance (escape) navigation upon encountering a strong aversive stimulus. We dissect trajectory and postural statistics to characterise the full repertoire of reorientation behaviours, including gradual reorientations and various posturally distinct sharp turns. In both contexts (i) and (ii), we show how bias in turning behaviour (an effective handedness) diminishes performance, but the class of turns in which bias imposes performance constraints differs between the two contexts.

During exploration, the bias of gradual turns fluctuates over long times, even changing sign within an individual, suggesting it may originate in the limited precision of orientation-control physiology. On faster timescales, orientation fluctuations are well-described by a (symmetric) angular diffusion process, and we develop a minimal theoretical model for worm trajectories that incorporates both the gradual-turn bias and angular diffusion, in addition to sharp turns. We

demonstrate that under the constraint of a finite bias in gradual turns, there exists an optimal angular diffusivity that maximises exploration propensity, and our measurements indicate that the angular diffusivity of *C. elegans* is, on average, set at this optimum. During the escape context, the well-known dorso-ventral (D-V) bias in sharp-turn directions proves detrimental. By analyzing the statistics of incoming and outgoing angles of escape turn events relative to the gradient of an escape-triggering chemical stimulus, we find evidence for strong modulation of not only the amplitude (~ 2-fold) but also the D-V bias (~ 8-fold) of sharp turns to probablistically steer the exit angle toward the optimal direction. Thus, although sharp-turn bias in *C. elegans* is clearly tied to anatomical asymmetry, it is evidently a soft constraint that can to some extent be overridden by context-dependent control physiology. Our results demonstrate how biasing constraints on turning impact both exploration and navigation, and that optimization and control of turns can be leveraged to increase performance under anatomical and physiological constraints.

3.1. INTRODUCTION

Changing course effectively is fundamental to exploration and navigation by motile organisms. Although the mechanisms that underlie motility are diverse, the motile strategy of many organisms can be described as a biased random walk, in which the statistics of reorientation (turns) determine how the organism explores space, and are modulated to achieve navigation [1, 2]. A ubiquitous yet underappreciated aspect of turning, as implemented in these strategies, is the need to overcome inherent asymmetries in the actuating anatomy and control physiology to optimise performance. The biased random walk is effective as a motile strategy precisely because the bias is imposed in response to the environment. Biases arising from internal factors uncorrelated with the environment can thus generically be expected to diminish performance and in turn act as constraints in optimizing behavior.

One simple strategy for overcoming such biasing constraints is to randomise the direction of the bias relative to the environment. This is implemented, for example, in the swimming kinematics of *E. coli* bacteria, which effectively eliminate the effects of anatomical asymmetry (due e.g. to the random positioning of flagella on the cell surface) by incessantly rolling their cell body about the direction of motion as they explore their environment by swimming (runs), thereby eliminating correlations between any turning bias and the environment [3]. As a result, the bacterium can optimise its exploration and navigation performance by tuning only two variables — the temporal frequency at which erratic turns (tumbles) are generated, and the average (unsigned) angle of tumble-induced turns [4]. By contrast, within the animal kingdom, the kinematics of locomotion tend to more faithfully reflect the asymmetries of animal anatomy. The vast majority (> 99%) of animal species have a bilateral body plan, meaning radial symmetry about the anterior-posterior (A-P) axis is broken to yield two more orthogonal axes of polarity: the dorso-ventral (D-V) and left-right (L-R) axes [5]. This three-axis anatomical frame has tangible advantages for directed locomotion as it enables distinct motor patterns in the vertical (i.e. gravitational) and lateral directions, across which resource distributions tend to be very different [6]. But these advantages also come with a cost: breaking rotational symmetry eliminates the possibility of removing detrimental directional bias by rotation about the locomotion direction. Indeed, the statistics of turning behaviour demonstrate some degree of lateral bias (handedness) across the immense diversity of bilaterian animals, from invertebrates [7–11] to humans [12, 13].

The causal factors that underlie turning biases are not well understood, but are likely to be diverse in origin, given the broad spectrum of reported phenomenologies. Some instances of reported turning bias were in the gradual reorientation (path curvature) during intervals of relatively smooth forward or backward motion [8, 11, 12], which might arise from imperfect lateral symmetry in the kinematic cycle of the animal's gate. In other examples, turning bias was observed in the more discrete sharp-turn behaviours that occur either spontaneously during unbounded locomotion [7] or upon forced decisions in a Y-maze [9, 10]. Some of these turning biases persisted throughout the lifetime of an individual [7, 9, 10], whereas in at least one example they were found to vary, and even change sign, over relatively short times [12]. The mechanistic origins are therefore likely different from case to case, and relatively few studies have been able to directly address causal factors experimentally. Nevertheless, the available data point towards neural control physiology [7, 9, 13], rather than hard constraints at the anatomical level, as causative factors for turning bias during locomotion.

In this study, we investigate bias in the turning behaviour of the nematode *C. elegans*, arguably the simplest and best characterised animal model for locomotion [14]. The adult hermaphrodite body plan comprises just 959 somatic cells [15], of which 302 are neurons with a fully mapped connectome [16, 17]. Despite this compact anatomy, these worms perform a variety of locomotion tasks, such as exploration for food, chemotaxis, and escape. The relative simplicity of its anatomy, control physiology, and postural kinematic repertoire positions *C. elegans* as a compelling minimal model system to address fundamental questions about behavioural strategies of animal locomotion and the underlying neural control mechanisms. Previous work has identified significant orientational biases in *C. elegans* turning behavior [7, 8, 11], but how such biases affect performance in specific locomotion tasks remains an open question.

Turning during *C. elegans* locomotion occurs both abruptly and gradually as the worm crawls on surfaces. Crawling is driven by undulatory propulsion, in which body bends in the D-V direction (*C. elegans* crawls while lying 'on its side', with its L-R body axis normal to the surface) are initiated near the head and propagated along the length of its anatomy towards the tail, resulting in postures and trajectories of motion that are approximately sinusoidal in shape. Occasionally, these forward runs are interrupted by sharp reorientation events called Ω-turns in which the body bends deeply (rendering the worm's shape reminiscent of the greek letter Ω) to generate a large change in orientation[18], as well as brief reversal events in which propagation direction of the body wave (and hence also the worm's movement direction) is inverted but do not otherwise change the direction of motion. When navigating environmental gradients by chemotaxis, reversals and sharp turn events are often clustered in time, generating short intervals of frequent turning (pirouettes) that interrupt otherwise smooth crawling trajectories, and modulating the temporal frequency of pirouettes in response to the environment provides *C. elegans* with one mechanism for biasing its random walk to achieve chemotaxis [19]. Between these abrupt reorientation events, more gradual changes in orientation also occur, resulting in trajectories that are curved and meandering over lengthscales greater than those of the aforementioned body wave [8, 11], and it has been shown that worms can also bias this curvature in response to environmental gradients to enhance chemotactic performance [20, 21].

Directional biases are known to exist for both sharp and gradual turns of *C. elegans*[8, 22], even in the absence of environmental gradients, yet their impact on locomotion performance has yet to be studied systematically. The sharp Ω-turns are known to be strongly biased in the ventral direction [7, 18]. The biological reason for this D-V bias is not well understood, but it evidently reflects neural control, as ablating a single neuron (RIV) results in a much larger fraction of Ω-turns in the dorsal direction, largely eliminating this bias [7]. Bias in gradual turns is less well characterized, perhaps because it is an inherently long time- and length-scale phenomenon, and thus accurately quantifying it requires extensive statistics from long trajectory recordings. However, recent studies have provided evidence that orientational statistics of crawling *C. elegans* trajectories collected over 30-80 min are not isotropic [8], and that biases in gradual turns (of ~2 degrees per second) can be detected even within 30 min trajectories [11].

Here, we present an extensive study of *C. elegans* turning statistics in two contrasting behavioural contexts: exploration in the absence of environmental gradients, and escape upon encountering a strong aversive stimulus. To sufficiently sample both sharp- and gradual-turn statistics within each individual, we recorded long (120 min) trajectories within an arena enclosed by a repellent boundary. The worms spend most of their time exploring the arena by freely crawling in the absence of environmental gradients, allowing us to sample the statistics of "spontaneous" turns, which the worms execute without a triggering environmental stimulus. In addition, upon encountering the boundary impregnated with a chemical repellent, an escape response [23–25] is triggered, causing the worm to turn around. We quantify the strength of orientational biases in both sharp and gradual turns, and quantify their effects on performance in both behavioural contexts.

3.2. RESULTS

3.2.1. WORMS IN REPELLENT-BOUNDARY ARENAS DEMONSTRATE BOTH EXPLORATION AND ESCAPE BEHAVIORS

Globally, the worm's motile behaviour can be described as intervals of relatively straight forward motion (runs) interrupted by brief intervals of backward motion (reversals) and abrupt reorientation events (sharp turns). Some reorientation also occurs during runs, which are comparatively subtle, but could cumulatively impact the navigational strategy over long times [11, 26]. Reversals have a negligible net effect on orientation once the worm reverts to forward motion. Sharp reorientation events are defined as any event where the worm performs a deep body bend and folds onto itself.

To extensively sample the reorientation behaviour of worms, we imaged the motility of *C. elegans* strain N2 individuals crawling on agar plates for a duration of approximately 2 hours (Methods). Worms were confined by a repellent boundary to within a 38 mm × 38 mm arena, the entirety of which can be imaged at a resolution sufficient to resolve not only the worm's position but also its postural dynamics (effective pixel size 18.7 µm). The motility of up to eight worms was measured simultaneously within these arenas. Throughout the duration of the measurement, the identity of each worm was tracked, enabling us to study variability in behaviour between individuals. The arena contained no food, and worms were kept off food for 15 minutes prior to the experiment, to reduce non-stationarities in behaviour that are known to affect worm motility (including sharp turn rates) for several minutes after transitioning from an on-food to an off-food environment [7, 22, 27]. Reorientation statistics of 100 individual worms were obtained by analysing the video recordings (Methods), yielding a total of 12,475 sharp reorientation events within 197 hours of trajectories. In 85% of these identified sharp turns, postural dynamics could be unambiguously resolved, thus allowing analysis of postural kinematics for 98% of the total trajectory duration.

The repellent boundary not only served to confine worms to within the camera's field of view, but also allowed us to study reorientation statistics in two contrasting behavioural contexts within a single measurement: (1) exploration in the absence of environmental stimuli and (2) the escape response upon encountering the strongly aversive repellent boundary. For most of the trajectory duration, worms engaged in exploratory behaviour across the arena, characterised by long runs interrupted by spontaneous sharp turns [22, 28]. Upon encountering the repellent boundary, an escape response was reliably triggered, where the worm executed a sharp turn following a brief reversal (Figure 3.1). The spatial distribution of these escape turns (*i.e.* sharp turns that immediately follow a reversal) was highly concentrated near the repellent boundary, in stark contrast to that of spontaneous turns during forward runs that occurred randomly across the arena (Figure 3.1). Therefore, turning behaviour during exploration and escape can be studied, respectively, through the reorientation statistics of trajectory segments far from (> 7 mm) and close to (< 7 mm) the repellent boundary. Some escape turns were observed far away from the repellent boundary, but these were infrequent (14% of all turns > 7 mm from the boundary) and we therefore did not consider them explicitly in subsequent analyses of exploratory behavior.

Finally, we note that worm behaviour was not significantly perturbed by collisions with other worms within the arena. Collisions did occur at a finite rate, but these were infrequent (on average, once every 7.8 min), could be unambiguously resolved (see Methods) and no effect on crawling speed or sharp turn frequency was detectable beyond the duration of the collision event (Figure S3.1).

Thus, simultaneous tracking of multiple worms in repellent-boundary arenas enabled efficient acquisition of individual turning statistics across two contrasting behavioral contexts.

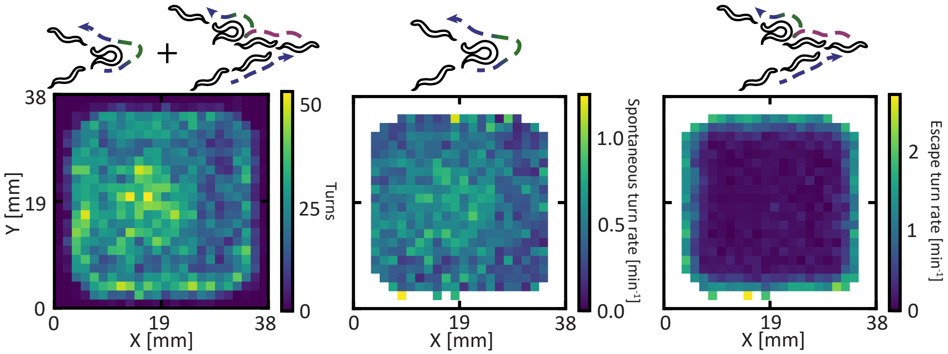

Figure 3.1: (left) The spatial distribution of both spontaneous sharp turns and escape turns inside the arena. (Middle) Spontaneous turns, defined as sharp turns that occur during forward crawling, occur at an equal rate. (right) The escape turn rate, defined as sharp turns following a reversal, is sharply increased near the repellent boundary of the arena. Pixels at the edge that have been occupied by a worm with fewer than 5k data points (≈ 7 min) are not included.

3.2.2. VARIABILITY IN SPONTANEOUS SHARP TURN BEHAVIORS REVEAL THEIR IMPACT ON SPATIAL EXPLORATION

The most prominent reorientation behaviours during the worm's exploration of free space are spontaneous sharp turns, which are executed at random times even in the absence of environmental stimuli [19, 28]. These turns involve a deep body bend, which can occur in either the dorsal or ventral direction, but with a strong statistical bias towards the ventral side [7, 18]. Sharp turns can be further classified into Ω- and δ-turns, on the basis of postural statistics [22]. Compared to Ω-turns, δ-turns exhibit even higher body-bend amplitudes, such that the strongly curved body not only touches but also crosses itself, resulting in larger reorientation angles.

To correctly assign sharp turns into these categories, we analysed the postural dynamics throughout each turn. Because δ-turns have been shown to occur only in the ventral direction [22], we assigned the ventral orientation of each worm to the direction that demonstrated a greater extent in the body-bend amplitude distribution (see Methods). After this D-V orientation assignment, the distribution of body-bend amplitudes for the dorsal direction demonstrated a single peak corresponding to dorsal omega turns, whereas that for the ventral direction was better described as a sum of two overlapping peaks, with one corresponding to ventral Ω-turns and the other to ventral δ-turns (Figure 3.2A). Sorting all ventral turns into bins corresponding to each of these peaks further confirmed that δ-turns do indeed, on average, generate larger angle changes $\Delta\theta$ in the worm's trajectory (Figure 3.2B).

Thus, in addition to the angle change $\Delta\theta$, three random variables suffice to characterize the statistics of sharp turns (Figure 3.3A): (1) the rate ζ (min^{-1}) at which sharp turns are executed, (2) the probability $P(\mathrm{D})$ that an executed sharp turn is in the dorsal direction, and (3) the probability $P(\delta)$ that an executed ventral sharp turn is a δ-turn. The statistics aggregated over all 100 worms confirmed that during exploration, there is a strong preference for ventral turns over dorsal turns, and within ventral turns Ω- over δ-turns (Figure 3.3, 3.2) [7, 29, 30]. However at the level of individual trajectories, all three random variables demonstrated substantial variation about the population (Figure 3.3B-D, blue). Across individuals, the sharp turn frequency was found to vary by at least an order of magnitude. Some worms did not execute any dorsal turns or δ-turns over the course of the 2 h measurement, whereas at the opposite extreme, such turns accounted for more than half of all sharp turn events. The variability across individuals was not trivially explained by the finite number of samples within the 2 h measurement, as the distribution of all three random variables from the measured data were broader than that for Monte Carlo simulations (see Methods) that assumed all worms were realizations of identical random variables with parameters corresponding to the population mean (Figure 3.3B-D, orange, S3.3).

To evaluate how each of these sharp-turn parameters are related to exploration performance, we computed for each trajectory its persistence length P, which can be extracted from the relationship between the mean-squared displacement (MSD) and contour length (Figure S3.5, see Methods) and quantifies the effective area covered by trajectories as function of the contour length. It is closely related to the diffusion coefficient D_{diff} and the velocity v by $P = D_{\mathrm{diff}}/v$, therefore time-independent and more sensitive to the properties of trajectory rather than the pace at which it is generated, which is the trivial solution towards changing the exploration rate. Comparing the persistence length against the turning parameters for each trajectory revealed that the D-V sharp turn bias was not significantly correlated (-0.13 ± 0.25, 95% CI) to the persistence length, and the Ω-δ preference was only weakly correlated (-0.20 ± 0.14, 95% CI) (Figure 3.3FG). Thus, neither of these sharp-turn biases substantially affect exploration propensity. By contrast, the temporal frequency of sharp turns demonstrated a strong negative correlation with the persistence length (-0.59 ± 0.12, 95% CI); worms that turn at higher frequency explore smaller areas (Figure 3.3E). In short, we found that each of the random variables (ζ, $P(D)$, and $P(\delta)$) vary significantly among individuals, but while sharp turn frequency is strongly negatively correlated with the persistence length, the D-V and Ω-δ biases have little impact on this measure of exploratory propensity.

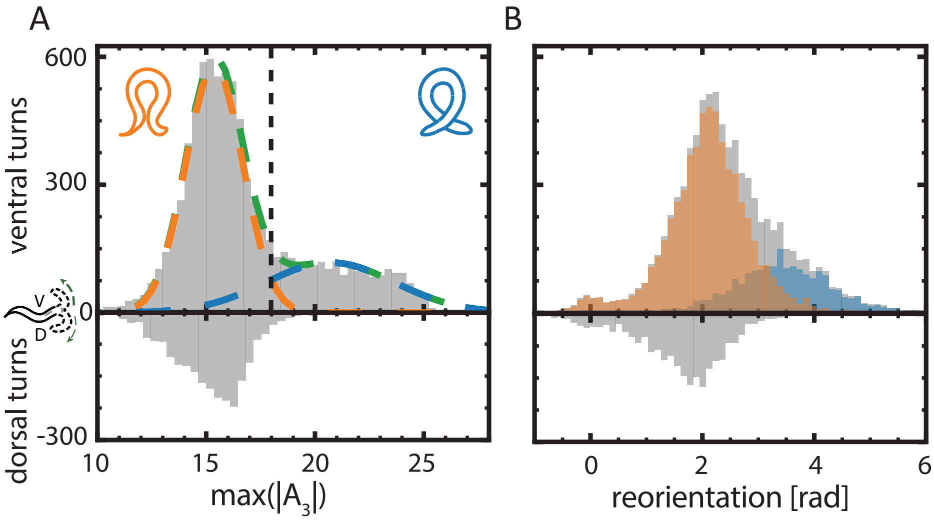

Figure 3.2: Ω and δ turns are separated by thresholding the loading of the third Eigenworm[22, 31]. (A) The distribution of (top) ventral and (bottom) dorsal maximum Eigenmode loadings across both spontaneous sharp turns and escape turns. The ventral distribution can be approximated as the sum of 2 Gaussians (green). The orange Gaussian is an approximation of the Ω turn distribution, and the blue Gaussian is an approximation of the δ distribution. The A_3 value where the lines cross, 18.0 (black dashed line), is henceforth used as the threshold to separate Ω and δ turns. The dorsal distribution only includes Ω turns. (B) The distribution of (top) ventral and (bottom) dorsal reorientation angles towards the direction of the body bend. The distribution of Ω and δ turns after thresholding the maximum A_3 amplitude in orange and blue respectively.

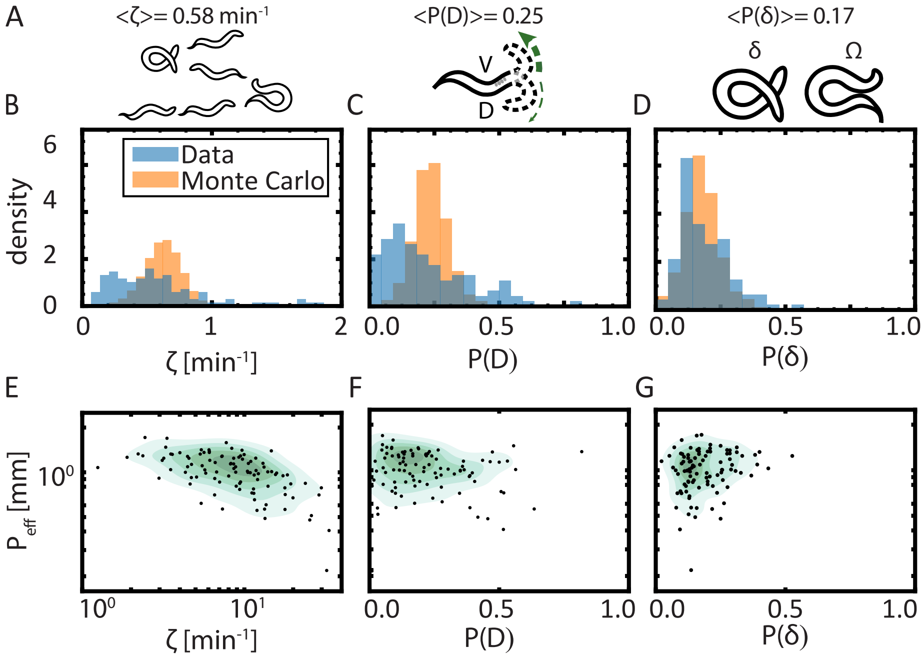

Figure 3.3: **Variability in turn frequency, but not D-V bias or Ω-δ bias, substantially affects exploratory propensity.** (A) Schematic illustration and population-average statistics of the three random variables that govern spontaneous sharp turns: (left) the turn frequency, ζ; (center) the dorsal turn probability $P(D)$, a measure of D-V bias in sharp turn orientation; (right) the δ-turn probability $P(\delta)$, a measure of Ω-δ bias for ventral turns. The most common turn type is an Ω-turn in the ventral direction. (B-D) Distribution across the population of the three random variables ζ (B), $P(D)$ (C), and $P(\delta)$ (D) indicate substantial variability across individuals. Blue bars represent statistics for individual measured trajectories, and orange bars are from Monte Carlo simulations assuming all individuals are sampled from a population with identical parameters for the corresponding random variable (see Methods). (E-G) Relationship between the trajectory persistence length P_{eff}, a measure of exploratory propensity, and the three random variables ζ (F), $P(D)$ (G), and $P(\delta)$ (H). P_{eff} demonstrates a substantial negative correlation with the sharp turn rate ζ (-0.59 ± 0.12, 95% CI; $p \leq 7.7 \cdot 10^{-11}$), but its correlation with D-V bias and Ω-δ bias was, respectively, insignificant (-0.13 ± 0.25, 95% CI; $p \leq 2.1 \cdot 10^{-1}$) and marginally significant (-0.20 ± 0.14, 95% CI, $p \leq 4.2 \cdot 10^{-2}$). Indicated p-values were computed using a t-test assuming a two-tailed probability.

3.2.3. BIAS AND FLUCTUATIONS IN GRADUAL TURNS NEGATIVELY IMPACT EXPLORATION

During exploration, gradual adjustments in the direction of movement occur between spontaneous sharp turn events [8, 27], causing meandering trajectories on length scales longer than the body wave and in some instances even forming loops (Figure 3.4A). Such effects on trajectories shape reduce the directional persistence of the worm's motion between sharp turn events, and hence could be expected to negatively impact the exploration propensity P_{eff}. We therefore proceeded to quantify the effects of these more subtle reorientations.

Gradual reorientation dynamics were extracted from the worm's body orientation (see Methods), which provides an accurate proxy for the direction of movement (*i.e.* the velocity bearing) during runs, even when moving at low speeds. Over the course of the experiment, the unwrapped body orientation (*i.e.* cumulative angle change) of most worms demonstrated many full rotations, indicating a significant bias in the gradual-turn dynamics (Figure 3.4B). Interestingly, whereas some worms accumulated rotations persistently in the dorsal (14/100 worms) or ventral (24/100) direction (Figure 3.4B, green and blue curves, respectively), most worms (62/100) demonstrated rotations in both the dorsal and ventral directions (Figure 3.4B, red curves).

The gradual-turn dynamics also feature faster orientation fluctuations, causing the unwrapped body-orientation trajectories to be jagged, rather than smooth curves (Figure 3.4B). To examine the statistics of gradual turns across timescales, we computed the mean-squared angular displacement (MSAD) of the unwrapped body orientation as a function of time (Figure 3.4C, blue curve), which showed similar dynamics compared to a previously published data set[32] (Figure 3.4C, green curve). For timescales longer than the body wave oscillations (~ 2 s) but less than ~ 10 s, the local power-law scaling exponent (*i.e.* the log-log slope) of MSAD(t) was close to unity (Figure 3.4C, Inset), indicating that fluctuations around this timescale are well-approximated as pure (*i.e.* Brownian) angular diffusion. Consistently, angular deviations observable at short times/lengths decorrelated nearly completely within a single body wave (Figure S3.6). Therefore, these random orientation changes on short time- and length-scales (comparable to the body wave) can be modeled as an angular diffusion process [11] (see Methods), characterized by a angular diffusion coefficient D_ψ which varied from worm to worm but most commonly was around 0.2 $\text{rad}^2\text{mm}^{-1}$ (Figure 3.4D). For longer timescales, the angular dynamics were increasingly super-diffusive, with the local scaling exponent plateauing around 1000 s at a maximum value of ~ 1.86 (Figure 3.4C, Inset), consistent with a persistent gradual-turn bias (perfectly circular trajectories would yield an exponent of 2.0). Thus, the worms' reorientation dynamics can be described as a combination of two processes: (1)

angular diffusion resulting in meandering trajectories and (2) a gradual-turn bias (rotational drift) causing the trajectories to form loops [11].

To quantify the gradual-turn bias, we computed the trajectory curvature κ, averaged over windows of 15 min, the time scale around which the slope of MSAD(t) was maximal (Figure 3.4C, Inset) and hence orientation dynamics were most persistent. The distribution of κ pooled from all 100 trajectories was distributed approximately symmetrically in the dorsal and ventral directions (Figure 3.4E) with a mean that is not significantly different from zero (0.00 ± 0.02, 95% CI), indicating no net D-V bias across the ensemble of trajectories. However, as noted above, the gradual-turn bias of individual trajectories tends to fluctuate slowly over time. To characterize the timescale of such slow fluctuations in the gradual-turn bias, we computed the autocorrelation function of κ ($\mathrm{ACF}_\kappa(t) \equiv \langle \kappa(0)\kappa(t) \rangle$) (Figure 3.4F). Within the timescale of the measurement, the ensemble average $\langle \mathrm{ACF}_\kappa(t) \rangle$ decayed to 0.2, with a profile consistent with a single-exponential $\langle \mathrm{ACF}_\kappa(t) \rangle \sim e^{-t/\tau}$ with decay time constant $\tau = 82 \pm 17$ min (see methods). Thus, although the 2 h timescale of our experiment precludes confirming the full decorrelation of these slow fluctuations, the data are compatible with a model in which gradual-turn bias fluctuates slowly in a manner that when averaged over very long times ($\gg \tau$) has little or no net bias (per the near-zero κ-distribution mean), but has at any instant of time a finite magnitude (in the range of the κ-distribution width).

As noted above, both the short-timescale angular diffusion and the longer-timescale bias of gradual turns can be expected to negatively impact exploration. Consistent with this idea, worm-to-worm variation in both the angular diffusivity D_ψ and the root-mean-square (RMS) magnitude of the gradual-turn bias (κ_{RMS}) demonstrated clear negative correlations with the exploration propensity P_{eff} of trajectories (Figure 3.4G,H).

In summary, although the gradual-turn bias is relatively weak ($\langle \kappa_{\mathrm{RMS}} \rangle \approx 0.2\,\mathrm{rad\,mm^{-1}}$) and fluctuates slowly over time with an approximate zero mean, its cumulative effect on the exploration propensity P_{eff} over long time- and length-scales are comparable to, or greater than, that of the short time- and length-scale angular diffusion.

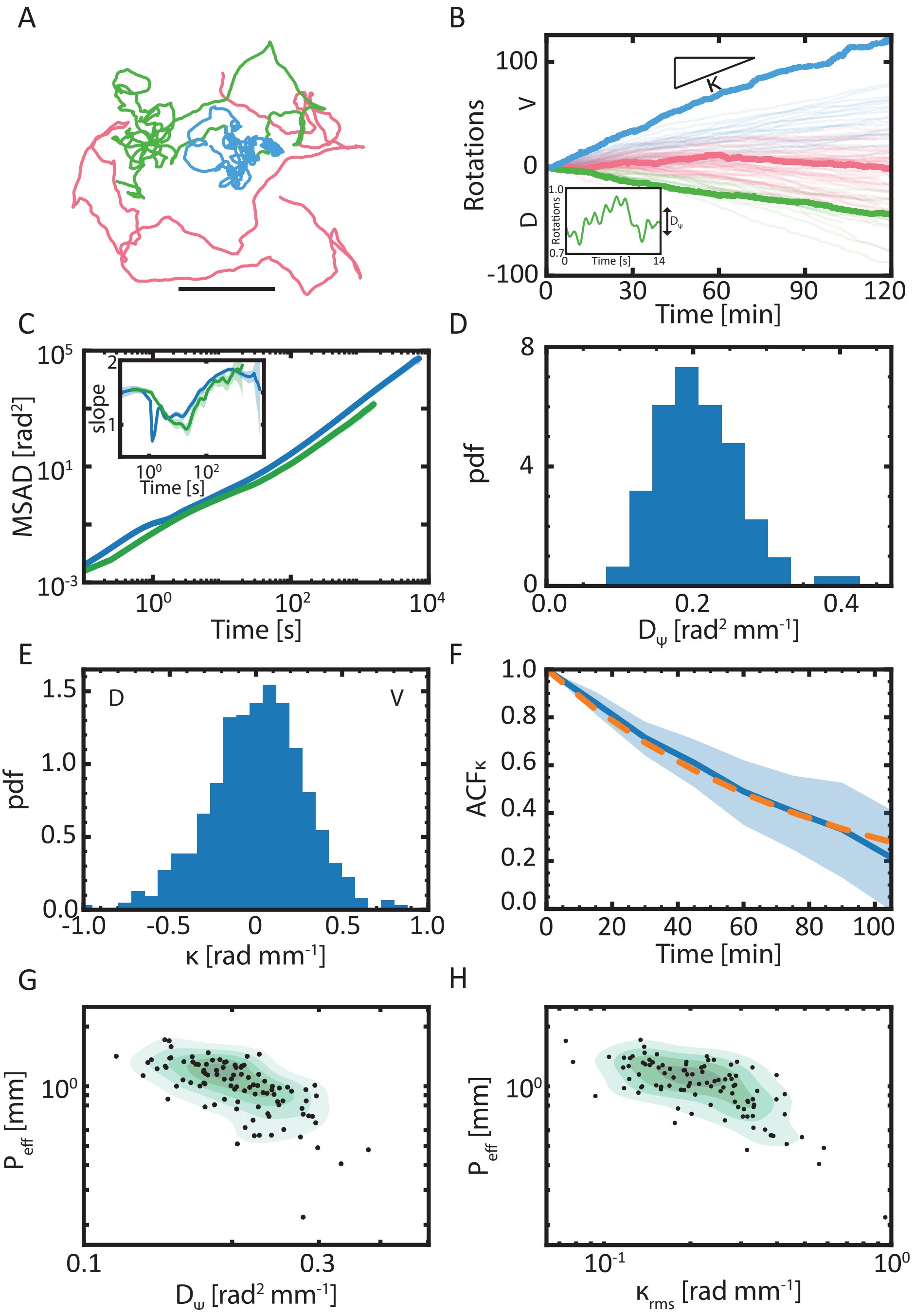

Figure 3.4: Caption is on the next page.

Figure 3.4: **Gradual turning behaviour during exploration demonstrates both short-time fluctuations and long-time biases.** (A) Representative trajectory segments (10,000 frames = 14.5 min) for 3 individual worms, demonstrating strong (blue), intermediate (green) and weak (red) gradual-turn bias and correspondingly different trajectory curvature. In addition to the 'loopiness' caused by the long-timescale bias, diffusive orientation fluctuations induce wiggles in the shape of trajectories. Scale bar 10 mm. (B) Gradual-turn bias can cause trajectories to accumulate many net rotations during the course of the experiment, resulting in a slope κ. A positive value means that the worm has rotated more in the ventral direction than in the dorsal direction. Inset: angular changes on short time scales from undulatory fluctuations, result in an effective angular diffusion D_{ψ}. (C) The average mean-square angular displacement (MSAD) and (inset) the local exponent (*i.e.* log-log slope) of the unwrapped average body angle across worms of our data set (blue) and a previously published data set from ref. [32] (green; see Methods) show near ballistic behaviour on long time-scales. A slope of 1 indicates diffusive angular dynamics, and a slope of 2 corresponds to ballistic angular dynamics. The dip in the slope of the blue curve of the MSAD at ≈ 2 s can be attributed to angular oscillations due to the body wave (and is not observed in the green curve, due to differences in the sampling rate and the manner in which angular dynamics were extracted; see Methods). (D) Probability density histogram of the angular diffusion coefficient D_{ψ}, extracted from each of 100 individual trajectories. (E) Probability density histogram of the local gradual-turn bias κ, defined as the average trajectory curvature within 15 min windows, extracted from all such non-overlapping windows in all 100 trajectories. The sign of κ was set to be positive in the ventral (V) direction and negative in the dorsal (D) direction. The average rotational drift for each worm shows no dorso-ventral population mean. (F) Slow fluctuations gradual-turn bias decorrelate on a timescale comparable to the duration of the measurement, and can be fit by a single-exponential decay with a time constant of 82 ± 17 min. Because the time scale of the fluctuations is similar to the length of the measurement, the mean cannot be established of individual measurements, and the global mean value of 0 is used. (G) The angular diffusivity D_{ψ} is negatively correlated with the persistence length P_{eff}, with a correlation coefficient -0.57 ± 0.13 (95% CI) ($p < 2.9 \cdot 10^{-10}$). (H) The root-mean-square gradual-turn bias κ_{RMS} is strongly negatively correlated with the persistence length P_{eff}, with a correlation of -0.72 ± 0.11, (95% CI) ($p < 1.3 \cdot 10^{-17}$). Indicated p-values were computed using a two-tailed t-test.

3.2.4. A FINITE GRADUAL-TURN BIAS LEADS TO AN OPTIMAL CHOICE FOR ANGULAR DIFFUSIVITY

The data presented above demonstrate that each of three turning-behavior parameters — the sharp turn rate ζ, gradual-turn diffusivity D_ψ and bias magnitude κ_{rms} are negatively correlated with the exploratory propensity P_{eff} (*i.e.* the persistence length) of trajectories. Yet the manner in which these different turning components affect exploration might not be independent. To gain insight into the relative contributions of, and interactions between, these parameters in determining the overall exploratory propensity P_{eff}, we constructed a minimal model of the worm's turning behaviour.

Changes in the lab-frame orientation ψ along the trajectory contour x is described as a sum of two terms: a constant angular drift accounting for the gradual-turn bias, and angular diffusion:

$$d\psi(x) = \kappa dx + \sqrt{2D_\psi} dW_x. \tag{3.1}$$

where κ [rad mm^{-1}] is the angular drift, D_ψ [rad^2/mm] is the angular diffusion coefficient, and W_x [mm$^{1/2}$] is a Gaussian white noise process with zero mean and unit variance. Sharp reorientation events occur with a uniform probability per unit length along the trajectory contour, determined by the turn frequency ζ [s^{-1}] and speed s [mm s^{-1}] of the worm:

$$p_{\text{turn}} = \zeta / s dx. \tag{3.2}$$

The experimental observation that sharp turns do not completely randomize the orientation but are instead biased, on average, slightly towards the reverse direction (i.e. $\langle \cos \Delta\theta \rangle < 0$; Figure 3.2B) can be accounted for by scaling the sharp turn frequency by a factor $\alpha = 1 - \langle \cos \Delta\theta \rangle$ [33, 34], for which we use the population averaged value $\alpha = 1.33$.

These dynamics can be solved analytically for the expected persistence length P, yielding a simple closed form expression (see SI text):

$$P = \frac{1}{2} \frac{\epsilon}{\kappa^2 + \epsilon^2}. \tag{3.3}$$

Here $\epsilon = \alpha\zeta / s + D_\psi$ is the effective rate of random reorientation, combining the effects of sharp turns and angular diffusion. The persistence length computed using this analytical solution is in excellent agreement with numerical simulations of the model (Figure S3.11), and further accurately predicts the persistence length of the measured worm trajectories (Figure 3.5C; Pearson correlation ≈ 0.8).

The simple analytical form of Eq. (3.3) also provides some insight into the dependence of this measure of exploratory propensity on the underlying parameters. It is clear that a non-zero curvature ($|\kappa| > 0$) monotonically impairs the persistence length (*i.e.* $\partial P/\partial\,|\kappa| < 0$; Figure 3.5A,B). Interestingly, it also reveals that, given any nonzero value of κ, there exists a a finite value of ϵ that maximizes P (*i.e.* $\partial^2 P/\partial\,\epsilon^2 < 0$ at $\partial P/\partial\,\epsilon = 0$). When $\epsilon \gg |\kappa|$, effects of the gradual-turn bias are negligible and the exploratory propensity becomes inversely proportional to ϵ. When $\epsilon \ll |\kappa|$, the trajectory becomes circular, leading to oversampling of space within a region of length scale κ^{-1}, the circling radius. In this latter regime, P increases with ϵ because random reorientations are required to free the worm from the circular orbit. Thus, P increases with ϵ at small ϵ but decreases with ϵ at large ϵ, and an optimum in P occurs when the random reorientation rate is balanced with the curvature (*i.e.* when $\epsilon = \kappa$).

Interestingly, although both ϵ and κ were found to vary substantially across individuals, when averaged over the entire measured population (Figure 3.5D, white points), these values were nearly identical to one another (Figure 3.5D, red point). This can be largely attributed to the contribution of the rotational diffusivity D_ψ, which for exploring worms in the absence of food, evidently dominates over the sharp turn rate ζ and is by itself comparable in magnitude to ϵ (Figure 3.5D, compare orange and points). Our model therefore indicates that, on average, the rotational diffusivity D_ψ of worms is set very close to the optimal value that balances their finite gradual turn bias κ to maximise the exploratory propensity P.

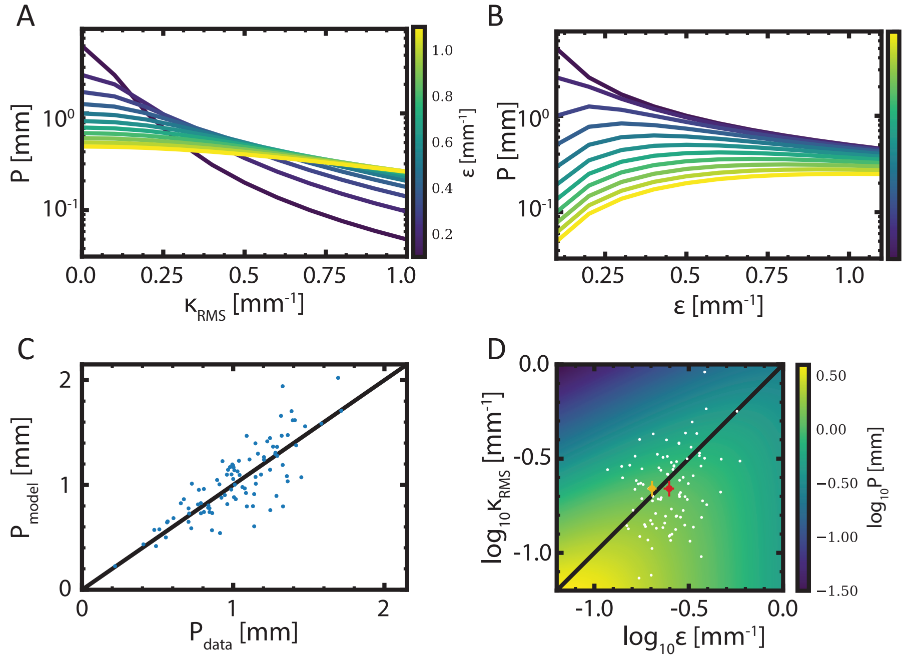

Figure 3.5: **A simple turning model explains the data and reveals an optimality principle for exploration under biasing constraints** (A) Exploratory propensity, characterized by the trajectory persistence length P, decreases monotonically with increasing turning bias κ_{RMS}, regardless of the rate of random reorientations ϵ. (B) By contrast, P can either increase or decrease with ϵ, depending on the value of κ_{RMS}. (C) The measured exploratory propensity P_{data} agrees well with predictions of the model P_{model} based on the turning parameters κ_{RMS} and ϵ measured in each worm. (D) The magnitude of the gradual-turn bias κ_{RMS} and the effective random-reorientation rate ϵ is of the same order. Each trajectory is displayed as a white point. The red point is the population average, computed from all trajectories. The orange point indicates the population average for the case that sharp turns are ignored (equivalent to the limit $\alpha \to 0$ in our model), so that ϵ is defined by rotational diffusion alone (*i.e.* $\epsilon \to D_\psi$). Error bars represent 95% confidence intervals.

3.2.5. BOTH D-V AND Ω-δ BIASES ARE MODULATED DURING ESCAPE TURNS

Although we found that neither D-V bias (as quantified by $P(D)$; Figure 3C,F) nor Ω-δ bias (as quantified by $P(\delta)$; Figure 3D,G) significantly correlates with the exploratory propensity, we envisaged that these statistical biases that modulate the direction and amplitude of sharp turns might have a greater impact during escape responses, which present an acute challenge for trajectory reorientation. The goal of an escape response is to rapidly change the direction of motion so as to crawl away from the perceived source of an aversive stimulus (within our experiment, the arena boundaries impregnated with a chemorepellent) (Figure S3.7). In the optimal case, the outgoing worm orientation after the escape turn θ_{out} points in the direction exactly orthogonal to and away from the repellent boundary ($\theta_{\text{out}} = 180°$; we define 0° to be the direction of the shortest path to the boundary). Since the angle of incidence θ_{in} (the angle in the reference frame of the worm with respect to the repellent boundary just before the turn, but after the reversal, Figure 3.6A) varies per turn, so does the optimal reorientation $\Delta\theta \equiv \theta_{\text{out}} - \theta_{\text{in}}$. We resolved a total of 3,531 escape responses within our dataset, mostly triggered near the repellent boundary (Figure 3.1). Overall, compared to spontaneous turns during exploration, the average dorsal-turn probability $P(D)$ is decreased from 0.24 ± 0.01 to 0.17 ± 0.01 and the average delta-turn probability $P(\delta)$ is increased during escape turns from 0.18 ± 0.01 to 0.38 ± 0.02 (95% CI, using bootstrapping). Interestingly, individual average dorsal and δ-turn statistics of the escape turn are not correlated with the aforementioned individual preference during exploration (Figure S3.8).

Closer inspection of the data revealed that these probabilities during escape turns are strongly modulated in response to the direction of the repellent boundary (as captured by θ_{in}). When the repellent boundary is on the dorsal side ($\theta_{\text{in}} < 0$), the dorsal turn probability is strongly suppressed (Figure 3.6B) below that for spontaneous turns during exploration (Figure 3.6B, dashed line), down to nearly zero as θ_{in} approaches −90°. This modulation of D-V bias is likely beneficial because performing a dorsal turn when the repellent is on the dorsal side would tend to orient the worm in the undesirable direction up the repellent gradient. Interestingly, however, the modulation of $P(D)$ is more modest when the repellent is encountered on the ventral side ($\theta_{\text{in}} > 0$), with worms making ventral turns more than half of the time even when θ_{in} approaches +90° (Figure 3.6B).

The less extensive modulation of the D-V bias for $\theta_{\text{in}} > 0$ implies that worms relatively frequently execute ventral turns even when the repellent stimulus is on the ventral side. We wondered whether worms might compensate for this by modulating in addition the turn amplitude $\Delta\theta$, which could in turn be controlled by the Ω-δ bias, the amplitude of Ω-turns, the amplitude of δ-turns, or any combination thereof. We found that Ω-δ bias of ventral turns is indeed strongly modulated by θ_{in}, with $P(\delta)$ increasing more than 2-fold across the full range of possible incident angles ($-90° < \theta_{\text{in}} < 90°$) (Figure 3.6C). By contrast, the amplitude of Ω- and δ-turns remained relatively constant as a function of θ_{in}, but demonstrated a mildly increasing trend (Figure 3.6D, green and orange curves, respectively). Combined, these effects cause the reorientation angle $\langle\Delta\theta\rangle$ of ventral turns to be strongly dependent on θ_{in} (Figure 3.6D, blue curve). This modulation of $\langle\Delta\theta\rangle$ is instrumental to escape, because when a ventral turn is triggered with the repellent boundary on the ventral side, larger reorientation angles increase the chances of the worm turning through and away from the boundary. No evidence of angular modulation is observed for turns in the dorsal direction, which were exclusively Ω-turns ($\langle\Delta\theta\rangle = 105° \pm 8°$ for $\theta_{\text{in}} < 0$ and $\langle\Delta\theta\rangle = 103° \pm 4°$ for $\theta_{\text{in}} > 0$, 95% CI using bootstrapping). Thus, modulation of both the D-V bias and the angular amplitude of turns contributes to control over the final exit angle of escape, θ_{out}, but the control mechanisms that contribute to modulation differ in the dorsal and ventral directions. On the dorsal side, the modulation of D-V bias evidently serves as the primary mechanism of control over $\Delta\theta$, with weak if any modulation of the amplitude of turns. On the ventral side, modulation of D-V bias is less extensive, and control over $\Delta\theta$ is predominantly achieved through modulation of turn amplitude, with a strong contribution from Ω-δ bias modulations, and weaker contributions from modulation of the amplitude of $\Omega-$ and $\delta-$turns.

The combined effects of all of these modes of control can be observed in the distribution of the final exit angle θ_{out} ($= \theta_{\text{in}} + \Delta\theta$) (Figure 3.6E), which demonstrates substantially increased weight near the most favorable exit angle ($\theta_{\text{out}} = 180°$) and decreased weight near the least favorable exit angle ($\theta_{\text{out}} = 0°$) compared to the distribution expected if neither D-V bias nor amplitude were modulated by θ_{in} (Figure 3.6E, red curve). To further quantify the effects of each mode of control, we defined as a measure of escape efficiency $E_{\text{eff}} \equiv -\langle\cos\theta_{\text{out}}\rangle$, which quantifies how well aligned θ_{out} is, on average, with the optimal exit angle of 180° (Figure 3.6F). This quantity takes values within the range $-1 < E_{\text{eff}} < 1$, where the high and low extremes correspond to the exit angle being perfectly parallel ($\theta_{\text{out}} = 180°$) and antiparallel ($\theta_{\text{out}} = 0°$) to the optimal orientation, respectively. We computed E_{eff} as a function of θ_{in} for a number of hypothetical control scenarios, in which effects of removing control over one or more of the controlled variables (D-V bias, Ω-δ bias, $\Delta\theta$ for $\Omega-$ and δ-turns) were excluded by randomly resampling the experimental data for each variable without preserving the correlations with θ_{in} due to control. In the first scenario, we considered a drastically simplified escape-turn repertoire in which every escape turn is a ventral Ω-turn with no θ_{in}-dependent turn-amplitude modulation (Figure 3.6F, green curve). In this case, the performance as a function of θ_{in} is highly skewed, with E_{eff} surpassing that of the measurements (Figure 3.6F, blue curve) when the repellent is encountered on the dorsal side ($\theta_{\text{in}} < 0$, peaking at $\theta_{\text{in}} \approx -60°$), but with drastically degraded E_{eff} when encountered on the ventral side ($\theta_{\text{in}} > 0$). Notably, for a substantial range of incoming angles ($\theta_{\text{in}} \gtrsim 45°$) E_{eff} reaches negative values, meaning the average exit angle points towards the repellent boundary. As a result, the overall performance (E_{eff} averaged over all incoming angles) is reduced to nearly half of that in the measured data (Figure 3.6F, inset). The second scenario adds both dorsal turns and δ-turns, but without any θ_{in}-dependent modulations. This more diversified repertoire decreases the D-V asymmetry in θ_{in}-dependent performance, bringing the peak in E_{eff} closer to $\theta_{\text{in}} = 0°$ (Figure 3.6F, red curve), without compromising the overall performance relative to the first scenario (Figure 3.6F, inset). The third scenario adds θ_{in}-dependent control of D-V bias, and we find that this indeed increases performance at all incoming angles (Figure 3.6F, yellow curve) and hence also overall performance (Figure 3.6F, inset) relative to the second scenario. Finally, the difference between the third scenario and the experimentally observed performance (Figure 3.6F, yellow and blue, respectively) reveals the effect of turn-amplitude control.

In summary, our results provide strong evidence that worms modulate both the D-V bias as well as the amplitude of sharp turns to optimise the efficiency of escape upon encountering an aversive stimulus gradient. The ability to make dorsal, as well as ventral, sharp turns is essential in ensuring good escape performance across all possible angles of incidence, and modulation of the angular amplitude of turns, which further increases performance, can be explained primarily by modulation of the Ω-δ bias of ventral turns.

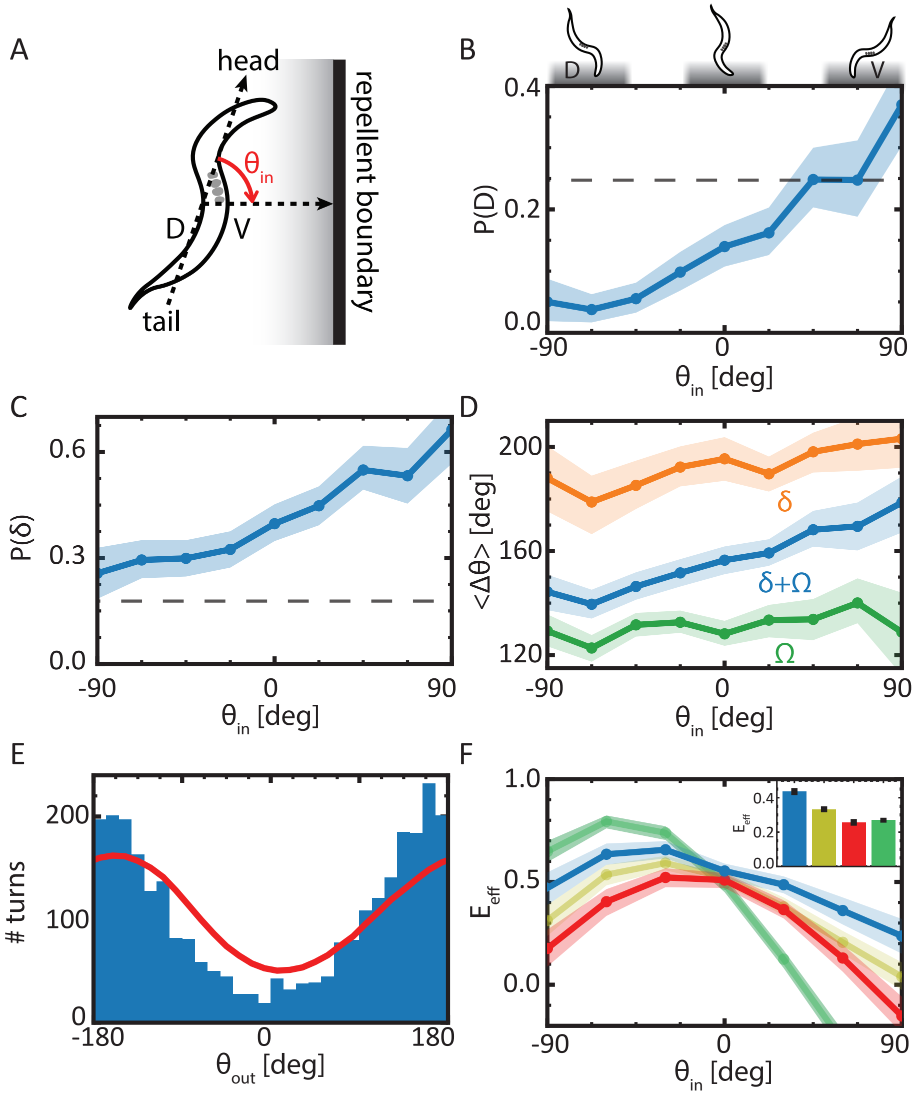

Figure 3.6: Caption is on the next page.

Figure 3.6: **Control of turn direction and amplitude increases escape efficiency.** (A) We characterise worm orientation during escape turns by the angle θ of the body orientation vector (pointing from tail to head) relative to the repellent gradient (approximated as the vector pointing from the worm centroid to the nearest point on the repellent boundary), where $\theta = 0°$ means the worm points directly up the gradient and $0 < \theta < 180°$ and $-180 < \theta < 0°$ correspond to the nearest repellent boundary being on the ventral and dorsal sides, respectively. (B) The D-V bias of escape turns is modulated such that the dorsal turn probability $P(D)$ is suppressed when the repellent is encountered on the dorsal side ($-90° < \theta_{\mathrm{in}} < 0°$). Dashed line: average $P(D)$ for spontaneous turns during exploration. (C) The Ω-δ bias of ventral escape turns is also modulated, with the δ-turn probability $P(\delta)$ being augmented when the repellent is encountered on the ventral side ($0° < \theta_{\mathrm{in}} < 90°$). Dashed line: average $P(\delta)$ for spontaneous turns during exploration. (D) For ventral escape turns, the average reorientation angle $\langle\Delta\theta\rangle$ demonstrate only a weakly increasing dependence on θ_{in} for for Ω- (green) and δ-turns (orange) separately, but increases much more strongly when both are combined (blue) with a profile strongly resembling that of $P(\delta)$ (C). Thus, Ω-δ bias dominates the control of the angular amplitude of ventral escape turns. (E) Histogram of exit angles θ_{out} after reorientation (blue bars), and after random resampling of the experimental data without regard to the dependence of $P(D)$ and $P(\delta)$ on θ_{in} (red curve). (F) Escape efficiency $E_{\mathrm{eff}} \equiv -\langle\cos\theta_{\mathrm{out}}\rangle$ as a function of the incident angle θ_{in} (main panel) and averaged over all incident angles (inset) computed for the experimental data (blue) and random resamplings of the same data corresponding to three hypothetical control scenarios: a reduced turn repertoire of ventral Ω-turns only, with no θ_{in}-dependent control (green); the full turn repertoire including also δ and dorsal turns, but with no θ_{in}-dependent control (red); the full turn repertoire with θ_{in}-dependent control of D-V bias (yellow). In all panels, shaded regions and/or error bars correspond to 95% confidence intervals.

3.3. DISCUSSION

By developing a novel behavioural assay that enables tracking multiple *C. elegans* individuals over long times (2 h), we quantified the statistics of turning behaviour in both exploration and escape navigation contexts. The data revealed significant biases in both gradual- and sharp-turn behaviors, which impose constraints on exploration and escape performance, respectively. In the context of exploration, quantifying the diversity of motility phenotypes within an isogenic population allowed us to identify the subset of reorientation behaviours that correlate most strongly with exploration performance, from which we derived a minimal model of motile trajectories. Analysis of this model identified a novel optimality principle for maximising exploratory propensity under the constraint of finite gradual-turn bias. In the context of escape navigation, studying the statistics of escape angles as a function of the encounter angle with the repellent gradient revealed how worms exert control over directional bias, in addition to the amplitude, of sharp turns to enhance escape efficiency.

3.3.1. OPTIMIZING EXPLORATORY PROPENSITY UNDER GRADUAL-TURN BIAS REQUIRES NONZERO ANGULAR DIFFUSIVITY

Optimality is useful as a guiding concept for studying biological design, given that natural selection tends to drive some performance measures of the system towards a maximum. In the context of behavior, identifying the relevant performance measure being optimised provides a framework to study the design of the underlying control strategies and their physiological implementation. However, identifying these objective functions on which selection acts is often not trivial, as in nature, one can expect selection to be acting simultaneously on multiple such performance criteria that may be in conflict and, as a result, impose constraints on one another. Within our study, we identified as a performance measure for exploration the trajectory persistence length, and found that maximizing this performance under the constraint of finite gradual-turn bias (*i.e.* trajectory curvature) requires a nonzero rotational diffusivity. A gradual-turn bias resulting from a lack of control of orientation is not unique to the worm, but has been observed across a wide variety of organisms, for navigational tasks in environments that lack sufficient sensory cues for direction. The causal factors leading to such biases are difficult to resolve, and could be manifold. For example, loopy trajectories created by blindfolded humans have been hypothesised to arise from anatomical asymmetries[35], an imperfect 'sense of straight ahead' [13] and accumulating noise in the sensimotor system [12]. Recent research on *Drosophila* revealed a persistent crawling preference which is not linked to body asymmetries[10], but suggests a neuronal origin[9]. *C. elegans* can be used as a useful model organism to fundamentally study the (neuronal) origin of such a rotational drift. Our minimal model of exploratory trajectories (Eq. 3) does not address the causal factors leading to such gradual-turn biases, but rather predicts their consequences. In particular, for any given trajectory curvature κ, the model reveals that the maximal exploratory propensity P will be achieved when the rate of random orientation ϵ (which in *C. elegans* is dominated by orientational diffusion) exactly balances the magnitude of κ, and our data indicate that *C. elegans* trajectories indeed demonstrate, on average, this optimal balance. Thus, although the trajectory curvature induced by the worms' gradual-turn bias does impair exploratory performance, the latter achieves the greatest value possible under that constraint of finite bias to enhance the spatial extent of exploration.

Interestingly, however, we found considerable variability at the level of individual worms in both gradual-turn bias κ and random reorientation ϵ, with only a weak correlation between these parameters across individuals (Figure 5D). Thus, although this optimal balance between κ and ϵ is evidently achieved at the level of the population average, this balance is not tightly controlled at the level of individuals. From a mechanistic point of view, it is in fact interesting that these variations in gradual-turn bias and angular diffusion appear to be nearly independent of one another, given that they are both represent errors and/or fluctuations in the body-wave dynamics driving the worms' undulatory propulsion. Naively, one might expect a stronger correlation between these, if they were both the product of finite control over the locomotor wave. One compelling hypothesis is that the angular diffusivity due to finite errors in locomotor wave control is in fact considerably lower and that the observed diffusivity is actually dominated by yet another type of reorientation behavior. It has been documented by Kim et al. [26] that *C. elegans* trajectories can feature a high frequency of "shallow turns" during runs with reorientation angles much < 90°. In our analysis, reorientations due to such shallow turns would not be detected as sharp turns, but instead contribute to the magnitude of the angular diffusivity. Interestingly, inspection of reorientation statistics between consecutive body waves in our data revealed a broad distribution that could be fitted by the sum of two Gaussians (Figure S3.9). Thus, it is conceivable that the broader of these two Gaussians, which contributes the majority of the variance ($\sigma = 28.3 \pm 0.4$, as compared to $\sigma = 13.5 \pm 0.1$ for the narrower Gaussian), reflects shallow turns. Finally, regardless of the underlying mechanisms, the nearly uncorrelated variation in gradual-turn bias and orientational diffusion leads to large variation in exploratory performance, which may be interpreted as a bet-hedging strategy[36, 37]. Exploring new regions of space and exploiting local resources is a well-known trade-off in foraging strategies, and hence expressing a diversity of phenotypes along this exploration-exploitation axis could provide isogenic worm populations with an effective adaptive strategy in rapidly changing and/or information-scarce environments where sensory modulation of behaviour is less effective [38].

Our minimal model of trajectory statistics combines the effects of sharp turns, orientational diffusion, and gradual-turn bias, and accurately predicts the experimentally observed trajectory persistence lengths. The simplicity of the model offers key insights into how variations in these parameters interdependently affect this measure of exploration performance, and provides a basis for future studies that examine the effect of perturbations such as genetic mutations or neural ablations. Furthermore, its construction is sufficiently general that it can be readily applied to any organism (or motile particle/agent) whose motion can be described by trajectory curvature, effective diffusivity, and intermittent sharp turns, for instance the run-and-tumble motion of swimming bacteria near surfaces that induce curved runs [39], or other nematodes such as larvae *Ancylostoma tubaeforme*[40]. Our model reveals that any nonzero trajectory curvature sets an upper limit to the persistence length, which during exploration in the absence of external guiding cues significantly reduces the performance. Whether and to what extent *C. elegans*' gradual-turn bias also impacts the performance in other environments (e.g. during chemotaxis) remains an open question and will provide fertile ground for future studies. During taxis strategies, gradual-turn bias might be expected to reduce, but not abolish, taxis efficiency. The head-bend mutant *unc-23* creates spiral-shaped tracks with a stronger curvature compared to worms in this study, but can still perform navigational tasks like chemotaxis [41–43]. Of particular interest would be to investigate the relationship between the gradual-turn bias we have observed here in the absence of environmental gradients and the 'weathervaning' (klinotaxis) strategy of chemotaxis that has been shown to steer trajectory curvature in response to strong environmental gradients [20]. For example, testing whether the weathervaning response completely overrides the gradual-turn bias, or acts additively could shed light on whether the bias and weathervaning response are controlled by the same neural circuitry. In Appendix A, we present preliminary experiments that address the effect of gradual-turn bias on chemotaxis. Perhaps because the chemoeffector gradient was too weak, we did not observe evidence of a weathervane response, but interestingly, we found that the gradual turn bias negatively impacts chemotactic efficiency, and that its magnitude may be attenuated during chemotaxis relative to that during exploration in the absence of chemoeffector gradients. Although more experimental effort will be required to confirm these findings, these preliminary results indicate that examining gradual-turn bias during chemotaxis could be a fruitful avenue for future investigations.

3.3.2. CONTEXT-DEPENDENT CONTROL OVER SHARP-TURN BIAS ENHANCES ESCAPE FROM ACUTE AVERSIVE STIMULI

A striking degree of directional control was observed in the worms' sharp-turn response to an acute aversive stimulus: the chemorepellent (SDS) boundary of the arena, which triggers an escape response. The D-V bias, characterized by $P(D)$, the Ω-δ bias, characterized by $P(\delta)$, were strongly modulated by the incoming angle θ_{in}, in a manner that enhances escape efficiency E_{eff}. Modulation of these biases was highly asymmetric with respect to their baseline values in spontaneous sharp turns: $P(D)$ is strongly modulated downwards but only weakly upwards, and $P(\delta)$ was modulated exclusively upwards during escape turns. Although, the angular amplitude of turns $\Delta\theta$ was also weakly modulated by θ_{in} for both Ω- and δ-turns, the overall modulation of $\Delta\theta$ was dominated by modulation of $P(D)$, *i.e.* the Ω-δ bias.

3.3.3. NEURAL CONTROL OF REORIENTATION STATISTICS: POSSIBLE TARGETS FOR FUTURE STUDIES

The control of reorientation statistics (or lack thereof) described in this study, raises the question which neuronal circuitry could be underlying. The neuronal signalling network underlying weathervaning-type control of *C. elegans* trajectory curvature [20] has yet to be uncovered, but it possibly involves sampling the environment by oscillatory-like head-swings required for propulsion[44, 45], possibly through the SMB neuron associated with head oscillations and gradual turning via interneurons like AIY and AIZ[46]. Killing of the SMB neurons results in large head-swings during forward crawling with high-curvature trajectories[7], suggesting a possible mode of control for the crawling bias. However, it has to be seen to what extent the set of neurons involved in control during escape and weathervaning responses overlap, given that weathervaning is described at the level of more gradual rather than sharp reorientations[20] and the SDS sensing ASH neuron directly synapses to the reversal triggering AVA neuron, bypassing much of the chemotaxis circuitry (although ASH is connected to AIA[47]).

Some of the involved neurons reported to affect the sharp turn that might be involved in sharp turn control during the escape are RIM, RIV, RIB, and SMD. RIV (and RIB) activity rises at the onset of the turn[48] and RIV ablated worms lack a ventral bias[7], suggesting their involvement in modulation of $P(D)$. RIM is a tyraminergic neuron that aides in the hyperpolarization of ventral muscles to execute the ventral Ω-turn[49, 50], and therefore might be related to the δ-turn modulation. Similarly, ablation of the SMD neuron results in sharp turns with smaller reorientation angles[7] which suggests its involvement in the sharp turn amplitude. The SMDD, and also DVA neurons have been reported to provide proprioceptive feedback (i.e. sensing of the body bending angle)[51, 52], and therefore might be involved in the regulation of (sharp) turn direction, enabling angular-dependent control. In addition, asymmetric feedback from such proprioceptive neurons or mechanosensory neurons (worms lacking mechanosensory neurons, PVD and FLP produce circular trajectories [53]) might be the cause of a rotational bias. It would be exciting in further studies to examine the effects of perturbing these neurons (via e.g. ablation, genetic mutations, or optogenetic stimulation) on the control of reorientation behaviours we studied here.

CONCLUSIONS

Our results revealed how *C. elegans* reorientation statistics demonstrate significant biases. In the context of random spatial exploration, the reorientation parameters appear to be tuned to maximise exploratory propensity, under the constraint of finite bias. In the context of escape, worms demonstrated the ability to strongly modulate these biases to optimise escape efficiency. Our minimal model provides a basis for further investigation of the relationship between these reorientation behaviors, their mechanistic origins, and their functional consequences.

ACKNOWLEDGMENTS

We thank Antonio Carlos Costa, Laetitia Hebert, and members of the Shimizu and Stephens groups, as well as Dr. Andre Brown and his lab members, for helpful discussions. We would like to thank Liam O'Shaughnessy, who customised code from Broekmans et. al.[22] to resolve postures during sharp turns. We are grateful for the help and support provided by the Scientific Computing section of the Research Support Division at OIST.

3.4. METHODS

Behavioural experiments

Worms are cultivated on NGM plates (3 g NaCl, 17 g agar, 2.5 g peptone, 1 mL 5 mg mL^{-1} cholesterol in EtOH in 975 mL water, with 1 mL 1 M $CaCl_2$, 1 mL 1 M $MgSO_4$, 25 mL 1 M KPO_4 pH 6, 1 mL 200 mg mL^{-1} streptomycin in water) seeded with *E. coli* HB101. A copping ring (a 38 mm × 38 mm square with rounded corners and a total surface area of 13.8 mm^2) soaked in 1% SDS is put on a food-free NGM plate. 8 well fed young adult worms are washed for 15 min in a 1 µL M9 minimal media (3 g KH_2PO_4, 6 g Na_2HPO_4, 5 g NaCl, 1 mL 1 M $MgSO_4$ in 1 L water) solution and pipetted onto the arena. The motility of the plate is recorded for 2 h at 11.5 Hz using a PointGrey GX-FW-60S6M-C. During the experiment, the average speed of the worms remained mostly constant (Figure S3.10).

Tracking of worms

Worms are tracked using custom tracking software written in Python. Collisions are semi-automatically resolved, using a combination of the worm lengths, collision duration, and direction of motion before and after the collision of each worm. Ambiguous collisions, or collisions involving more than 2 worms are resolved by hand. Automatically resolved collisions are all manually inspected.

Sharp turn extraction

Sharp turns are differentiated from gradual turns by the body posture's topology. During a sharp turn, the worm folds onto itself, creating a doughnut topology. The starting and end time points of a turn are marked by the last and first local extrema of body amplitude (the third Eigenworm[31]) before and after the worm's posture folds onto itself. These postures cannot trivially be extracted from the spline of the binarized worm image. Therefore, a customised version of a previously published algorithm by Broekmans et. al. is used to solve sharp turn body postures [22], using the OIST's Sango cluster parallel computation cluster. Turns with an error with at least 3 consecutive frames > 12 are flagged as unsuccessful and not included in the analysis. 10625 out of 12475 sharp turns could be resolved using this method. A manual annotation of a random selection of turns that could not be resolved did not reveal obvious biases towards a certain turn type. Therefore the assumption is made that sharp turns that could and could not be resolved follow similar statistics.

Monte-Carlo simulations of variability

To test if the observed variability is not trivially explained by stochasticity, measured worm-to-worm variability in turning behaviour is compared with simulations from a stochastic model. In the model, all worms are assumed to follow the same stochastic process determined by population average statistics, and each turn is independent. The sharp turn rate stochastic process is described by the population average interval distribution (Figure S3.2). Drawing from this distribution, using Monte Carlo sampling, a simulated number of sharp turns can be obtained for the duration of each worm in the measurement, resulting in a different distribution of turn frequencies (Figure 3.3B). Since the simulations are subject to stochasticity as well, the process is repeated 1000 times. The measured distribution was found to consistently exhibit larger variation compared to the simulated distributions (Figure S3.3A). In the case of worm-to-worm variability in $P(D)$ and $P(\delta)$, the corresponding stochastic process is a coin flip (i.e. Bernoulli process), with the population average probability. A number of dorsal or δ turns is randomly drawn from a binomial distribution using the population average probability, and a number of coin flips is specified for each worm by the number of sharp turns in the case of the $P(D)$ and the number of ventral sharp turns in the case of $P(\delta)$ (Figure 3.3BC). Likewise, the resulting distributions were found to be more variable compared to the simulated distribution for a significant fraction of the simulations (Figure S3.3B,C). Variations in sharp turning frequency can be partially attributed to batch effects of worms measured simultaneously on the same plate. However, a larger fraction of the observed variability in both frequency, $P(D)$ and $P(\delta)$ is of unknown origin and might stem likewise from experiences of the environment as well as from intrinsic stochasticity (Figure S3.4).

Extraction of model parameters

To compute the curvature and rotational diffusion, first the unwrapped (accumulative) average worm body orientation in a window of 5 s around sharp turn events and worm collisions is excluded. We found that the average body orientation is an accurate proxy of the worm's body velocity bearing during runs. However, it is well-defined throughout the trajectory, even at low speeds, and thus the accumulative angle does not suffer from artifacts.

The orientation is computed as a function of trajectory length, by evaluating it at equally spaced intervals of 100 µm. The curvature is estimated in windows of 15 min as the average spatial rotation rate. The rotational diffusion D_ψ is extracted by fitting the function $y = 2D_\psi x + bx^2$ to the MSD (evaluated up to 1 mm) of the spatial orientation.

Computing the persistence length

The persistence length is extracted using the MSD of the worm's centroid position (evaluated at the 100 µm intervals along the trajectory contour). For a diffusive process with diffusion coefficient D in n dimensions, the mean-squared displacement as a function of time t follows the equation $\mathrm{MSD} = 2nDt$. Assuming a constant speed of diffusive process $s = X/t$, 2 dimensions, and a definition $P \equiv D/v$, we obtain that $P = \mathrm{MSD}/4X$. Theoretically, in the diffusive regime a constant can be fitted to MSD/X. Due to confinement, this curve decreases when the MSD approaches the size of the arena. Furthermore, MSD/X fluctuates slightly, because trajectories are described by a random process. Therefore, the persistence length is evaluated as the average value where the MSD is linear; in the range where the slope of $\log \mathrm{MSD}$ vs $\log X$ is in between 0.9 and 1.1.

Computing the gradual turn bias decorrelation time τ.

The ACF cannot be accurately estimated on a single-worm basis, because the fluctuation time scales of κ are of the same order as the length of the measurement. It can be computed on a population level, assuming that each worm follows the same stochastic process. With this assumption, we compute the ACF using the population variance and mean (0) of κ for each worm and subsequently average across worms. The resulting curve is fitted to the function $\langle \mathrm{ACF}_\kappa(t)\rangle = e^{-t/\tau}$ using the 'curve_fit' function of the scipy Python package. To obtain a confidence interval, the process of computing the ACF and fitting τ is repeated 1000× after bootstrapping for worms. The reported error is the standard deviation of bootstrapped values of τ.

Ventral annotation

The resolution of the camera did not allow one to visually separate dorsal from ventral. However, we find that for each worm δ turns almost exclusively turns in a consistent direction. We infer this to be the ventral direction.

Derivation of the model

We consider a simple random walk as a minimal model for *C. elegans* locomotion. We take three observations about the worm movement into account: (i) worms move along a curved trajectory with a constant curvature κ [mm^{-1}], (ii) This run is interrupted by occasional random reorientation of rate ζ/v [mm^{-1}]. (iii) The worm trajectory is subject to rotational diffusion with diffusion coefficient D_ψ [mm^{-1}].

First, we neglect rotational diffusion and only consider random orientation events and a curved trajectory. The probability density of turning again after walking a length s since the last turn is

$$P(s) = (\zeta/v)\, e^{-s\zeta/v}\,. \tag{3.4}$$

As the worm moves along the perimeter of the circle, the Euclidean distance between turns is

$$x = (2/\kappa)\,\sin(s\kappa/2)\,. \tag{3.5}$$

We can map this random walk to a wait-and-jump process, where the worm waits for a time t at a position and jumps a distance x. As a consequence, the effective diffusion coefficient in $d = 2$ dimensions is

$$D = \langle x^2\rangle/(2d\langle t\rangle) = \langle x^2\rangle/(4\langle t\rangle)\,. \tag{3.6}$$

In the following, we will consider the persistence length $P = D/v$:

$$P = \langle x^2\rangle/(4\langle s\rangle)\,, \tag{3.7}$$

where $s = vt$ with a constant velocity v. We can derive the average run length:

$$\langle s\rangle = \int_0^\infty s\, e^{s\zeta/v}(\zeta/v)\, ds = 1/(\zeta/v)\,. \tag{3.8}$$

The average distance from the origin is

$$\langle x^2 \rangle = \int_0^\infty \Big((2/\kappa)\, \sin(s\kappa/2) \Big)^2 e^{-s\zeta/v} (\zeta/v)\, ds = 2/(\kappa^2 + (\zeta/v)^2) \tag{3.9}$$

$$P = (\zeta/v)/(2\kappa^2 + 2(\zeta/v)^2)\,. \tag{3.10}$$

The same result has been derived by Martens *et al.* in analogy to electrons in a magnetic field [54].

We can consider two limiting cases. If the worm turns very often such that $\kappa \gg \zeta/v$ and the path is straight between reorientation events, the persistence length decreases with higher turn frequency according to $P \propto 1/\zeta$. In contrast, for circular trajectory with $\kappa \ll \zeta/v$, reorientation events are beneficial to explore a larger area and thus $P \propto \zeta$.

Next, we include rotational diffusion. If the runs have no gradual turning bias ($\kappa = 0$), the effective diffusion coefficient on large scales is [55]

$$P = 1/(2\epsilon)\,, \tag{3.11}$$

with an effective reorientation frequency in $d = 2$ dimensions

$$\epsilon = (d-1)D_\psi + \zeta/v = D_\psi + \zeta/v\,. \tag{3.12}$$

The rotational diffusion has an analogous effect as abrupt reorientation events on sufficiently large scales. In this spirit, we replace ζ/v by ϵ in Eq. 3.10 and obtain

$$P = \epsilon/(2\kappa^2 + 2\epsilon^2)\,. \tag{3.13}$$

This analytic solution very closely agrees with simulations over a wide range of parameters (Figure S3.11). In the case that the sharp turn does not fully randomize the reorientation, but is biased along the direction of motion with $\alpha = 1 - \langle \cos\Delta\theta \rangle$, ζ has to be replaced by $\bar{\zeta} = \zeta\alpha$[33, 34].

3.5. SUPPLEMENTARY FIGURES

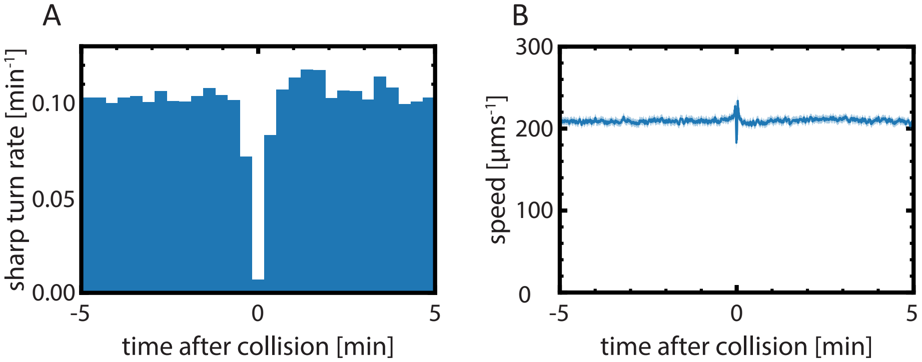

Figure S 3.1: Worm collisions minimally impact the trajectory dynamics. (A) The sharp turn frequency with respect to the time of a collision (the time in the middle between first and last contact with another worm) fluctuates only slightly. The dip at $t = 0$ is from the duration of the collision. (B) A collision event has no long-term effects on the speed. Shaded regions show the 95% confidence interval, bootstrapped for collisions.

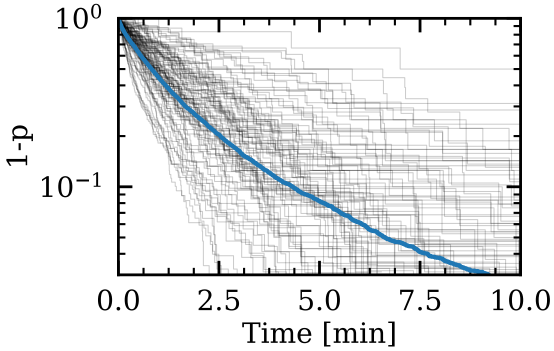

Figure S 3.2: The interval distribution of spontaneous turns for (blue) all worms and (black) individuals.

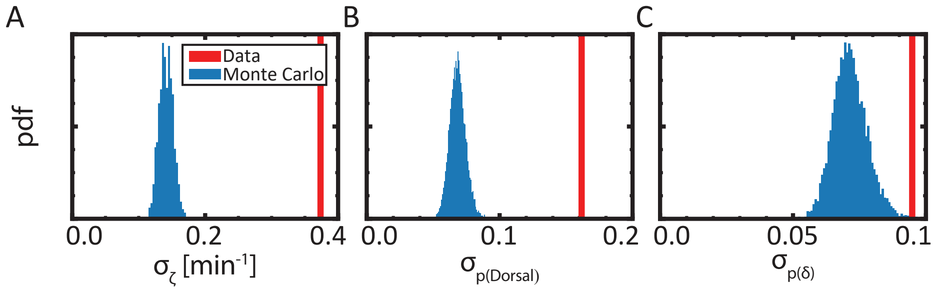

Figure S 3.3: The observed variability across worms is significantly larger compared to random resampling using population averaged statistics. (A) The standard deviation of (red) the population average turn frequency and (blue) the standard deviation of resampled statistics using the interval distribution (Figure S3.2). (B) The standard deviation of the measured dorsal turn probability, weighted by the total number of spontaneous turns, is significantly larger compared to that obtained from random sampling using a coin-flip model using the population average statistics. (C) The standard deviation of the measured delta turn probability, weighted by the total number of ventral turns, is significantly larger compared to that obtained from random sampling using a coin-flip model using the population average statistics.

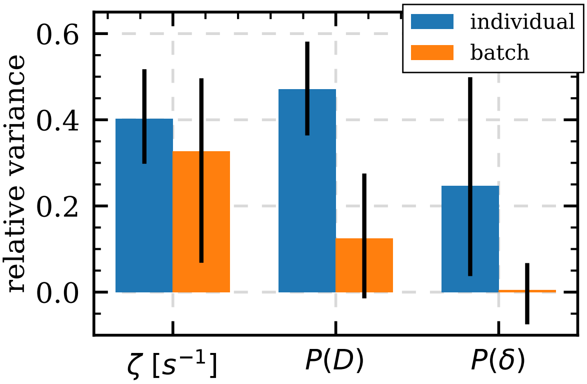

Figure S 3.4: The portion of the variance in the measurements that can be attributed to (blue) individual experience and (orange) batch effects. The remaining part is attributed to the stochastic nature of the process. Individual experience is estimated by sampling either the interval distribution in the case of turn frequency or sampling from a binomial distribution in the case of dorsal-δ-turns, where the probabilities are sampled from pooled data from the same batch. This way, batch effects and stochastic effects are included, while individual effects are removed. The relative change in variance is referred to as the individual contribution. The sampling process is repeated to estimate the uncertainty. To estimate the effect of batches, first the mean of each batch is subtracted, and subsequently the total variance is estimated (reducing the degrees of freedom by the number of batches). This is compared against the total variance without subtracting batches. 95% confidence intervals are obtained by bootstrapping for batches. The fraction of variance not accounted for can be attributed to variability as a result of stochastic processes.

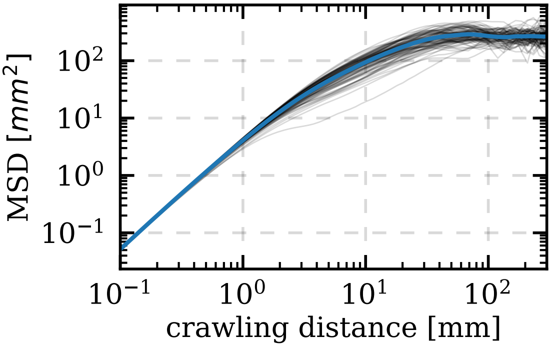

Figure S 3.5: The mean-squared displacement of the individual worms (black) and their population average (blue), as function of the trajectory length. The mean squared displacement is ballistic for short length-scales, then becomes diffusive proportional to the persistence length, and finally stops increasing due to the confinement of the arena.

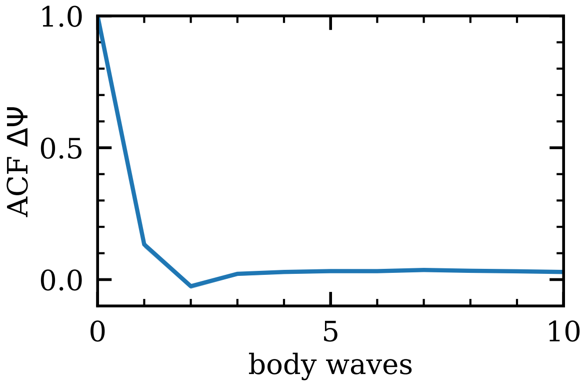

Figure S 3.6: Reorientations are nearly decorrelated after a single body wave. To eliminate the effect of the body wave oscillations, the orientation ψ was evaluated every body wave at the same body posture, computed from the phase of the first 2 Eigenworms[31]. $\Delta\psi$ is the difference of ψ after exactly 1 body wave. The distribution flattens at a value slightly greater than 1, due to the rotational bias. Interval distributions show the 95% confidence interval of the mean across all worms.

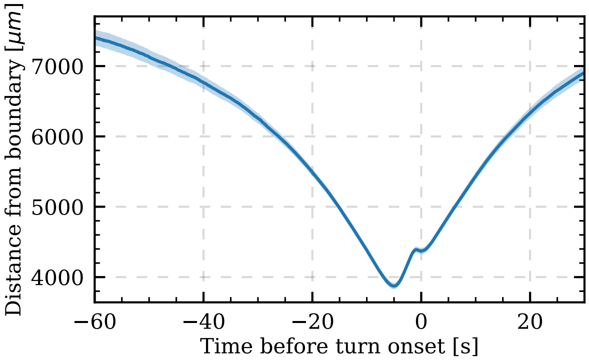

Figure S 3.7: Escape turns are triggered when the worm approaches the boundary and reorients itself away from the boundary. The average distance from the boundary, across escape turns.

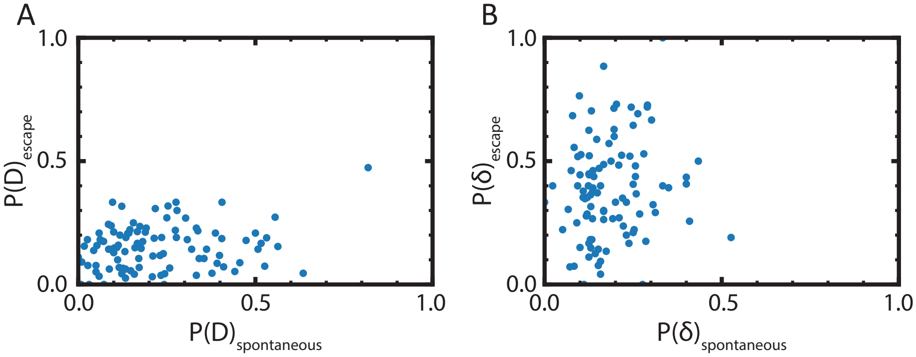

Figure S 3.8: Worm variability in (A) dorsal and (B) δ preference during the escape response and spontaneous turns is not significantly correlated.

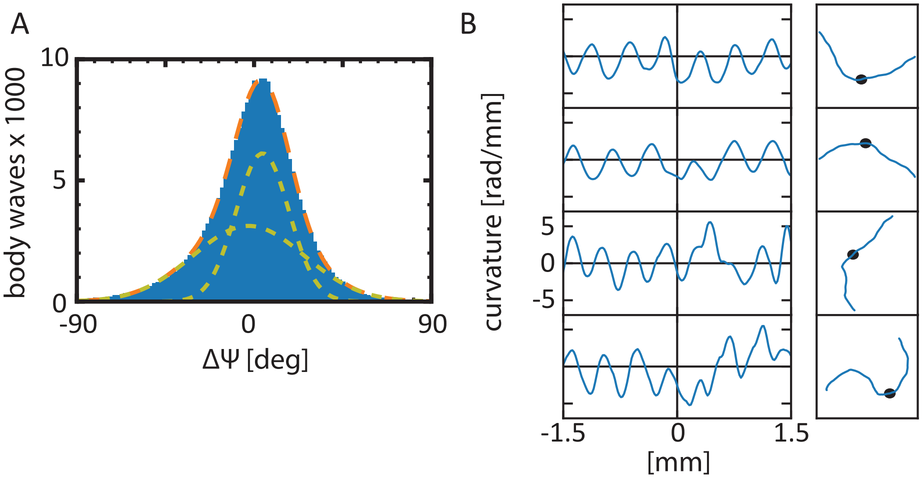

Figure S 3.9: The reorientation distribution is well fitted by 2 Gaussians, which may indicate the existence of small reorientations. The orientation has been evaluated after subsequent body waves during runs at similar body postures (evaluated from the first 2 Eigenworms [31]), ignoring the effect of the oscillatory motion. (A) The reorientation angle $\Delta\psi$ is well fitted as the sum of 2 Gaussians (orange curve), with a standard deviation of $13.5 \pm 0.1°$ and $28.3 \pm 0.4°$ with mean values of 4.3 ± 0.9 and -2.8 ± 0.3, respectively (yellow curves). Fits are performed with the lmfit package in Python using the Levenberg-Marquardt method. (B) Four exemplary (left) time series and (right) centroid trajectories of potential shallow turns with a reorientation angle $> 45°$. To compute the curvature rate, the average body angle of the worm is evaluated at equally spaced distances of 20 µm and the derivative is computed using a Savitzky–Golay filter (3rd order with a window size 300 µm).

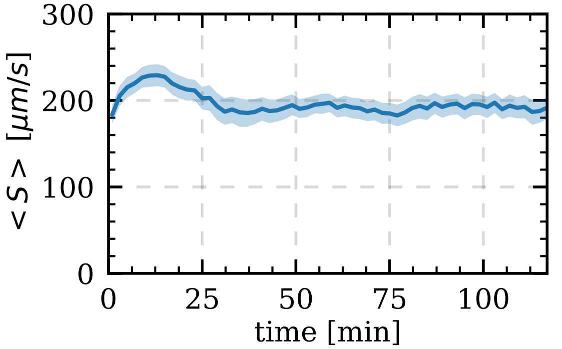

Figure S 3.10: The average speed across all worms has a small increase during the first 20 minute, but remains constant for the remaining duration of the measurement.

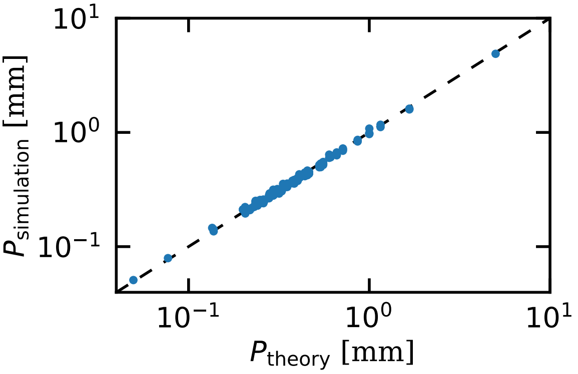

Figure S 3.11: The analytic solution of the model closely follows simulations. Simulations are performed with constant speed ($s = 0.15$ mm s^{-1}) and $2 \cdot 10^6$ data points at 2 Hz, using the orientational dynamics described in equations (3.1) and (3.2). A large space of motility parameters has been simulated, including those of the measurements. κ and ζ / ν have been varied from 0 mm^{-1} to 1 mm^{-1} in steps of 0.2 mm^{-1}. D_ψ has been varied from 0.1 mm^{-1} to 0.9 mm^{-1} in steps of 0.2 mm^{-1}. Sharp turn are modelled as a complete randomization of the reorientation. The persistence length extracted from the simulated trajectories is practically identical (correlation of 99.8%) to that computed from the model (equation (3.3)).

3.6. APPENDIX A

VARIABILITY IN CURVATURE AND TURN RATE INFLUENCES THE CHEMOTACTIC INDEX

In the main text of this chapter, we showed how both sharp turns and a rotational drift influence the persistence length of motile trajectories of worms navigating in a nearly uniform off-food environment. On the other hand, worms performing chemotaxis in the presence of spatial chemoeffector gradients have been shown to modulate the curvature of their trajectory in response to the gradient to bias their orientation in the preferred direction[20]. It is therefore not a priori clear whether and to what extent the gradual-turn bias observed in the exploratory context persists during chemotaxis. Although a full resolution of this question is beyond the scope of this thesis, we present here the results of preliminary experiments that we hope will stimulate future investigations.

We measured the motile trajectories of worms performing chemotaxis up a linear NaCl gradient (Figure S3.12, see Methods). In accordance with the 'pirouette model' of chemotaxis[19], we found that sharp turns were triggered, on average, when worms were moving down the gradient (Figure S3.13), thus facilitating migration up the gradient. Perhaps because the gradient was relatively shallow ($59\,\mu\mathrm{M}\,\mathrm{mm}^{-1}$), we found no evidence of chemotaxis via the 'weathervaning' strategy[20] in these experiments.

The measured trajectories did demonstrate a significant gradual-turn bias during chemotaxis. However, trajectories of worms performing chemotaxis on average have reduced gradual-turn bias compared to worms engaging in exploratory behavior off food ($p \leq 1.7 \cdot 10^{-3}$) (Figure S3.14A). Especially the fraction of strongly curving worms is reduced in comparison to worms off food. This suggests that worms may be able to 'straighten' trajectories in response to the sensed environment. However, it should be noted that the worm treatment prior to the measurement is different from the exploration experiments presented in this chapter (see methods) which could also contribute to this difference. To test if trajectory curvature is also associated with chemotactic performance, the chemotaxis index is computed, defined as the displacement projected in the gradient direction relative to the total displacement[21]. Despite the smaller amplitude, the rotational drift has a significant effect on the chemotaxis index: worms with stronger curvature bias perform weaker (negative correlation of $-0.35, p \leq 2.7 \cdot 10^{-8}$) (Figure S3.14B). Turn rates are drastically increased compared to freely moving worms in an off food environment. Likewise, a significant negative correlation of $-0.29, p \leq 6.9 \cdot 10^{-6}$ between the chemotactic index and the turn rate is observed (Figure S3.14B); higher turning worms are on average less efficient.

Methods for chemotactic experiments

Worms are well-fed and cultivated on NGM plates seeded with OP50. A linear NaCl gradient from 0 mM to 50 mM is created on CELLSTAR FourWell Plates with dimensions 85 mm × 30 mm, using the methods described in [21]. A full plate of worms is washed in 3 steps of 5 min. At $T = 0$ s worms are placed at about 25% up the gradient, in a tiny droplet. For analysis, we have only included trajectories with a length of at least 10 mm. Due to the shorter trajectory length and low turn count of some worms, the dorsal-ventral axis cannot always be reliably inferred. P values are computed using a t-test assuming a two-tailed probability.

ACKNOWLEDGMENTS

We want to thank Dr. G. Jansen and S. van der Burgt for their feedback and suggestions for the salt experiments. S. van der Burgt also participated in the salt experiments.

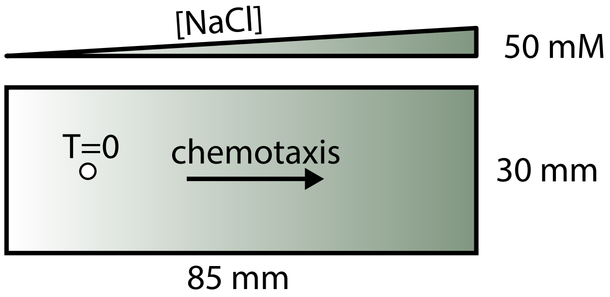

Figure S 3.12: The salt experimental setup. A linear salt gradient is created (0-50 mM on a 85 mm × 30 mm arena.

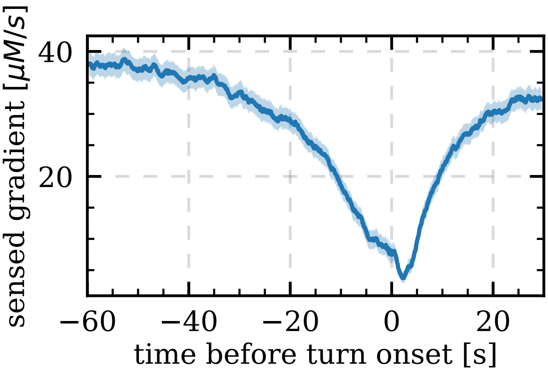

Figure S 3.13: Turns are triggered when the experienced concentration gradient decreases. The sensed gradient is computed from the centroid position of the worm, assuming a linear gradient.

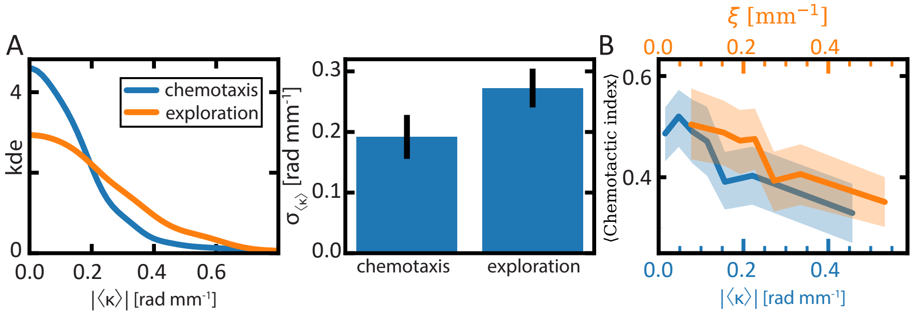

Figure S 3.14: **The rotational drift during chemotaxis up a salt gradient is reduced, but significantly influences the chemotactic index.** (A, left) Worms performing chemotaxis have reduced rotational drift compared to freely moving worms. (A, right) The standard deviation of the mirrored absolute rotational drift distribution weighted by trajectory length, bootstrapped for batches. The rotational drift in freely moving worms is estimated in 10 min windows. (B) Trajectories with a higher rotational drift or turn rate have a lower chemotactic index. Trajectories with a negative chemotaxis index or shorter than 10 mm are omitted. Error bars indicate 95% bootstrapped confidence intervals.

BIBLIOGRAPHY

[1] Berg HC. Random walks in biology. Princeton University Press; 1993.

[2] Codling EA, Plank MJ, Benhamou S. Random walk models in biology. Journal of the Royal society interface. 2008;5(25):813–834.

[3] Berg HC. E. coli in Motion. Springer Science & Business Media; 2004.

[4] Berg HC, Brown DA. Chemotaxis in Escherichia coli analysed by three-dimensional tracking. Nature. 1972;239(5374):500–504.

[5] Levin M. Left–right asymmetry in embryonic development: a comprehensive review. Mechanisms of development. 2005;122(1):3–25.

[6] Holló G, Novák M. The manoeuvrability hypothesis to explain the maintenance of bilateral symmetry in animal evolution. Biology direct. 2012;7(1):1–7.

[7] Gray JM, Hill JJ, Bargmann CI. A circuit for navigation in Caenorhabditis elegans. Proceedings of the National Academy of Sciences. 2005;102(9):3184–3191.

[8] Peliti M, Chuang JS, Shaham S. Directional locomotion of C. elegans in the absence of external stimuli. PLoS One. 2013;8(11):e78535.

[9] Buchanan SM, Kain JS, De Bivort BL. Neuronal control of locomotor handedness in Drosophila. Proceedings of the National Academy of Sciences. 2015;112(21):6700–6705.

[10] Ayroles JF, Buchanan SM, Oâ€™Leary C, Skutt-Kakaria K, Grenier JK, Clark AG, et al. Behavioral idiosyncrasy reveals genetic control of phenotypic variability. Proceedings of the National Academy of Sciences. 2015;112(21):6706–6711.

[11] Helms SJ, Rozemuller WM, Costa AC, Avery L, Stephens GJ, Shimizu TS. Modelling the ballistic-to-diffusive transition in nematode motility reveals variation in exploratory behaviour across species. Journal of the Royal Society Interface. 2019;16(157):20190174.

[12] Souman JL, Frissen I, Sreenivasa MN, Ernst MO. Walking straight into circles. Current biology. 2009;19(18):1538–1542.

[13] Bestaven E, Guillaud E, Cazalets JR. Is circling behavior in humans related to postural asymmetry? PloS one. 2012;7(9):e43861.

[14] Gjorgjieva J, Biron D, Haspel G. Neurobiology of Caenorhabditis elegans locomotion: where do we stand? Bioscience. 2014;64(6):476–486.

[15] White J. The anatomy. The Nematode Carnorhabditis elegans. 1988:81–122.

[16] White JG, Southgate E, Thomson JN, Brenner S. The structure of the nervous system of the nematode Caenorhabditis elegans. Philos Trans R Soc Lond B Biol Sci. 1986;314(1165):1–340.

[17] Cook SJ, Jarrell TA, Brittin CA, Wang Y, Bloniarz AE, Yakovlev MA, et al. Whole-animal connectomes of both Caenorhabditis elegans sexes. Nature. 2019;571(7763):63–71.

[18] Croll NA. Components and patterns in the behaviour of the nematode Caenorhabditis elegans. Journal of zoology. 1975;176(2):159–176.

[19] Pierce-Shimomura JT, Morse TM, Lockery SR. The fundamental role of pirouettes in Caenorhabditis elegans chemotaxis. Journal of Neuroscience. 1999;19(21):9557–9569.

[20] Iino Y, Yoshida K. Parallel use of two behavioral mechanisms for chemotaxis in Caenorhabditis elegans. Journal of Neuroscience. 2009;29(17):5370–5380.

[21] Luo L, Wen Q, Ren J, Hendricks M, Gershow M, Qin Y, et al. Dynamic encoding of perception, memory, and movement in a C. elegans chemotaxis circuit. Neuron. 2014;82(5):1115–1128.

[22] Broekmans OD, Rodgers JB, Ryu WS, Stephens GJ. Resolving coiled shapes reveals new reorientation behaviors in C. elegans. Elife. 2016;5:e17227.

[23] Ghosh R, Mohammadi A, Kruglyak L, Ryu WS. Multiparameter behavioral profiling reveals distinct thermal response regimes in Caenorhabditis elegans. BMC biology. 2012;10(1):85.

[24] Mohammadi A, Rodgers JB, Kotera I, Ryu WS. Behavioral response of Caenorhabditis eleganst localized thermal stimuli. BMC neuroscience. 2013;14(1):66.

[25] Leung K, Mohammadi A, Ryu WS, Nemenman I. Stereotypical escape behavior in Caenorhabditis elegans allows quantification of effective heat stimulus level. PLoS computational biology. 2016;12(12):e1005262.

[26] Kim D, Park S, Mahadevan L, Shin JH. The shallow turn of a worm. Journal of Experimental Biology. 2011;214(9):1554–1559.

[27] Salvador LC, Bartumeus F, Levin SA, Ryu WS. Mechanistic analysis of the search behaviour of Caenorhabditis elegans. Journal of The Royal Society Interface. 2014;11(92):20131092.

[28] Srivastava N, Clark DA, Samuel AD. Temporal analysis of stochastic turning behavior of swimming C. elegans. Journal of neurophysiology. 2009;102(2):1172–1179.

[29] Kato S, Kaplan HS, Schrödel T, Skora S, Lindsay TH, Yemini E, et al. Global brain dynamics embed the motor command sequence of Caenorhabditis elegans. Cell. 2015;163(3):656–669.

[30] Nagy S, Goessling M, Amit Y, Biron D. A generative statistical algorithm for automatic detection of complex postures. PLOS Comput Biol. 2015;11(10):e1004517.

[31] Stephens GJ, Johnson-Kerner B, Bialek W, Ryu WS. Dimensionality and dynamics in the behavior of C. elegans. PLoS Comput Biol. 2008;4(4):e1000028.

[32] Stephens GJ, Johnson-Kerner B, Bialek W, Ryu WS. From modes to movement in the behavior of Caenorhabditis elegans. PloS one. 2010;5(11):e13914.

[33] Taktikos J, Stark H, Zaburdaev V. How the motility pattern of bacteria affects their dispersal and chemotaxis. PloS one. 2013;8(12):e81936.

[34] Locsei JT. Persistence of direction increases the drift velocity of run and tumble chemotaxis. Journal of mathematical biology. 2007;55(1):41–60.

[35] Maus HM, Seyfarth A. Walking in circles: a modelling approach. Journal of The Royal Society Interface. 2014;11(99):20140594.

[36] Slatkin M. Hedging one's evolutionary bets. Nature. 1974;250(5469):704–705.

[37] Philippi T, Seger J. Hedging one's evolutionary bets, revisited. Trends in ecology & evolution. 1989;4(2):41–44.

[38] Xue B, Sartori P, Leibler S. Environment-to-phenotype mapping and adaptation strategies in varying environments. Proceedings of the National Academy of Sciences. 2019;116(28):13847–13855.

[39] Lauga E, DiLuzio WR, Whitesides GM, Stone HA. Swimming in circles: motion of bacteria near solid boundaries. Biophysical journal. 2006;90(2):400–412.

[40] Croll NA. Behavioural analysis of nematode movement. In: Advances in parasitology. vol. 13. Elsevier; 1975. p. 71–122.

[41] Waterston RH, Thomson JN, Brenner S. Mutants with altered muscle structure in Caenorhabditis elegans. Developmental biology. 1980;77(2):271–302.

[42] Ward S. Chemotaxis by the nematode Caenorhabditis elegans: identification of attractants and analysis of the response by use of mutants. Proceedings of the National Academy of Sciences. 1973;70(3):817–821.

[43] Pierce-Shimomura JT, Dores M, Lockery SR. Analysis of the effects of turning bias on chemotaxis in C. elegans. Journal of experimental biology. 2005;208(24):4727–4733.

[44] Izquierdo EJ, Lockery SR. Evolution and analysis of minimal neural circuits for klinotaxis in Caenorhabditis elegans. Journal of Neuroscience. 2010;30(39):12908–12917.

[45] Kato S, Xu Y, Cho CE, Abbott L, Bargmann CI. Temporal responses of C. elegans chemosensory neurons are preserved in behavioral dynamics. Neuron. 2014;81(3):616–628.

[46] Izquierdo EJ, Williams PL, Beer RD. Information flow through a model of the C. elegans klinotaxis circuit. PloS one. 2015;10(10):e0140397.

[47] Murayama T, Maruyama IN. Decision making in C. elegans chemotaxis to alkaline pH: Competition between two sensory neurons, ASEL and ASH. communicative & integrative Biology. 2013;6(6):1007–12.

[48] Wang Y, Zhang X, Xin Q, Hung W, Florman J, Huo J, et al. Flexible motor sequence generation during stereotyped escape responses. Elife. 2020;9:e56942.

[49] Donnelly JL, Clark CM, Leifer AM, Pirri JK, Haburcak M, Francis MM, et al. Monoaminergic orchestration of motor programs in a complex C. elegans behavior. PLoS Biol. 2013;11(4):e1001529.

[50] Kagawa-Nagamura Y, Gengyo-Ando K, Ohkura M, Nakai J. Role of tyramine in calcium dynamics of GABAergic neurons and escape behavior in Caenorhabditis elegans. Zoological letters. 2018;4(1):19.

[51] Li W, Feng Z, Sternberg PW, Xu XS. A C. elegans stretch receptor neuron revealed by a mechanosensitive TRP channel homologue. Nature. 2006;440(7084):684–687.

[52] Yeon J, Kim J, Kim DY, Kim H, Kim J, Du EJ, et al. A sensory-motor neuron type mediates proprioceptive coordination of steering in C. elegans via two TRPC channels. PLoS biology. 2018;16(6):e2004929.

[53] Cohen E, Yemini E, Schafer W, Feitelson DG, Treinin M. Locomotion analysis identifies roles of mechanosensory neurons in governing locomotion dynamics of C. elegans. Journal of Experimental Biology. 2012;215(20):3639–3648.

[54] Martens K, Angelani L, Di Leonardo R, Bocquet L. Probability distributions for the run-and-tumble bacterial dynamics: An analogy to the Lorentz model. The European Physical Journal E. 2012;35(9):84.

[55] Cates ME, Tailleur J. When are active Brownian particles and run-and-tumble particles equivalent? Consequences for motility-induced phase separation. EPL (Europhysics Letters). 2013;101(2):20010.

4

LONG TIMESCALE WHOLE-BRAIN IMAGING OF SEMI-IMMOBILIZED *C. elegans* REVEALS RESPONSE, OUTPUT AND MODULATION OF COLLECTIVE NEURONAL MODES

ABSTRACT

Recent experimental advances have enabled recordings of brain-wide dynamics at single-neuron resolution in the nematode *C. elegans*. A major goal of such efforts is to link the collective dynamics of neural processing to sensory input and behavioural output, but whole-brain imaging measurements performed so far have been of short duration (typically $< 10-20$ minutes), limiting the statistical power of stimulus-response measurements within individuals, and/or performed on paralysed worms, rendering the connection to behavior output indirect. To overcome these limitations, we developed a pipeline combining widefield deconvolution microscopy with microfluidics, that allows measurement of brain-wide neuronal dynamics of confined, but not paralyzed, worms as they experience temporally modulated chemical stimuli over durations exceeding one hour. This semi-immobilized configuration precludes locomotion by confinement within a PDMS channel, but permits deformations of the worm anatomy parallel to the axial direction of the confining channel, which we analyse as a one-dimensional behavioural output of brain activity. We demonstrate the utility of this approach by testing three hypotheses inspired by recent work on *C. elegans* brain dynamics

and behavior: (i) the collective motor-command hypothesis, which postulates that collective patterns of neural dynamics recently discovered by whole-brain imaging in paralysed worms represent motor commands encoded by the correlated dynamics of many neurons, (ii) the apparent stochasticity hypothesis, which postulates that the influence of ensemble neural dynamics can render the response of individual neurons to sensory stimuli appear stochastic, and (iii) the brain-state neuromodulation hypothesis, which postulates that the action of extrasynaptic neuromodulators can trigger switches between functionally distinct global brain states — persistent epochs of brain-wide neural activity with distinct dynamical patterns. Our experiments yielded positive evidence in support of all three hypotheses. Taken together, these results provide direct evidence that collective modes of neural dynamics link both sensory stimuli and neuromodulation changes to behavioural output, and demonstrate the power of our approach for whole-brain stimulus-response measurements.

4.1. INTRODUCTION

Understanding how the brain internalises and processes information to actuate organism-scale behaviour is one of the main goals in neuroscience. At first sight, the sheer complexity of the problem is nothing short of daunting — how can we hope to understand the collective activity of billions of neurons, actuating a myriad of anatomical and physiological processes to control behavior? One promising approach is to start with the simplest model systems, in which neural dynamics and its output behaviors can be followed with relative ease and at a higher degree of completeness. The nematode *C. elegans* presents unique advantages for such studies of brain-wide information processing due to its transparent and compact anatomy that allows non-invasive optical imaging of brain-wide neural activity. The hermaphrodite body layout is conserved across individuals, with a nervous system consisting of just 302 neurons, with a fully mapped connectome [1]. Around 200 of these neurons are concentrated in the head region, making it feasible to characterise the dynamics of most, if not all, neurons of this compact brain simultaneously. In addition, the behavioural repertoire of the worm is readily quantifiable by imaging, and sophisticated analysis methods are now available to parameterize its postural and motile trajectory dynamics [2–5], making it a particularly compelling system in which to study how the brain controls organism-scale behavior.

In the last two decades, genetically encoded calcium indicator (GECI) proteins, which enable optical measurements of neuronal activity *in vivo* [6], have emerged as a powerful tool for characterising neural circuits — subgraphs of the connectome involved in specific tasks underlying sensing and behavior. The ability to genetically target the expression of these optical reporters to specific neurons has proved especially powerful in *C. elegans*, given its unique status as a genetic model organism with a fully mapped connectome, leading to the definition and functional characterization of numerous circuits in the worm's brain [7–12]. While these circuit-level interrogations have been powerful in connecting specific sets of neurons to various sensory and behavioural functions, the brain is a highly connected network and it can be expected that the activity of its many subcircuits is not independent from one another [13]. Indeed, despite the many insights delivered by circuit-level studies, it remains uncertain whether and to what extent brain function can be understood as the sum of many individual circuits.

A complementary approach, made possible by continued advances in GECI technology, as well as fast volumetric microscopy methods, is optical imaging of neural dynamics at the level of the entire brain. In a number of model organisms with compact brains, including *Drosophila* [14], zebrafish [15], and *C. elegans* [16–24], it is now possible to optically record the activity of the majority of brain neurons simultaneously, at single-neuron resolution. In *C. elegans*, these approaches are now able to resolve the activity of the majority of the neurons in the head region, aided by nuclear localization of the GECI proteins to facilitate 3D segmentation of individual neuron signals [16]. In *C. elegans* so far, such brain-wide neuronal recordings have been predominantly performed on paralyzed worms, with a few exceptions on freely moving worms [19, 20, 25, 26]. Most of these 'whole-brain' imaging experiments in *C. elegans* have been performed using spinning disc confocal microscopy, which limits the maximum recording duration due to strong bleaching (with a notable exception [26]), although some studies have used wide-field deconvolution imaging [21] or light-sheet imaging [24, 27]. Finally, repeated stimulus-response measurements to study the brain-wide neural responses have only been performed on a limited number of stimulus types, namely heat stimuli delivered by infrared lasers [20, 21], and oxygen stimuli, delivered in the gas phase [16, 18].

In this study, we have implemented a contrasting approach to whole-brain imaging, on worms that are semi-immobilized (rather than paralysed or freely moving) and that enables long timescale recordings exceeding 1 h by using wide-field deconvolution microscopy, fast modulation of arbitrary chemical stimuli in the liquid phase, and simultaneous measurement of confined worm motion as a behavioural output. To confine the worm and apply chemical stimuli, we use a microfluidic device, first described by Chronis et al. [28], in which the worm is sufficiently constrained to preclude locomotion, but still allows for anatomical deformations within the confining channel. This stretch-shrink motion serves as a one-dimensional behavioural output to which brain dynamics can be related in our analysis.

Although a number of studies to date have used whole-brain imaging to relate collective neural activity to motile behavior, the exact relationship between anatomical movement and brain dynamics remains an open question. In paralysed worms in the absence of applied stimuli, neuronal dynamics were found to be low dimensional: the top three modes from a principal component analysis (PCA) accounted for 65% of the variance [18]. By analysing how specific neurons associated with different locomotor behaviours (forward, backward, and turning) were represented in each of these modes, it has been hypothesised that the collective neural activity represented in the observed PCA modes encodes motor commands [18]. In contrast, whole-brain imaging studies in freely moving worms have reported neural dynamics that appear more complex [19, 20, 25], with the top PCA modes capturing a smaller fraction of the total variance and predicting the simultaneously acquired behavioural dynamics (speed and curvature) relatively poorly. A sparse linear model trained on the joint set of neural and behavioural data performed much better in predicting the same dynamics [25].

Thus, the validity of the ’motor-command hypothesis’, in which collective modes of brain-wide neural activity (such as those resolvable by PCA analysis) drive the worm’s anatomical motion remains unresolved. Our approach of studying a semi-immobilized (i.e. confined, but not paralyzed) worm provides a compromise between paralysed and freely moving, and thus may help to bridge these contrasting observations of previous studies.

Our combination of long-timescale whole-brain recordings with microfluidic control of chemical stimuli inputs greatly facilitates the study of sensory processing at the level of brain-wide neural dynamics. *C. elegans* responds to a rich set of chemical stimuli, sensed by its chemosensory neurons [29] with distinct behavioural responses. For instance, the sensory neuron ASH senses aversive stimuli (such as copper, pH, and SDS), which triggers an escape response [30, 31]. The escape response is a highly stereotyped behaviour involving a well-defined sequence of behavioural motifs [32] that is crucial for survival upon encountering noxious environments [33]. By contrast, the chemotactic strategy of biassing the worm’s random walk motility in response to gradients of stimuli (such as NaCl) involves stochastically modulating the frequency of ’pirouettes’ (bouts of reversals and sharp turns) [34] paired with gradual orientation corrections during forward crawling [35]. NaCl is sensed by the ASE neuron pair [36], which has an asymmetric functional relationship where ASEL and ASER activity increases after a sudden increase or decrease in salt concentration, respectively [37]. In addition, the ASER neuron encodes information of the preferred concentration [38] (associated with food), making the neuronal response when provided with a salt gradient experience dependent [10, 39]. How the response of repetitions of these distinct stimuli is encoded by the brain has not been studied using whole-brain imaging.

Given that behavioural responses to many stimuli demonstrate apparent stochasticity (i.e. variable responses from trial to trial) [34, 35], it can be expected that brain-wide neural activity responses could also be highly variable, requiring many repeats of identical stimuli to characterise responses in statistical terms. Indeed, the only study to date that characterised the response of brain-wide activity patterns to repeated stimuli (by oxygen partial pressure changes) revealed highly variable responses at the level of neural activity trajectories in PCA space [18]. Furthermore, even in the absence of (externally) applied stimuli, brain-wide neural activity exhibits significant temporal dynamics [18–20, 25], and distinguishing responses to stimuli from these ‘resting-state dynamics’ would again require many repeated stimulations. Interestingly, at the circuit level, it was recently established that the variable response of individual interneurons in an olfactory circuit depends on the state of other neurons within the circuit [12]. Combined with the resting state dynamics observed at the whole-brain level [18–20, 25], this raises the question of whether such ’network states’ that generate apparent stochasticity are confined to local circuits, or rather are attributable to the larger collective dynamics observed across the whole brain. With sufficient statistics for brain-wide neural activity patterns both in the resting state dynamics and during response, it may be possible to address this 'apparent stochasticity hypothesis' at the whole-brain level.

Neural dynamics in the brain can be affected not only by external stimuli, but also by neuromodulator molecules, such as biogenic amines [40] and neuropeptides [41], that are secreted by the neurons themselves, often into extrasynaptic space to produce effects over longer length and time scales compared to synaptic neurotransmission. Because of these long-range effects, it is of interest to study neuromodulation beyond the circuit level, using whole-brain imaging. Among these chemicals are four biogenic amines used by *C. elegans*, that can be exogenously applied and function as neuromodulators to modulate behaviour in response to the environment: serotonin, dopamine, tyramine, and octopamine [42–46]. We study the whole-brain response of the exogenously applied serotonin to test the hypothesis that long-range action of neuromodulators can trigger switches between global brain states — persistent epochs of brain-wide neural activity that affect organism-scale behavior [47, 48].

In what follows, we first describe our experimental setup and the general features of the measured brain dynamics. Subsequently, we demonstrate the power of our approach by experiments that address each of the three hypotheses introduced above, namely: (i) the *collective motor-command hypothesis*, which postulates that collective patterns of neural dynamics recently discovered by whole-brain imaging in paralyzed worms represent motor commands encoded by the correlated dynamics of many neurons; (ii) the *apparent stochasticity hypothesis*, which postulates that the influence of ensemble neural dynamics can render the response of individual neurons to sensory stimuli appear stochastic; and (iii) the *brain-state neuromodulation hypothesis*, which postulates that the action of extrasynaptic neuromodulators can trigger switches between functionally distinct global brain states.

4.2. RESULTS

4.2.1. MEASURING BRAIN DYNAMICS OF A SEMI-IMMOBILIZED WORM IN A MICROFLUIDIC CHIP.

To understand how the brain processes information, it is useful to relate the brain activity dynamics to the sensory inputs and behavioural output. The interpretation of complex brain dynamics is facilitated when these inputs and outputs are simple. Additionally, the non linearity of the brain dynamics requires thorough sampling. Therefore, our approach to studying whole-brain dynamics uniquely combines two elements. Firstly, we record whole-brain dynamics in semi-confined worms in a microfluidic device described by Chronis et al. [28], instead of fully paralysed or freely moving worms used hithero (Figure 4.1A). This allows the direct delivery of a wide range of stimuli, which are carefully timed by switching between two flow channels, typically a buffer medium and a stimulus. In addition, a confined worm can deform along the axis of the channel, contracting and extending, providing a low-dimensional behavioural output. This motion is captured by a single parameter henceforth referred to as 'stretch' (quantified by the average displacement D of tracked neurons along the direction of the confining microfluidic channel, measured in units of µm; see Methods), with a positive and negative sign corresponding to extension (positive stretch) and contraction (negative stretch) of the worm's head region (Figure 4.1B). This provides a means to investigate the global brain dynamics directly in the context of behaviour. Secondly, by using widefield-fluorescent imaging with deconvolution (a method also used by Kotera. et al. [21]) we were able to record calcium signals of head neurons for a timescale exceeding an hour with a frequency of 2.0-2.5 Hz (see methods). This allows us to not only study neurons directly responding to chemical stimuli, as was recently done by Yemini. et al. [49], but also to study dynamics of potentially stochastically responding neurons, such as the global modes described by Kato. et al. [18].

We reasoned that increasing the measurement duration to 1 h could be a viable strategy to more intensively sample brain dynamics with relatively modest influence of stress factors. Gonzales. et al. have demonstrated that microfluidic-induced sleep-like behavioural quiescence (which might be stress-induced [51]) in large arenas is still modest at this time scale for large microfluidic devices [52]. Semi-immobilized worms in a comparably small microfluidic device used in that study, however, demonstrated elevated sleep behaviour, possibly related to touch, but not paired with an elevated *daf-16* related stress response [52]. Thus, while confinement can induce a sleep-like state, such episodes are generally brief, and about half of the worms studied in Gonzales et al. [52] demonstrated no sleep episodes for measurement durations up to 1 h.

To study brain dynamics over long time scales, we constructed a wide-field

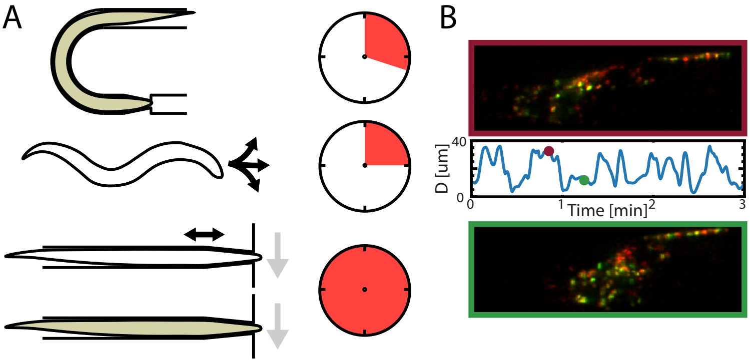

Figure 4.1: **Whole-brain imaging approach for long timescale measurements with a behavioural output.** (A) Contrasting experimental paradigms for whole-brain imaging in *C. elegans*. Left: Past whole-brain recordings in *C. elegans* were performed on either (top) paralyzed (indicated by the green shading) worms [18, 22, 23] or (middle) freely moving (indicated by black arrows) worms [19, 20, 23], whereas in this study, we (bottom) confined worms, both with and without paralysis, with a stimulus fluid flow (grey arrows). Right: The use of wide-field imaging allows measurements exceeding an hour, far exceeding the typical recorded times on previous studies on paralysed [18] or freely moving [50] worms. (B) The average stretch *D* of each neuron in µm, along the body axis. A positive and negative stretch correspond to extension or compression of the body, respectively.

fluorescent imaging system that simultaneously captures the intensity of two fluorophores pan-neuronally expressed and localised to the nucleus: a red fluorophore (tagRFP/tagRFP-T) used to localise and track neurons through time, and a calcium-sensitive green fluorophore (GCaMP6s) to record neuronal dynamics (see methods). Computing the green/red ratio largely corrects for spurious changes in the segmented green fluorescence due to movement and/or deformation of the neuronal nuclei (motion artefacts) and is used for analysis of brain dynamics [19]. We modified the tracking algorithm of Nguyen et al. [53] to improve robust performance under the large deformations of the worm's brain inside the microfluidic channel (see methods).

Deformations of the brain might, despite using the ratiometric signal, affect the obtained neuronal time series as a result of chromatic aberrations of the optical setup or wavelength-dependent properties of absorption refraction of the sample itself. Therefore, to test if the neuronal time series represent true changes in calcium levels, a comparison of the time series dynamics was made between recordings of the AML70 strain expressing the calcium-sensitive GCaMP6s and the AML175 control strain expressing the calcium-independent GFP [50]. The ratiometric signal of the AML70 strain clearly reveals a wide dynamic range both between neurons and within neurons over time, with distinct groups of neurons with correlated dynamics (Figure 4.2A). Correlated dynamics can also be observed across neurons in the control strain AML175 (Figure 4.2B). However, the modulation amplitude is much lower compared to the base line fluorescence, and the remaining dynamics are mostly dominated by noise.

It is possible to test whether the obtained intensity time series reflect true changes in GCaMP ([Ca2+] activity or are the result of motion artifacts. Firstly, as a result of deformation artefacts, the red and green channels are expected to respond with similar relative magnitude to the stretch resulting from the worm's motion (see methods), which can be quantified by the coefficient of variance (henceforth CV). Whilst the variability in the red channel of the AML70 strain is comparable to the control strain, the green channel shows a much broader distribution across neurons of the CV with on average higher magnitudes (Figure 4.2C). In contrast, the red and green channels of the control strain reveal dynamics of similar magnitude (Figure 4.2D). This indicates that the amplitude of green-channel dynamics is much larger than expected from motion artefacts. Secondly, intensity dynamics as a result of motion artefacts are expected to occur simultaneously with the motion. To examine the relative timing of worm movements and changes in the fluorescence signals, we performed peak detection on the cross correlation of the stretch with the fluorescent signals (Figure S4.1, see methods). As expected for the control strain, both the red and ratiometric channels have, on average, a lag of at most a few seconds with largely overlapping distributions (Figure 4.2F). However, the ratiometric signal of the AML70 strain shows that a large fraction of the neurons are time-delayed, with 55% of the neuronal activities (green/red ratio) exhibiting a larger delay time than the 90th percentile of the delay of the red channel (Figure 4.2E). We therefore conclude that the obtained neuronal time series from unparalyzed worms constrained in our microfluidic channel predominantly reflect changes in neuronal calcium concentrations, rather than artefacts that arise from motion and/or deformations of the segmented neuronal nuclei.

4.2.2. COLLECTIVE NEURONAL DYNAMICS OF SEMI-IMMOBILIZED WORMS ARE HIGHLY NON-STATIONARY OVER LONG TIMESCALES

A previous whole-brain imaging study on paralysed worms found that global brain dynamics are low dimensional, with 65% of the total neural activity variance captured by the top three principal modes in a PCA analysis [18]. We performed a similar analysis to describe and create a framework in which to analyze the global brain dynamics in semi-immobilized worms for longer time scales and to compare global brain dynamics of paralyzed worms described in literature. To identify global patterns in the dynamics, in an analysis similar to Kato. et al. [18] we conducted a principle component analysis (see methods).

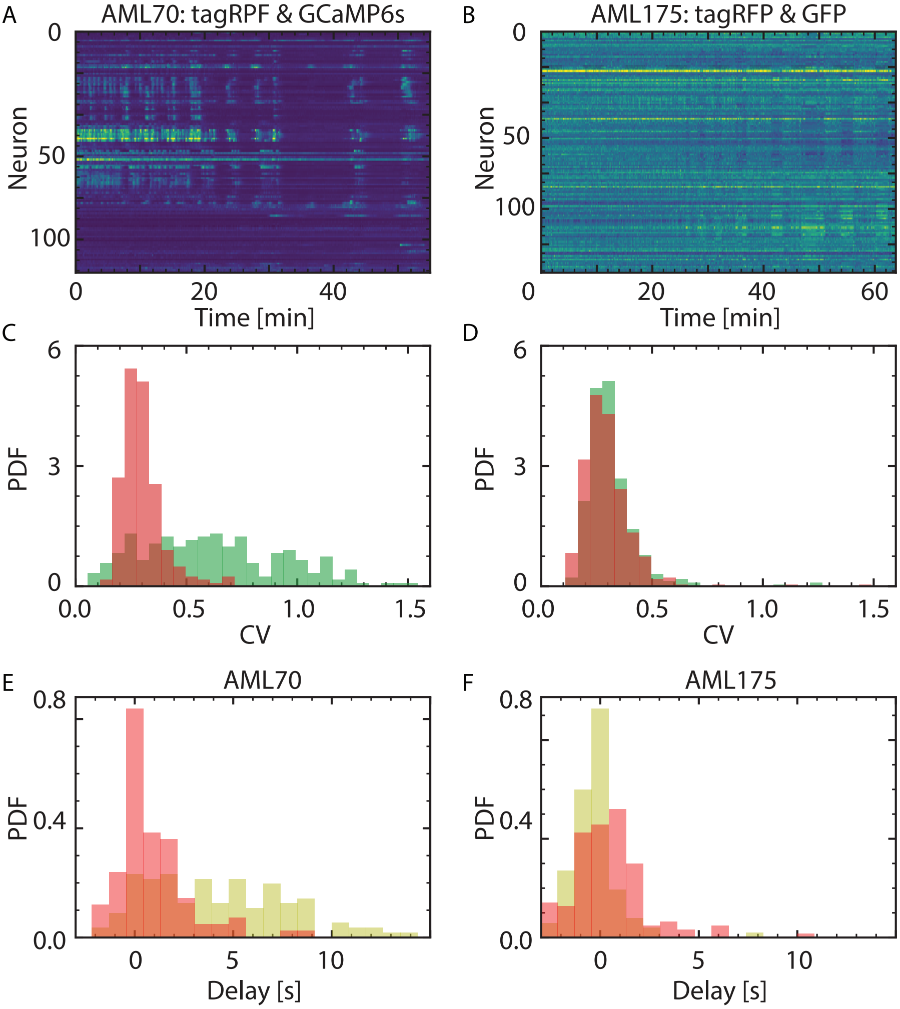

Figure 4.2: Caption is on the next page.

Similarly to Kato. et al., a large portion of dynamics can be described by a few dimensions (Figure 4.3A-D), with the top three modes accounting for 27% ± 7.4%, 11 ± 2% & 8 ± 2% (SEM, N=9) of the variance. Both in our measurements and the paralysed worms from Kato. et al., the principal mode captures a much greater fraction of total variance compared to the second mode (in our measurements by a factor of 2.60 ± 0.25 (SEM), $N = 9$), and describes the dynamics of two large anti-correlated oscillatory clusters of neurons. This suggests that the measurements describe similar dynamics and that the principal mode is robust under

Figure 4.2: **Neuronal Ca^{2+} dynamics dominate over motion artefacts in the observed GCaMP intensity changes.** (A) An exemplary measurement of the neuronal ratiometric signal measured of 116 neurons from the AML70 strain expressing GCaMP6s and TagRFP reveals correlated dynamics across neurons. Neurons are sorted by the dendogram order constructed from hierarchical single linkage clustering on the euclidean distance. (B) The ratiometric signal of an exemplary control (AML175) measurement shows comparatively small variation across and within the 136 tracked neurons over time. The plotted activities are smoothened using a Savinzky-Golay filter with a second-order polynomial on a 5-second window. Neurons are sorted using the same method as described in panel A. (C) The coefficient of variance (CV) of the neuronal GCaMP6s signals (green) reveals a wider distribution with a (on average) larger mean as compared to the TagRFP (red) ($N = 2$). (D) The variability of the GFP (green) and TagRFP (red) channels is similar for the control strain ($N = 3$). (E) The delay time of the maximum cross correlation (see methods) of the deformation and the fluorescent signals is larger for strongly correlated neurons. The red channel shows almost no delay, whereas the ratiometric signal shows a large number of neurons that have a delayed response. (F) Both the TagRFP and the GFP/TagRFP signal show much smaller time offsets. Time derivatives are computed using a Savinzky-Golay filter with a 4th order polynomial on a 10 s window). For panels E and F, only delays of neurons with a correlation of at least 0.27 are included (Figure S4.1).

paralysis. The next two lower modes also show oscillatory dynamics. To study the relationship between the top two modes, in an analysis analogous to Kato et al., phase space trajectories were plotted for the time series of the top two modes (Figure 4.3E). These trajectories reveal patterns that are complex yet also possess visually discernible regularity (Figure 4.3E). In particular, the trajectories draw out paths that are relatively smooth and loop-like, despite considerable variability in the size, location, and orientation of loops. The overall cyclical nature of these trajectories was often more clearly demonstrated in phase-space flux diagrams, where vortex-like flux patterns could be observed in the field of flux vectors in Mode1-Mode2 space (Figure 4.3F).

It should be noted that the second and lower modes do not unambiguously contrast from subsequent modes in terms of explained variance, and hence could be subject to rank-swapping across individual measurements. Indeed, we noticed variability in the Mode1-Mode2 phase relationship across measurements. Therefore, caution is required in the comparison and interpretation of phase-space patterns in the Mode1-Mode2 plane depicted in Figures 4.3E,F).

The long duration of our measurements enabled the investigation of changes in these dynamics over extended times, revealing strong non-stationarities. Periods of neuronal quiescence, in which activity of the top three modes are essentially silent, were observed after ~ 20 min. These quiescent intervals contribute to an increased inter-peak interval, defined as the time duration between subsequent peaks of the principal mode time series, with a duration $\gtrapprox 1$ min of the principal mode dynamics (Figure 4.3G, S4.2). These periods of brain quiescence are strongly reminiscent of a recently reported confinement-induced sleep-like state in *C. elegans* [52]. Gonzales et. al. reported periods of motile inactivity, paired with a reduction of brain activity of most neurons, but could only track 10 neurons simultaneously. Our measurements show that the brain quiescent state is paired with stretch inactivity, which remains constant at large positive values (Figure 4.3C, black). An extension of the body suggests a relaxation of the body wall muscles, which is associated with sleep [54]. We can therefore confirm that the brain quiescent state is the microfluidic-induced sleep state, and show that this sleep state is paired with a quiescent state at the level of mode dynamics.

Non-stationarities can also be observed in the phase relationship of the first two modes, with decreasing regularity in the phase-shape trajectories over time and a change in the amplitude of the oscillations (Figure 4.3E III-VIII). These changes in the phase-space relationship over the course of the measurement are paired with noticeable changes in activity of some of the strongly loaded neurons onto the modes: for instance at the onset of the measurement, the principal mode consists of two large anti-correlated clusters of neurons, where towards the end one of the clusters exhibits virtually no activity, while in the other cluster some neurons have decreased considerably in activity. This suggests that phase relationships among these collective modes and the neurons contributing to them are not fixed, but may change depending on conditions.

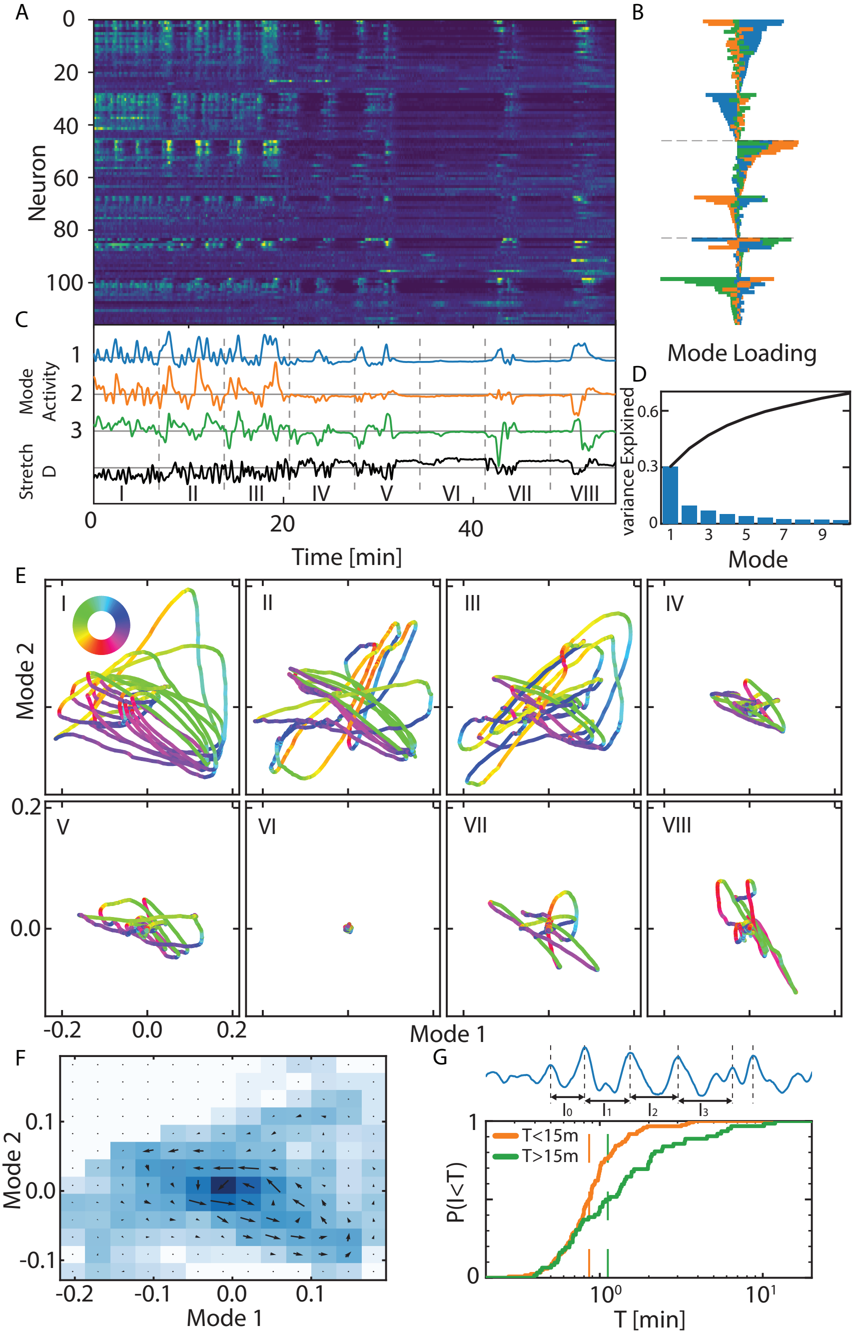

Figure 4.3: Caption is on the next page.

Figure 4.3: **Activity dynamics of the neuronal population demonstrate irregular low-dimensional oscillations and strong nonstationaries.** (A) A representative 55 min recording of the brain activity of an unparalyzed worm in a microfluidic channel. (B) The mode loadings of each neuron of the first 3 Eigenmodes. Blue, orange, and green are the first, second, and third mode respectively. (C) Time series corresponding to the first 3 modes and the stretch, D (black). (D) The loadings of the first 10 modes (blue) and the respective cumulative explained variance (black), shows the principal mode is dominant. (E) The phase space trajectories of mode 1 and 2 reveals cycles and non-stationarity of the dynamics. (F) A clear phase relationship between the first two principal modes can be observed from a flux plot, computed over the entire recording. (G) A longer interpeak distance of the first mode is observed after longer times ($N = 9$). Top: Peaks are selected from the local maxima, larger than the standard deviation of the mode, and with a minimum distance of 50 data points (about 20 s). Bottom: Cumulative interval distribution of the inter peak time of the first mode loading, corresponding to a rise in the cluster dynamics for times $t < 15$ min (yellow) and $t > 15$ min (green). The dashed lines correspond to the median value of the respective condition.

4.2.3. THE PRINCIPAL MODE OF BRAIN DYNAMICS CLOSELY REFLECTS CONFINED WORM MOTION

Our observation that global brain dynamics of confined, yet not completely immobilized worms closely resemble those previously reported for paralyzed worms provided an opportunity to directly test whether and how the observed collective modes relate to motion of the worm. The study of Kato et al. established the compelling hypothesis that the stereotypic phase space trajectories of the top three modes of collective neuronal dynamics map to different aspects of behavior, based on separate experiments in freely moving worms that observed the activity of a small subset of mode-associated neurons in freely moving worms. Yet a subsequent whole-brain imaging study by Scholz et al. failed to resolve similar stereotypical trajectories, and thus the relationship between collective modes of neuronal dynamics observed under paralysed conditions and worm motion under non-paralyzed conditions remains an unresolved issue. Our experimental configuration enables a direct comparison of the collective neuronal dynamics with the simultaneously observed stretch behavior, D of worm's head region, respectively (Figure 4.1B).

To assess the relationship between the stretch behaviour and neuronal dynamics, a cross-correlation analysis was performed between the dynamics of head stretching and those of individual neuronal and collective mode dynamics, respectively (Figure 4.4A; see Methods). For individual neurons, the maximum absolute cross-correlation value (see methods), C, is on average 0.31 ± 0.01 (95% CI, bootstrapped), but broadly distributed (Figure 4.4B, gray bars) (dominated by spurious correlations) with a long tail up to 0.74. A similar analysis on mode dynamics reveals that the principal mode strongly correlates with the head stretch — on average 0.58 ± 0.07 (95% CI). In contrast, mode 2 and 3 have a correlation of 0.34 ± 0.06 and 0.34 ± 0.09 (95% CI) respectively. In 7 out of 8 measurements, the principal mode ranked as the top correlated mode with stretch.

The strong cross-correlation between the principal neuronal mode and stretch behaviour is not imposed by the quiescence behaviour, which is paired with expansion, as we found similar correlations for worms not exhibiting quiescent behaviour (exempt of a non-quiescence time period shown in Figure 4.4B, inset). These results show that the principal mode is strongly related to stretching behaviour.

The strong relation between mode and stretch dynamics raises the question of whether and how the principal mode might respond to immobilisation of the worm. We therefore performed experiments in which the worm was initially not paralysed and free to move its head along the dimension along the confining channel, and 10 mM of the paralytic tetramisole was added halfway through the measurement (Figure 4.4B, S4.3). Upon adding the paralytic, the position of the head moved towards the body as a result of the body wall muscle hypercontraction, and the movement of the head was drastically reduced in amplitude, while the oscillatory dynamics of the principal mode persisted. This observation shows that, although strongly correlated with motion, motion is not required for the dynamics of the principle mode.

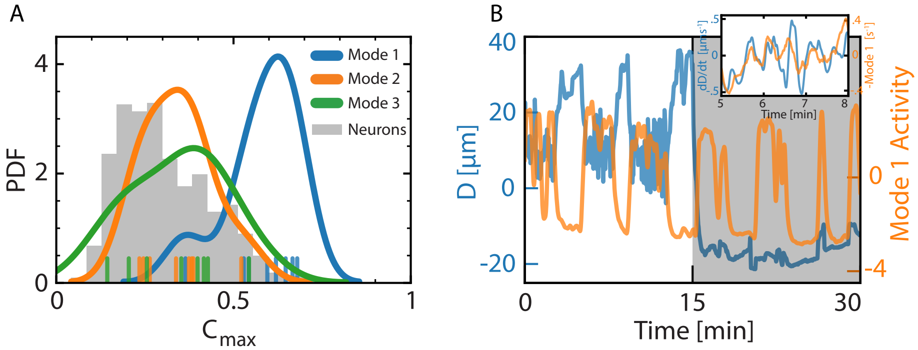

Figure 4.4: **The principal mode of whole-brain dynamics is strongly related to stretch-shrink behavior of the worm's head.** (A) The derivative of the stretch is strongly correlated with the mode time series. On the x-axis is the maximum absolute cross correlation $C_{\text{max}} = \max|C(\dot{D}, \text{Mode})|$ (see methods) between the stretch derivative and the first 3 modes time series, or time derivative of individual neuron activity. The correlation is much larger than that of most lower order modes or individual neurons. This plot contains data from 8 different measurements of semi-confined, unparalyzed worms. (B) Upon addition of the paralytic (10 mM Tetramisole) at $t = 15$ min (shaded region), fluctuations in the average position of the neurons (blue) are reduced, while the principal mode dynamics continue (computed from the entire time series) (orange). The orange line represents the integrated dynamics of the principal mode. Inset: During periods of high activity, stretch dynamics and principal mode dynamics are correlated.

4.2.4. GLOBAL BRAIN DYNAMICS UPON PULSE STIMULATION WITH A NOXIOUS CHEMICAL

We seek to study the whole-brain response towards different chemical stimuli. This includes studying the individual, but also the collective dynamics at the level of the modes, as Kato et al. reported stochastic modulation of the mode dynamics towards repeated exposure to O_2 [18]. In order to obtain data of stochastically responding neurons, long timescale measurements are required. On semi-contrained worms, microfluidic-induced sleep may occur within an hour in a confined arena, causing a decreased sensitivity to externally applied stimuli [52]. However, these sleep states had considerably decreased upon paralysis [52]. We therefore measured brain activity on paralysed worms (see methods) without stimulus for a duration of 60 min (Figure S4.4). No mode quiescent states could be observed. Therefore, stimulus response measurements are performed on paralysed worms.

Noxious stimuli trigger in *C. elegans* an acute behavioural response that enables rapid avoidance of the sensed noxious condition. We used our whole-brain imaging setup to simultaneously follow both individual and collective neuronal responses to SDS, a noxious detergent. SDS is sensed in the head region by the amphid ASH neurons, and in the tail region by the phasmid PHBA/B neurons, which trigger an escape response (rapid reversal followed by a sharp turn) and acceleration response, respectively [30]. In our experiments, the worm experiences applied chemical stimuli primarily at its head, given the geometry of the device, in which only the nose of the worm protrudes into the stimulus flow channel (Fig. 4.10). The SDS stimulus was delivered in brief (5 s) pulses to mitigate potential toxicity, but was applied repeatedly to enable statistical analyses of neuronal responses. Each stimulus pulse delivered SDS at a concentration of 0.1%, which has been reported to cause in the ASH neuron a fast rise of [Ca^{2+}] upon addition taking ≈ 5 s to decrease in concentration upon removal [55]. In each stimulus repetition cycle, the 5 s stimulus pulse was followed by a 60 s recovery period in which buffer flowed through the stimulus channel.

To quantitatively determine which neurons are significantly responding to the addition or removal of the stimulus, the neuronal activity was cross-correlated with the stimulus. We then extracted the cross-correlation value C for each neuron (see Methods) and computed its cumulative distribution (Figure 4.5A, blue curves). This quantity is insensitive to the sign of the neuronal response or delays of response with respect to the stimulus. To distinguish between spurious correlations and significantly correlated neurons, the distribution of C from stimulated worms was compared against that of a control group, obtained by applying the same cross-correlation analysis between the stimulus time series of these experiments and neuronal time series from other experiments in which no stimulus was applied (Figure 4.5A, Black). A substantial fraction, 16.4% ± 1.9% (obtained by bootstrapping for stimulated worms and using CI/4 where CI is the 95% confidence interval), of the identified neurons had a value of C equal to or greater than the 99th percentile of the control group.

These significantly correlated neurons demonstrated diverse response waveforms, differing in the sign (positive or negative) and timing (defined by the delay at which the cross-correlation reaches it speak value, C). Single-neuron time series from a representative experiment are shown in Figure 4.5B and S4.5). Some neurons respond immediately at the onset of the stimulus, and also immediately relax upon removal (Figure 4.5B, I). In other neurons, the onset of response follows an initial lag, with the change in activity typically starting a few seconds after the stimulus (Figure 4.5B, right). Although most neurons responded with an increase in GCaMP signal (and hence increase in Ca2+ concentration), there were also neurons that responded with a decrease (Figure 4.5B, III). We also identified a neuron demonstrating strong habituation, with a strong response upon the first of the SDS stimulus pulse, but weaker responses upon subsequent repetitions (Figure 4.5B, IV, S4.5A).

These strongly responding neurons only represent a minor fraction of the total loading of the top modes. For example, in the experiment of Figure 4.5B, the 17 significantly responding neurons represented 19, 4 and 3% respectively, of the total variance of the top 3 modes. This does not necessarily mean that the mode itself is unresponsive; it remains possible that a collection of neurons that are modulated only weakly at the individual level could collectively generate a more significant response. Indeed, Kato et al. [18] reported a rather subtle entrainment-like response of collective neuronal activity in response to cyclic oxygen-level shifts. To test whether a mode is responding significantly to a stimulus is not trivial, as it ideally requires knowledge of the dynamics of the same mode in the absence of the stimulus under the exact same conditions. Since no such information is available, no analysis is perfect, and assumptions have to be made about the mode dynamics in the absence of a stimulus. We therefore used two approaches: (1) comparing the mode correlations of a mode with those of other modes of unstimulated worms, and (2) comparing the mode to generated time series with similar dynamics.

To test for responses at the collective level, we applied to the top PCA modes the same cross-correlation analysis as that for single neurons, described above. $5.2\pm0.7\%$ of the modes across measurements correlate more strongly with the SDS stimulus than the 99^{th} percentile of a control group of modes from unstimulated worms (Figure 4.5C). Thus, the fraction of PCA modes responding to the SDS stimulus is considerably ($\sim$ 3-fold) lower than the fraction of individual neurons that respond to the same stimulus. In the representative experiment of Figure 4.5B, these significantly correlated modes included the principal mode, as well as several lower modes (Figure 4.5D). The lower modes (4 and 9) consist mainly of the previously identified responding neurons. In an alternative analysis, we modelled each mode's response waveform as a stochastic process and asked whether its amplitude of modulation is greater than that expected for a simulated mode that is blind to the stimulus but otherwise obeys similar statistics as the measured mode. This analysis is solely based on the observed dynamics of the mode itself, albeit with simplifying assumptions about the waveform. Specifically, the observed time series are reduced to a 2-state telegraph process (assuming that it assumes either an ON or an OFF state at every moment in time) by training a Hidden Markov Model (HMM) on the measured data (Figure 4.5E, blue curve, see methods). To simulate stimulus-blind realizations, these binary time series were randomised by separately shuffling the ON- and OFF-state intervals, thus scrambling the temporal relationship with stimulus input. To test whether the resulting probability curve is significantly modulated, the variance of the averaged on-probability p_{ON} of the measured data is compared to that of the randomized time series (Figure 4.5E, shaded regions). The results confirmed that the principal

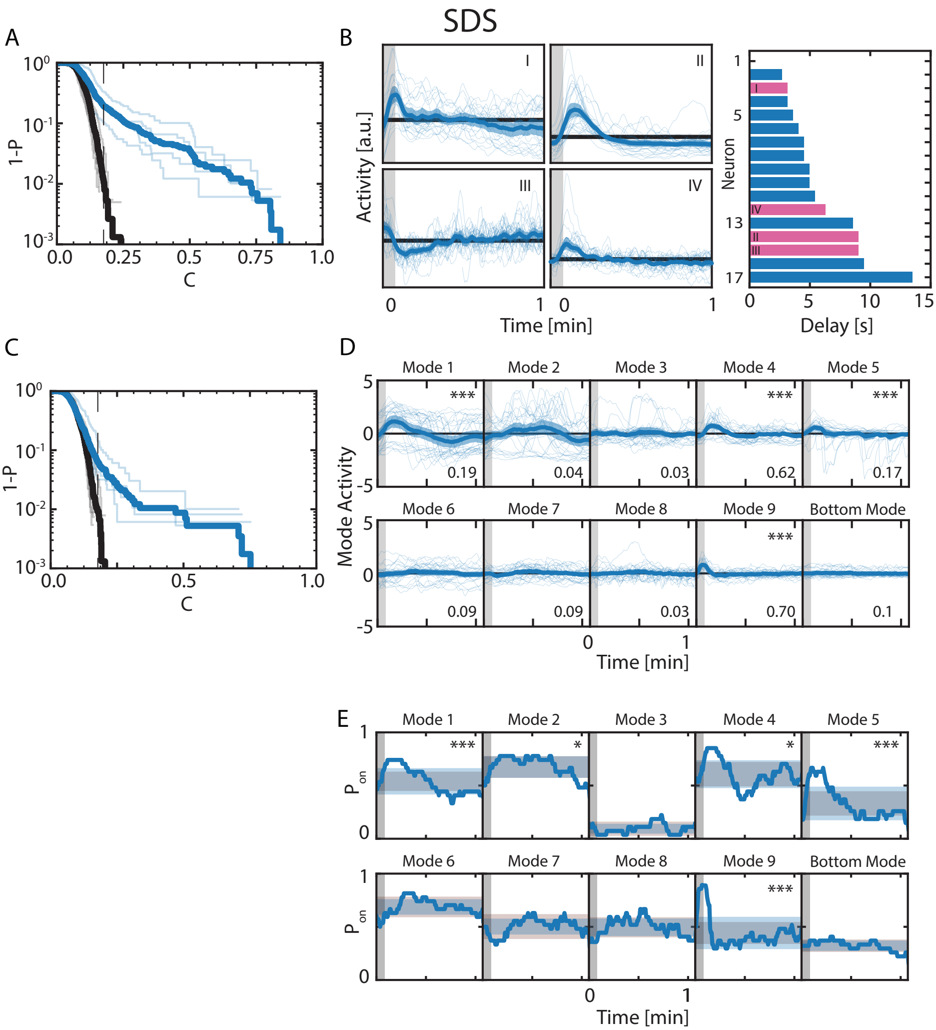

Figure 4.5: Caption on the next page.

mode is significantly modulated (in 3 out of 4 worms), and also identify the lower mode number 4 as significant ($p < 0.05$), and modes 5 and 9 as strongly significant ($p < 0.001$). In addition it includes the second top mode as significantly modulated. Taken together, these results show that the neuronal response to a brief pulse of SDS involves many individual neurons that respond stereotypically, and which contribute mainly to lower (rank> 3) PCA modes. In addition, they revealed stochastic modulation of some of the top PCA modes, possibly related to reversal and the sharp turn, describing the collective dynamics of many neurons

Figure 4.5: **Response of individual neurons and collective modes to a repeated** 0.1% **SDS pulse stimulation.** (A) An interval distribution of the maximum absolute cross correlation, C, of the derivative of the input signal with the derivative of individual neurons and (C) PCA modes reveals that a significant fraction of the neurons or modes of SDS-stimulated worms (blue, $N = 4$) is stronger correlated compared to unstimulated worms (black, $N = 8$). Transparent curves represent individual measurements. The black dashed line indicates the 99% value for nonstimulated worms. Cross correlations are computed for lag times up to 1 min. The time derivative of the stimulus is computed using the same filter (see methods) as the neuronal signals. (B) (left) Time series of exemplary significantly responding neurons with distinct signatures from a single measurement: a (I) fast (II) delayed, (III) negatively, (IV) habituation responding neuron. Thin blue lines represent times series of individual stimulus repeats. Thick blue lines with a shaded region show the average response with 95% CI, by bootstrapping for repeats. The grey region indicates the timing of the SDS stimulus. (right) The time lag corresponding with the maximum value of C for each of the significantly correlated neurons, including the exemplary neurons (pink bars). Time series of the other neurons can be observed in figure S4.5. (D) Significantly responding modes of an exemplary measurement include the principal mode describing global brain dynamics and other top-loaded modes. Exemplary mode activity of the top 9 modes and the bottom mode of a representative worm (same as in panel B). The number on the bottom right indicates the accumulated squared weight of the eigenvector (which adds up to 1 for all neurons for each mode) of the 17 significantly responding neurons identified in panel B. In the top-right corner, some modes show $***$ to indicate that such a correlation is not observed in any of the 760 reference modes. (E) Two-state time series of the on-probability p across repetitions for the top 9 modes and bottom mode reveals significant modulation. Mode time series are modelled using a 2-state Hidden Markov Model (HMM) (see methods). To test for significant modulation of the time signal, the standard deviation of the probability of a high state (blue shaded region is $<p> \pm \sigma_p$) is compared with bootstrapped time series, where the duration of the on and off states are separately shuffled (repeated $10k$ times). Red shaded region indicates the mean value of $p \pm$ the 95% CI of the standard deviation of the bootstrapped time series. Significantly responding modes are indicated by $*$ ($p \leq 0.05$) or $***$ ($p < 0.001$)

even though these dynamics are largely composed of neurons that were not identified individually as significantly correlated.

4.2.5. GLOBAL BRAIN DYNAMICS UPON STEP STIMULATION WITH A CHEMOTACTIC STIMULUS

By contrast to strong noxious stimuli such as SDS, which trigger a stereotyped escape response in freely moving worms, chemotactic stimuli produce a more subtle probabilistic modulation of the ’pirouette’ frequency (bouts of sharp turns and reversals) to favourably bias their random walk [34], as well as modulation of crawling path curvature to steer towards favourable gradient directions [35]. To test how both individual neurons and collective modes of neuronal dynamics are modulated during such chemotactic stimuli, we monitored global brain dynamics under repeated stimulation of the worm with NaCl. NaCl is known to be sensed primarily by the ASE neuron pair [36], where the right neuron (ASER) increases Ca^{2+} concentration upon a downward NaCl concentration change and the left neuron (ASEL) does so upon an upward NaCl concentration change [37]. As the behavioural response could integrate longer timescales as compared to a noxious stimulus such as SDS, we applied a waveform that repeats successive up- and down-steps of varying duration (30, 60 and 120 seconds) between the preferred concentration (50 mM, in which worms were grown) and a higher concentration (75 mM) of NaCl. The steps of different durations are used to study the time-dependent neuronal response on the recent stimulus history.

As with the SDS-response experiments (above), we first identified significantly responding individual neurons by the same cross-correlation approach, comparing the maximum input-output cross-correlation C for the test data (in which the stimulus was applied) against that against control data (from experiments in which no stimulus was applied). We found that $8.3 \pm 0.9\%$ of the correlation values C of the stimulus measurements fall outside the 99th percentile of that of unstimulated measurements, a smaller fraction compared to the SDS stimulated worms (Figure 4.6A). The responding neurons thus identified revealed various waveforms indicative of analogue computations to process the input signal. Example waveforms of a representative measurement are shown in figure 4.6B and S4.6. Two of these neurons (Figure 4.6BI,III) responded with waveforms indicative of time differentiation of the stimulus. Neuron I responds to an increase in salt by rapidly increasing activity and slowly relaxing toward the pre-stimulus steady-state baseline level. This response waveform is reminiscent of that for ASEL [10, 37], but could also be one of several other sensory neurons (ADF, ASI, ASK, AWB) or interneurons (AUA, AVH, AVJ, URB) recently shown to respond with a similar waveform to NaCl as ASEL [49]. Neuron III responds to a decrease in salt, similar to the ASER neuron [10, 37]. We also notice that the waveform of the responses for these neurons is dependent on the duration of the stimulus steps: the peaks in the responses of neuron I (and to some extent neuron III) have a higher amplitude when the neuron spent more time at its baseline value before the stimulus. Two other neurons, II and IV, responded with waveforms indicative of time integration, with their activity gradually increasing in response to high and low salt concentrations, respectively, until eventually reaching a plateau when the stimulus step is sustained for long enough (Figure 4.6B, II,IV). These integrator-like waveforms are in stark contrast to the differentiator-like waveforms typical of sensory neurons, and thus may represent downstream interneurons involved in the salt response. However, given their highly stereotyped response waveforms, they are unlikely to be AIB or AIY, the two interneurons that synapse directly with the ASE neuron pair, as these have been shown to encode quite faithfully the stochastic reversal behaviour and we would hence expect AIB and AIY responses to be less stereotyped [10]. Other significantly correlated loaded neurons (e.g. Figure S4.6A10,14) respond to the stimulus, but also process other signals as there is no stereotypic response.

To study whether and how the NaCl stimulus affected collective neuronal dynamics, we first identified significantly responding modes, again using the same cross-correlation analysis as was done for the SDS experiment (above). The fraction of significantly responding modes according to this analysis (7.1 ± 1.1) is comparable to the fraction of significantly responding individual neurons (Figure 4.6C).

Overall, at the level of collective modes, the salt response was found to be more subtle compared to the SDS response. Firstly, within the same measurement, there is no consistent salt response of collective PCA modes after each of the concentration changes up or down. For instance, in the experiment of Figure 4.6B, the modes, although significantly correlated according to the analysis in figure 4.6C, most notably responded at the onset of the 2 min [NaCl] increase, but not at the onset of the 0.5 min (Figure 4.6D). The lack of a consistent response is also confirmed by the result of the same randomization test described for SDS, using the 2-state HMM to binarize the time series and shuffle the intervals (Figure 4.6E). Secondly, the salt response of the top PCA modes is not reproducible across worms. According to the randomization test, in only 3 of the 11 worms tested, the principal mode responded significantly to salt. Moreover, among the 3 significantly responding worms, the principal mode response dynamics are not stereotypical, exhibiting different wave forms of the principal mode in response to salt. The small relative number of salt worms with responding principal modes contrasts the SDS measurements, where 3 out of 4 principal modes responded significantly (Figure 4.7). Similar differences were also observed for other highly ranked modes (specifically, modes 2 and 4). For lower modes (mode 5 and downwards), the NaCl and SDS experiments had a similar fraction of significantly responding modes.

Concluding, we find a rich set of neurons responding stereotypically to a step increase or decrease of salt, performing analog computations, some of which might have been reported before: differentiating or integrating the stimulus. At the level of collective dynamics, the response is less pronounced compared to SDS, which might reflect the difference in behavioural context.

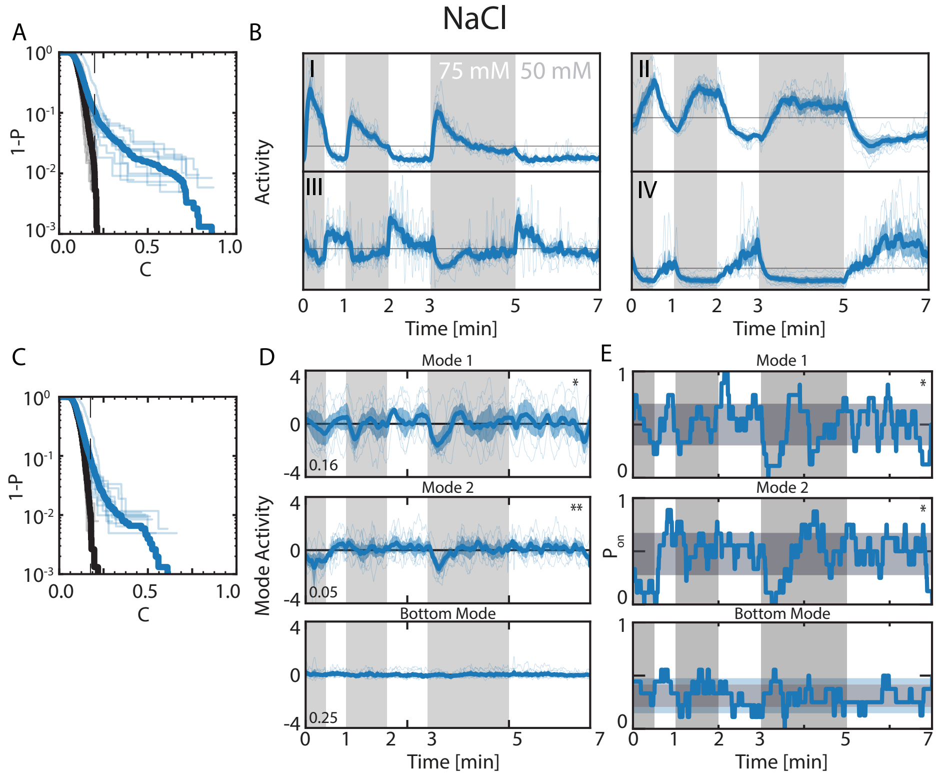

Figure 4.6: **Response of individual neurons and collective modes to repeated NaCl step stimulation.** (A) In analogy to figure 4.5A, a significant portion of the neurons and (C) PCA modes of worms receiving a salt stimulus ($N = 11$) have an absolute cross correlation value, C, larger than that of unstimulated worms (black, $N = 8$). Transparent curves represent individual measurements. The black dashed line indicates the 99% value for nonstimulated worms. Cross correlations are computed for lag times up to min. The time derivative of the stimulus is computed using the same filter (see methods) as the neuronal signals. (B) Exemplary strongly correlated neurons with the stimulus from a single measurement with distinct stereotypic responses. Other significantly responding neurons from the same measurement can be found in figure S4.6. (D) Dynamics of the two top modes and the bottom mode. The number on the bottom left indicates the accumulated squared weight of the eigenvector (which adds up to 1 for all neurons for each mode) of the 22 significantly responding neurons identified in panel B and figure S4.6. (E) Probability of the on state (corresponding with a high mode value) for the two top modes and the bottom mode (blue lines). The average probability ± the standard deviation of the measurement (blue shaded region) is significantly larger than the 95% confidence interval from simulated measurements (red shaded region).

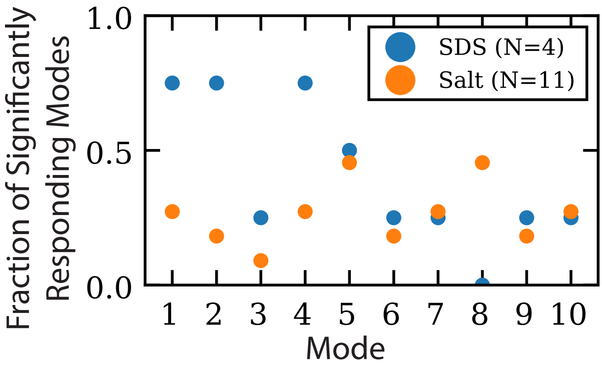

Figure 4.7: **Collective modes respond more strongly to** 0.1% **SDS than to changes in NaCl concentration.** For each of the top 10 PCA modes, an analysis has been performed, similarly as described for SDS (binarizing the mode using a 2-state HMM), where the probability has been computed that a randomly generated mode with similar dynamics exceeds the modulation of the true mode. The fraction of measurements significantly ($p < 0.05$) responding is shown for (blue) 4 SDS response measurements and (orange) 11 salt response measurements.

4.2.6. EXOGENOUS SEROTONIN INDUCES A REVERSIBLE BRAIN-WIDE QUIESCENT STATE

Whereas chemicals such as SDS and salt are external signals that require detection by the sensory neurons and further processing by downstream neurons to evoke a behavioural response, neuromodulators are signalling molecules used internally that can more directly affect many behaviours. We therefore wondered whether neuromodulators might elicit a more direct effect on collective neuronal dynamics, compared to sensory stimuli such as SDS and NaCl. To test this idea, we monitored brain-wide neuronal dynamics in paralyzed worms subjected to exogenously applied serotonin, a biogenic amine neuromodulator, suggested to be an indicator for feeding state / satiety [44] and associated with a wide range of behaviours [40]. It has been shown using mutants defective in serotonin synthesis (*tph-1*) or reception (*mod-1*) that serotonin promotes dwelling (local exploitation of food) over roaming (long-range exploration) in motile behaviour [56], and further work on behavioural individuality in roaming-dwelling behaviours also implicated serotonin signalling [57]. In addition, serotonin affects the response towards external stimuli: the sensitivity of the sensory neuron ASH towards octanol or touch stimuli is increased in the presence of serotonin [55, 58]. Physiological regulation of serotonin is complex, with its synthesis distributed across several neuron types broadly distributed across the worm's anatomy [40]. Yet, the relatively simple experimental strategy of exogenous application has yielded numerous insights regarding its neuromodulatory effects at the behaviour level, including promotion of egg laying and pharyngeal pumping [44], and slowing/inhibition of locomotion [59] in a dose-dependent manner [60].

To study the effects of exogenously applied serotonin on brain-wide neural activity, worms were subjected to a protocol in which brain dynamics were recorded first in the absence of exogenous serotonin for 15 min, followed by 30 min with exogenous serotonin, and finally without exogenous serotonin again for 15 min. Measurements were performed in unbuffered water, as Gurel. et al. found that in water, the serotonin concentration required to inhibit locomotion is reduced, compared to in buffer, by a factor of ~ 30 (and hence to below the solubility limit, where concentrations are better controlled) [60]. We confirmed that switching the medium from buffered (as in all other experiments in this study) to unbuffered water did not substantially affect brain dynamics, by conducting control experiments in which worms were subjected to switches between the two media (Figure S4.10).

We first applied exogenous serotonin at a concentration of 5 mM, which has been reported to immobilise nearly all worms in a population within 20 min [60]. At the molecular level, immobilisation of worms by exogenous serotonin has been shown to be mediated primarily by two serotonin receptors, SER-4 and MOD-1 [60], but the neural dynamics that lead to immobilisation remain unknown. Whereas MOD-1 is expressed in muscles and motor neurons directly controlling locomotion, SER-4 is expressed in interneurons that affect locomotion in a more indirect way [60]. Thus, serotonin-induced immobilisation could occur due to functional perturbations at the level of downstream motor actuations, upstream interneuron dynamics, or both. In the first 15 min of the recording prior to exogenous serotonin exposure, global brain dynamics were qualitatively similar to those of unstimulated worms in buffer, with a single mode dominating the neuronal dynamics (Figure 4.8A, S4.4). Strikingly, the addition of 5 mM serotonin drastically attenuated the dynamics of all collective modes within one minute, switching brain-wide activity into a quiescent state. Thus, high concentrations of exogenous serotonin can largely shut down brain activity, raising the possibility that the immobilisation observed in behavior-level experiments [60] could be due, at least at high concentrations, to such a brain-wide quiescence of neuronal activity, rather than paralysis at the level of motor function alone.

The brain-wide quiescence in neuronal activity observed here is reminiscent of those recently observed in worms during episodes of behavioural quiescence occurring at developmental lethargus [22] and under long periods of starvation [23]. In addition to satisfying a number of defining criteria for sleep, such as homeostasis, increased threshold for arousal, and rapid reversibility, a characteristic feature of these quiescent states at the neuronal level is that a small number of neurons (most notably RIS, which has been implicated as a sleep-inducting neuron [61], but also RMED/V and others) demonstrate persistent activity while in nearly all others the activity rapidly drops to and remains near zero [22, 23]. In the serotonin-induced brain-wide quiescence observed in our experiments, we did not find high levels of persistent activity in any neuron, but a handful of neurons exhibited episodes of activity (Figure S4.8).

One of the defining features of sleep is rapid reversibility [62] — by contrast to recovery from coma or anesthesia, animals return rapidly to wakefulness from sleep [63]. The dynamics of entry into and recovery from brain-wide quiescence can be compactly represented by the principal PCA mode (Mode 1; Figure 4.8A, blue curve), which captures the most variance in brain-wide activity. A comparison of Mode 1 dynamics across replicate experiments on different individuals ($N = 7$) revealed that 5 mM serotonin reproducibly induces brain-wide quiescence, albeit with brief bursts of dynamic activity during serotonin exposure in a subset (3/7) of experiments (Figure 4.8B). Upon removal of serotonin, Mode 1 activity recovered within minutes in nearly all (6/7) experiments. Thus, serotonin-induced brain-wide quiescence is clearly reversible on a short timescale.

To quantify the degree to which serotonin-induced quiescence is reversible at the level of neuronal activity, we binarized the Mode1 time series by thresholding the absolute mode time series $|M1|$ and computed the average Mode 1 activity, as the fraction of time the mode time series was in the high (i.e. above-threshold) state. The choice of the threshold h was motivated by the observation that the $|M1|$ was well-fit by a bi-exponential function $P = ce^{-b_1 x} + (1-c)e^{-b_2 x}$ (Figure 4.8C), and h was set to the value for the argument x at which the two exponential terms have equal probability $h = (\log(1-c) - \log c)/(b_2 - b_1)$. The average Mode 1 activity after removal of 5 mM serotonin was equivalent to that before the stimulus (Figure 4.8D). Thus, recovery of neuronal activity upon serotonin removal was not only fast, but also complete with respect to the amplitude of dynamics

At the level of Gurel et al. found that serotonin-induced immobilisation of worms is dose-dependent, with concentrations lower than 5 mM of exogenous serotonin leading to immobilisation of only a fraction of the population [60]. To test the effect of lower serotonin concentrations on collective brain dynamics, we measured whole-brain dynamics before, during, and after exposure to 0.5 mM and 1.5 mM serotonin (Figure S4.9). For both of these lower concentrations, we did not observe the rapid and drastic shift to quiescence observed upon addition of 5 mM serotonin. In a subset of experiments, sharp changes in activity patterns did occur near the times of serotonin addition or removal, but considering the substantial temporal and trial-to-trial variability in the unstimulated dynamics (Fig. S4.4), a considerably larger number of measurements would be required to determine whether and to what extent global brain dynamics are perturbed by exogenous serotonin at these lower concentrations.

In summary, these experiments demonstrated that a high concentration (5 mM) of exogenously applied serotonin can reversibly induce a global quiescent state in the *C. elegans* brain. The similarity of this quiescent state to those observed during sleep-like states during lethargus [22] and under prolonged starvation [23] 2018) raises the intriguing possibility that the well-documented inhibition of locomotion by exogenous serotonin [59, 60] could be due, at least at very high concentrations, be mediated by a sleep-like quiescent state of the brain.

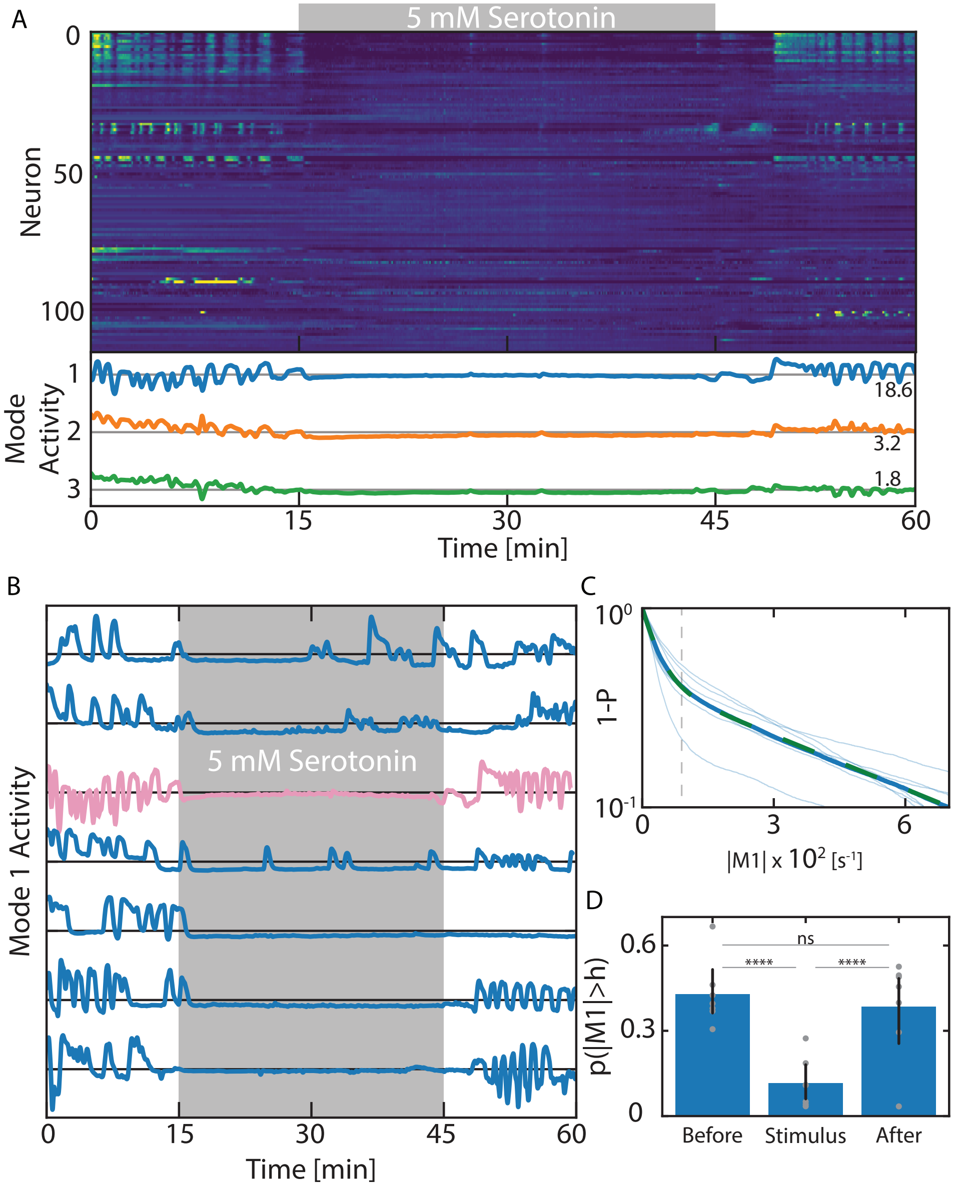

Figure 4.8: Caption on the next page.

Figure 4.8: **Exogenous addition of** 5 mM **induces a sleep-like brain state characterized by strong and reversible global quiescence.** (A) The individual neuronal dynamics (top) and activity of the top 3 PCA modes (bottom) of an exemplary measurement. The shaded region indicates the duration of the 5 mM serotonin stimulus. The number on the bottom right indicates the effective number of contributing neurons to the respective mode (see methods). (B) The activity of the first PCA mode for different worms. The activity of the principal mode extracted from the measurement represented in panel A is shown in pink. (C) The cumulative probability function of the absolute mode 1 time series ($|M1|$) across measurements (blue, solid) can be approximated by a bi-exponential (green, dashed). The gray dashed line represents the crossover value h where both distributions have equal probability. The fit is performed using the least-squares method. (D) A Significant change in activity is observed upon addition of serotonin, which largely recovers after removal. The fraction of time before, during, and after the stimulus that the mode activity exceeds the threshold h (individual measurements in gray). Statistical tests are performed by bootstrapping for measurements.

4.3. DISCUSSION

Whole-brain imaging is a powerful method to study neural dynamics beyond the circuit level, and its relation to sensory stimuli and behavioural outputs. We recorded brain dynamics on semi-immobilized worms, which allowed us to directly relate global brain dynamics to a behavioural output in the form of a stretch mode of anatomical deformations. Our use of wide-field deconvolution microscopy enabled light-efficient volumetric imaging, which was necessary to achieve measurement times exceeding one hour. The long duration of recordings in turn enabled the statistical characterization of responses to stimuli on a single-worm basis, by sampling the highly variable collective neural dynamics across many repeated stimulations. This statistical power at the single-worm level is particularly important, given the substantial worm-to-worm variation in both resting-state and response dynamics of neural activity [9, 12, 18]. We demonstrated the power of our approach by conducting experiments that addressed three compelling hypotheses regarding the role of collective neural activity. While these exploratory experiments do not amount to conclusive tests of each hypothesis, our results yielded positive evidence in support of each, and indicate a path towards more comprehensive tests in future whole-brain imaging studies. We discuss below our results in the context of each of these hypotheses, together with possible avenues for further improving our experimental approach.

4.3.1. THE COLLECTIVE MOTOR-COMMAND HYPOTHESIS: HOW BRAIN DYNAMICS DRIVE BEHAVIOUR

The semi-immobilized configuration of our whole-brain imaging setup provided an opportunity to directly test the hypothesis, advanced by Kato. et al. [18], that collective modes of neural activity (such as those identifiable by PCA analysis) serve as motor commands driving specific components of motile behavior. Whereas that hypothesis was developed by analysis of whole-brain imaging data acquired in paralysed worms, a subsequent study that applied whole-brain imaging to freely moving worms [50] found that PCA modes performed poorly in predicting behavioural dynamics that were recorded simultaneously. However, the control experiments in freely-moving worms expressing GFP instead of GCaMP indicated a non-negligible contribution of motion/segmentation artefacts to the whole-brain activity recordings [25]. Thus, whether and to what extent the dynamics of PCA modes first identified in paralysed worms can be interpreted as motor commands remains an open question. Within our microfluidic device, worms are confined within a narrow channel but are still able to make stretch-shrink deformations of their anatomy along the direction of the channel, which is readily quantifiable as a one-dimensional behavioural output, with negligible contributions from motion artefacts. Thus, our approach provides a middle ground between whole-brain imaging in paralysed (or fully immobilized) animals and freely moving animals.

We found that a large fraction of the variance in neural activity was captured by the top three PCA modes, and these modes demonstrated very similar dynamics to the top three PCA modes of paralysed or immobilised worms in previous studies [18, 25]. Kato. et al. had concluded from their analysis of paralyzed-worm data that forward-reverse locomotor behaviour is encoded predominantly by the principal mode of neural activity, and turning behaviour by the second and third PCA modes [18]. By simultaneously measuring the stretch-shrink motion of the head region and whole-brain neuronal dynamics, we have provided direct evidence for a strong relationship between the principal PCA mode and anatomical movement. It is plausible that the stretching behaviour is related to attempted forward/reverse locomotion, which is precluded by the worm's confinement within the channel. The strong relationship between the PCA modes and behaviour on semi-immobilized worms is in contrast with measurements on freely moving worms by Hallinen et al., who found that the top modes encode relatively little information about the velocity and curvature of locomotion [25]. Hallinen et al. reported that the top PCA mode predicted the velocity only about as well as the best single neuron, and is outperformed by the result of a sparse-linear-model [25]. This is not inconsistent with our measurements, as we noted that, although the top mode in our measurements is the most strongly correlated mode, it doesn't fully predict the stretch; especially rapid fluctuations in stretch, in the order of seconds, are not necessarily encoded by the principal mode. Also in our measurements, the top mode is correlated with the stretch with similar magnitude as the top correlated single neuron. The resulting discrepancy in absolute predictive value could be partially the result of differences in the processing of data (we low-pass filter data using SG-filtering), or as a result of confinement.

This raises the question to what extent the observed neuronal dynamics are affected due to confinement or other persistent environmental factors or stressors, including the expression of fluorophores. Indeed, the timescales of fluctuations in the principal PCA mode of our measurements are considerably faster than the forward/reverse switching timescales during roaming behaviour of a freely moving worm, which is characterised by long periods of forward motion, occasionally interrupted by a short reversal and/or a sharp turn [4, 64]. Interruption of the forward state could in principle be caused by unintended sensory inputs in our experiments, such as the blue light [65, 66] used for fluorescence excitation, or touch sensations [67] triggered by the microfluidic confinement. Blue light, however, is probably not the main driver of the rapid oscillatory dynamics of the principal mode, as this was also observed in the light-insensitive *lite-1* mutant AML70. Confinement and immobilisation have been shown to strongly affect brain dynamics. Scholz. et al. reported a slowdown in dynamics upon immobilisation [50]. Kaplan. et al. have shown that slowing of neural dynamics occurs upon immobilisation and especially affects neurons responding with fast timescales: for instance, the SMD neuron fluctuations are reduced an order of magnitude [68]. This might be related to the body's inability to propagate dorso-ventral waves, as in the study of Kaplan et al., peaks in SMDD/V dynamics are strongly related to the phase of the head [68]. The slowing down of brain dynamics is thus a potential drawback of our measurement design, as it means fewer statistics of the dynamics can be collected within a measurement of a given duration. This however is compensated by performing long-timescale measurements.

Confining *C. elegans* worms in a microfluidic device has been shown to induce sleep-like quiescence at the level of both anatomical movement and neural activity [52]. Indeed, within our semi-immobilized measurement configuration, we observe recurrent epochs of brain quiescence paired with reduction of anatomical movement. These sleep states are clearly a nuisance for stimulus-response experiments, for which a consistent 'unstimulated baseline' of brain activity is desired. We therefore opted to conduct our stimulus-response measurements on paralyzed worms, which exhibit little or no microfluidic induced sleep [52].

4.3.2. THE APPARENT STOCHASTICITY HYPOTHESIS: HOW BRAIN DYNAMICS RESPOND TO SENSORY STIMULI

Based on experiments that monitored the activity of a small number of neurons within an olfactory circuit, it has been suggested [12] that variable responses in neural activity, and hence also behavior, can be generated by the interplay between sensory inputs and 'network states', i.e. the activity pattern of other neurons of the same circuit. On the other hand, the discovery that brain-wide neural activity is highly correlated and dynamic even in the unstimulated state [18, 25] raises the question of whether these correlated modes of neural dynamics could represent network states that interact with sensory inputs to generate variability in the behavioural output of the brain. Indeed, if such collective modes of brain-wide activity themselves have a tendency to respond stochastically to sensory stimuli, it is plausible that the individual neurons that contribute to the modes also respond with apparent stochasticity, as was observed in the circuit-level experiments of Gordus et al. [12]. Our results from experiments with both SDS and salt stimuli support this view, as the top two PCA modes of neural activity responded significantly, but with a high degree of apparent stochasticity.

Although worms were paralysed in our stimulus response experiments, it is possible to interpret the responses we observed of brain-wide activity to SDS within a fictive behaviour paradigm along the lines of Kato. et. al. [18], who assigned various 'lobes' of the neural activity trajectories in the space of the top three PCA modes to various behaviours such as forward runs, reversals, and turns. More specifically, we may conjecture that the SDS stimulus triggers within the brain a sequence of motor commands to perform the escape response, which is triggered by the same stimulus in freely moving worms. The dynamics of the PCA modes during the SDS experiments were similar to those in unstimulated experiments both by us (Figure 4.3) and Kato. et. al. [18], with the top two PCA modes demonstrating oscillatory dynamics whose waveforms and phase relationships are readily visualized as phase-space trajectories with a characteristic topology (Figure S4.7). In response to SDS, we found that mode 1 rose immediately upon stimulation, which was subsequently followed by an increase of mode 2 paired with a decrease of mode 1. Thus, if we apply the interpretation of Kato. et. al. [18] that mode 1 is associated with Fwd/Rev motion and mode 2 is associated with ventral turns, we can interpret the observed pattern in the mode 1-mode 2 cycle of brain activity, as motor commands for a reversal followed by a ventral turn and a return to forward crawling: the characteristic behavioural sequence of the escape response [3]. Although, as discussed just above, the temporal sequence of SDS responses in the top PCA modes can be consistent with an attempted escape response, the high degree of stochasticity in the timing and amplitude of these responses is in contrast to the highly stereotyped escape behavioural sequences exhibited by freely moving worms upon encountering SDS [30]. It is plausible that the stronger apparent stochasticity of the brain SDS response we observed could in our experiments result from unintended sensory inputs resulting from our experimental configuration, e.g. confinement within the microchannel, that are being integrated with the applied SDS signal within the worm brain [69].

The behavioural response of freely moving worms on salt gradients is described to be stochastic modulation of reversals and turns [34, 35]. A modulation of the top modes observed is to be expected. However, the modulation that we observed at the level of the collective modes is much weaker compared to SDS, with only a small fraction of worms significantly responding, and not stereotypically. One possibility could be that the salt stimulus is relatively weak and therefore almost completely overwritten by other inputs. Further experiments could characterize the collective neuronal response to various concentrations to investigate if this can result in a stronger modulation of the brain-wide dynamics. Another possibility is that salt and SDS are processed by different circuits with different relations to the global modes. Such a possibility is partially supported by recent studies investigating the *C. elegans* connectome, which have shown that the circuitry involved in avoidance (SDS) and taxis (salt) appear in different clusters that are spatially separated [70, 71].

In both the SDS- and salt-response experiments, whereas some individual neurons responded nearly deterministically, the collective dynamics of neurons (most notably the principal PCA mode) responded with a higher degree of apparent stochasticity. The individual neurons responding stereotypically were diverse in their response timing and waveform, suggesting that these may perform different computations on the sensory input signals. In the salt experiments, neurons were identified with response waveforms indicative of a differentiator, reminiscent to the sensory ASE neuron pair [10], or that of an integrator. Further investigation of the sensory circuitry would benefit from identifying the specific cell type of these neurons exhibiting response waveforms indicative of various analogue computations. In the SDS experiments, deterministically responding neurons were somewhat less diverse in their waveforms, but they exhibited a distinct hierarchy in response timing, which might be interpreted as a sequence of signaling events within a circuit. However, it should be noted that the temporal hierarchy obtained from our calcium activity measurements might not exactly reflect the order in which neurons respond, because our GCaMP reporter expression is localised to the nucleus. It has been shown that for some neurons, this can result in a slower rise of calcium signals by up to 10 seconds [12], as signals can be compartmentalised outside the nucleus [72, 73]. This could partially explain the temporal hierarchy obtained from SDS measurements. However, Gordus et al. reported that compartmentalization of neuronal signalling in the 3 exemplary neurons measured in that study did not shift the onset of change in activity [12], which is also visibly different in our measurements. We therefore believe that some of the dynamics reflect true temporal differences in signaling.

4.3.3. THE NEUROMODULATED BRAIN-STATES HYPOTHESIS: SLEEP-LIKE REVERSIBLE QUIESCENCE INDUCED BY EXOGENOUS SEROTONIN

Neuromodulation is an important but understudied aspect of behavioural regulation [74]. Although most studies of neuromodulation to date have focused on effects at the circuit level [75, 76], it has recently been hypothesised that neuromodulators might trigger switches between global brain states — persistent epochs of brain-wide neural activity that affect organism-scale behaviour [47, 48]. Our experiments with exogenously applied serotonin provided a test for this hypothesis with respect to a recently identified brain state in *C. elegans* - a sleep-like quiescent state that was discovered by whole-brain imaging during developmental lethargus upon oxygen stimulation [22]. Specifically, we asked whether the application of exogenous serotonin, which is known to trigger sleep-like quiescence at the level of motile behaviour [60], might trigger brain activity patterns similar to those found during sleep-like quiescence during developmental lethargus [22].

Serotonin signalling is reported to be mediated primarily by the receptor MOD-1, expressed in muscles and motor neurons directly controlling locomotion, and SER-4 is expressed in interneurons that affect locomotion in a more indirect way [60]. Previous studies showed that the addition of 5 mM exogenous serotonin to freely moving worms results in a large fraction of the population exhibiting behavioural quiescence, which was described as ’paralysis’ [60]. Our experiments demonstrated that the same stimulus causes a dramatic decrease of brain activity, largely shutting down the dynamics of collective modes with just brief bursts of activity. This dramatic change in brain activity upon serotonin stimulation suggests that the previously reported immobilisation of freely moving worms may not merely reflect effects of MOD-1 signalling, but might also involve SER-4. The dramatic decrease in brain activity is strongly reminiscent of the oxygen-induced sleep states reported during lethargus or starvation [22, 23], and confinement-induced sleep in microfluidic channels of unparalyzed worms [52]. Further research should be conducted to confirm whether this is indeed a sleep state, which should meet the conditions of a stereotypic posture, elevation of the arousal threshold, rebound effects upon deprivation, and reversibility [62]. Indeed, we found that brain dynamics recovered within minutes after the removal of serotonin, demonstrating reversibility. Future experiments could test changes in arousal thresholds by measuring responses to other chemical stimuli in the presence and absence of serotonin. To investigate the similarity of the serotonin-induced quiescence brain state we discovered with previously reported sleep-like brain states in *C. elegans*, future experiments should investigate activity levels of individual neurons that exhibited high levels of activity during the sleep states reported in other studies, such as RIS and RME in response to oxygen [23] or RIV, ALA associated with stress [52]. Of particular interest is the activity of the sleep promoting RIS neuron [61]. RIS is reported to express the serotonin receptor SER-4 [77] at an expression level higher than any other neuron [78]. It is therefore plausible that exogenous serotonin via SER-4, which triggers an excitatory calcium response in HEK293 cells [79], could increase RIS activity to trigger a sleep-like brain state. To our knowledge, serotonin has not previously been implicated in *C. elegans* sleep, but interestingly, a recent study found that serotonic raphe neurons are involved in the initiation and maintenance of sleep in both zebrafish and mice [80]. Thus, though highly speculative at this stage, our observation that exogenous serotonin can trigger a sleep-like brain state in *C. elegans* might indicate an evolutionarily conserved role for serotonin in the neuromodulatory control of sleep-like brain states.

These results demonstrate the strength of combining whole-brain imaging with microfluidic control of the chemical environment, which is not limited to sensory stimuli or neuromodulators as there are many other chemicals to which brain functionality can be studied when exogenously applied. For instance, there is potential to screen for and study the effects of drugs that affect the nervous system of *C. elegans* [81] (e.g. providing the anaesthetic isoflurane, which disrupts the neuronal coordination, abolishing the stereotypical global brain modes [27]), or the downstream effect on brain dynamics can be studied by silencing expression using RNAi [82]. Such tests could be performed efficiently without any additional genetic manipulation of the worm, although performing such tests with both wild-type and mutant animals could prove particularly powerful.

4.3.4. IMPROVING THE EXPERIMENTAL DESIGN

The results presented in this study are permitted by the choice of experimental design combining microfluidics to apply stimuli and confine the worm and widefield fluorescent microscopy with deconvolution. Modification of the setup, especially the microfluidic design, could facilitate follow-up experiments. Firstly, the microfluidic design could be altered to force the worm into a fixed orientation, for instance by using a curved loading channel [83]. This would decrease the variability across measurements in the subset of neurons that can be tracked. More importantly, a stereotypic orientation would facilitate the annotation of individual neurons. Annotation of individual neurons is complex, because neuronal positions can vary across worms [84], not all neurons are tracked, and the neurons in the head are densely packed. Recently, a strain has been constructed where each neuron has a different (but reproducible across worms) expression profile of 4 fluorophores, aiding the annotation [49]. Stimulus response recordings in this study have been performed using this strain (OH15500), but could not yet be annotated due to a misalignment with the reference maps. Annotation of neurons could tremendously benefit the interpretation of neuronal recordings, as many individual neurons have been extensively studied. In addition, annotation would allow to compare dynamics of global modes, recently applied by Linderman. et al. [85], or individual neurons across worms. Multiple measurements can also be combined to study weakly responding modules (such as the main mode to salt) to stimuli.

Secondly, more neurons could be tracked, and a higher signal-to-noise ratio could be achieved by minimising refraction at the interfaces of the worm, medium, and PDMS device. This would provide a more complete picture of the processing circuits. Neuronal signals nearby the PDMS interface show visible distortion and decreasing contrast for deeper laying tissues (i.e. tissues imaged through a longer optical pathway). These distortions also increase the difficulty of neuronal annotations, as the colour balance is dependent on the position. Refraction interface differences can be minimised by either changing the refractive index of the medium [86], but especially, by changing the material of the microfluidic device [87].

Thirdly, a larger microfluidic device permitting dorso-ventral body waves would allow to study the global modes in the context of more complex behaviours.

Moreover, this could decrease the rate microfluidic induced sleep [52] stress on the worm and increase the frequency of dynamics. However, it would require a more complex imaging system to track the head with a higher volumetric acquisition rate. Finally, a microfluidic design allowing multiple fluid inputs could be used to study the whole-brain response to multiple combinations of stimuli in a single experiment. For instance, sensory stimulation in combination with serotonin could be performed to investigate whether the brain's quiescent state is a sleep state. Multiple inputs can also be used to study the strength of the global response to different salt or SDS concentrations.

A more complete description of the sensory processing could be obtained by constructing strains with a more homogenous expression of fluorophores across neurons. Variability in expression levels results in the fact that some neurons cannot be tracked, especially when in close proximity to bright neurons. We noticed that this included some sensory neurons, including some that responded stereotypically to the stimulus. Alternatively, contrast could be enhanced by changing the optical setup, although this would increase its complexity. Light sheet microscopy doesn't require imaging the entire volume to obtain a single brain slice [88, 89] and has recently been proven to work with neuronal imaging *C. elegans* [24, 27]. In a different approach, the use of two-photon volumetric imaging could provide higher contrast and allow capturing neurons with larger optical path lengths [90]. Finally, the extraction of neuronal signals could be performed with improved algorithms. Recently, a method has been developed to extract up to 189 neuronal signals from semi-immobilized animals and normalise neuronal data to compare time series across worms [91].

ACKNOWLEDGEMENTS

This research could not be conducted without Marko Kamp who has helped assembling and maintaining the optical setup. We want to thank Bas van der Hoeven for his help with experiments. Furthermore we would like to thank Greg Stephens and Antonio Carlos Costa for their discussions. This work was carried out on the Dutch national e-infrastructure with the support of SURF Cooperative.

4.4. METHODS

An experimental setup and data analysis pipeline have been developed to measure global brain dynamics within semi-immobilized worms with fast microfluidic control of the chemical environment. This section explains the details of the measurements and processing. Section 4.4.1 describes the widefield imaging setup, which enables long-timescale measurements within the finite photon budget. Section 4.4.2 describes the microfluidic setup that achieves semi-immobilization of the worm with fast switching between buffer and stimulus media. To generate neuronal activity time series from the imaging data of a deforming brain, a succession of steps need to be performed, including image deconvolution, segmentation, tracking, and post-processing, which are discussed in section 4.4.3. Finally, further details of the experimental protocols and *C. elegans* strains used for measurements are given in sections 4.4.4 and 4.4.5 respectively.

4.4.1. ACQUISITION OF 3D FLUORESCENCE MOVIES BY WIDE-FIELD DECONVOLUTION IMAGING

Our objective of carrying out stimulus-response measurements on the global brain dynamics of semi-immobilized worms placed a number of demands on the measurement system: (1) Fast volumetric fluorescence imaging — the entire head region of the worm, spanning 111x222x43 microns and comprising approximately 200 neurons, is needed at subsecond time resolution to fully capture the GCaMP ($[Ca^{2+}]$) dynamics. (2) Efficient use of the limited photon budget — to enable long time-scale measurements across many repetitions of chemical stimuli (3) Simultaneous two-color imaging — with one fluorophore used for tracking and segmentation of neurons and another to read out neuronal $[Ca^{2+}]$ activity.

Different imaging techniques can and have been used to image the fluorescence of a brain volume to in order extract brain dynamics of *C. elegans.* Most fast volumetric imaging techniques rely on rapid acquisition of single planes through the sample. The exception is light field microscopy, where the 3D volume can be reconstructed by imaging a matrix of small lenses [92] to record brain dynamics [17] or organism behaviour [21].

The most used imaging method in recent literature using global brain imaging in *C. elegans* is fast multi-point confocal imaging using a spinning disc [18–21]. By quickly sweeping a lattice of pinholes, this technique has the advantage of confocal microscopy, where rejecting out-of-focus light results in high-contrast images without sacrificing acquisition speed. The main drawback however is that the sample is illuminated every slice, and since a brain volume requires ≈ 30 slices, $1 - 1/30 \approx 97\%$ of the emitted light is rejected for the image acquisition, resulting in bleaching. Similarly, fast structured illumination microscopes setups can be built using microlens arrays [93]. (In fact, we tested such a system for our experiments but ultimately opted against its use for worm-brain imaging as it suffered from, in addition to the photon-budget inefficiency noted above, striping artefacts due to inhomogeneous illumination of the sample.) Other imaging methods rely on exciting fluorophores exclusively within the sample focal plane and therefore efficiently use the fluorophore photon budget. Two-photon imaging techniques exploit the inherent nonlinearity of multiphoton excitation to only obtain light from the focal plane and have been used to visualise the worm's brain dynamics [16]. However, two-photon excitation requires relatively costly pulsed lasers, and achieving imaging speeds sufficient for whole-brain imaging requires rather involved setups such as spinning disk [94] or temporal focusing [16]. Light sheet microscopy is another option that has been applied to study brain dynamics in zebrafish [88], and recently also in *C. elegans* [24, 27]. Here, the illumination pathway is separated and enters the sample under a different plane using spherical lenses. Systems have been developed relying on only a single objective for both illumination and imaging [89], that can be used on *C. elegans* [24].

Arguably the simplest method to image the brain of the worm in terms of the complexity of the optical setup is widefield fluorescence microscopy, where most of the fluorescent light is captured by the camera, including out-of-focus light. Although the out-of-focus light contributes significant background to each acquired planar image, in theory a true image of the sample can be reconstructed from a series of such images acquired at multiple image planes (z-stacks) if the point-spread function (PSF) of the system is known (see section 4.4.3). This method has been successfully applied in *C. elegans* whole-brain imaging to study the asymmetric AWC neurons [21] and allows long time-scale measurements of brain dynamics, because the out-of-focus light, which constitutes the majority of captured photons, is used for the reconstruction of the true image. Because of its simplicity and cost effectiveness, wide-field imaging was chosen for this study.

Our optical setup for wide-field microscopy is comparatively straightforward (Figure 4.9). Lasers with a wavelength of 405, 488, 561 and 640 nm are coupled to an acousto-optic tunable filter (AOTFnC-400.650-TN, AA OPTO-ELECTORNIC, Orsay, France) to rapidly switch between laser lines. The laser light is subsequently expanded before it enters the Nikon TI-Eclipse inverted microscope equipped with a 60x 1.2NA water immersion objective (Nikon CFI Plan Apochromat VC 60XC WI) and a multiband excitation filter (ZT405/488/561/640x, Chroma Technology Corporation, Bellows Falls, USA). A piezoelectric Z-stage (Nano-Z200, Mad City Labs Inc., Kloten, Switzerland) is used to move the sample to image different planes in the worm. The captured fluorescent light is reflected by a multiband dichroic mirror (ZT405/488/561/640rpc, Chroma Technology Corporation, Bellows Falls, USA), filtered by a multiband emission filter (ZT405/488/561/640m, Chroma Technology Corporation, Bellows Falls, USA) and exits the microscope. An image splitter (Optosplit II LS image splitter, Cairn-Research Inc., Faversham, UK) splits the emission light using a second dichroic mirror at a wavelength of 565 nm (t565lpxr, Chroma Technology Corporation, Bellows Falls, USA). This allows to measure two fluorophores simultaneously; a constitutive expressed red fluorophore to track neurons and a calcium sensitive fluorophore that is a proxy for the neuronal activity. Light is captured by the camera (OrcaFlash 4.0 V2/V3, Hamamatsu, Hamamatsu City, Japan) using 4 × 4 binning, such that the length of a pixel represents 433 nm of the sample. Binning (4x4, such that one pixel corresponds to 433 nm on the sample) is used to increase the S/N ratio and reduce the amount of data. The readout time of the camera and the stabilization time of the z-stage are both 10 ms, thus the maximum recording frequency is 1/(10 ms+exposure time) < 100 Hz. An illumination time of 5 ms is chosen, hence the acquisition frequency is ≈ 67 Hz.

Volumetric images are acquired by creating ≈ 27-33 slices spaced at ≈ 1.3 μm, bringing the volumetric rate at ≈ 2.0-2.5 Hz. The z-position of the stage follows a triangular waveform in time during volumetric image acquisition, meaning that successive volume image stacks are obtained in reverse vertical order to ensure a continuous flow of images at high vertical precision. A custom written software package is used to control the optical setup, designed to automatically execute protocols required for measurements (e.g. making a single stack with each laser for NeuroPAL strains). This software package produces two files: (1) a text file containing metadata and the acquisition time of each frame and (2) a binary file with the raw image data.

4.4.2. MICROFLUIDIC CONTROL OF STIMULUS TIME SERIES

Stimulus-response measurements have been performed on worms using a device following the design by Chronis et al. [28] (Figure 4.10A). This microfluidic design provides two key features necessary for our experiments: (1) semi-immobilisation of the worm, meaning that worms are sufficiently confined to ensure head-region neurons remain within the microscope field of view without the need of paralytic drugs or stage movements to track a crawling worm, and (2) precisely controlled delivery of chemical stimuli with subsecond accuracy. The device possesses four inlets (I-IV) for fluid flow at the top, one inlet for the worm (V) in the middle, and an outlet at the bottom(VI). The geometry of the confining chamber (between inlet V and one of the two main flow channels) is such that when loaded into the chamber, the worm's nose protrudes slightly outward into the flow channel. Channels I-II are connected to a reservoir containing a medium with stimulus, and channels III-IV to a reservoir containing a buffer medium. To stimulate the worm, the pressure of channel IV relative to that of I-III is decreased (Figure 4.10B,

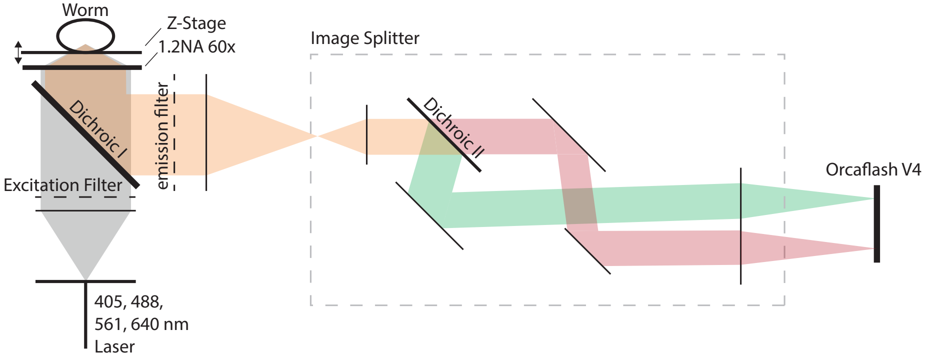

Figure 4.9: **Optical configuration of for widefield volumetric fluorescence imaging.** A schematic view of the widefield optical setup used to record brain dynamics. Laser light is expanded, filtered and focused onto the worm. Fluorescent light is reflected and filtered by dichroic I and the emission filter. The fluorescent light enters the image splitter, which splits the red and green fluorescent light using dichroic II and subsequently focuses two images, one for the red channel and one for the green channel, onto two different halves of the camera (Orcaflash V4) sensor.

right). To return to the unstimulated state, channel I requires a lower pressure than channels II-IV (Figure 4.10B, left). We found that setting the low pressure to 25 mbar and the high pressure to 50 mbar results in robust switching between the two fluids. This is a slightly different method to control the fluid flow compared to Chronis et al., where a negative pressure is applied at the bottom and fluid flow to either channel I or IV is blocked.

Reservoir pressures are controlled as described by Gómez-Sjöberg [95]. The pressures are modulated using Feste solenoid valves, controlled by a programmable controller (model 787-712, WAGO inc., Minden, Germany) connected to the same system controlling the imaging setup. Software written in Matlab is used to execute stimulation protocols and save the valve states as well as the timings of the pressure changes in a text file.

To characterise the response of the device, the fluorescence was recorded in the microfluidic device at a frequency of 20 Hz, while repeatedly changing between a stimulus and a fluorescent dye every second (Figure 4.10C). To characterise the fluorescent response, we correlated the derivative of the stimulus (a pulse train with alternative positive and negative pulses) with the derivative of the intensity (Figure 4.10D). This reveals that the response peak responds with a time delay less than a single frame (50 ms). More importantly, the FWHM of the response is just 109 ms (computed using linear interpolation), or approximately 1/4 of the volumetric acquisition interval. We therefore conclude that, for the purposes of this experiment, the medium change is essentially instantaneous with the change in pressures.

A few minor modifications are made to the design of Chronis et al. Four variant designs have been created with different widths of the confinement channel, with sizes of 61, 65, 68 & 72 µm, to ensure that worms of different sizes fit the devices. A variant is created with a height of 28 and 43 µm. The larger device results in a smaller deformation of the worm's head, but requires more z-slices to acquire a volumetric image and performs worse at segmenting neurons as the optical path length is increased.

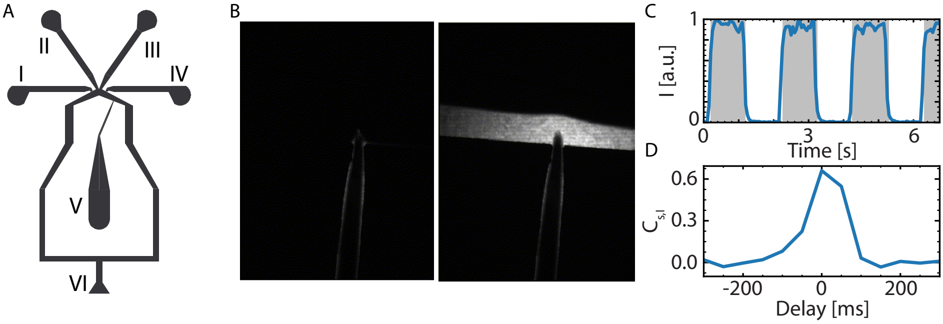

Figure 4.10: **A microfluidic chip is used to apply controlled stimuli.** (A) Schematic view of the microfluidic device used to apply stimuli [28], where channels I-IV are the chemical inlets, V is the worm inlet, and VI the waste outlet. Flows from inlets I-IV diverge at the central junction into two flow channels (left and right) that converge just before the outlet VI at the bottom. The confinement chamber of the worm connects inlet V and the right flow channel, and is narrow enough to preclude lateral movement of the worm. (B) Representative images from a control measurement in which the flow was switched between buffer (left) and buffer with fluorescent dye (right). Note the visible protrusion of the confined worm's nose into the flow channel. (C) The fluorescence intensity of the medium (blue curve) at the position of the head while switching between buffer (white background) and buffer with fluorescent dye (shaded background). (D) Cross correlation of the derivative of the applied stimulus with the derivative of the fluorescence intensity at the nose detected no lag within the time resolution of the measurement.

4.4.3. IMAGE PROCESSING

A series of computational steps are required to obtain neuronal activity time series from raw image data. First, the wide-field images are deconvolved using the point-spread function of the imaging system, which attenuates out-of-focus contributions to improve contrast and minimise mixing of fluorescence signals between neighbouring neurons (section 4.4.3). Subsequently, neurons are segmented based on the (constitutive) red fluorescence signal that is used for neuron tracking (section 4.4.3). Tracking neurons across frames is required because the worm's body deforms over time. The implemented tracking algorithm is closely based on Nguyen et al. [53], but with a few adaptations optimised towards tracking of neurons in semi-immobilized worms within the confinement chamber of our microfluidic device (section 4.4.3). Additional post-processing steps performed on the time series obtained from segmented neurons are described in section 4.4.3.

This sequence of computations is implemented in a suite of programs and scripts that requires relatively little user input but many computational hours (in the order of ≈ 3500 core hours for a 1 hour measurement, but variable depending on movement of the worm and sensitivity threshold for segmentation) to extract from each experiment the ensemble of neuronal time series. A more detailed description of the implemented analysis pipeline is given below.

PSF ESTIMATION AND DECONVOLUTION

Widefield imaging does not reject out-of-focus light from fluorophores above and below the sample plane. Consequently, image contrast is low, and the signals of nearby neurons can be mixed. This mixing depends on the point spread function (PSF) of the imaging system [96]. For any optical measurement, the measured 3D image $I(x)$ at position x is a convolution of the true fluorescence image $A(x)$ with the PSF $P(x)$, with noise $N(x)$ (e.g. shot noise, thermal noise),

$$I(x) = A(x) \circledast P(x) + N(x). \tag{4.1}$$

Thus, an improved estimate of the true image $A(x)$ can be obtained given $I(x)$, an estimate of $P(x)$, and a deconvolution scheme that appropriately regulates the noise.

The PSF of the system can be either measured using subdiffraction-size fluorescent beads, theoretically calculated, or reconstructed from a measurement using blind deconvolution. Fluorescent light is not only distorted by the optical system, but also by the sample itself, which means that the PSF is also dependent on the sample. Computing the theoretical PSF does not take into account aberrations from the imaging system or sample refraction and absorption. Measuring the PSF using small beads does take system aberrations into account, however it is not trivial because the signal-to-noise ratio of a measured bead is small and sample distortions are still not taken into account. We thus chose to estimate the PSF via the blind deconvolution approach, using a commercially available algorithm

(AutoQuant X3, Media Cybernetics inc., Rockville, USA). In this code, the original image and PSF can be estimated in a single iterative scheme, given a z-stack of images sampled at sufficiently high z-resolution. We run this code on data from a control measurement on an exemplary worm expressing the same fluorescent proteins in a microfluidic device, sampled with a z-resolution of 250 – 350 nm. For light captured from each fluorophore, this process is repeated 10 times, and the average PSF obtained is computed. The estimated PSF is downsampled to match the z-resolution of our 3D volumetric experiments to deconvolve z-stacks for all neuronal recordings of worms expressing the same fluorophores.

We choose to use the iterative Richardson-Lucy deconvolution scheme [97] to reconstruct the true fluorescence image without excessively amplifying noise. This iterative scheme to update the approximated true fluorescent image A each subsequent iteration $k+1$ can be derived using maximum likelihood optimization, when the measured image I is assumed to have Poisson noise, and is given by

$$A^{k+1} = A^{k} \times \mathscr{F}^{-1}\left[\mathscr{F}\left[\frac{I}{o^{k} \circledast \mathrm{P}}\right] \times \mathrm{OTF}^{*}\right], \tag{4.2}$$

where $\mathscr{F}$ is the Fourier transform operator, OTF^{*} $(=\mathscr{F}\,[P]^{*})$ is the complex conjugate optical transfer function, and $\circledast$ the convolution operator. We implemented this scheme in Python and integrated it into the processing pipeline. A key parameter is the number of iterations, where too few iterations will result in a poorly reconstructed image, and too many iterations will increase noise and waste computing power. By manual inspection, we have set the number of iterations at 75.

Neuronal segmentation

The red channel images the constitutively expressed fluorophore localised in the nucleus of each neuron, and is used for segmentation. This process can be subdivided into two steps: (1) separation of the foreground and background pixels, and (2) segmentation of the individual neurons. To separate foreground from background, the deconvolved image is first blurred to remove high frequency components and low pass filtered to remove background light, using a fourth order Butterworth filter with a cutoff distance at 2.5 µm and 20 × 20 × 5 µm (the last dimension being the along the direction of the optical axis), respectively. Subsequently, the foreground of the image is separated from the noise background by a user-guided thresholding scheme, where the threshold is given as a fraction of a value obtained from Otsu-tresholding [98] of the maximum intensity projection. This threshold negotiates a tradeoff between segmentation accuracy (*i.e.* avoiding false-positive detection of noise, imaging artefacts, and cell/tissue autofluorescence) and sensitivity (*i.e.* avoiding false-negative misdetection of neurons of low

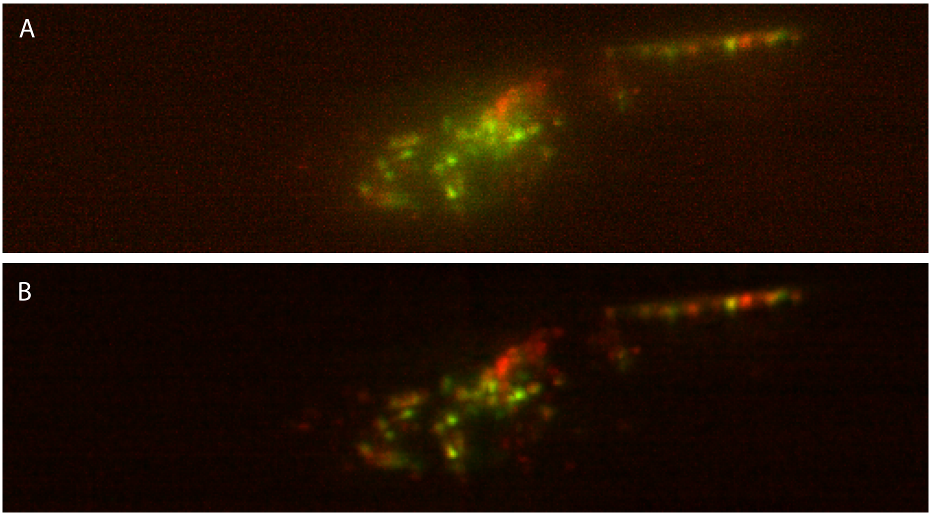

Figure 4.11: Representative images for the maximum intensity projection of the volumetric image frame (z-stack) of the head region of a worm expressing TagRFP (red) and GCaMP6s (green) (A) before and (B) after deconvolution using the PSF estimated in a separate control measurement (see text).

brightness). Two values of the Otsu-threshold fraction are provided by the user, a lower bound below which no pixel can be selected, and a higher bound above which all pixels are selected (usually about a factor of 1.5 apart). The ambiguous intensity values in between these thresholds are automatically determined using a random walker segmentation [99]. The random walker segmentation annotates pixels by solving a diffusion equation where the local diffusion coefficient is dependent on the local gradient. This reduces segmentation of small objects resulting from noise around the threshold value, but allows segmentation of neurons just above the noise threshold.

The foreground image requires a further segmentation step, as nearby neurons can be erroneously merged by the random-walker segmentation. Such undersegmentation can occur for nearby neurons in regions with high neuronal density (which includes most neurons in the head) when segmentation is performed based on local maxima in the intensity image [100]. Therefore, instead of using local maxima in the intensity, according to a method described by Toyoshima. et al. areas of concavity (points where the curvature of iso-intensity contour lines is in the direction of low intensity) are removed from the foreground image [100] and individual neurons are subsequently segmented based on the shape of the remaining volumes using a watershed segmentation. Individual neurons are segmented from this image using random walker segmentation on the distance transform (the minimum distance from each pixel to the boundary of the segmented area), where each local maximum is seeded as an individual neuron.

Due to the low signal-to-noise ratio and relatively large pixel size compared to the size of the nucleus, this typically results in over-segmentation of the image. Segmented neurons with centroids closer than 2.0 μm, or with a contact surface area of more than 40% are merged. Additionally objects with a volume $< 2\ \mu m^3$ are removed. After segmentation, the intensity values of the deconvolved red and green channels are extracted within a radius of 1.5 μm from the centroid of each segmented volume (including only pixels belonging to the segmented volume).

NEURONAL TRACKING

To generate the GCaMP intensity time series for each neuron, tracking of neurons across frames is required. This is a non-trivial task for a number of reasons. The number of segmented objects within each volumetric image frame is variable. Additionally, there is no true positive image to which each of the segmented frames can be compared. Comparing consecutive frames for tracking accumulates errors, which will likely happen with many thousands of volumes, each with a different subset of segmented objects. Manual inspection of each volume is unfeasible, since there are thousands of segmented volumes. Further, the worm can, even when confined, deform its body. Consequentially, the position of each neuron, also relative to its neighbours, can vary throughout the measurement.

We have adopted a method developed by Nguyen et al. [53], developed for neuronal tracking in freely moving worms. This algorithm is preferred over that of Tokunaga et al., who have developed a tracking method using KDE's [101], but it performs weakly if the subset of segmented neurons is variable across frames. For clarity, a brief description of the Nguyen et al. method is given here. We have adopted the core ideas of this method and written a python code, as the original code was provided in MATLAB, to integrate the tracking with the other steps of the image processing pipe line.

The key idea is that rather than comparing consecutive frames, it compares every frame to every other frame. To make this comparison computationally feasible, it selects a random subset of n frames as reference frames. It then maps all segmented points X_i from each frame i to those of each of the n reference frames by a point-set registration (PSR) algorithm. This mapping results in an n-dimensional registration vector for each point in X_i.

Registration vectors corresponding to the same neuron in different frames are expected to be similar. Thus, clustering the registration vectors of all neurons across all frames provides a means of tracking neuron identity across frames.

Our implementation adds some modifications to make it suitable for our experimental configuration (see below).

Point-Set Registration

Comparing and linking the points of two manifolds is called point-set registration (PSR). In this case, the coordinates of a set of segmented points X from a single frame is represented by a Gaussian Mixture given by (4.3) [53, 102]

$$g(\eta, X) = \sum_i A_i \exp(-\frac{|\eta - x_i|^2}{2\lambda^2}), \tag{4.3}$$

where A_i is the amplitude of each neuron, η the coordinate, x_i in X the position of a neuron, and λ a scaling parameter of the mixture. To compare a set S with a reference set R we need to find the transformation $u[S]$ that minimizes the function

$$E(u) = \int \left[g(\eta, u[S]) - g(\eta, R) \right] d\eta + E_{def}(u). \tag{4.4}$$

The minimization is now a trade-off where the deformation is rewarded when the point sets overlap, but penalised for the deformations themselves. The deformation penalty is for non-affine transformations. In Nguyen et al., point-set registration is performed after an initial worm straightening step before segmentation using a low-magnification dark field image, which roughly aligns the neurons and hence requires only relatively small deformations of the PSR manifold. In our experimental setup, we do not record the postural information of the worm, so no straightening step is applied and stronger deformations of the manifold are required, making the minimization problem in PSR more challenging (Figure 4.12A). However, additional information can be used to navigate the minimization problem. The worm can move but is constrained in the channel, and hence the brain mainly deforms along the head-tail axis of the worm. Therefore, deformations along this 'soft' direction are penalised less compared to the other two directions in which the neurons move less, i.e. the energy-penalty is *anisotropic*. An estimate of the relative contribution and direction of the anisotropic penalty is obtained from a principal component analysis of the variance of the spatial point distribution across time. This results in the direction of the most deformation as well as its relative contribution.

To illustrate how this modification aids in PSR, frames with different postures are compared (selected from the pool of the 20$^{\text{th}}$ percentiles of the most and least compressed point sets). As a 'true positive' the tracking matrix is used after both clustering and error correction (see sections below). This results in both a significant reduction of falsely assigned neuron pairs as well as an increase in correctly assigned neurons (Figure 4.12BC).

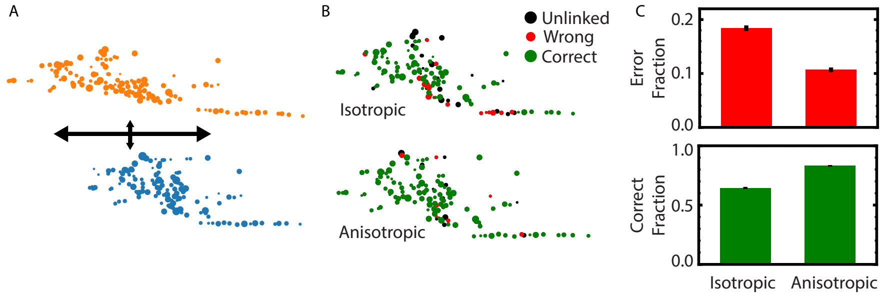

Figure 4.12: **PSR is aided by allowing an anisotropic deformation penalty.** (A) A 2D representation of the position of the segmented points for 2 different frames with different postures show significant deformation of the brain manifold. During PSR, the yellow point cloud has to be mapped to the blue point cloud. (B) Using anisotropic deformations, the PSR wrongly maps many neurons from the blue to the yellow point cloud. When anisotropic deformation is used, this error is reduced. As part of positive control, the neuronal identities are obtained after error correction and clustering. (C) The average fraction of wrongly assigned points (top, red) and correctly assigned points (bottom, green) for 1000 frame pairs with different postures. Error bars represent the bootstrapped 95% confidence interval of the mean.

Construction of the registration vector

Each of the volumes is compared to a reference set of 200 evenly spaced volumes across time. After the anisotropic deformation, in theory, the two volumes have the same shape and neurons of the two volumes can be paired. Pairing is performed based on the distance between neurons using the Hungarian method [103]. The cost function is set to increase proportionately with the squared distance between neurons and stays flat for distances larger than 4 µm. Pairs at distances larger than 4 µm are removed, as this would increase the risk of wrongly assigning neighbouring neurons in dense regions. A registration vector of length 200 containing the identity of the matching neurons in the reference set is constructed for each neuron in every volume of the measurement.

Neuron identification using clustering

The key assumption of the method is that the registration vectors of the same neuron across frames will be similar, or at least more similar to each other than the registration vectors of other neurons. Therefore, these can be identified using clustering methods. As described in Nguyen et al. [53], first a small subset of the frames is used to define clusters, that correspond to individual neurons. Then, each data point is assigned to the nearest cluster when it is sufficiently close by.

A subset of 100 randomly chosen frames is used to cluster the registration vectors so as not to overload the memory of the system. Registration vectors with fewer than 50 (25%) linked neurons are disregarded. A distance between registration vectors is computed based on the number of matching identities (a correlation between the two vectors, where matching identities count as 1 and non-matching identities as 0), excluding frames where no neuron is linked. A hierarchical cluster tree is constructed using complete linkage clustering. Each cluster should consist of registration vectors for the same neuron across different time points. In the optimal case, the number of clusters should therefore be identical to the number of neurons. A distance threshold value of 0.9 is used on the linkage matrix to define the clusters. Clusters consisting of ≤ 40 registration vectors are disregarded. We find that with these parameters, practically no two registration vectors from the same time point are assigned to the same cluster. With the clusters defined based on a small subset of the time points, each registration vector across time points can be compared to the cluster and assigned accordingly. Therefore, the distance of each registration vector is computed to the centroid of each cluster, and the neuron is assigned to the nearest cluster. Registration vectors at a distance greater than 0.4 to the nearest cluster are not assigned. This value is determined by comparing the distributions of the distances to the nearest and the second-nearest clusters. For values < 0.4, the probability of assigning a neuron to the wrong cluster is very low.

Error correction

Now that neurons are tracked across frames, and thereby the deformation of the manifold is known, it is possible to deform one manifold into the other [53]. A comparison of the positions of the neurons can be used to correct tracking errors and add unassigned objects. Each frame is deformed towards a set of 200 equally spaced reference frames. Nguyen. et al. [53] use the predictions to correct the centroid position of wrongly tracked neurons if the object lies far outside the prediction and add missing untracked positions of neurons using the prediction, even when there is no segmented object. We only use the set of previously segmented objects in a frame for error correction.

Occasionally, a single neuron is split into two clusters during the clustering step. Two neurons are merged when 2 criteria are met. Firstly, the time points will be distributed across two clusters, therefore there is a strong anti-correlation in their masks (a boolean vector containing information whether an object is assigned or not at each time point). Therefore, the masks should have a correlation < 0.5. Secondly, it is checked whether the predicted positions of the neurons are strongly overlapping. The distribution of the pairwise distances of the predicted positions from each of the reference frames for the same neuron is compared with that between the two neurons. When these largely overlap; when the Jensen-Shannon divergence (JSD) < 0.7 (bound between 0 and 1), the two neurons are merged.

A similar method of comparing distributions is used to remove incorrectly assigned objects and add unassigned objects at each time point. First, we predict the position of a neuron a at time x from each of the remaining 199 reference frames and compute the distances of the object associated with neuron a at time x with all 199 predictions. This is compared with the pairwise distance distribution between all combinations of the 199 predicted positions. If the position of the object a lies far outside the cloud of points predicted by other time points (a JSD > 0.8 is used), that time point becomes unassigned. This process is repeated for all objects across frames. Objects unassigned to a neuron are assigned by testing if they are positioned within the cloud of predicted positions of each of the neurons. The distance distribution of the unassigned object at time x towards each of the predicted positions the neuron a without an assigned object at x is computed. This is compared to the pairwise distance distribution of the predicted positions of the neuron a. Unassigned objects are added to the neuron with the lowest JSD in ascending order of JSD (for as long as the JSD < 0.8).

Post processing of the time series

Computation of neuronal activity

We found that a bleaching correction was not required for both the AML strains [20, 50] and the NeuroPAL strain OH15500 [49]. To account for motion artefacts and variability in segmentation, the ratio of the green channel with respect to the red channel, $A = G/R$, is defined as the activity of a neuron for subsequent analysis. The activity is subsequently smoothed using a Savitzky–Golay (SG) filter with a 5 s window and a second order polynomial [104]. Each neuron is normalized by $F = (A - A_0)/A_0$, where A_0 is the mean value of the respective time series, to ensure similar weights for each neuron irrespective of the dynamics. To compute the derivative of the time series, a Savitzky-Golay filter was used with a window of 30 s and a 4th order polynomial. We found that this obtained similar results to using a regularised total variation derivative scheme [105] with $\alpha = 10$, albeit with much faster computation times.

PCA analysis, mode time series and mode activity

Chen. et al. have shown on freely moving worms that the mutual information distribution of the derivatives is more distinct from control measurements [106]. We therefore performed the principal component analysis on the time derivatives (using a 30 s window, see above) of the neuronal signals. The principle component analysis is computed on the covariance matrix of the time derivatives (as described above) of the neuronal activity.

Mode time series are constructed using a weighted average of the neuronal time derivatives, weighted by the eigenvector of the respective mode. The activity displayed of PC time series in the figures represents intensities, not derivatives. The activity in Figure 4.3C, 4.4B, 4.8A/B, S4.3, S4.4C, S4.7A, 4.9AB and S4.10C shows the integrated mode time series. The activity displayed and used in the analysis in figures 4.5, 4.7, S4.5 and S4.6 is computed by directly weighting (after 5 s SG filtering) the neuronal time series, instead of mode time series, by the eigenvector of the respective mode, to include high-frequency dynamics lost by the computation of the 30 s derivative used prior to performing the PCA.

Worm stretch

The stretch of the worm's body provides valuable information of the worms behaviour. For each well tracked neuron (at least 90% assigned data points), the average displacement with respect to its mean position along the axis of the channel is computed. The stretching is quantified by taking the average of all neurons. To make sure that a positive stretch corresponds with an expansion of the worm's body, the sign is fixed by ensuring a positive correlation between the time derivative of the obtained value and the standard deviation. The standard deviation is not directly used as a measure of the stretching behaviour, as it is noisy due to unassigned data points. However, we found the standard deviation and average displacement to be highly correlated (0.77 ± 0.05). The displacement is filtered using a SG filter with a window of 5 s and a second order polynomial.

Cross correlations analysis

Cross-correlation analysis is performed on the time derivatives of both quantities. In the analysis of figure 4.2, the cross correlation is computed for a delay time up to ±20 s and the absolute maximum correlation value is used. To compute the relationship between modes and neurons dynamics with stretch (Figure 4.4), the cross correlation is computed with a delay of ±60 s. For SDS measurements, the cross correlations were computed up to a 1 min delay time with the stimulus leading the response and the absolute value is used to compute C. To compute the cross correlations used in the salt analysis, a delay of ±60 s is used.

PROCESSING PIPELINE

To create an efficient processing pipeline, each of the computational steps required to obtain time series, as described above, is written in Python. Python is an open source programming language widely used for scientific research. Therefore, many of the computational methods required to create time series did not have to be built from scratch; existing libraries could be used (e.g. core components of the PSR [102], or the random-walker segmentation algorithm [99]).

This section gives a very brief overview of the processing workflow. The code and documentation describing the different components of the code, along with a more detailed manual of the workflow, are available to anyone upon request. The processing pipeline requires very little user input to process the data. Parameters that have to be set for each experiment are the lower and upper thresholds used for segmentation (see section 4.4.3), the region of interest (excluding regions outside the microfluidic channel reduces computational costs), and the start and end frames of the analysis.

Each measurement consists of thousands of Z-stacks (adding up to ~ 120 GB h^{-1} of measurement), which means that deconvolution, segmentation, and tracking are computationally demanding tasks, and parallel processing is required to reduce the processing time. Therefore, this work was carried out on the Dutch national e-infrastructure (LISA cluster and CARTESIUS supercomputer) with the support of SURF Cooperative.

Processing is split into three parts. (1) PSF deconvolution and segmentation of each frame, computed in parallel on 15 nodes with 360 cores. The output is stored in a pickle file containing information of the position and intensity of the red and green channels (including that of each pixel belonging to the object). (2) PSR of the volumes, also also computed in parallel (on 30 nodes, 720 cores), as it is computationally the most expensive task. The positions of the deformed volumes are stored in a dictionary. (3) Construction of the registration vector, clustering of registration vectors, error correction, and constructing time series are performed on a single node. The result after each step is stored in dictionaries. Parameter settings used for segmentation, deformation, and clustering are stored in text files along with the data.

4.4.4. PROTOCOLS

Microfluidic devices are constructed from PDMS. Worms are cultivated on NGM plates (3 g NaCl, 17 g agar, 2.5 g peptone, 1 mL 5 mg mL^{-1} cholesterol in EtOH in 975 mL water, with 1 mL 1 M $CaCl_2$, 1 mL 1 M $MgSO_4$, 25 mL 1 M KPO_4 pH 6, 1 mL 200 mg mL^{-1} streptomycin in water) seeded with OP50 and regularly transferred. Experiments are performed in S-basal (6 g KH_2PO_4, 1 g K_2HPO_4, 2.9 g NaCl, 1 mL cholesterol (5 mg mL^{-1} in ethanol), 1 l H_2O, autoclaved) with 50 mM NaCl (matching the salt concentration during development) as buffered medium, unless otherwise specified. For stimulus experiments, the paralytic tetramisole is used (see section 4.4.5). Salt experiments are performed on S-basal with 50 mM NaCl with 25 mM sorbitol to balance the osmolarity [10] as buffered medium, and 75 mM NaCl as stimulus medium. SDS response measurements are performed in the buffer M13 instead, with 0.1% SDS in the stimulus medium. Experiments on serotonin are performed in unbuffered water, and serotonin is added on the day of the experiment and protected from light to avoid oxidation. To perform a measurement, healthy looking young adult/adult worm has been chosen by eye with bright fluorescence. An experiment is performed following the protocol described below.

Brain imaging experiments

- Prepare buffered medium and stimulus medium.
- Wash the liquid storage columns, tubing and microfluidic device with demineralized water (3×).
- Pick a worm into a droplet, and use a syringe containing buffer medium to load the worm into the microfluidic device.
- Apply pressure to the buffer reservoirs and connect the tubing to the microfluidic device (see section 4.4.2). Note: Make sure the pressure of the stimulus channel is lower prior to starting the measurement to avoid exposure during sample preparation. Connect the outlet to a tube for transporting the liquid to a waste container.
- Wait for air bubbles to leave the device (usually not necessary if the microfluidic device was flooded with buffered medium prior to loading the worm).
- Load the sample onto the Z-stage holder of the microscope. Acquire a bright-field image at 10× and 60× magnification for later inspection.
- Set a lower and upper limit for image acquisition by hand by slightly illuminating the worm with fluorescent light. Set the number of slices to approximately acquire an image with a spacing of approximately 1.3 µm.
- Start the imaging protocol. (see below)
- Immediately start the microfluidic protocol.

OH15500 imaging protocol

- Repeat 3×: Acquire a single volumetric image for each laser illuminating using a 640, 405, 488, 561 nm laser for 15 ms at 100, 20, 20, 40 mW respectively. This step is pre-programmed and takes ≈ 15 s.

- Acquire W-stacks (consecutive images at equally spaced steps and consecutive z-stacks are acquired in reversed vertical order) for the duration of the measurement using a 488 and 561 nm laser at 3 and 14 mW respectively simultaneously with an illumination time of 5 ms. The red fluorophore requires a strong light source but is highly photostabilized. To reduce the laser power, segmentation is performed by combining red fluorescent light of 5 consecutive frames, which is possible for paralysed worms.

AMLxxx imaging protocol

Acquire W-stacks for the duration of the measurement using a 488 and 561 nm laser at 1 mW simultaneously with an illumination time of 5 ms.

4.4.5. STRAINS AND MEASUREMENT CONDITIONS.

The AML10 and AML14 strains were used during the development of the experimental setup and processing pipe line. AML175 is used for experiments leading up to figure 4.2. AML70 has been used for brain imaging of unparalyzed worms (figure 4.2 & 4.4) in a microfluidic channel of height 28 µm. Stimulus response experiments (figure 4.5-4.8) were performed with the OH15500 strain, in which nearby neurons express distinct fluorescent expression profiles [49], requiring paralysis of the worm in a microfluidic channel with a height 43 µm. To paralyse worms, 1 mM of tetramisole was used for salt, SDS and serotonin response measurements, and 10 mM of tetramisole was used in the experiment of figure 4.4 & S4.4/4.6.

Table 4.1: *C. elegans* strains used in this study.

Strain list

name	genotype	source	Figures	μF dev. height
AML10	otIs355 [rab-3::NLS::tagRFP]. otIs45 [unc-119::GFP] V	[19]		
AML14	wtfEx4 [rab-3p::NLS::GCaMP6s + rab-3p::NLS::tagRFP]	[19]	S4.2	28 µm
AML70	lite-1(ce314) X; wtfIs5 [rab-3p::NLS::GCaMP6s + rab-3p::NLS::tagRFP]	[50]	4.2, 4.3, 4.4 S4.1,4.2,4.3	28 µm
AML175	lite-1(ce314) X; wtfIs3 [rab-3p::NLS::GFP + rab-3p::NLS::tagRFP]	[50]	4.2	28 µm
OH15500	otIs672 [rab-3::NLS::GCaMP6s + arrd-4:NLS:::GCaMP6s]; otIs669[TagRFP-T, mTagBFP2, CyOFP1, mNeptune2.5, CyOFP1 under various promotors] V	[49]	4.5, 4.6, 4.8 S4.4,4.5,4.6 S4.9, 4.10	43 µm

Strains were provided by the CGC, which is funded by NIH Office of Research Infrastructure Programs (P40 OD010440).

4.4.6. SUPPLEMENTARY FIGURES

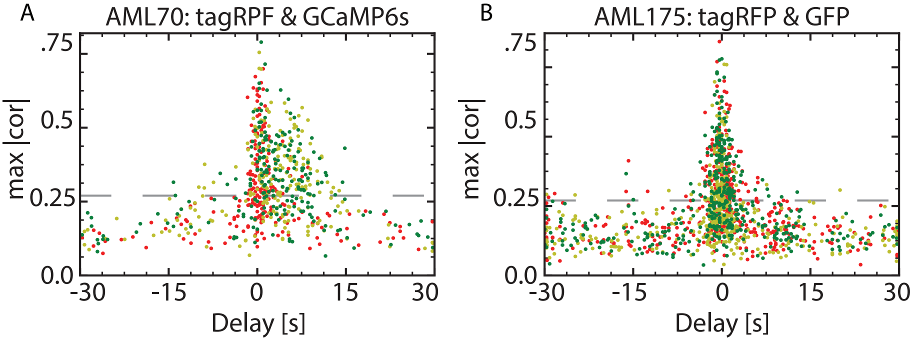

Figure S 4.1: Contrasting time delays of the stretch with calcium sensitive fluorophore and the stretch with calcium insensitive fluorophore indicate that the measured dynamics are not exclusively the result of motion artefacts. The maximum correlation between the neuronal time series and the stretch with its corresponding delay (evaluated in a 20 s window) of measurements performed on worms of the (A) AML70 strain expressing the red fluorophore tagRFP and green calcium indicator GCaMP6s and (B) AML175 strain expressing the two calcium insensitive fluorophores tagRFP and GFP (see methods). Red, green, and yellow indicate the red, green, and ratiometric signals, respectively.

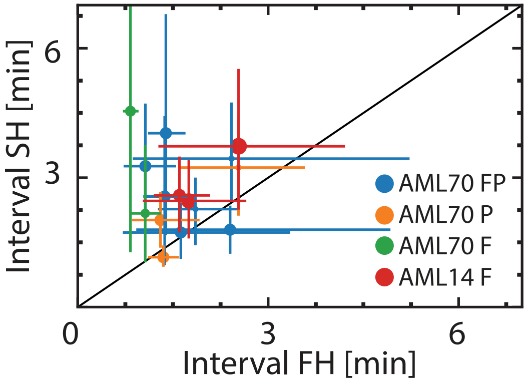

Figure S 4.2: The average peak-to-peak time of the second half of a measurement, for various conditions, is lower than the first half. Each dot is a measurement. P stands for paralyzed, F for freely moving (unparalyzed), and for FP the worm is paralysed in the second half of the measurement.

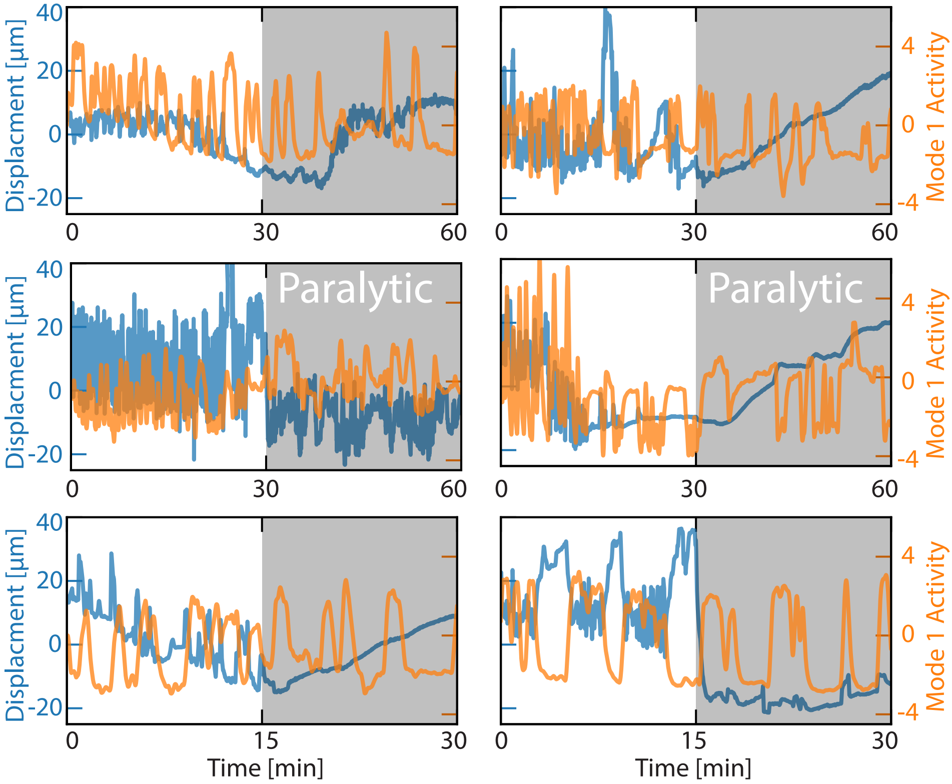

Figure S 4.3: Mode 1 activity (orange) is correlated with the average stretch of the worm's head (blue). Upon addition of 10 mM tetramisole, the movement relaxes, but mode 1 dynamics continue. The bottom right panel is the example shown in figure 4.4C.

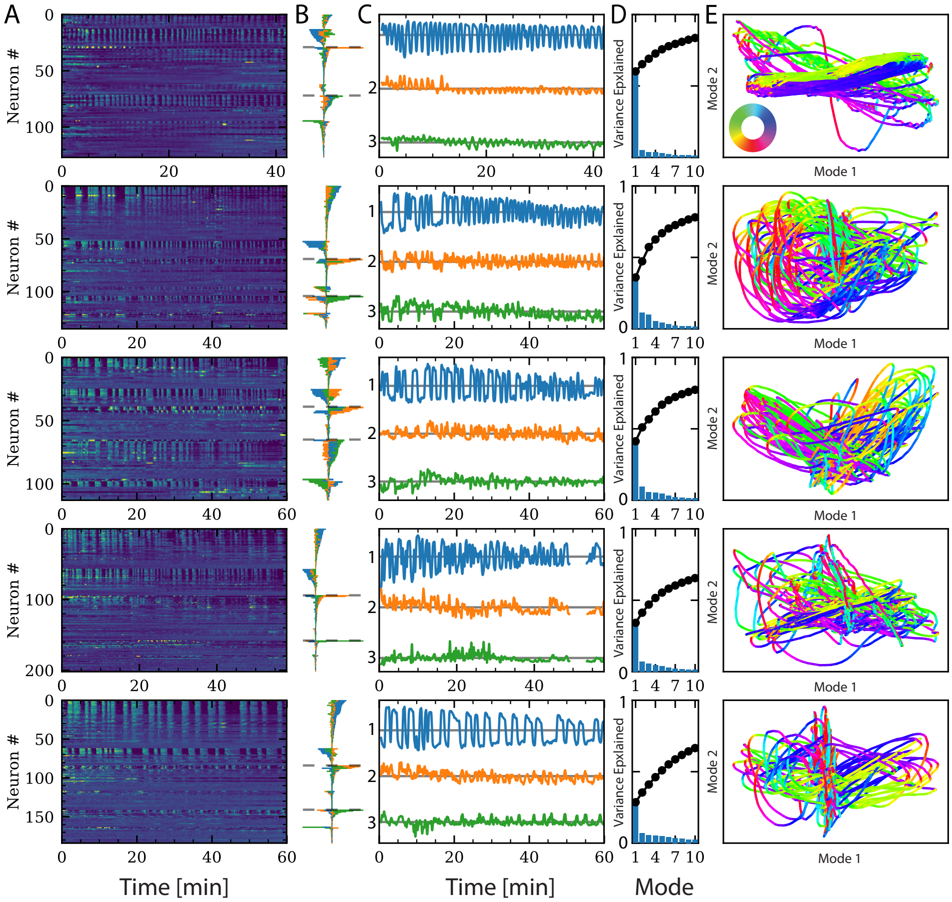

Figure S 4.4: Brain dynamics of various paralysed worms (OH15500) in buffer reveals a dominant principal mode with a phase relationship with the lower mode. (A) The activity for each neuron. Note: Oversegmentation may result in a larger number of objects than the actual number of neurons. (B) The loading of each neuron onto the first (blue), second (yellow), and third (green) top modes. Modes are computed on the time derivatives of the activity. (C) Representative time series of the top 3 modes (same colour coding as in B). Variance explained by the first 10 modes (blue bars). The cumulative variance explained of the first 10 modes (black lines). (E) The phase-space relationship between the time series of the top 2 modes, colour-coded by the direction of the trajectories.

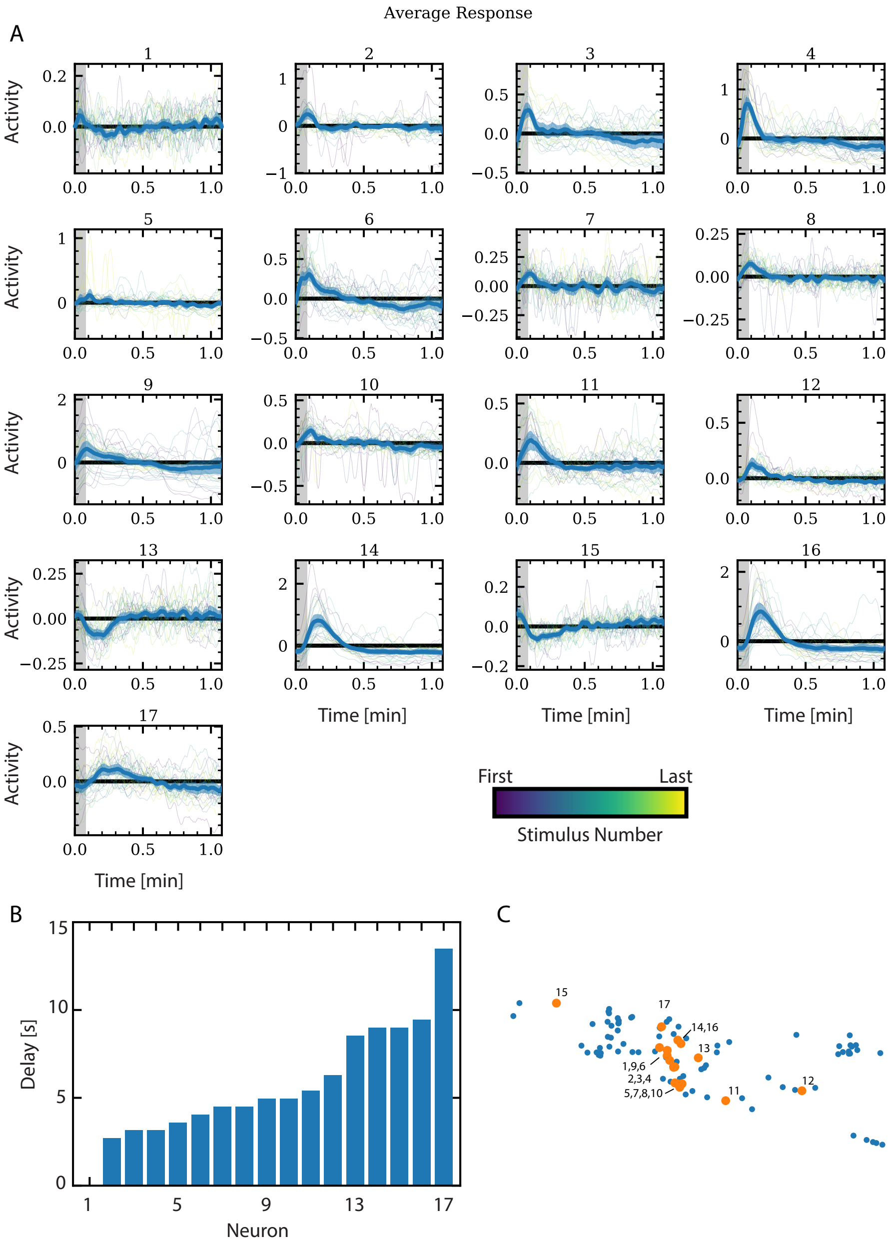

Figure S 4.5: Time series of correlated neurons of an exemplary measurement (the same as figure 4.5B). (A) The most strongly correlated neurons ($p < 0.01$) of an example worm with the time derivative of the stimulus. Time series are sorted by the delay time. The order of the neurons is sorted by the delay time (B) that corresponds to the maximum value of the absolute cross correlation, C, with the stimulus. (C) The positions of the strongly correlated neurons.

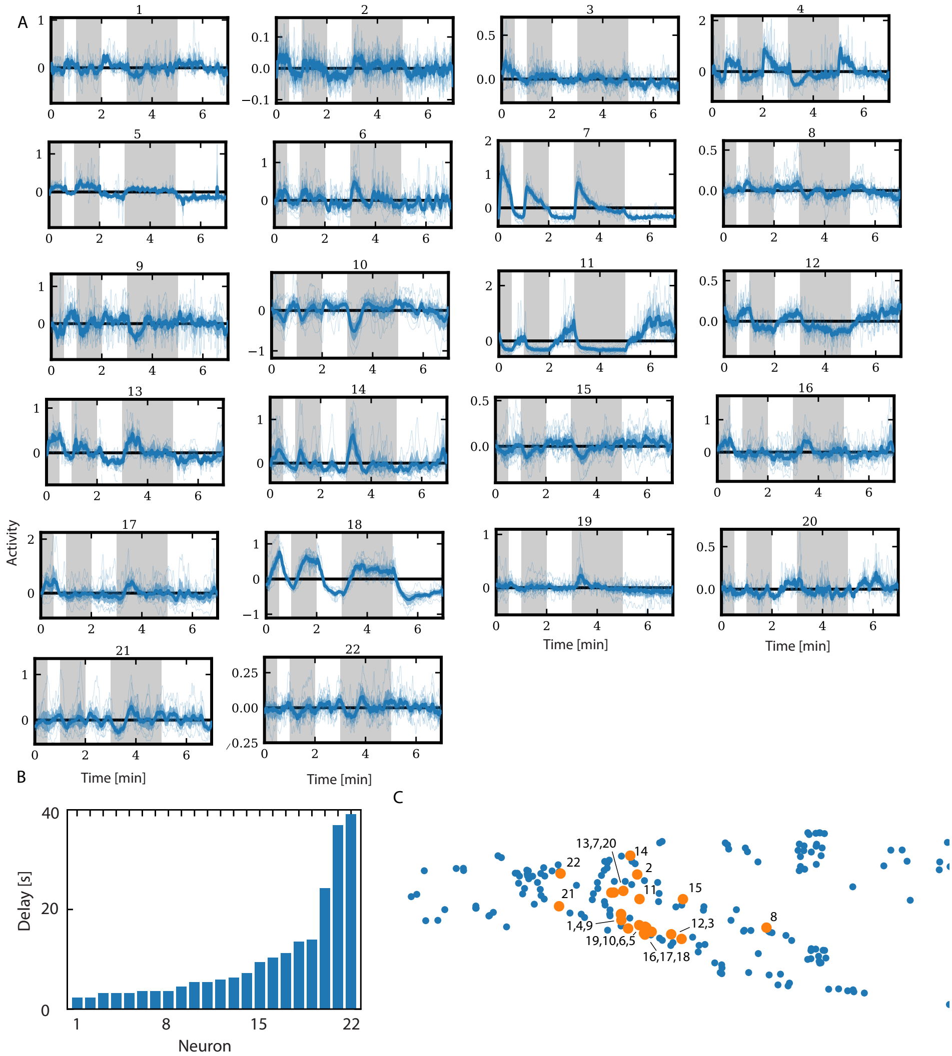

Figure S 4.6: (A) The most strongly correlated neurons of an example worm with the time derivative of the stimulus. Time series are sorted by the delay time. (B) The temporal hierarchy of the most strongly correlated ($p < 0.01$) neurons. (C) The positions of the strongly correlated neurons.

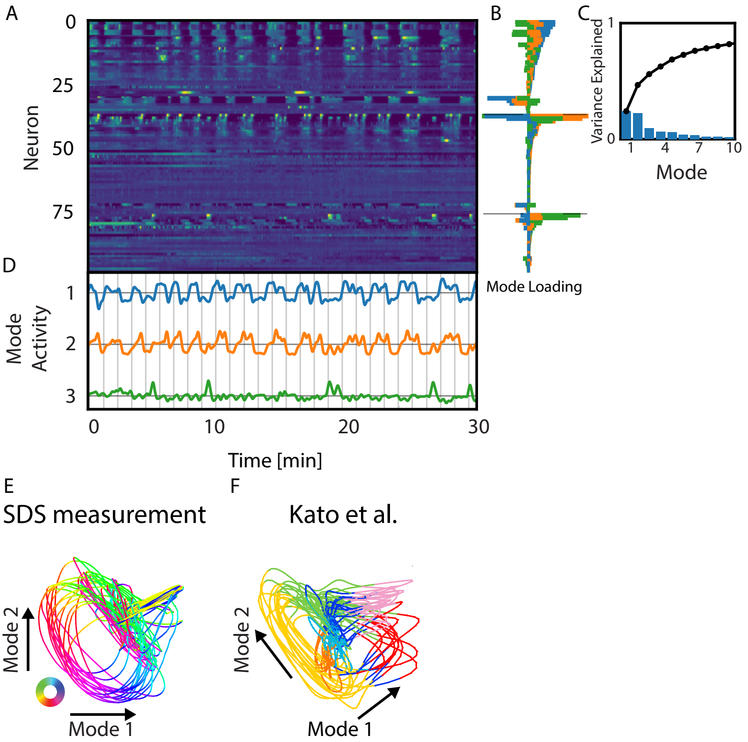

Figure S 4.7: Neuronal dynamics of an exemplary SDS response measurement (same as in figure 4.5 & S4.6). (A) The activity for each of the tracked neurons. (B) The loading of each neuron onto the first (blue), second (yellow), and third (green) top modes. Modes are computed on the time derivatives of the activity. (C)Variance explained by the first 10 modes (blue bars). The cumulative variance explained of the first 10 modes (black lines). (D) Representative time series of the top 3 modes (same colour coding as in B). The grey bars indicate the SDS stimulus. (E) The phase-space relationship between the top 2 modes, colour-coded by the direction of the trajectories. (F) Phase-space relationship of the top two modes in panel E map to those of a study presented by Kato. et al. on paralyzed worms [18]. This panel is adapted from Kato et al. figure 3B and rotated to match figure E. The blue, cyan, red, pink, green, yellow, and orange colours represent inferred corresponding forward, forward slowing, reversal I, reversal II, sustained reversal, ventral turn, and dorsal turn behaviours, respectively, as described by Kato. et al. [18].

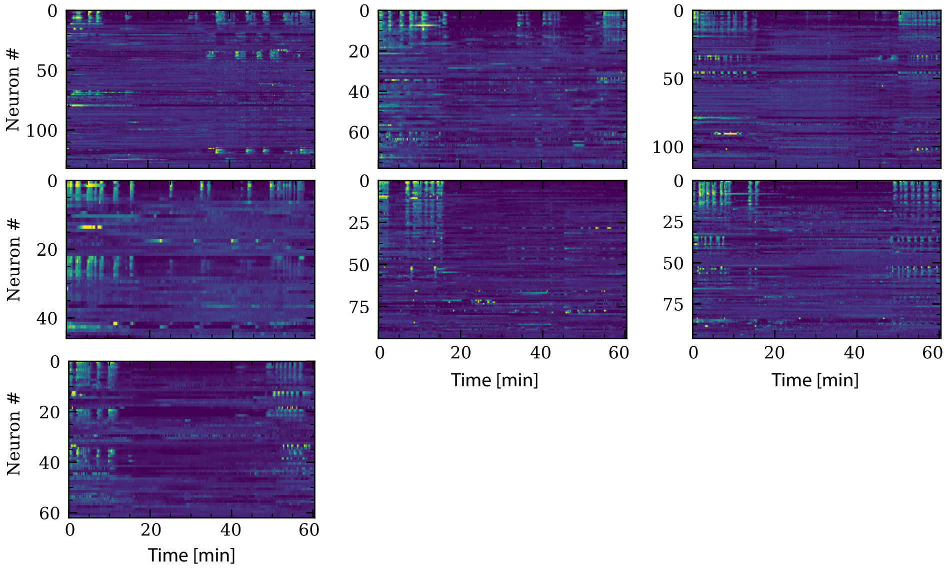

Figure S 4.8: Neuronal dynamics for worms ($N = 7$) stimulated with 5 mM serotonin during 15 min $< t <$ 30 min. Neurons are sorted by the loading onto the first 3 PCA modes.

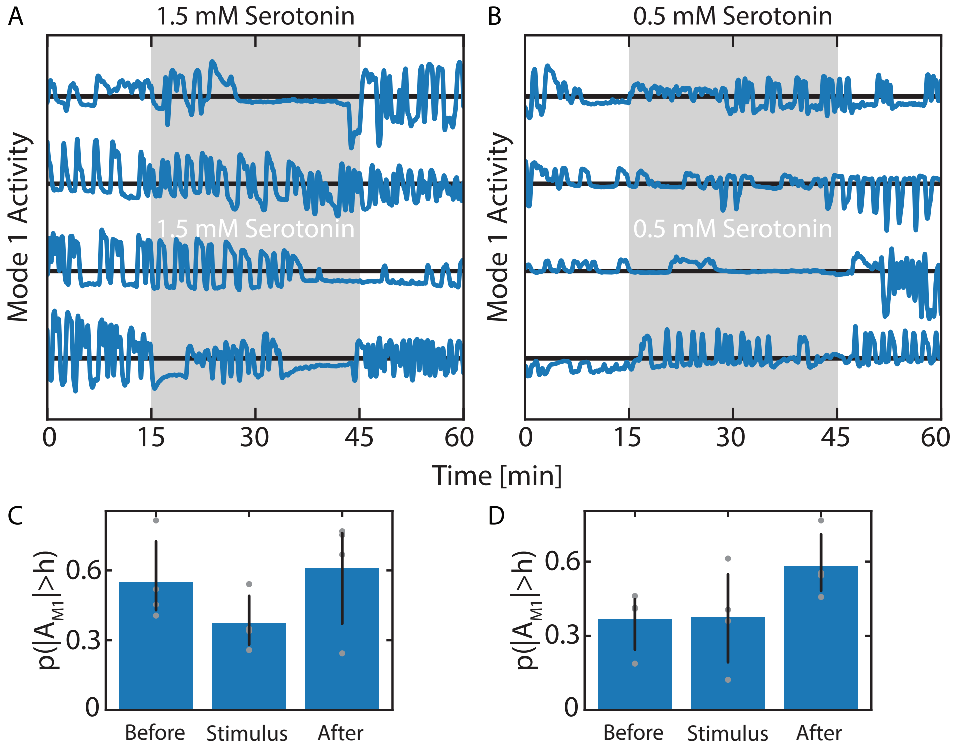

Figure S 4.9: The integrated activity of the first PCA mode for worms in unbuffered water stimulated with 1.5 mM serotonin or (B) 0.5 mM serotonin. In contrast to 5.0 mM stimulated worms, no dramatic decrease in activity is observed. The fraction of time that the absolute activity levels exceed a value h set by the crossover value from a bi-exponential fit to the absolute activity for (C) 1.5 mM serotonin and (D) 0.5 mM. Upon removal, the activity levels increase.

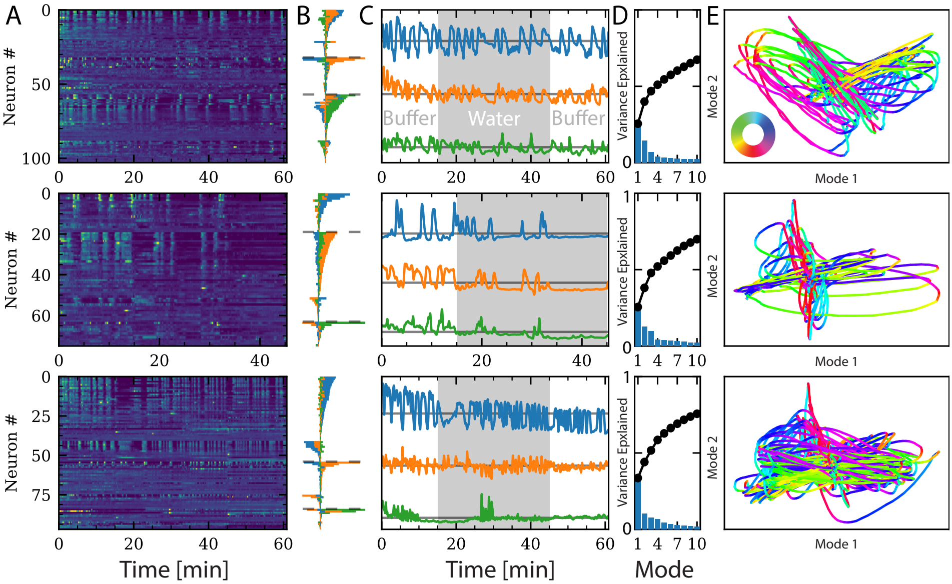

Figure S 4.10: Brain dynamics in response to water. (A) The activity for each neuron. (B) The loading of each neuron onto the first (blue), second (yellow), and third (green) top modes. Modes are computed on the time derivatives of the activity. (C) Representative time series of the top 3 modes (same colour coding as in B). (D) Variance explained by the first 10 modes (blue bars). The cumulative variance explained of the first 10 modes (black lines). (E) The phase-space relationship between the top 2 modes.

BIBLIOGRAPHY

[1] White JG, Southgate E, Thomson JN, Brenner S. The structure of the nervous system of the nematode Caenorhabditis elegans. Philos Trans R Soc Lond B Biol Sci. 1986;314(1165):1–340.

[2] Stephens GJ, Johnson-Kerner B, Bialek W, Ryu WS. Dimensionality and dynamics in the behavior of C. elegans. PLoS Comput Biol. 2008;4(4):e1000028.

[3] Broekmans OD, Rodgers JB, Ryu WS, Stephens GJ. Resolving coiled shapes reveals new reorientation behaviors in C. elegans. Elife. 2016;5:e17227.

[4] Helms SJ, Rozemuller WM, Costa AC, Avery L, Stephens GJ, Shimizu TS. Modelling the ballistic-to-diffusive transition in nematode motility reveals variation in exploratory behaviour across species. Journal of the Royal Society Interface. 2019;16(157):20190174.

[5] Ahamed T, Costa AC, Stephens GJ. Capturing the continuous complexity of behaviour in Caenorhabditis elegans. Nature Physics. 2021;17(2):275–283.

[6] Hires SA, Tian L, Looger LL. Reporting neural activity with genetically encoded calcium indicators. Brain cell biology. 2008;36(1):69–86.

[7] Kerr R, Lev-Ram V, Baird G, Vincent P, Tsien RY, Schafer WR. Optical imaging of calcium transients in neurons and pharyngeal muscle of C. elegans. Neuron. 2000;26(3):583–594.

[8] Chalasani SH, Chronis N, Tsunozaki M, Gray JM, Ramot D, Goodman MB, et al. Dissecting a circuit for olfactory behaviour in Caenorhabditis elegans. Nature. 2007;450(7166):63–70.

[9] Larsch J, Ventimiglia D, Bargmann CI, Albrecht DR. High-throughput imaging of neuronal activity in Caenorhabditis elegans. Proceedings of the National Academy of Sciences. 2013;110(45):E4266–E4273.

[10] Luo L, Wen Q, Ren J, Hendricks M, Gershow M, Qin Y, et al. Dynamic encoding of perception, memory, and movement in a C. elegans chemotaxis circuit. Neuron. 2014;82(5):1115–1128.

[11] Larsch J, Flavell SW, Liu Q, Gordus A, Albrecht DR, Bargmann CI. A circuit for gradient climbing in C. elegans chemotaxis. Cell reports. 2015;12(11):1748–1760.

[12] Gordus A, Pokala N, Levy S, Flavell SW, Bargmann CI. Feedback from network states generates variability in a probabilistic olfactory circuit. Cell. 2015;161(2):215–227.

[13] Urai AE, Doiron B, Leifer AM, Churchland AK. Large-scale neural recordings call for new insights to link brain and behavior. Nature neuroscience. 2022:1–9.

[14] Lemon WC, Pulver SR, Höckendorf B, McDole K, Branson K, Freeman J, et al. Whole-central nervous system functional imaging in larval Drosophila. Nature communications. 2015;6(1):1–16.

[15] Lin Q, Manley J, Helmreich M, Schlumm F, Li JM, Robson DN, et al. Cerebellar Neurodynamics Predict Decision Timing and Outcome on the Single-Trial Level. Cell. 2020;180(3):536–551.

[16] Schrödel T, Prevedel R, Aumayr K, Zimmer M, Vaziri A. Brain-wide 3D imaging of neuronal activity in Caenorhabditis elegans with sculpted light. Nature methods. 2013;10(10):1013–1020.

[17] Prevedel R, Yoon YG, Hoffmann M, Pak N, Wetzstein G, Kato S, et al. Simultaneous whole-animal 3D imaging of neuronal activity using light-field microscopy. Nature methods. 2014;11(7):727–730.

[18] Kato S, Kaplan HS, Schrödel T, Skora S, Lindsay TH, Yemini E, et al. Global brain dynamics embed the motor command sequence of Caenorhabditis elegans. Cell. 2015;163(3):656–669.

[19] Nguyen JP, Shipley FB, Linder AN, Plummer GS, Liu M, Setru SU, et al. Whole-brain calcium imaging with cellular resolution in freely behaving Caenorhabditis elegans. Proceedings of the National Academy of Sciences. 2016;113(8):E1074–E1081.

[20] Venkatachalam V, Ji N, Wang X, Clark C, Mitchell JK, Klein M, et al. Pan-neuronal imaging in roaming Caenorhabditis elegans. Proceedings of the National Academy of Sciences. 2016;113(8):E1082–E1088.

[21] Kotera I, Tran NA, Fu D, Kim JH, Rodgers JB, Ryu WS. Pan-neuronal screening in Caenorhabditis elegans reveals asymmetric dynamics of AWC neurons is critical for thermal avoidance behavior. Elife. 2016;5:e19021.

[22] Nichols AL, Eichler T, Latham R, Zimmer M. A global brain state underlies C. elegans sleep behavior. Science. 2017;356(6344).

[23] Skora S, Mende F, Zimmer M. Energy scarcity promotes a brain-wide sleep state modulated by insulin signaling in C. elegans. Cell reports. 2018;22(4):953–966.

[24] Voleti V, Patel KB, Li W, Campos CP, Bharadwaj S, Yu H, et al. Real-time volumetric microscopy of in vivo dynamics and large-scale samples with SCAPE 2.0. Nature methods. 2019;16(10):1054–1062.

[25] Hallinen KM, Dempsey R, Scholz M, Yu X, Linder A, Randi F, et al. Decoding locomotion from population neural activity in moving C. elegans. Elife. 2021;10:e66135.

[26] Ji N, Madan GK, Fabre GI, Dayan A, Baker CM, Kramer TS, et al. A neural circuit for flexible control of persistent behavioral states. Elife. 2021;10:e62889.

[27] Awal MR, Wirak GS, Gabel CV, Connor CW. Collapse of global neuronal states in Caenorhabditis elegans under isoflurane anesthesia. Anesthesiology. 2020;133(1):133–144.

[28] Chronis N, Zimmer M, Bargmann CI. Microfluidics for in vivo imaging of neuronal and behavioral activity in Caenorhabditis elegans. Nature methods. 2007;4(9):727–731.

[29] Bargmann CI. Chemosensation in C. elegans. In: WormBook: The Online Review of C. elegans Biology [Internet]. WormBook; 2006. .

[30] Hilliard MA, Bargmann CI, Bazzicalupo P. C. elegans responds to chemical repellents by integrating sensory inputs from the head and the tail. Current Biology. 2002;12(9):730–734.

[31] Hilliard MA, Bergamasco C, Arbucci S, Plasterk RH, Bazzicalupo P. Worms taste bitter: ASH neurons, QUI-1, GPA-3 and ODR-3 mediate quinine avoidance in Caenorhabditis elegans. The EMBO journal. 2004;23(5):1101–1111.

[32] Donnelly JL, Clark CM, Leifer AM, Pirri JK, Haburcak M, Francis MM, et al. Monoaminergic orchestration of motor programs in a complex C. elegans behavior. PLoS Biol. 2013;11(4):e1001529.

[33] Pirri JK, Alkema MJ. The neuroethology of C. elegans escape. Current opinion in neurobiology. 2012;22(2):187–193.

[34] Pierce-Shimomura JT, Morse TM, Lockery SR. The fundamental role of pirouettes in Caenorhabditis elegans chemotaxis. Journal of Neuroscience. 1999;19(21):9557–9569.

[35] Iino Y, Yoshida K. Parallel use of two behavioral mechanisms for chemotaxis in Caenorhabditis elegans. Journal of Neuroscience. 2009;29(17):5370–5380.

[36] Bargmann CI, Horvitz HR. Chemosensory neurons with overlapping functions direct chemotaxis to multiple chemicals in C. elegans. Neuron. 1991;7(5):729–742.

[37] Suzuki H, Thiele TR, Faumont S, Ezcurra M, Lockery SR, Schafer WR. Functional asymmetry in Caenorhabditis elegans taste neurons and its computational role in chemotaxis. Nature. 2008;454(7200):114–117.

[38] Tomioka M, Adachi T, Suzuki H, Kunitomo H, Schafer WR, Iino Y. The insulin/PI 3-kinase pathway regulates salt chemotaxis learning in Caenorhabditis elegans. Neuron. 2006;51(5):613–625.

[39] Kunitomo H, Sato H, Iwata R, Satoh Y, Ohno H, Yamada K, et al. Concentration memory-dependent synaptic plasticity of a taste circuit regulates salt concentration chemotaxis in Caenorhabditis elegans. Nature communications. 2013;4(1):1–11.

[40] Chase DL, Koelle MR. Biogenic amine neurotransmitters in C. elegans. In: WormBook: The Online Review of C. elegans Biology [http://www.wormbook.org]. WormBook; 2007. .

[41] Li C, Kim K. Neuropeptides. WormBook: the online review of C elegans biology. 2008:1.

[42] Sulston J, Dew M, Brenner S. Dopaminergic neurons in the nematode Caenorhabditis elegans. Journal of Comparative Neurology. 1975;163(2):215–226.

[43] Sanyal S, Wintle RF, Kindt KS, Nuttley WM, Arvan R, Fitzmaurice P, et al. Dopamine modulates the plasticity of mechanosensory responses in Caenorhabditis elegans. The EMBO journal. 2004;23(2):473–482.

[44] Horvitz HR, Chalfie M, Trent C, Sulston JE, Evans PD. Serotonin and octopamine in the nematode Caenorhabditis elegans. Science. 1982;216(4549):1012–1014.

[45] Alkema MJ, Hunter-Ensor M, Ringstad N, Horvitz HR. Tyramine functions independently of octopamine in the Caenorhabditis elegans nervous system. Neuron. 2005;46(2):247–260.

[46] Cermak N, Stephanie KY, Clark R, Huang YC, Baskoylu SN, Flavell SW. Whole-organism behavioral profiling reveals a role for dopamine in state-dependent motor program coupling in C. elegans. Elife. 2020;9:e57093.

[47] Kringelbach M, Deco G. Brain States and Transitions: Insights from Computational Neuroscience. Cell Rep. 2020;32(10):108128.

[48] McCormick DA, Nestvogel DB, He BJ. Neuromodulation of Brain State and Behavior. Annual Review of Neuroscience. 2020;43:391â€“415.

[49] Yemini E, Lin A, Nejatbakhsh A, Varol E, Sun R, Mena GE, et al. NeuroPAL: a multicolor atlas for whole-brain neuronal identification in C. elegans. Cell. 2021;184(1):272–288.

[50] Scholz M, Linder AN, Randi F, Sharma AK, Yu X, Shaevitz JW, et al. Predicting natural behavior from whole-brain neural dynamics. bioRxiv. 2018:445643.

[51] Hill AJ, Mansfield R, Lopez JM, Raizen DM, Van Buskirk C. Cellular stress induces a protective sleep-like state in C. elegans. Current biology. 2014;24(20):2399–2405.

[52] Gonzales DL, Zhou J, Fan B, Robinson JT. A microfluidic-induced C. elegans sleep state. Nature communications. 2019;10(1):1–13.

[53] Nguyen JP, Linder AN, Plummer GS, Shaevitz JW, Leifer AM. Automatically tracking neurons in a moving and deforming brain. PLoS computational biology. 2017;13(5):e1005517.

[54] Schwarz J, Spies JP, Bringmann H. Reduced muscle contraction and a relaxed posture during sleep-like Lethargus. In: Worm. vol. 1. Taylor & Francis; 2012. p. 12–14.

[55] Hilliard MA, Apicella AJ, Kerr R, Suzuki H, Bazzicalupo P, Schafer WR. In vivo imaging of C. elegans ASH neurons: cellular response and adaptation to chemical repellents. The EMBO journal. 2005;24(1):63–72.

[56] Flavell SW, Pokala N, Macosko EZ, Albrecht DR, Larsch J, Bargmann CI. Serotonin and the neuropeptide PDF initiate and extend opposing behavioral states in C. elegans. Cell. 2013;154(5):1023–1035.

[57] Stern S, Kirst C, Bargmann CI. Neuromodulatory control of long-term behavioral patterns and individuality across development. Cell. 2017;171(7):1649–1662.

[58] Chao MY, Komatsu H, Fukuto HS, Dionne HM, Hart AC. Feeding status and serotonin rapidly and reversibly modulate a Caenorhabditis elegans chemosensory circuit. Proceedings of the National Academy of Sciences. 2004;101(43):15512–15517.

[59] Sawin ER, Ranganathan R, Horvitz HR. C. elegans locomotory rate is modulated by the environment through a dopaminergic pathway and by experience through a serotonergic pathway. Neuron. 2000;26(3):619–631.

[60] Gürel G, Gustafson MA, Pepper JS, Horvitz HR, Koelle MR. Receptors and other signaling proteins required for serotonin control of locomotion in Caenorhabditis elegans. Genetics. 2012;192(4):1359–1371.

[61] Turek M, Lewandrowski I, Bringmann H. An AP2 transcription factor is required for a sleep-active neuron to induce sleep-like quiescence in C. elegans. Current Biology. 2013;23(22):2215–2223.

[62] Campbell SS, Tobler I. Animal sleep: a review of sleep duration across phylogeny. Neuroscience & Biobehavioral Reviews. 1984;8(3):269–300.

[63] Brown EN, Lydic R, Schiff ND. General anesthesia, sleep, and coma. New England Journal of Medicine. 2010;363(27):2638–2650.

[64] Gray JM, Hill JJ, Bargmann CI. A circuit for navigation in Caenorhabditis elegans. Proceedings of the National Academy of Sciences. 2005;102(9):3184–3191.

[65] Liu J, Ward A, Gao J, Dong Y, Nishio N, Inada H, et al. C. elegans phototransduction requires a G protein–dependent cGMP pathway and a taste receptor homolog. Nature neuroscience. 2010;13(6):715.

[66] Edwards SL, Charlie NK, Milfort MC, Brown BS, Gravlin CN, Knecht JE, et al. A novel molecular solution for ultraviolet light detection in Caenorhabditis elegans. PLoS Biol. 2008;6(8):e198.

[67] Chalfie M, Hart AC, Rankin CH, Goodman MB. Assaying mechanosensation. WormBook: the online review of C elegans biology. 2014.

[68] Kaplan HS, Thula OS, Khoss N, Zimmer M. Nested neuronal dynamics orchestrate a behavioral hierarchy across timescales. Neuron. 2020;105(3):562–576.

[69] Ghosh DD, Nitabach MN, Zhang Y, Harris G. Multisensory integration in C. elegans. Current opinion in neurobiology. 2017;43:110–118.

[70] Moyle MW, Barnes KM, Kuchroo M, Gonopolskiy A, Duncan LH, Sengupta T, et al. Structural and developmental principles of neuropil assembly in C. elegans. bioRxiv. 2020.

[71] Brittin CA, Cook SJ, Hall DH, Emmons SW, Cohen N. Beyond the connectome: A map of a brain architecture derived from whole-brain volumetric reconstructions. bioRxiv. 2020.

[72] Clark DA, Biron D, Sengupta P, Samuel AD. The AFD sensory neurons encode multiple functions underlying thermotactic behavior in Caenorhabditis elegans. Journal of Neuroscience. 2006;26(28):7444–7451.

[73] Hendricks M, Ha H, Maffey N, Zhang Y. Compartmentalized calcium dynamics in a C. elegans interneuron encode head movement. Nature. 2012;487(7405):99–103.

[74] Bargmann CI, Marder E. From the connectome to brain function. Nature methods. 2013;10(6):483.

[75] Harris-Warrick RM, Marder E, et al. Modulation of neural networks for behavior. Annual review of neuroscience. 1991;14(1):39–57.

[76] Marder E. Neuromodulation of neuronal circuits: back to the future. Neuron. 2012;76(1):1–11.

[77] Tsalik EL, Niacaris T, Wenick AS, Pau K, Avery L, Hobert O. LIM homeobox gene-dependent expression of biogenic amine receptors in restricted regions of the C. elegans nervous system. Developmental biology. 2003;263(1):81–102.

[78] Hammarlund M, Hobert O, Miller 3rd DM, Sestan N. The CeNGEN project: the complete gene expression map of an entire nervous system. Neuron. 2018;99(3):430–433.

[79] Petrascheck M, Ye X, Buck LB. An antidepressant that extends lifespan in adult Caenorhabditis elegans. Nature. 2007;450(7169):553–556.

[80] Oikonomou G, Altermatt M, Zhang Rw, Coughlin GM, Montz C, Gradinaru V, et al. The serotonergic raphe promote sleep in zebrafish and mice. Neuron. 2019;103(4):686–701.

[81] Artal-Sanz M, de Jong L, Tavernarakis N. Caenorhabditis elegans: a versatile platform for drug discovery. Biotechnology Journal: Healthcare Nutrition Technology. 2006;1(12):1405–1418.

[82] Ahringer J. Reverse genetics, WormBook, ed. The C elegans Research Community, WormBook doi. 2006;10.

[83] de Carlos Cáceres I, Valmas N, Hilliard MA, Lu H. Laterally orienting C. elegans using geometry at microscale for high-throughput visual screens in neurodegeneration and neuronal development studies. PloS one. 2012;7(4):e35037.

[84] Toyoshima Y, Wu S, Kanamori M, Sato H, Jang MS, Oe S, et al. Neuron ID dataset facilitates neuronal annotation for whole-brain activity imaging of C. elegans. BMC biology. 2020;18(1):1–20.

[85] Linderman S, Nichols A, Blei D, Zimmer M, Paninski L. Hierarchical recurrent state space models reveal discrete and continuous dynamics of neural activity in C. elegans. bioRxiv. 2019:621540.

[86] Boothe T, Hilbert L, Heide M, Berninger L, Huttner WB, Zaburdaev V, et al. A tunable refractive index matching medium for live imaging cells, tissues and model organisms. Elife. 2017;6:e27240.

[87] Kim DN, Kim KT, Kim C, Teitell MA, Zangle TA. Soft lithography fabrication of index-matched microfluidic devices for reducing artefacts in fluorescence and quantitative phase imaging. Microfluidics and nanofluidics. 2018;22(1):2.

[88] Ahrens MB, Orger MB, Robson DN, Li JM, Keller PJ. Whole-brain functional imaging at cellular resolution using light-sheet microscopy. Nature methods. 2013;10(5):413–420.

[89] Bouchard MB, Voleti V, Mendes CS, Lacefield C, Grueber WB, Mann RS, et al. Swept confocally-aligned planar excitation (SCAPE) microscopy for high-speed volumetric imaging of behaving organisms. Nature photonics. 2015;9(2):113–119.

[90] Song A, Charles AS, Koay SA, Gauthier JL, Thiberge SY, Pillow JW, et al. Volumetric two-photon imaging of neurons using stereoscopy (vTwINS). Nature methods. 2017;14(4):420–426.

[91] Nejatbakhsh A, Varol E, Yemini E, Venkatachalam V, Lin A, Samuel AD, et al. Extracting neural signals from semi-immobilized animals with deformable non-negative matrix factorization. bioRxiv. 2020.

[92] Levoy M, Ng R, Adams A, Footer M, Horowitz M. Light field microscopy. In: ACM SIGGRAPH 2006 Papers; 2006. p. 924–934.

[93] Curd A, Cleasby A, Makowska K, York A, Shroff H, Peckham M. Construction of an instant structured illumination microscope. Methods. 2015;88:37–47.

[94] Bewersdorf J, Pick R, Hell SW. Multifocal multiphoton microscopy. Optics letters. 1998;23(9):655–657.

[95] Rafael GÃ³mez-SjÃ¶berg LBNL Microfluidics Lab. Rafael's Microfluidics site. https://sitesgooglecom/site/rafaelsmicrofluidicspage.

[96] Goodman JW. Introduction to Fourier optics. Roberts and Company Publishers; 2005.

[97] Pawley J. Handbook of biological confocal microscopy. vol. 236. Springer Science & Business Media; 2006.

[98] Otsu N. A threshold selection method from gray-level histograms. IEEE transactions on systems, man, and cybernetics. 1979;9(1):62–66.

[99] Grady L. Random walks for image segmentation. IEEE transactions on pattern analysis and machine intelligence. 2006;28(11):1768–1783.

[100] Toyoshima Y, Tokunaga T, Hirose O, Kanamori M, Teramoto T, Jang MS, et al. Accurate automatic detection of densely distributed cell nuclei in 3D space. PLoS computational biology. 2016;12(6):e1004970.

[101] Tokunaga T, Hirose O, Kawaguchi S, Toyoshima Y, Teramoto T, Ikebata H, et al. Automated detection and tracking of many cells by using 4D live-cell imaging data. Bioinformatics. 2014;30(12):i43–i51.

[102] Jian B, Vemuri BC. Robust point set registration using gaussian mixture models. IEEE transactions on pattern analysis and machine intelligence. 2010;33(8):1633–1645.

[103] Kuhn HW. The Hungarian method for the assignment problem. Naval research logistics quarterly. 1955;2(1-2):83–97.

[104] Savitzky A, Golay MJ. Smoothing and differentiation of data by simplified least squares procedures. Analytical chemistry. 1964;36(8):1627–1639.

[105] Chartrand R. Numerical differentiation of noisy, nonsmooth data. ISRN Applied Mathematics. 2011;2011.

[106] Chen X, Randi F, Leifer AM, Bialek W. Searching for collective behavior in a small brain. Physical Review E. 2019;99(5):052418.

SUMMARY

How and why animals exhibit certain behaviours is one of the most interesting, but also among the most complex biological questions to answer. Traditionally, this question was approached from either ethology – focusing on strategy (the *why*) from an evolutionary perspective, or neuroscience – focusing on mechanism (the *how*) from a physiological perspective, but the gap between these approaches is now narrowing with technological advances allowing the collection of vast data sets to capture motile behaviour and brain dynamics, including its diversity and variability. In this thesis, we have taken a physical approach towards understanding motile behaviour, striving to uncover simple ideas from large, holistic data sets in a principled way, by applying dimensionality reduction and minimalistic modelling to the nematode *Caenorhabditis elegans*, a 1 mm-long nematode with just 302 neurons.

After a brief introduction in **Chapter 1**, in **chapter 2** we develop a quantitative and predictive description of motile behaviour and use it to study behaviour of a wide range of nematode species. For thism we construct a minimal 7-parameter model that captures the essential behaviours: speed, rotational, and reversal dynamics, including their fluctuations. We find that this model captures variation across individuals and a broad range of species within the *Nematoda* phylum. Interestingly, behaviour varies most prominently across a common mode, and moving along this mode strongly changes the exploratory propensity towards more roaming or more dwelling. In addition, variation across individuals is comparable to variation across species, which suggests a common underlying pathway. This simple model provides a basis for future investigations to uncover conserved mechanisms that generate behavioral variability.

Chapter 3 focuses on the turning aspect of behaviour and asks what are the modes of control, and how the system is optimised to mitigate limits of control and intrinsic biases. We realise this by extracting and analysing postures from a large number of worms performing exploratory and escape tasks during two-hour recordings, leveraging naturally occurring variability in turning statistics across time and individuals under similar conditions. The results show that during exploration, worms exhibit a slowly fluctuating but persistent gradual rotational bias, curtailing their exploratory propensity. However, with a simple model, we show that the effective rate of random reorientation, on average, minimises the negative impact of the rotational bias, which could reflect a constrained optimization.

Finally, we show how during escape responses, the worm exerts control over its sharp turn statistics, with respect to both direction and amplitude, to overcome its intrinsic biases that would be detrimental to escape.

In **Chapter 4** we investigate the neuronal signalling that underlies behaviour and its relationship to motility and sensory inputs. We develop a measurement-analysis pipeline that enables long timescale whole-brain recordings of brain dynamics with a simple one-dimensional behavioural output and the ability to provide temporally controlled chemical stimuli. With this system we investigate 3 hypotheses about *C. elegans* brain dynamics: (1) the collective motor-command hypothesis, which states that correlated activity of many neurons serve as motor commands, (2) the apparent stochasticity hypothesis, which states that individual neuron activity can appear stochastic due to influences of brain-wide dynamics, and (3) the neuromodulated brain-states hypothesis, which states that brain-wide activity states, such as sleep, can be triggered by neuromodulatory chemicals. Our results yield positive evidence in support of each of these hypothesis.

The results presented in this thesis contribute to closing the aforementioned gap between understanding the how and why of behaviour. On the one hand, tools have been developed to quantify, model, and analyse motile behaviour in the absence and presence of stimuli and in the context of behavioural strategies. On the other hand, we have made inroads to studying how the brain encodes and processes information, under the influence of the same stimuli. This thesis has largely been an exploratory effort, where along the way many new interesting angles have been opened up for future studies.

SAMENVATTING

Hoe en waarom bepaald bewegelijk gedrag tot stand komt is een fascinerende, maar ingewikkelde vraag om te beantwoorden. Van oudsher zijn er verschillende invalshoeken: ecologisch (de *waarom*-vraag) wat gedrag als onderdeel van een evolutionair voordelige strategie beschouwd, of mechanistisch (de *hoe*-vraag) waarin gedrag wordt gezien als de uitkomst van een ingewikkeld interactienetwerk, met een hoofdrol voor het brein. Door de opkomende technologie waarin gigantische datasets geproduceerd kunnen worden om gedrag en hersensignalen, inclusief variatie, te meten, komen deze invalshoeken steeds dichter bij elkaar. In dit proefschrift is een fysische benadering gebruikt om bewegingsgedrag te bestuderen, wat focust op simplificatie en het bestuderen van algemene principes gebruikmakend van deze grote datasets, door middel van dimensie-reductie, modellen om systemen te begrijpen, en het bestuderen van een minimaal biologisch modelorganisme *Caenorhabditis elegans*: een 1 mm lange nematode (rondworm) met slechts 302 zenuwcellen.

Hiervoor hebben we in **hoofdstuk 2** een voorspellend en interpretabel model gecreëerd met 7 parameters, wat de essentiële bewegingsdynamica, inclusief variatie op korte tijdschaal vastgelegd: snelheid, rotatie, en bewegingsommekeer. Dit model legt succesvol variatie vast in bewegingsgedrag tussen verschillende wormen van een brede set aan verschillende soorten van de *Nematoda* stam. Een interessante bevinding is dat de richting in de parameterruimte van het model die het beste gedragsverschillen beschrijft overeenkomt met een as waarop, als je er overheen loopt, sterk de verkeningsgraad veranderd. Verder vinden we dat variatie van individuen binnen hetzelfde soort vergelijkbaar is met variatie tussen verschillende soorten, wat kan duidelijk op een gemeenschappelijk onderliggend regulatienetwerk. Dit model vormt een basis voor vervolgstudies die de mechanismen willen onderzoeken die ten grondslag liggen aan variatie in gedrag.

Hoofdstuk 3 focust op het draai-aspect van gedrag waarin we ons af vragen wat de controlemechanismen zijn en hoe deze zijn geoptimaliseerd om de invloed van inherente limitaties in controle te beperken. Hiervoor meten en analyseren we het postuur van een groot aantal wormen gedurende meerdere uren in een omgeving waar ze verkenningsgedrag en vluchtgedrag vertonen, gebruikmakend van de van nature aanwezige variatie in gedrag over tijd en tussen individuen onder vergelijkbare omstandigheden. We vinden dat er tijdens de verkenning een relatief zwak, maar continu aanwezig en zeer langzaam fluctuerend voorkeursdraairichting aanwezig is, wat een limitiatie zet aan de ’rechtheid’ van het genomen pad. We kunnen met een model laten zien dat het willekeurig draaigedrag een dusdanig sterkte heeft dat die, met de aanname dat de voorkeursrichting een intrinsieke beperking is die niet verkleind kan worden, gemiddeld genomen voor alle wormen dit negatieve effect minimaliseert. Tot slot beschrijven we hoe de worm gebruikt maakt van controle in amplitude en richting van de ommedraai, vertoond tijdens het vluchtgedrag, om zo efficiënt mogelijk weg te draaien.

Het doel van **Hoofdstuk 4** is om de hersensignalen te onderzoeken die ten grondslag liggen aan gedrag, in relatie met de beweging en zintuigelijke stimuli. Hiervoor is een opstelling gecreëerd die voor langer dan 1 uur van een stubstantieel deel van het brein hersensignalen kan vastleggen, tezamen met een simpel 1-dimensionaal bewegingsparameter, terwijl er gecontroleerd vloeibare stimuli kunnen worden toegepast. We gebruiken deze opstelling om 3 bestaande hypothesen te testen: (1) de globale activiteitspatronen in het brein bevatten informatie van de bewegingstoestand, (2) de stochasticiteitshypothese, door middel van het herhaaldelijk toevoegen van een zout of SDS oplossing en (3) modulatie van de hersentoestand, in de vorm van een omkeerbare rusttoestand als gevolg van externe toevoeging van serotonine. De resultaten die we vinden zijn in lijn met deze hypothesen.

De resultaten die gepresenteerd worden in dit proefschrift dragen bij aan het verder verkleinen van het hierboven gat tussen verschillende invalshoeken in het bestuderen van gedrag. Enerzijds hebben zijn er middelen ontwikkeld om gedrag te kunnen kwantificeren en modelleren, om het vervolgens, met en zonder stimuli, te analyseren als onderdeel van een strategie. Anderzijds is er bestudeerd hoe het brein signalen verwerkt, soms zelfs dezelfde stimuli. De resultaten die gepresenteerd zijn in dit proefschrift zijn grotendeels exploratief en geven nieuwe invalshoeken voor veel vervolgestudies die hierop kunnen voortduren.

ACKNOWLEDGEMENTS

First, I want to thank Dr. Greg Stephens, Dr. Gert Jansen, Prof. Erwin Peterman, and Prof. William Ryu for taking the effort to read, comment, and be part of the promotion commission.

This thesis would never have seen the light of day without a large number of people that I really want to thank. My biggest thanks go to Tom for giving me the opportunity to work on this project. It has been a very interesting project, and it was wonderful to have the freedom to shape it. I have never met anyone so calm, detailed in his thoughts, and precise in his statements, which is in some sense diametrically opposed to myself. Under your supervision, I've come to appreciate that and even gotten slightly more coherent myself. Also, Greg deserves a huge thank you. Although not very frequent, every meeting we have had has been inspiring, not just for the scientific input. Your "greater picture" view has been tremendously helpful, and I loved the conversations we had. If you don't become a professor, I'll eat my hat. And then there's my postdoc, Steffen:), without whom I'd never have made it past the third year. You are an absolute jewel, a blessing to science, and I'm so happy that you have your own group. The best part of you is your optimism, enthusiasm, and infinite energy to help other people. I'm sure you'll become a great group leader.

Also, I've had the pleasure, especially in the first year, to work closely with Antonio. You're not just ludicrously smart and talented, but also super kind and fun to hang out with. The highlight was the summer school in Cargese (also with Harmen). Also Liam, your work has been extremely valuable. I loved to have you on the escape room events that we've had with Antonio and Steffen.

In the last few years, I've seen a few generations of people in the Shimizu group come and go. Johannes, I've enjoyed your council and your provocative discussions; it's never boring with you around. Ercag, you are such a pure soul. Please, don't forget to live outside the lab. The same goes for you, Fotios. Thank you for teaching me microfluidics;) Katherina, you're one of the kindest people I've ever encountered. Victor, I've enjoyed your creativity and positivity. Keita, you're super helpful, and I'm impressed with how you managed to pull off your impossible project by sheer will. Bas, you have taken up a quite challenging project really well. Not only did you do the measurements we thought of, but you also took initiative and came up with more experiments yourself. Also, I've enjoyed the sharp mind of Katja, the booming laugh of Sebastian, the artistic lab notes of Loreto, the relaxed attitude of Jacopo, and the cheerfulness of Guillia. Thank you, Simone Boskamp and Yvonne, for teaching me how to behave in a lab. That sure wasn't an easy task.

There are also the people from the consortium who have been helpful and a joy to work with. Joleen, you've had an incredibly difficult project, but you've managed to finish it. Thank you for your support throughout the years. Anna and Annabel, it was insightful to discuss with you the sequencing experiments. It's great to see another perspective on these experiments. Although the results were not what I was after, the data you have sequenced has been incredibly valuable for Steffen's work. Ser, I'm grateful for your input on salt behaviour experiments. Jaap, you were a pleasure to talk with during our meetings. Also, a big shout-out to the group leaders, most notably Jeroen.

The experiments would never have taken place without the help of the great technical support staff, which makes AMOLF a unique place to work. Marko Kamp, I've lost count of the days you've worked on the setup to get it working for me. You always find time to work on it, even though you've got a dozen other people that need you. Marco Seynen, every time I needed more features of the software, you managed to implement them very quickly and better than I dared hope for. Bob, thank you for showing me around the lab, and I'm sorry for breaking that incredibly expensive quartz plate D: Then there are numerous people in the support department who helped with designing setups, 3D-printing prototypes, IT support, and manufacturing components.

I would like to thank Mark, Sjoerd, Marnix, Christiaan, Jan-Bonne and Melle whom I've had to pleasure to sit in the works council for two years. Taking on the role of secretary was a(n intentional) challenge, as it requires being structured and punctual, but you helped me get through it. Mark, you're a good leader and also friendly and constructive. Sjoerd, you've had a rough year, and still you managed to be pivotal to the OR. I wish you the best in your new job. Paula and Huib, you're a great team, and I really appreciated that you always took us seriously and were constructive, setting an example.

I've always said that the best part of AMOLF is the people working there. And the best of those people I got to share the office with for many years. Federica and Mario, you're two of the smartest, funniest, and kindest people I've ever met, and sharing the office with you has been awesome. I'm surprised that after these many hours of ~~hard work~~ pure craziness, such as throwing a ball in the sombrero hat, frisbeeing in the office, making funny sounds, singing about hobbits being taken to Isengard, lively discussions, tea breaks, and making weird faces, you managed to get your PhD degree. And both rightfully so cum laude! Also, a shout-out to the many generations of master students that have been in the office: Rosalie, Mick, Faan, and Leonie. Christiaan, you're super positive, and I'm impressed by your results. You'll do an excellent PhD!

Also, the other AMOLF people have been awesome. Marco, you are hilarious, a good friend, and I simply love you. We should play Arkham when we meet. Yuval is just objectively infinitely ad rem (only rivalled by Hannah), incredibly funny, and reasonably smart. There's just never a dull moment together. You've become a great friend, and I hope that we'll stay in touch for a very long time. Bart, you are a well of happiness, and you actually laugh at my jokes. I hope we get to play Eldrich again. Joris, I've enjoyed your humour and class. It seems I've found my match in making funky sounds. Martijn, thank you for your counselling conversations. Aditya, you're surrounded by an aura of fun. I have great memories of hikes with Nicola, Parisa, Olga, Mario, Fede, Allesandro, Marco, Elena, Masha, and Agata. Thank you for organising those hikes, Nicola! I hope we'll have another one in the future. Parisa, you just radiate positivity, and I've enjoyed our skiing trip. Simone Kienle, you're a very good listener, and I'm glad you were present at our gatherings long after you had left AMOLF. Agata, you might be the person with more energy than me. Olga, thank you for your support. I will organise a reunion with all of you when possible. Vanda, you are the mother of the biodepartment. Thank you for being helpful and looking out for everyone. Lennard, we had a great moment when we made the video for Yuval. Ruslan, thank you for running 30k with me as training. Annemarie, you're super supportive. Nasim, you dwarf others with your positivity. Anne-Sophie, you're hilarious, and I wish you the best with your PhD. Mareike, thank you for organising board game days. Thank you, Iarik and Tom, for joining soccer matches (sorry Iarik for running into you all the time). Florian, did the wall ever talk back? Anne-Bart, I think you're essentially made out of jokes. Also, a big shout out to the support I had from Jeff, Galja, Harmen, Anders, Celine, Katharina, Tzeni's, Christina, and Lukas. I would like to thank the AMOLF PV for organising so many memorable events that keep the community together. There are great memories of AMOLF Christmas (yearly epic silent disco dancing with Isabelle), Sinterklaas, ice skating, barbecue, borrels, board game nights (thank you, Yvonne), the yearly 'uitje'.

Doing a PhD is not only about science but also about developing oneself. I've had great pleasure doing that with sports such as soccer, spinning, running, condition training with Stephen, Alexander, Ruben, Renz, Joao, Bart, Eduart, Ruslan, Christiaan, and many others. Victor was the only one stupid enough to run a full marathon length obstacle course through muddy terrain with me. Singing with Louise and Daphne has been tremendously scary and rewarding. I've learned a lot about climate policy from my fellow members of the D66 climate group in Amsterdam. There were many relaxing cups of tea with my talented neighbour, Yael. In the last two years I had the pleasure of performing improv comedy with a large number of people in Amsterdam. It turns out that making

jokes is also something that can be done on stage, and some people might even pay for that (usually it's the other way around). Special thanks to the 'File Not Found' family with Willem, Nirvi, Guru, Karin, and Kristina. Guru, you are a genius improviser and good friend. Willem, you've actually got more energy than me, and with your unparalleled drive and talent, you'll soon become a professional. Within two years, you've made the improv community in Amsterdam crucially dependent on you. Nirvi, there is no way I can properly express how much I love you. You have a gigantic heart, are incredibly smart, funny, and have become one of my best friends. Rodrigo, you've been a great support for my PhD during our lunch breaks. A great thanks to Saskia, Amanda, Roisin, Ionut, Samy, Stacey, Joran, Thomas, Nicola, Huib, Jeanette, Elena, Mimi, Ben, Marco and many others of the improv community.

There are some great friends that live outside of Amsterdam that I love to thank, especially the 'bros', many of whom I still speak with at least on a weekly basis. Michiel de Goede, there's so much I admire about you that you've set the example for what I want to be since we met. Our trip to Africa was awesome. Olav, with you it's always laughter and energy, but you are also someone who you can share feelings with. Our trip to Nepal was awesome. Thijs, I think we have practically every interest in common, and it has been great to travel in Central America. I also enjoyed Portugal with you and Michiel Visscher, and the many games that we played together. Alistair, it's awesome to see you owning every ski slope, and you have the most clever jokes. Misha, I enjoyed our trips to Israel (also with Adriaan and others) and Morocco. Nick, you've been my oldest friend, and I wish you a happy life. Jordi, I love the many (long) board games that we play, and I greatly appreciate your kindness and serenity. Mick, I've had the pleasure of watching you transform during my PhD into the successful person you deserve to be. Jasper, I hope you're the pilot when I go on vacation. Jennifer, thank you for your support, and you have the cutest kids. Kasia, you're incredibly strong and supportive, and I hope we'll be in touch for a long time. Serena, thank you for your support and for showing me around during the worm meeting, I'm sure you'll become a successful group leader. Anna, our trip to South-Africa has opened my eyes, and I love the many discussions on life we have had.

Finally, there are the most long-term supporters. Mom and dad, there's no doubt that I owe you not just my mental capacity (and lack of beard growth), but more importantly the positive, open, and scientific attitude required to get a PhD. Thank you for being unconditionally supportive, despite my stubbornness. You've deserve all the success that you got. My big brother Chris, I've lifted so much on your wisdom and people's knowledge. No doubt my technical interests came from the many hours of playing LEGO and K'NEX when we were little. It's been great to see you become a father with Saskia by your side and Jasper, and

Floris (and Mickey) running around. And of course, my sweet twin sister Vivian, I'm so happy to hear that you'll start a new phase in your life with Steven and Sebas. It's incredible how much you've grown as a person in a few years. You've gained confidence and become the woman you deserve to be. I'd like to thank my genetic half brothers and sisters (my mom is an identical twin) Marloes, Adriaan, and Cathelijne, who have been supportive and very close friends for as long as I can remember. And thanks to the rest of the family, who are always interested in listening and applaud efforts to learn.

And thank you for reading.

LIST OF PUBLICATIONS

5. **W. Mathijs Rozemuller**, Steffen Werner, Greg J. Stephens, Thomas Shimizu *Long timescale whole-brain imaging of semi-immobilized C. elegans reveals response, output and modulation of collective neuronal modes.*, in prep. (2022)

4. **W. Mathijs Rozemuller**, Steffen Werner, Greg J. Stephens, Thomas Shimizu *Variability reveals optimality and control in C. elegans turning behaviour.*, in prep. (2022)

3. Werner, Steffen, **W. Mathijs Rozemuller**, Annabel Ebbing, Anna Alemany, Joleen Traets, Jeroen S. van Zon, Alexander van Oudenaarden, Hendrik C. Korswagen, Greg J. Stephens, and Thomas S. Shimizu. *Functional modules from variable genes: Leveraging percolation to analyze noisy, high-dimensional data.* bioRxiv (2020).

2. Helms, Stephen J., **W. Mathijs Rozemuller**[†], Antonio Carlos Costa, Leon Avery, Greg J. Stephens, and Thomas S. Shimizu. *Modelling the ballistic-to-diffusive transition in nematode motility reveals variation in exploratory behaviour across species.* Journal of the Royal Society Interface 16 (2019)

1. Heerema SJ, Schneider GF, **Rozemuller M**, Vicarelli L, Zandbergen HW, Dekker C. *1/f noise in graphene nanopores.* Nanotechnology. 2015

[†] Joint first author